"AN INVESTIGATION INTO THE PREDICTION OF THERMAL AND STRESS DISTRIBUTIONS SET UP DURING WELDING USING FINITE-ELEMENT ANALYSIS"

by

D J KESLER

A thesis submitted in partial fulfillment of the requirements for the Degree of Master of Science in the Faculty of Engineering

Department of Civil Engineering
UNIVERSITY OF CAPE TOWN

November 1983

DECLARATION

I, DAVID JONATHAN KESLER, hereby declare that this thesis is my own work and that it has not been submitted for a Degree at any other University.

Signed by candidate

November, 1983.

DEDICATION

I would like to dedicate this thesis to my wife Helene and my parents for their encouragement and support throughout this work during the last two years.

ACKNOWLEDGEMENTS

I would like to extend my appreciation to Associate Professor W.S. Doyle* under whose supervision this thesis was conducted, for his help, enthusiasm and suggestions which made this research a reality.

Mr D Botha and Mr G Bertuzzi for their assistance in the Civil Engineering Workshop.

Mr A Brink, of the Department of Metallurgy, University of Cape Town for the use of his original program "HOT" which was modified for use in this research.

The Council for Scientific and Industrial Research for their financial assistance.

The University of Cape Town for their financial assistance.

My sister, Andrea Lewis, for her immaculate typing of this document.

* Associate Professor, Department of Civil Engineering
University of Cape Town

ABSTRACT

During the welding process, thermal and stress distributions are set up in the workpiece. These thermal stresses are recognized as among the most important factors affecting the weldability of steels, producing distortion and cracking in weldments.

This thesis examines the history and theory of the welding process, including the mathematical and finite-element theory of heat conduction. Using simple models, the finite-element method is also compared with theoretical Fourier analysis solutions.

In addition, a complex two-dimensional finite-element thermal and stress analysis of the welding process is performed, in which a thermo-elastic-plastic finite-element model is used to predict the longitudinal welding stresses perpendicular to the weld. In this model, the weld is represented simply as a high temperature load acting at a predetermined position for a particular time interval. The metallurgical phase transformations and work hardening effects are ignored.

The predictions from the finite-element analysis are then compared with experimental data obtained from a welding test.

NOTATION

ROMAN UPPER CASE

A	Cross-sectional area
E	Young's Modulus, Energy
F	Force
G	Shear Modulus
H	Electrical Power
I	Arc Current
L	Length
M	Moment
P	Tensile Force
Q	Internally Generated Heat Flow
R	Strain Gauge Resistance
T	Temperature
V	Arc Voltage

ROMAN LOWER CASE

c	Specific Heat
dA	Incremental Area
dM	Incremental Moment
dS	Incremental Length
e	Electomotive Force
k	Thermal Conductivity
q	Heat Flux
$\dot{q}$	Energy Generated per Unit Volume
s	Direction
t	Time, Absolute Temperature
u	Temperature
x,y,z	Cartesian coordinates

GREEK UPPER CASE

Δ	Change in
Π	Total Potential Energy
Σ	Summation of

GREEK LOWER CASE

α	Thermal Diffusivity, Coefficient of Linear Expansion, Seebeck Coefficient
γ_{ij}	Shear Strain on Face i in Direction j
δ	Change in
ε_i	Normal Strain in Direction i
θ	Temperature
κ	Thermal Diffusivity
λ	Eigenvalue, Thermal Conductivity
$\mu\varepsilon$	Microstrain
ν	Poisson's Ratio
ρ	Density
σ_i	Normal Stress in Direction i
τ	Thickness
τ_{ij}	Shear Stress on Face i in Direction j

MATRICES AND VECTORS

B	Strain Matrix
C	Damping Matrix
K	Stiffness Matrix
M	Mass Matrix
N	Interpolation Function Vector
T	Nodal Degrees of Freedom
U	Displacement Matrix
$\dot{U}$	Velocity Matrix
$\ddot{U}$	Acceleration Matrix

CONTENTS

CHAPTER ONE

INTRODUCTION TO WELDING

1.1 DEFINITION OF WELDING

It has often been attempted [1, 2, 3] to assign a definition to the term "welding" but this has proved difficult due to its wide scope and many fields of application. Being basically a metallurgical operation, it can be performed in widely differing situations in different ways and on many different materials. Some of these widely differing situations include the fabrication of car bodies, the site welding of buildings and bridges, the manufacture of aircraft components and even the construction of giant reactor pressure vessels for nuclear applications.

Due to the lack of knowledge or understanding of the different technologies used to make the process of welding effective, welding has remained partly obscure and has been accepted as just another fabrication tool.

1.2 HISTORICAL BACKGROUND

Welding techniques during the prehistoric days [2], before 3000 B.C., consisted of soldering with lead-tin or copper-gold alloys. The joining processes were limited to brazing, soldering and forging because of the relatively low temperatures availible. The reason for this low available temperature was that only wood and coal could be used as a heat source.

The earliest known example of welding dates back to around 3000 B.C. and was found in Mesopotamia. It consisted of a brazed joint in a piece of copper panelling. In this Bronze age, a casting-in process had been used to join together components. An example of this process can be described in the production of a sword [2]. To make this sword, its blade and handle were placed close together. This was followed by building a mould around the joint to be made between the blade and handle. Superheated metal was then poured into the mould, forming a bridging casting. Another fact known at the time was that certain alloys would melt at a lower temperature than other alloys or even pure metals. In particular, it was known that gold-silver alloys would melt at a lower temperature than gold. These gold-silver alloys were joined together using a process that we would now call "hard soldering", and which was used to produce extremely skillful work in Ur dated at 3000 B.C.

Examples of solid-phase welds of the blacksmith type [1] are known from about 1320 B.C. in the Middle East, one example having been found in the Tomb of King Tutankhamen in Egypt.
Similar examples of solid-phase welds are known from about A.D. 310 in India (the Delhi Pillar) and from A.D. 400 in Europe. Very early examples of full fusion welding, possible "burning-on" joining of cast parts and repairing of defective castings, do exist and are dated at 500 B.C.
In the Iron Age [2] forge welding was developed by the discovery that pieces of wrought iron could be joined by heating the pieces and hammering them together.
The development of modern welding technology in general was initiated when electricity became commercially available after the latter half of the nineteenth century. During the period between 1880 and 1900, most of the important discoveries leading to modern welding processes were made, the processes invented being arc welding, oxyacetylene welding and electrical resistance processes.
Other than the processes of riveting and bolting, the only metal joining processes until the 1890's had been forge welding and hard soldering.
In 1724, Reverend Desagulier discovered what we would now call "pressure welding" [2] . In 1856 Joule found that metals could be joined using contact resistance heating but both of these important discoveries were ignored. In 1885 a process was invented by Bernados in which the edges of two pieces of metal were heated by an electric arc and joined together. This event precipitated the development of a large range of arc welding processes which today are used for the welding of a far larger volume of metal than any other joining process. Round about 1885, an important discovery by Elihu Thompson was made [2]. He discovered that if a heavy current passed through two pieces of metal in contact, they became joined together. This discovery initiated the resistance welding processes which are today vital in the mass-production industries.
In the 1890's the French chemist, Le Chatelieur realized that if one could burn oxygen and acetylene together, the resulting flame would have a temperature greater than that of any flame known at the time. This flame would also have the capacity to melt steel.
This discovery led to the development of the oxy-acetylene welding

process which is now widely used for limited production welding and jobbing work.

Before the Industrial Revolution, the development of welding was given the most incentive by the need for armaments and in many parts of the world, examples of welded chain link armour, welded swords and welded metal inlaying of armour still survive today.

However, the development of welding in civil applications was spurred by the Industrial Revolution and thus the invention of the oxy-acetylene blowpipe was quickly adapted to fabrication and repair. This did not happen with the electric arc and resistance heating processes until a military spur was applied by the First World War (1914-1918) and later the Second World War (1939-1945).

During the First World War [3] the process of metal arc welding was used in ship construction for the first time, although the primary use was for repair. The first all-welded ocean-going ship was built in 1921 and from this begining, welding applications increased at a steady pace during the 1930's. The development of inert-gas arc welding processes was accelerated by the demand for reliable methods for welding the light-metal alloys used for aircraft.

During the Second World War [3] a drastic change occured in ship construction when there was a swing away from riveting with welding taking dominance. The United States of America, in particular, entered into the large scale production of welded ships for the first time in history. This aimed at meeting the urgent demand for a large number of ships needed for the war and by this time, the technique of steel plate welding had been well established. A major disadvantage had been the lack of knowledge and experience regarding the design and fabrication of large welded structures and their fracture characteristics. This was manifested by the fact that of about five thousand merchant ships built during the Second World War in the United States of America, about one thousand experienced strucural failures with about twenty breaking in two or being abandoned. The result of these failures was an enormous research programme in the field of welding and fracture and before 1955, the technology for the fabrication of welded ships and other structures was established, with most ships built in the world being fabricated by welding by 1960.

Welding practice and theory [1] has advanced more since 1939 than in the whole of the previous history of welding, hence a previously secretive art has now devloped into an established and progressively

modern technology with special techniques being developed which offer special advantages over other processes.

Some of these processes [2] are extremely sophisticated, involving the use of lasers for the formation of small localized welds in fragile components, or the use of high-energy electron beams in a vacuum to provide the heat for melting metal.

The last thirty years has seen the development of new welding processes including carbon-dioxide gas shielded arc welding, ultrasonic welding, friction welding, plasma arc welding and laser processes [3] . As a result of this, most metals used today can be welded, although the properties of the available filler metals and the heating source characteristics dictate primarily present day practice.

Today, the most widely used material for large structures remains steel although other construction materials have been developed. Low carbon steels are used for most applications, although high-strength steels are being used increasingly.

1.3 INTRODUCTION TO SHIELDING

Basically, welding is a process whereby a heat source is used to melt the abutting edges of the components to be joined, the most common heat source being oxy-fuel gas flame, resistance heating and high-energy beams [4] . The molten metal produced by the heating must be shielded from the oxygen and nitrogen in the atmosphere. Shielding methods include flux shielding (metal arc, submerged arc or electroslag welding) or gas shielding (carbon-dioxide welding). Welding is usually done using a coated electrode, whose coating decomposes to provide shielding. The electrode coating must provide gas shielding for the arc, easy arc shielding and adequate mechanical properties of the weld metal , in addition to providing a protective slag preventing oxidation of the weld metal as mentioned above. In the case of gas-shielding, the shielding was originally obtained by using cellulose in the electrode coating. A protective atmosphere is formed upon the combustion of the cellulose: [2]

$$(C_6H_{10}O_5) + \frac{n}{2} O_2 = 6\ CO + 5\ H_2$$

On the outer fringe of the flame, the carbon monoxide and hydrogen react further with oxygen from the air.

$$2CO + O_2 = 2CO_2$$

$$2H_2 + O_2 = 2H_2O$$

1.4 WELDING PROCESSES

At the present time, there are more than fifty different types of welding processes that can be used commercially to join metals. We can classify the joining processes into 5 categories [3] :

1. Fusion Welding In this process, the parts to be joined are heated until they melt together, with pressure not being necessary to effect the bond.
   Examples of this type of welding are arc welding, gas welding, electron-beam welding and laser welding.

2. Electrical Resistance Welding In this process, the parts to be joined undergo two stages. Initially, heating is carried out by passing an electric current through them. Second stage involves the application of pressure to effect the bond.
   Examples of this type of welding are spot welding, upset welding and percussion welding.

3. Solid-phase Welding In this process, pressure is applied to the metals to be joined but no melting occurs, except for the very thin layers near the surfaces to be joined.
   Examples of this type of welding are forge welding, friction welding and pressure welding.

4. Liquid-solid Phase Joining In this process a dissimilar molten metal is added when the parts to be joined have been heated to a temperature lower than their melting points. This forms a solid joint upon cooling.
   Examples of this type of joining process are soldering and brazing.

5. Adhesive Bonding In this method, the molecular attraction between the adhesive and the surface to be bonded results in the formation of a joint.

The adhesives are usually animal and vegetable glues, cements, asphalts and various plastics such as epoxy.

The following welding processes are commonly used for the fabrication of large structures:

1. Shielded metal-arc welding
2. Submerged arc welding
3. Gas shieled-arc welding
4. Vertical automatic welding (electroslag and electrogas)

1.4.1 SHIELDED METAL-ARC WELDING

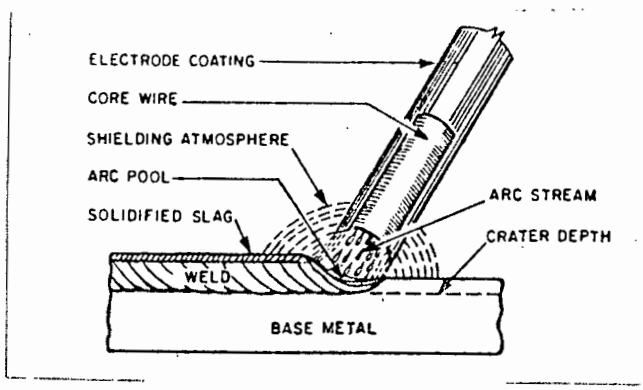

Fig 1.1 Shielded metal-arc welding

In this arc-welding process, heating with an electric arc between a covered electrode and the work produces coalescence. The decomposition of the electrode covering provides the shielding. No pressure is used and filler metal is obtained from the electrode. The process is limited to a manual one as a welding operator is required to manipulate the covered electrode.
Fig 1.1 represents the shielded metal-arc process. The equipment necessary to operate the electrode comprises an electric power supply designed specifically for the process, insulated elctrode holders which should have an adequate electric and thermal capacity, cables and grounding clamps. The process can use alternating or direct current with currents between 15A and 500A and arc voltage between 14V and 40V. The resulting welds are usually built up in thin layers, allowing a partial refining of the grain of proceeding layers. This will result in the improvement of ductility and impact resistance of

the weld metal.

For over thirty years, the idea of mechanizing the shielded metal-arc process had existed. Attempts had been frustrated by the fact that the electrodes were not advanced enough to be used for large scale production. The development of modern contact electrodes using high iron-oxide and iron powder coating has shown that a sound quality weld metal can now be obtained without the necessity of electrode manipulation.

1.4.2 SUBMERGED-ARC WELDING

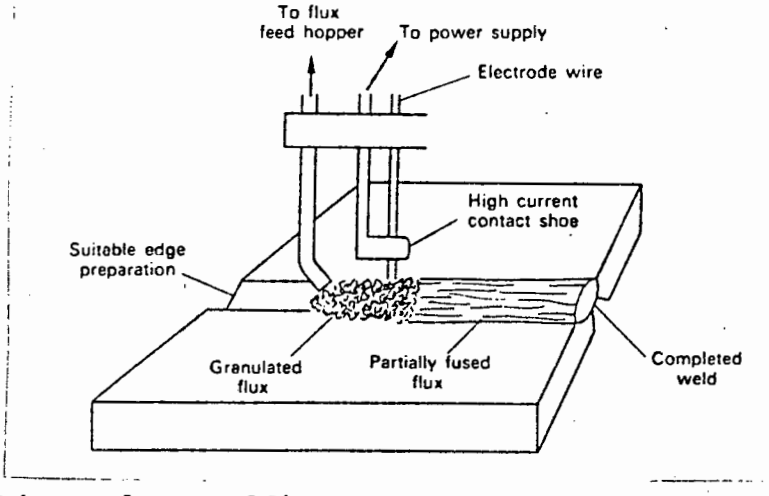

Fig 1.2 Submerged-arc welding

This is an arc-welding process whereby coalescence is produced by heating with an electric arc between a bare metal electrode and the work, the shielding being provided by a layer of granular, fusible material on the work. Pressure is not used and the electrode provides the filler metal, although this is often supplemented by another welding rod. Fig 1.2 shows the process schematically.

The fusible shielding metal is known as "flux" which consists of a finely crushed mineral composition that when cold is a non-conductor of electricity, but in the molten state, is highly conductive. Due to its ability to produce satisfactory welds at high deposition rates, this submerged-arc process is widely used.

The currents used are much higher than those used in manual metal-arc welding, the maximum current for one electrode being 2000A. As a result of these high currents, a very coarse columnar structure forms in the weld metal with an enlarged heat-affected zone in the base metal as compared to multi-pass welding when the input of energy

is smaller.

As the sizes of the structures began increasing, one-sided submerged-arc welding became necessary as difficulties were experienced when trying to turn over large plate assemblies. The main advantage of one-sided submerged-arc welding is that the flow line of the fabricating system is simplified at the assembly state. Due to the fact that the work does not have to be turned over, the whole assembly can be placed on a conveyor system hence production efficiency can be increased and the entire process of production can be systematically controlled.

1.4.3 GAS-SHIELDED-ARC WELDING

In this process, coalescence is produced by fusion from an electric arc maintained between the end of a metal electrode and the part to be welded. A shield of protective gas surrounds the arc and the weld region. The electrode is either consumable or non-consumable with pressure and filler material addition usually associated with the process.

Two types of gas shielded-arc welding processes exist.

1.4.3.1 Gas-tungsten-arc Welding

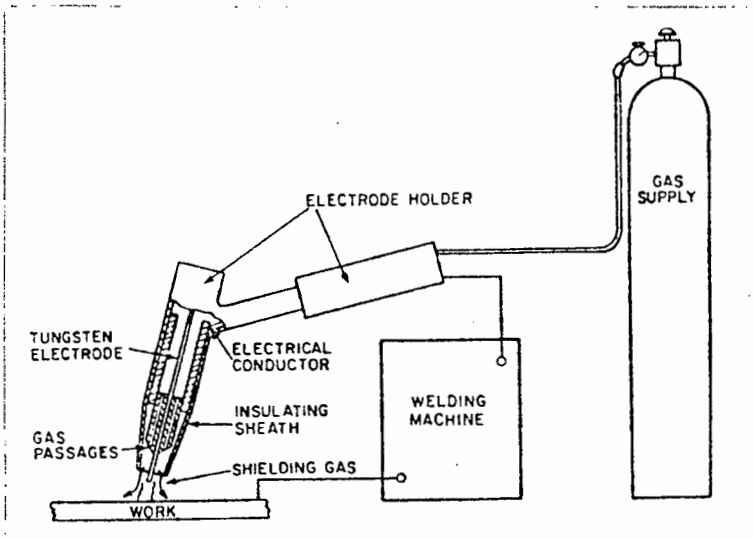

Fig 1.3 Gas tungsten-arc welding

In this method, the shielding gas is fed through an elecrode holder, commonly known as a "torch".

The inert gas, argon, is usually used as the shielding gas.

A tungsten or graphite electrode, which will not vaporize or melt too quickly in the intense arc heat, is used.

1.4.3.2 Gas Metal-arc Welding

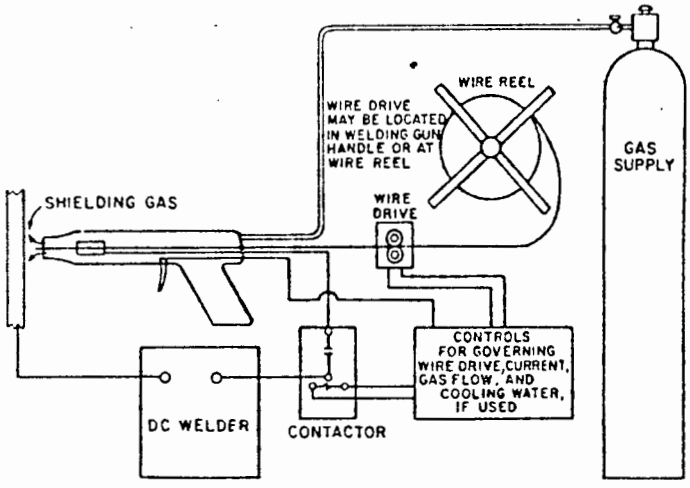

Fig. 1.4
Gas metal-arc welding

In this process, a filler wire in coil form is fed mechanically into the welding arc, whose travel can be controlled manually or mechanically. The electrode is usually just a bare wire, but flux covered wires are also commonly used. The shielding gases include argon, helium and carbon dioxide. Often carbon dioxide and a mixture of carbon dioxide and oxygen are used for welding carbon steel as the inert gases are very expensive. By comparison to the previous process, the gas metal-arc welding process is known for its high deposition rate hence it is used chiefly for welding heavy plates. The welding of thin sheets is done mainly using the gas tungsten-arc process.

1.4.4 VERTICAL AUTOMATIC WELDING PROCESSES

1.4.4.1 Electroslag Welding

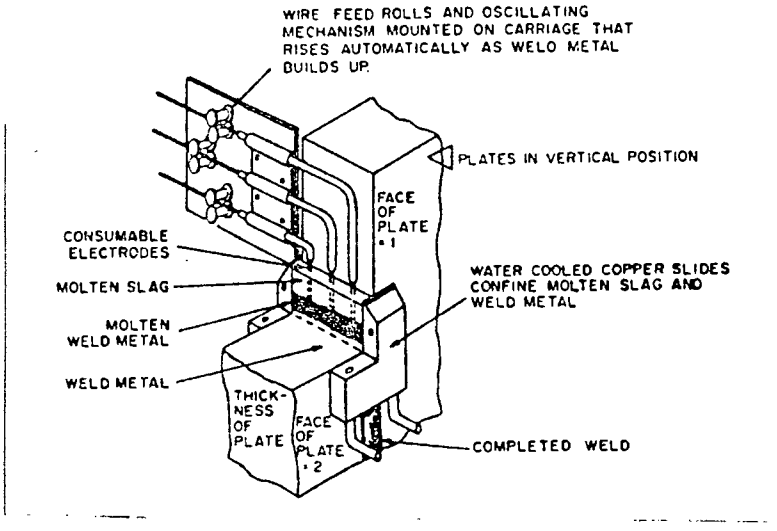

Fig 1.5 Electroslag welding

This process is based on the principle that heat is produced by passing an electric current through molten slag. The electrode is immersed in the molten slag between the work to be welded and the moulding devices. A current passing between the electrode and the base metal heats the melt to a high temperature resulting in an increase in the electrical conductivity. The melting point of the base and filler metal must be exceeded by the temperature of the slag pool. The slag then melts the faces of the work and the electrode is immersed in the molten slag. When the molten base and filler metal collect at the bottom of the slag pool, the weld pool is formed which solidifies and forms the weld which joins the faces of the components. As the electrode melts and shortens, it is lowered.

This method was developed for joining of thick sections positioned vertically with welding beginning at the bottom of the joint and progressing upwards by moving the welding head and auxilliary equipment.

1.4.4.2 Electrogas Welding

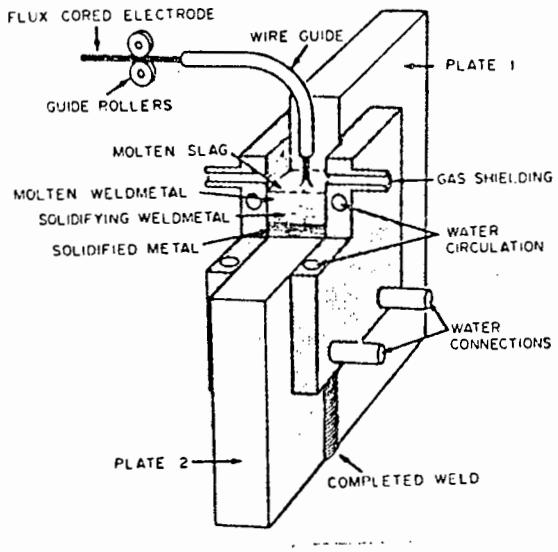

Fig 1.6 Electrogas welding

This process is a fully automatic one, providing a method of fusion welding butt, corner and tee-joints in the vertical position. In electrogas welding, the gap between the components being welded is bridged by water-cooled copper bridges forming a rectangular cavity containing the welding operation. A flux-cored wire is fed into the cavity by a wire guide. An electric arc is established between the electrode and the weld pool and is maintained continuously. Helium, argon, carbon dioxide or mixtures of these gases are fed into the cavity continuously to provide a suitable shielding atmosphere for the arc and weld pool.

Deoxidisers and slagging materials provided by the flux core of the electrode clean the weld metal. Upon deposition of the weld metal, the wire feed, carrying the wire guide and copper shoes, moves upwards at a steady rate providing a weld capacity of uniform width in which the weld is deposited.

1.5 TYPES OF WELDS

Two types of welded joints are used in the welding of structural steels. These are butt welds and fillet welds. [5,6]

1.5.1 BUTT WELDS

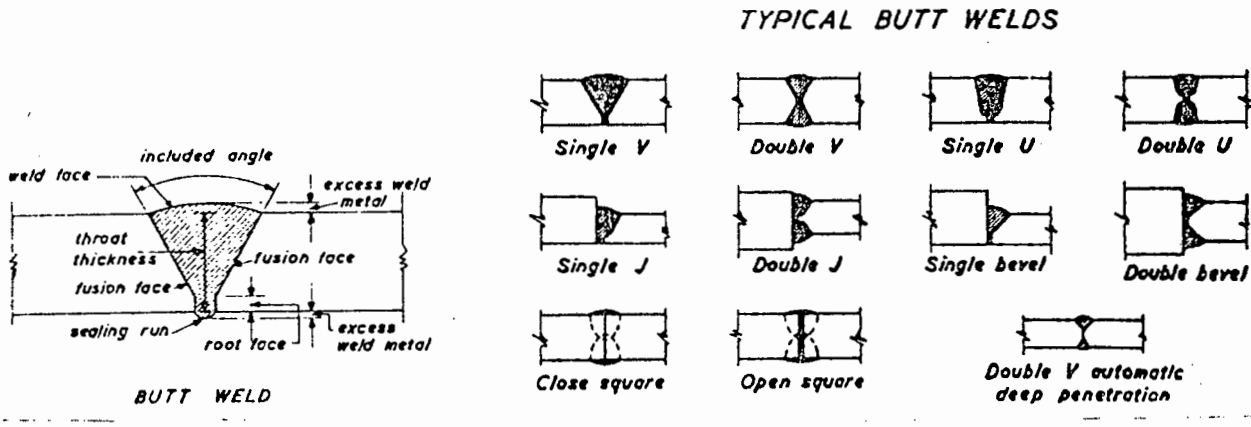

Fig 1.7 Butt welds

The names of the butt welds describe the edge preparation of the plates. The strength of a butt weld is the same as the strength of the parent plate if the weld can be made from both sides or a sealing run can be placed on the side away from where the weld is laid down. The stresses are the same as for the parent metal. With correct edge preparation and a properly controlled welding process, butt welds are perfectly reliable.

Butt welds are used extensively in welded structures for the following reasons:

1. The joint efficiency is high (joints with 100% efficiency can be achieved for a number of materials).

2. Airtight and watertight joints can easily be obtained.

3. The design of the joint is simple.

4. The joint surface is almost flush.

1.5.2 FILLET WELDS

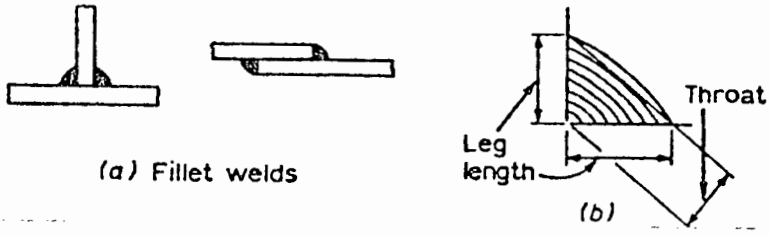

Fig 1.8 Fillet welds

The size of a fillet weld is specified by the leg length while the strength of the weld is calculated on the throat thickness.
In modern fabrication, automatic prosses are finding increasing use, and continuous fillet welds on web-to-flange welds of plate girders is standard practice, having better fatigue properties and resistance to brittle fracture.

1.6 BASIC METALLURGICAL ASPECTS OF FUSION WELDING

Schlenker [7] shows that four steps are necessary in every fusion-welding process:

1. The heating of the parent metal.

2. Weld metal deposition by the correct manipulation of the torch flame or electrode.

3. The cooling of the weld.

4. Possible reheating of the welded zone to relieve stress within the weld itself or the parent metal or both.

If we examine a polished, etched section through a fusion weld under a microscope, three main zones will be noticed:

1. The unaffected parent metal, either side of the weld.

2. The weld deposit.

3. The "heat-affected-zone" which exists along the boundaries of the weld deposit, being an area where the welding process has caused changes in the parent metal structure. (abbreviated HAZ)

All these zones are shown in Fig 1.9

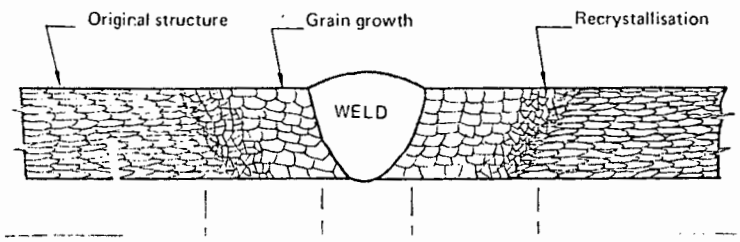

Fig 1.9 Section through a fusion weld

It is of interest to examine two of the zones.

1. The Weld metal
2. The "heat-affected-zone"

1.6.1 THE WELD METAL

The weld deposit resembles a miniature casting which has been cooled rapidly from an elevated temperature. A number of factors dictate the actual crystalline structure, the most important being the number of "runs" performed to deposit the weld metal.
In the case of a single run weld, examination will show long columnar crystals growing outwards from the side of the weld. (see fig 1.10). With an exceedingly high welding temperature, a plane of weakness will be formed by these columnar crystals meeting at the centre of the weld deposit. This condition causes inter-crystalline cracking within the weld. By using the correct welding temperature, equaxial grains form at the centre of the weld before the columnar crystals have a chance to meet. This condition results in a stronger joint.

Fig 1.10 Structure of single run arc weld

A different pattern emerges during multi-run welding. In this case, the initial run has the structure as mentioned in the single run weld. The difference occurs when the second run normalizes the first run causing grain refinement and destruction of the original columnar structure. Each additional run normalises the previous one so that the only run that shows the coarse cast structure typical of a single run weld will be the final run (see fig 1.11)
It should also be noted that the possibility of weld defects increase in a multi-run weld.

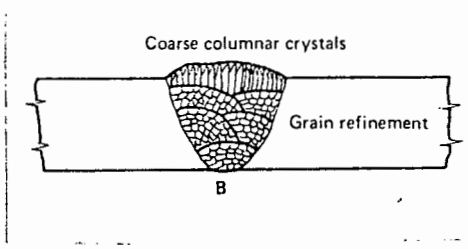

Fig 1.11 Structure of a typical multi-run arc weld

1.6.2 THE "HEAT-AFFECTED ZONE"

A large number of factors dictate the extent of changes caused in the "heat affected zone", the most important factors being the dimensions of the object being welded, the composition and thermal conductivity of the parent metal and the duration that the metal is heated above critical temperatures during the welding process.
The easiest ferrous metal to be welded is mild steel with a typical heat affected zone ranging from an overheated zone near the weld metal to an under-annealed structure further away from the weld itself.
Welding difficulty is experienced with medium and high carbon steels, as complex structures form within the heat affected zone due to the rapid rate of cooling. This rapid cooling generally causes an

increase in hardness across the weld and for this reason, these steels usually undergo a controlled cooling procedure to prevent martensite formation, martensite being the hardest form of steel known.

1.7 JOINT PREPARATIONS

Joint preparations are carried out to ensure the degree of penetration and ease of welding that is necessary to obtain a satisfactory weld [4]. Main factors affecting the choice of preparation are the type and thickness of the metal, the process of welding being used, the degree of penetration required to effect the weld, the economy and weld metal consumption, the welding accessibility, the control of distortion of the piece being welded and the type of joint required.

In the case of a fillet weld, no preparation of the edges of the parts being joined is necessary. This does not generally apply to butt welds, in which the weld metal lies substantially within the planes of the surfaces to be joined. The rest of the discussion about joint preparation will be directed at the butt weld.

1.7.1 REASONS FOR JOINT PREPARATIONS

1.7.1.1 Penetration

In this discussion we consider the manual metal-arc welding process with a weld being laid on a plate [4]. Unless we use a special type of electrode called a "deep penetration" electrode, the depth of penetration will be limited, as shown in Fig 1.12a If a butt weld was made with no edge penetration, the resulting joint would have incomplete penetration and consequently would lack strength unless the thickness of the plate was very small, as shown in Fig 1.12b. If a gap is left between the plates, a better joint would result, but if the gap is made too large, the weld metal would fall through and the thickness would still be limited, as shown in Fig 1.12c.
Hence, the only way to increase the gap size without the weld metal falling through would be to use a backing strip, although

lack of fusion of the sides is possible due to inadequate electrode access, as shown in Fig 1.12d

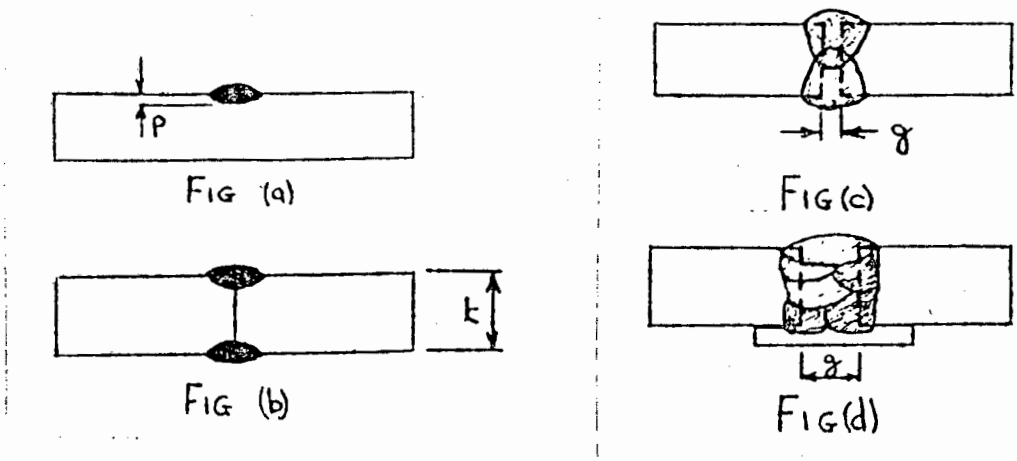

Fig 1.12 Penetration

If one wants to obtain good fusion as well as full penetration, edge preperation is essential to give access to the electrode, shown in Fig 1.13. The magnitude of the groove angle, α, depends on the electrode diameter, arc length and welding position. The angle should also be as small as possible to give a minimum deposited weld metal for economic and distortion reasons.

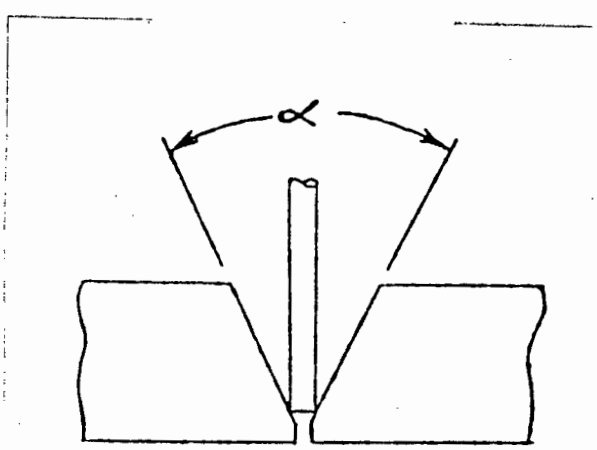

Fig 1.13 Weld section showing groove angle

1.7.1.2 Heat Flow

The main requirement of a fusion weld is heat. The rate at which heat, via the arc, is input to the joint depends on the welding current, the arc voltage and the speed at which the weld is being laid. Heat is also removed from the joint at a rate which is a function of the size and conductivity of the material. In general, the thicker the plate used, the higher the rate of heat loss into the plate neccessitating a higher rate of heat input to produce the weld, shown in Fig 1.14

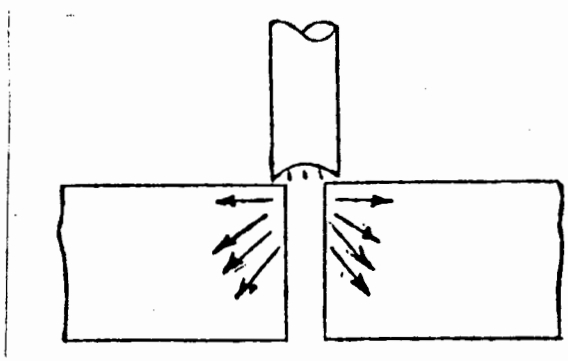

Fig 1.14 Heat loss in a thick plate

The above conditions can be modified using edge preparation. For example, a single V preparation will reduce the plate thickness locally and hence reduce the ammount of heat escaping into the plate, shown in Fig 1.15

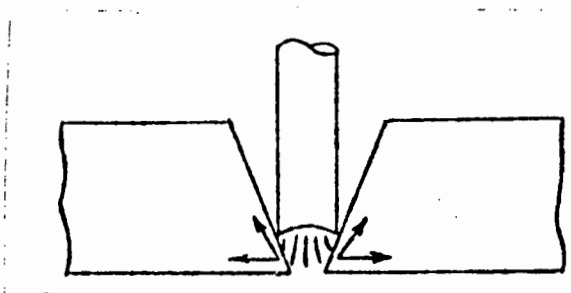

Fig 1.15 Single V preparation

If the bevel on the plate edges is taken right through the plate, as shown in Fig 1.15, the possibility arises that because there is too little metal to allow heat escape, the arc will burn completely through the plate instead of making a weld. (see Fig 1.16) For this reason, a small root face is usually left in practice when using this joint preparation.

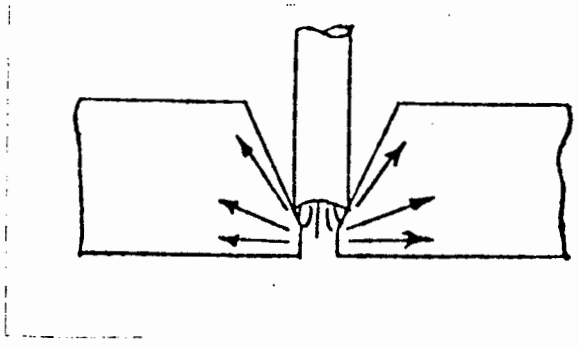

Fig 1.16 "Burnt-through" plate joint

1.7.1.3 Distortion

Upon cooling from its molten temperature, the deposited weld metal will attempt to shrink and accomodate this shrinkage, hence distortion will take place, as shown in Fig 1.17

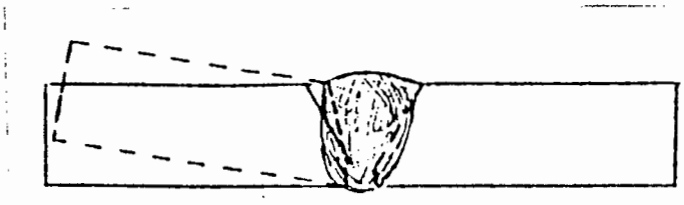

Fig 1.17 Distortion due to shrinkage

In a V-butt weld, the shrinkage on each side of the weld can differ resulting in a rotation of one part to the other. As the plate thickness increases, the difference in shrinkage from one side to the other will increase and hence the total distortion will increase. This distortion can be controlled by using a double-sided preparation (see Fig 1.18) so that welding on alternate sides of the joint will balance the heat input and hence the distortion.

The cost of turning the work over several times, however, must be investigated against the cost of correcting the distortion.

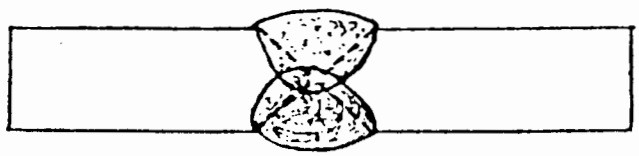

Fig 1.18 Double-sided preparation

1.8 PROBLEMS WITH WELDED STRUCTURES

Welded structures are not free from problems [3] and some of the major difficulties with welded structures are as follows:

1.8.1 DIFFICULT-TO-ARREST FRACTURE

Once a crack starts to propogate in a welded structure, it is very difficult to arrest it, hence the study of fracture in welded structures is very important.

1.8.2 POSSIBLITY OF DEFECTS

Welds are often plagued by defects such as porosity, cracks and slag inclusion.

1.8.3 SENSITIVITY TO MATERIALS

Some materials are more difficult to weld than others, for example, high-strength steels are generally more difficult to weld without cracking and are more sensitive to even small defects.

1.8.4 LACK OF RELIABLE NON-DESTRUCTIVE TESTING TECHNIQUES

No non-destructive testing methods are completely satisfactory in terms of cost and reliability.

1.8.5 RESIDUAL STRESS AND DISTORTION

Due to local heating during welding, complex thermal stresses occur with residual stresses and distortion resulting. Thermal stresses, residual stresses and distortion cause cracking and mismatching while high tensile residual stresses in areas near the weld may cause fractures under certain conditions. Distortion and compressive residual stresses in the base plate may reduce the buckling strength of structural members.

1.9 WELD DEFECTS

Welds often contain various types of defects, the commonest being as follows:

1.9.1 POROSITY

This is shown in Fig 1.19

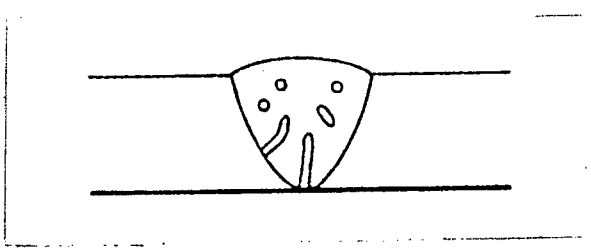

Fig 1.19 Porosity

The term porosity refers to gas pockets or voids free of any solid material either scattered uniformly throughout the weld, isolated in small areas or concentrated at the root. Porosity is caused by the release of gas as the weld metal cools and its solubility is reduced, and also from gases formed by chemical reactions in the weld. It can be caused by excessive welding temperatures or incorrect manipulation and can have various shapes, being spherical, worm shaped or elongated in the solidification direction of the weld metal.

1.9.2 SLAG INCLUSIONS

This is shown in Fig 1.20

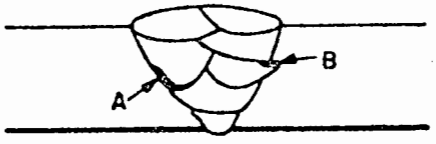

Fig 1.20 Slag inclusions

This term describes the oxides and non-metallic solids that become trapped in the weld metal or between the weld metal and the base, generally coming from the electrode covering material or from fluxes used in the welding operation. In multilayer welding operations slag inclusions will result if the slag between layers is not removed. Slag removal is readily accomplished by chipping.

1.9.3 TUNGSTEN INCLUSIONS

If access difficulties require the electrode to stick excessively, the occasional touching of the electrode to the work or to the molten weld metal in the gas tungsten-arc welding processes may transfer particles of tungsten into the weld deposit. These tungsten inclusions are generally undersirable.

1.9.4 INCOMPLETE FUSION

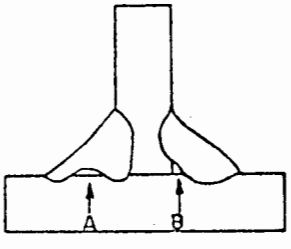

a. Incomplete fusion in fillet welds.
B is often termed "bridging"

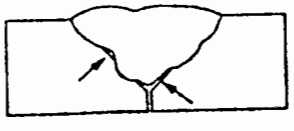

b. Incomplete fusion in a groove weld.

Fig 1.21 Incomplete fusion

This is shown in Fig 1.21. Incomplete fusion describes the failure to fuse together adjacent layers of weld metal or adjacent weld metal and base metal. This type of failure can occur at any point in the welding groove. It may be caused by failure to raise the temperature of the base metal (or previously deposited weld metal) to the melting point, or failing to remove slag, mill scale, oxides or other foreign material present on the surface to which the deposited metal must fuse.

1.9.5 INADEQUATE JOINT PENETRATION

This is shown in Fig 1.22

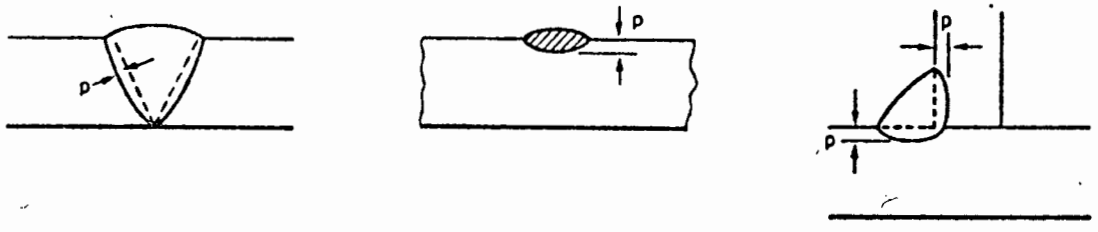

Fig 1.22 Inadequate joint penetration

Penetration describes how far the weld extends into a joint. In the condition above, the penetration is less than that specified and can hence be termed a defect, depending on what is specified for the weld. Reasons for inadequate penetration are inaccurate preparation where the root face is too thick or no root gap exists, low power input or travel speed that is too high.

1.9.6 UNDERCUT

This is shown in Fig 1.23

Fig 1.23 Undercutting

This describes a groove melted into the base metal adjacent to the toe of the weld and left unfilled by the weld metal. It also describes the melting away of the side wall of a welding groove at the edges of a layer of bead, forming a sharp recess in the sidewall in the area to which the next layer of bead must fuse.
This can occur if a weld is specified between the materials of widely differing melting points. Undercutting is also a result of energy inputs which are too great for the section thickness, incorrect electrode angle, excessively slow travel speeds or even the incorrect shielding gas.

1.9.7 CRACKS

Cracks result from ruptures of metals under stress and can be large or very narrow seperations in the weld metal, heat-affected zone or base metal. Cracks are one of the most harmful of welding defects with most specifications prohibiting them. Very small cracks, too small to be resolved by inspection procedure, are permitted, as they may not reduce the service of the weld.
In the weld metal, cracking often occurs if the joint is restrained due to contractional strains set up in the metal as it cools [7]. This is called "hot cracking" and is usually of an intercrystalline nature. Crater cracks often form down the centre of an electric-arc weld deposit due to hot shrinkage, but can be prevented by the correct manipulation of the electrode during the welding operation.
In the heat affected zone, cracking may occur in high carbon steels due to the formation of a martensitic structure. If the joint is prepared under restraint, this cracking is very pronounced. The cracks are related to the presence of hydrogen in the weld which, because it is insoluble in martensite, collects in microfissures in the metal and exerts sufficient pressure to cause metal cracking in the heat affected zone. This cracking can be prevented by preheating since it slows down the cooling rate in this zone.
In the parent metal, cracks called "lamellar tearing" can occur and display a stepped formation [4] which are usually parallel to the plate surface. These cracks can originate due to strain which occurs if welding is introduced at right angles to the section thickness, as shown in Fig 1.24.

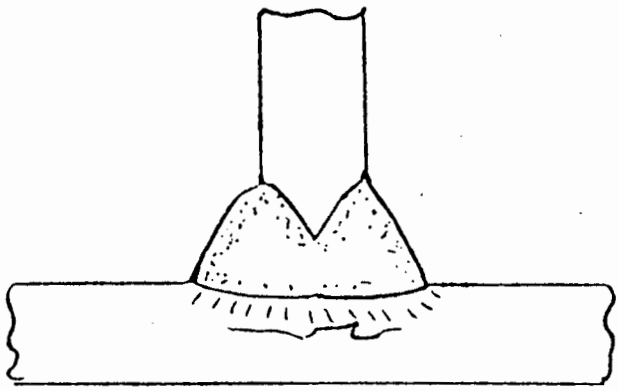

Fig 1.24 Lamellar tearing

1.9.8 ARC STRIKES

Although arc strikes are not normally considered defects, fractures often initiate from them which are formed during the unintentional melting or heating of areas outside the intended weld deposit area. They are usually caused by the welding arc but can also be produced beneath a badly secured ground connection. This results in a small melted area which can produce undercut, hardenings or local cracking, depending on the base metal.

1.9.9 OVERLAP

This is an imperfection at the toe or root of a weld and is caused by metal flowing onto the surface of the parent metal without fusing to it. In the manufacturing process, overlapping can occur due to excessive weaving, the incorrect electrode angle or a travel speed that is too low. Also an excessively low energy input prevents fusion to the parent metal (See Fig 1.25)

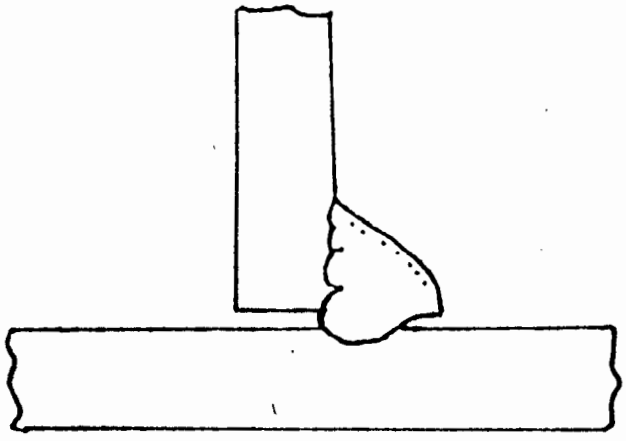

Fig 1.25 Overlapping

1.10 CONCLUSIONS

In order to design and fabricate a soundly welded structure, the following points should be adhered to:[3]:

1. The design should be adequate.

2. The materials should be properly selected.

3. The equipment used should be adequate.

4. The proper welding procedures should be followed.

5. Good workmanship is essential.

6. Strict quality control should be maintained.

CHAPTER TWO

INTRODUCTION TO RESIDUAL STRESSES

2.1 WELDING STRESSES

There are three ways in which stress can arise in welding [1]:

1. Deliberately applied stresses.

2. Incidentally applied stresses.

3. Incidentally developed residual stress.

Deliberately applied stress is related to solid-phase welding and is most likely to be compressive with incidental shearing and tension. Incidentally applied transient and residual stresses can develope in any type of welding process. These stresses can be great if a large amount of plastic deformation, likely to leave appreciable amounts of residual stress when the applied stress is removed, takes place. As far as the stress intensity is concerned, if the purpose is to keep two faces in contact, then the stress may be low, but if plastic deformation is required, the yield stress of the material must be overcome during welding. Stress may fall off from a high intensity as the temperature increases.

During a welding process, local stress is generated by differential expansion as heat flows away from the source. This flow is likely to create compression near the source as expansion occurs against the resisting cold backing material and tension in the backing material as it resists the adjacent expansion. This is shown in Fig 2.1

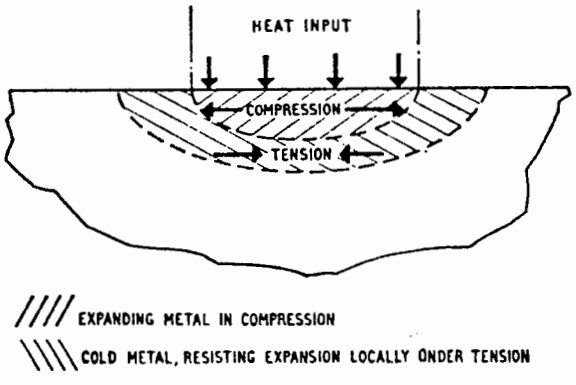

Fig 2.1 Stress effect of heat flow in local surface heating

If a high stress exists plastic deformation can occur initially in the zone of compression. This deformation will then spread out into the tension zone. When cooling begins, the compressed zone will be potentially shortened hence the stress pattern will reverse as the temperature decreases to a normal value. At room temperature, residual tension will remain in the originally compressed zone which will be opposed by a compressive stress in the previously tensile zone. This is shown in Fig 2.2

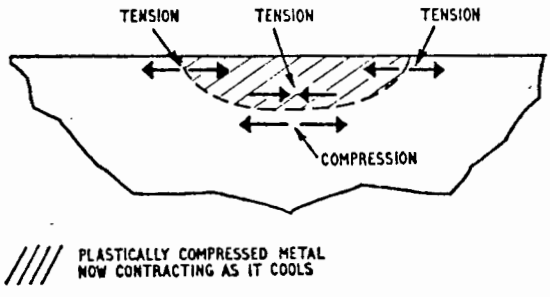

Fig 2.2 Residual stresses resulting from local heating

Any local plastic deformation during the welding process will generate residual stress, the nature depending on the mode and deformation pattern. If a progressive weld is being made, the speed of progression relative to the thickness and quality of the material will modify the amount and nature of the plastic deformation and hence, residual stress. Another influence affecting expansion and contraction is a structural change in the material. Any phase change in the material is a potential cause of plastic deformation and residual stress.

2.2 STRESS AND STRAIN

If a set of forces is acting on a body and the body is in a state of equilibrium, it is said to be in a state of stress. These stresses can cause deformations or strains in the body. [3]

2.2.1 STRESS

Stress is usually expressed as a load or force per area, metric units of stress being Newtons per square millimeter (N/mm^2).

In the case of a simple prismatic bar subject to tension, the stress σ is

$$\sigma = \frac{P}{A} \tag{2.1}$$

where P = total tensile force

A = cross-sectional area of the bar

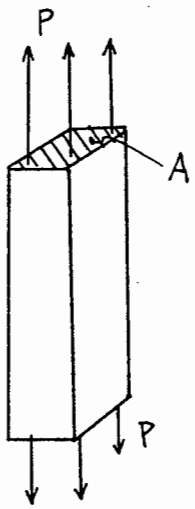

Fig 2.3 Bar subjected load axial load P

In a general stress field, the stresses are not uniaxial and nor are they uniformly distributed. Fig 2.4 shows how the stress components act on a three-dimensional body.

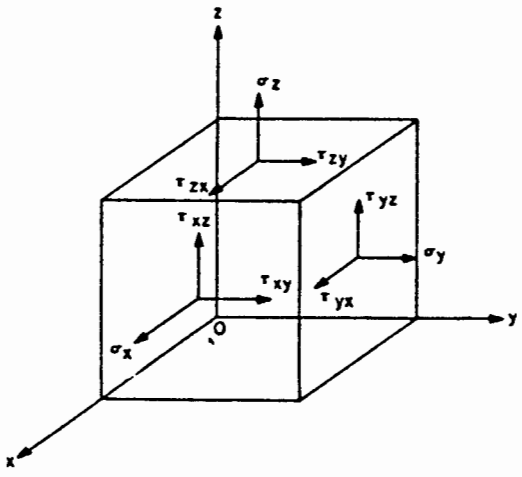

Fig 2.4 Stress components

3 components act on each pair of parallel planes, these being a normal stress perpendicular to the plane and two shear stress components acting in the plane. If we consider the plane

perpendicular to the z-axis in an isotropic material we have a normal stress σ_z and the two shear stresses τ_{zx} and τ_{zy}, acting in the x and z directions. Because the element is in equilibrium, only six of the nine components are independant, that is:

$$\sigma_x;\quad \sigma_y;\quad \sigma_z;\quad \tau_{xy} = \tau_{yx};\quad \tau_{xz} = \tau_{zx};\quad \tau_{yz} = \tau_{zy}$$

2.2.2 STRAIN

If a body is subjected to a set of forces, the body will deform slightly. In the case of the prismatic bar subject to tension, the length of the bar will increase from its original length L to a new value of L + ΔL. See Fig 2.5

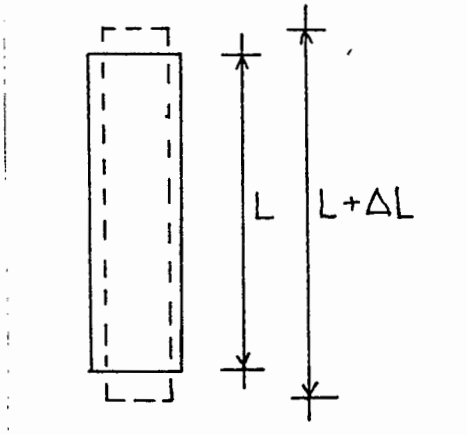

Fig 2.5 Strain in a prismatic bar

The strain, ε, is expressed as:

$$\varepsilon = \frac{\Delta L}{L} \qquad (2.2)$$

Again in the general strain field, six independant strain components exist, being normal strains ε_x, ε_y and ε_z, and shearing strains γ_{xy}, γ_{yz} and γ_{xz}.

2.3 STRESS-STRAIN RELATIONSHIPS

The general stress-strain relationship is known as Hooke's Law. In engineering stress analysis, we usually assume that materials used for structural purposes are elastic, isotropic and homogeneous. According to Hooke's Law, the magnitude of strain and stress [3] are related as follows:

$$\varepsilon_x = \frac{1}{E}\{\sigma_x - \nu\,(\sigma_y + \sigma_z)\}$$

$$\varepsilon_y = \frac{1}{E}\{\sigma_y - \nu\,(\sigma_z + \sigma_x)\}$$

$$\varepsilon_z = \frac{1}{E}\{\sigma_z - \nu\,(\sigma_x + \sigma_y)\}$$

$$\gamma_{xy} = \frac{1}{G}\,\tau_{xy}$$

$$\gamma_{yz} = \frac{1}{G}\,\tau_{yz} \qquad (2.3)$$

$$\gamma_{xz} = \frac{1}{G}\,\tau_{yz}$$

where E = Young's Modulus

ν = Poisson's ratio

$G = \dfrac{E}{2\,(1+\nu)}$ = shear modulus

2.4 RESIDUAL STRESSES

The stresses that would exist in a body if all external loads were removed are called "residual stresses". Other names for these stresses are "locked-in stresses" or"internal stresses". These residual stresses can occur if an object is subjected to a non-uniform temperature change and are hence called "thermal stresses"

2.4.1 MACROSCOPIC RESIDUAL STRESS

There exists a great scale of areas in which residual stresses can exist, varying from a large part of a metal structure right down to the areas measured on the atomic scale. Figure 2.6 shows the thermal distortions and thermal stress in the entire structure produced when the structure is heated by solar radiation from one side.

Fig 2.7 shows highly localized residual stresses produced in a thin layer near the surface by grinding.

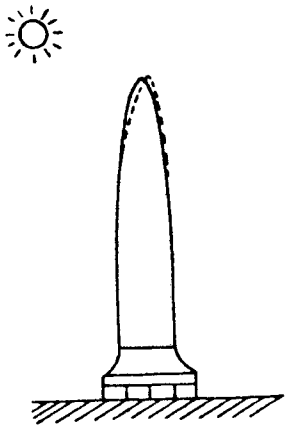

Thermal Distortion in a Structure Due to Heating by Solar Radiation

Fig 2.6

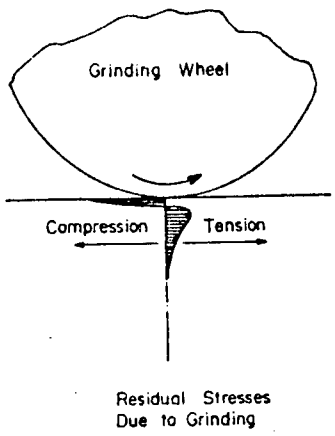

Fig 2.7

2.4.2 EQUILIBRIUM CONDITION OF RESIDUAL STRESS

Due to the fact that residual stresses can exist without any external forces, the resultant moment and resultant force produced by the residual stresses must equal zero. That is, on any plane section:

$$\int \sigma \, dA = 0 \quad \text{and} \quad \int dM = 0 \tag{2.4}$$

These conditions must be satisfied in any experiment involving residual-stress data.

2.4.3 OCCURENCE OF RESIDUAL STRESSES

Residual stresses in metal structures can occur during the manufacturing process. They can be produced during rolling or casting, during forming and shaping of metal parts, or during the fabrication process. Residual stresses can also be influenced by heat treatments during the manufacturing process, for example, quenching induces residual stresses whereas heat treatments reduce

them [3]. The heat treatment which reduces residual stress is called "normalization". [7] , a process in which metal is heated up and then air-cooled.

2.4.4 RESIDUAL STRESSES PRODUCED BY STRUCTURAL MISMATCHING

Fig 2.8 is an example where residual stresses are produced by mismatching. Here bars of differing lengths have been forcibly joined to form a system. In the shorter bar Q, the joining action creates a tensile stress in the member, whereas the longer bars P and P' are forced into compression by the above action, causing compressive stresses in them.

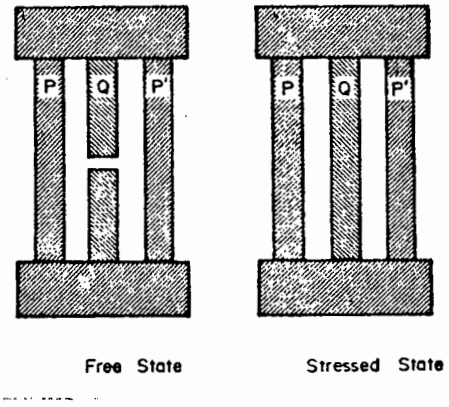

Fig 2.8 Residual stresses caused by mismatching

2.4.5 RESIDUAL STRESSES PRODUCED BY UNEVEN DISTRIBUTION OF NON-ELASTIC STRAINS

No thermal stresses are produced if a material is heated uniformly and expands in a uniform fashion. Thermal stress is produced though, if the material is heated unevenly and also when non-elastic strains such as plastic strains are present. The application of constraints also produce thermal stresses upon heating.

2.5 DISTORTION

Every engineer will face the problem of distortion during welding due to the differential heating and cooling cycle [2]. The amount of distortion can be controlled to a certain degree by restraining the structure to be welded, the greatest distortion occuring when the

structure is free to move and the least occuring when the structure is fully restrained. However, completely restraining the structure will not solve the distortion problem as very high residual stresses or even cracking can occur. Another difficulty is that residual stresses caused by the rolling or casting process can be relieved locally by the welding process and can distort unpredictably. Fig 2.9 shows a number of ways that welds can distort. The most common form of distortion in butt and fillet welds is bending. In sheet material, bowing and buckling due to weld metal shrinkage, occurs, with longitudinal and transverse shrinkage always occuring in long lengths of weld.

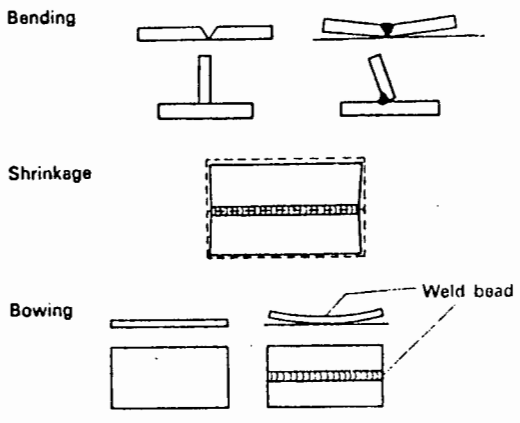

Fig 2.9 Modes of distortion in welded joints

2.5.1 MULTI-RUN DISTORTION SEQUENCE

Kuzmanovic and Willems [8] show that if two plates are to be joined together using a butt weld, the first run will pull the plates closer towards each other.

If a second run of weld metal is deposited on top of this, it will also try to pull the plates closer together, but this is prevented by the first run which would have to be compressed before the plates could come closer together at the root. The second run, contracting transversely, will create a "pull" at the weld face and the first run, resisting compression, will create a "push" at the root of the weld, causing a lifting out of alignment of the plates. This sequence is shown in Fig 2.10. Angular distortion will be increased proportionately to the number of runs deposited in the

in the weld (approx 1° per run) and is shown in Fig 2.11

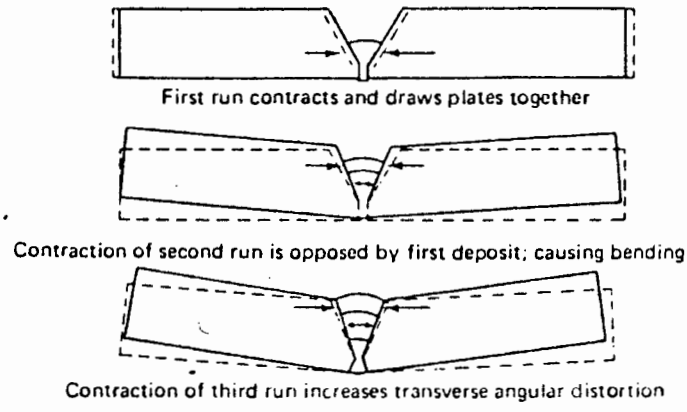

Fig 2.10 Multi-run distortion sequence in a butt-weld

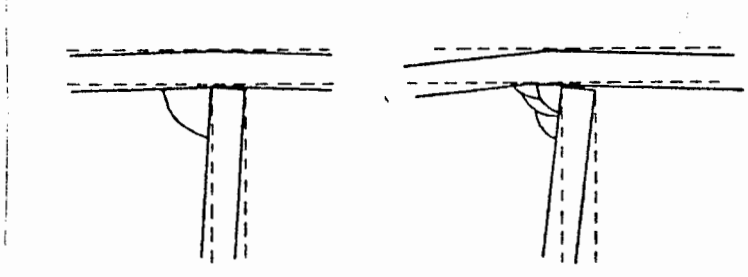

Fig 2.11 Multi-run angular distortion in a fillet weld

2.5.2 CONTROL OF DISTORTION

Distortion, although cannot be overcome, can be minimized by a good design, aiming to use the minimum number of parts and weld metal. Balanced welding gives the best results [2] (Double V or U joints) whereas single V or U welds are unbalanced. In fact, the U joint is better than the V joint since a larger quantity of weld metal is deposited at the top of the V, causing greater shrinkage. Generally, the weld should be as narrow as possible. Also slow welding speeds in conjuction with a diffuse heat source increases the distortion whereas a narrow welding zone and concentrated heat source will decrease the distortion.

As mentioned previously, distortions can be decreased by restraining the structure, for example, by clamping. An attractive alternative to this method is to pre-set the components so that the distortion actually brings the final structure into its correct shape and dimensions, but this method will give completely satisfactory results only in very simple fabrications. This is shown in Fig 2.12. The direction of welding also has a bearing on distortion. A structure welded from the restrained end to the free end will keep distortion to a minimum.

Finally, the act of machining a component after welding can lead to distortion as the removal of metal can upset the residual stress balance.

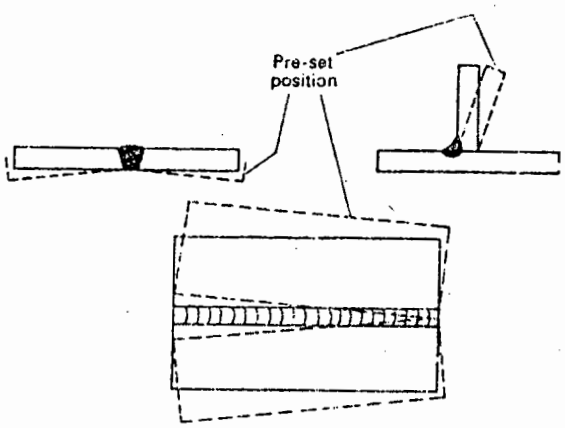

Fig 2.12 Distortion control by pre-setting

CHAPTER THREE

THEORY OF HEAT CONDUCTION

3.1 CONDUCTION OF HEAT

The process by which heat flows from a region of higher temperature to a region of lower temperature within a medium or between different mediums in direct physical contact, is called conduction [9]. In conduction heat flow, energy is transmitted by direct molecular communication without appreciable displacement of the molecules. According to the Kinetic Theory, the temperature of an element of matter is proportional to the mean kinetic energy of its constituent molecules. The faster the molecules move, the greater will be the temperature of an element of matter.

When molecules in one region aquire a mean kinetic energy greater than that of molecules in an adjacent region, manifested by a difference in temperature, the molecules possessing the greater energy will transmit part of their energy to the molecules in the lower temperature region. In metals, this transfer of energy takes place by diffusion of faster-moving electrons from the higher temperature regions to the lower temperature regions. The observable effect of heat conduction is hence an equalization of temperature.

3.1.1 CONDUCTION OF HEAT IN STEADY-STATE

A body in which heat is flowing is said to have reached a steady state when the temperatures of its different parts do not change with time. Such a state occurs in practice only after the heat has been flowing for a long time. Each part of the body then gives up on one side as much heat as it receives on the other, and the temperature is therefore independant of the time t, although it varies from point to point in the body, being a function of the spacial coordinates.

3.1.2 CONDUCTION OF HEAT IN THE TRANSIENT STATE

A body in which heat is flowing is said to be in a transient state when the temperatures of its different parts change with time. Transients are relatively common in engineering design and an accurate knowledge of the temperature variation is often neccessary. Circumstances arise frequently in which the success of the design depends on the accurate prediction of temperature levels in some

critical part. In devices intended to operate only a relatively short time in high temperature surroundings, it is not always necessary to design for the steady-state case.
Cost savings may be obtained from designing only for the conditions reached during the transient period when successful functioning is required. Transient characteristics may also be important in devices which are intended to operate in steady-state but which change from one operating level to another.

3.2 CONDUCTION HEAT TRANSFER

When a temperature gradient exists, energy is transferred from a region of higher temperature to a region of lower temperature [10]. Energy is thus transferred by conduction and the heat transfer rate per unit area is proportional to the normal temperature gradient:

$$\frac{q}{A} \propto \frac{\partial T}{\partial x} \qquad \text{or} \qquad q = -k \frac{\partial T}{\partial x} \tag{3.1}$$

Considering the heat transfer in one dimension:

It can be shown[10]that:

Energy conducted in left face and heat generated within the element = change in internal energy and energy out of the right face (3.2)

or $$E_{LF} + E_{GEN} = E_{\Delta} + E_{RF} \tag{3.3}$$

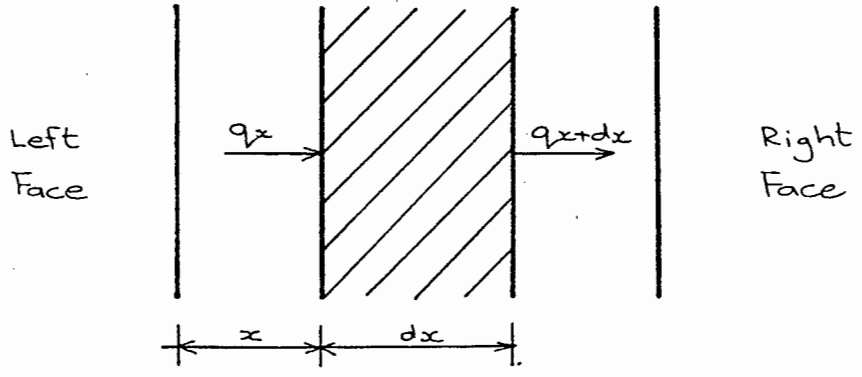

Fig 3.1 1- dimensional heat transfer

$$E_{LF} = -kA \frac{\partial T}{\partial x} \qquad k = \text{conductivity}, \quad A = \text{cross sectional area} \tag{3.4}$$

$$E_{GEN} = \dot{q}A\,dx \qquad \dot{q} = \text{energy generated per unit volume} \tag{3.5}$$

$$E_{\Delta} = \rho cA \frac{\partial T}{\partial t} dx \qquad \rho = \text{density}, \; c = \text{specific heat}, \; t = \text{time} \tag{3.6}$$

$$E_{RF} = q_{x + dx} = -kA \left. \frac{\partial T}{\partial x} \right|_{x + dx} \tag{3.7}$$

Using a Taylor Expansion on (3.7), get

$$E_{RF} = -A \left[\left(k \frac{\partial T}{\partial x}\right) + \frac{\partial}{\partial x} \left(k \frac{\partial T}{\partial x}\right) dx \right] \tag{3.8}$$

Substituting (3.4), (3.5), (3.6) and (3.8) into (3.2) yields:

$$-kA \frac{\partial T}{\partial x} + \dot{q}A dx = \rho cA \frac{\partial T}{\partial t} dx - A \left[k \frac{\partial T}{\partial x} + \frac{\partial}{\partial x} \left(k \frac{\partial T}{\partial x}\right) dx \right] \tag{3.9}$$

This can be rewritten as:

$$\frac{\partial}{\partial x} \left(k \frac{\partial T}{\partial x}\right) + q = \rho c \frac{\partial T}{\partial t} \tag{3.10}$$

For all three-dimensional case, consider heat flows in and out of a unit volume in all three coordinate directions:

$$q_x + q_y + q_z + \dot{q}_{GEN} = q_{x + dx} + q_{y + dy} + q_{z + dz} + \frac{dE}{dt} \tag{3.11}$$

where $\frac{dE}{dt}$ = change in internal energy. As before,

$$q_x = -kA \frac{\partial T}{\partial x}$$

$$q_{x + dx} = - \left[k \frac{\partial T}{\partial x} + \frac{\partial}{\partial x} \left(k \frac{\partial T}{\partial x}\right) dx\right] dy\, dz$$

$$q_y = -kA \frac{\partial T}{\partial y} \tag{3.12}$$

$$q_{y + dy} = - \left[k \frac{\partial T}{\partial y} + \frac{\partial}{\partial y} \left(k \frac{\partial T}{\partial y}\right) dy\right] dx\, dz$$

$$q_z = -kA \frac{\partial T}{\partial z}$$

$$q_{z+dz} = -\left[k \frac{\partial T}{\partial z} + \frac{\partial}{\partial z}\left(k \frac{\partial T}{\partial z} dz\right)\right] dx\, dy$$

$$q_{GEN} = \dot{q}\, dx\, dy\, dz$$

$$\frac{dE}{dt} = \rho c\, dx\, dy\, dz \frac{\partial T}{\partial t}$$

Substituting (3.12) into equation (3.11) yields

$$\frac{\partial}{\partial x}\left(k \frac{\partial T}{\partial x}\right) + \frac{\partial}{\partial y}\left(k \frac{\partial T}{\partial y}\right) + \frac{\partial}{\partial z}\left(k \frac{\partial T}{\partial z}\right) + \dot{q} = \rho c \frac{\partial T}{\partial t} \qquad (3.13)$$

This equation (3.13) is known as the General Conduction Equation [10]

From Masubuchi [3],

Equation (3.13) can be written as

$$\rho c \frac{\partial T}{\partial t} = \dot{q} + k\left[\frac{\partial^2 T}{\partial x^2} + \frac{\partial^2 T}{\partial y^2} + \frac{\partial^2 T}{\partial z^2}\right] + \frac{\partial k}{\partial t}\left[\left(\frac{\partial T}{\partial x}\right)^2 + \left(\frac{\partial T}{\partial y}\right)^2 + \left(\frac{\partial T}{\partial z}\right)^2\right] \qquad (3.14)$$

If the value of the thermal conductivity k does not change with temperature, then we have the case of constant thermal conductivity and $\frac{\partial k}{\partial t} = 0$

Then equation (3.14) can be reduced to a linear differential equation;

$$\frac{\partial^2 T}{\partial x^2} + \frac{\partial^2 T}{\partial y^2} + \frac{\partial^2 T}{\partial z^2} + \frac{\dot{q}}{k} = \frac{\rho c}{k} \frac{\partial T}{\partial t} = \frac{1}{\alpha} \frac{\partial T}{\partial t} \qquad (3.15)$$

where $\alpha = \frac{k}{\rho c}$ = thermal diffusivity of the material

If, in addition, no heat is generated within the element, $\dot{q} = 0$ hence we have the Fourier equation:

$$\frac{\partial^2 T}{\partial x^2} + \frac{\partial^2 T}{\partial y^2} + \frac{\partial^2 T}{\partial z^2} = \frac{1}{\alpha} \frac{\partial T}{\partial t} \qquad (3.16)$$

If, in addition, we have a steady-state condition, $\frac{\partial T}{\partial t} = 0$

hence we have the Laplace equation in 3-dimensions:

$$\frac{\partial^2 T}{\partial x^2} + \frac{\partial^2 T}{\partial y^2} + \frac{\partial^2 T}{\partial z^2} = 0 \qquad (3.17)$$

3.3 STEADY-STATE THEORY

3.3.1 ONE-DIMENSIONAL CASE

In this case, the equation is such that the steady-state heat conduction through the system has temperature and heat flow as a function of a single spacial coordinate, x

ie. $$\frac{\partial^2 T}{\partial x^2} = 0 \qquad (3.18)$$

The solution of this equation is obtained by integrating it twice. This yields:

$$T = Ax + B \qquad (3.19)$$

where A and B are the constants of integration and are solved for each problem using known boundary conditions.

3.3.2 TWO-DIMENSIONAL CASE

In this case, the equation is such that the steady-state heat conduction through the system has temperature and heat flow as a function of two spacial coordinates, x and y

ie. $$\frac{\partial^2 T}{\partial x^2} + \frac{\partial^2 T}{\partial y^2} = 0 \qquad (3.20)$$

The Fourier series method is particularly well adapted to solving steady-state temperature problems for flat rectangular plates. In general we start with a sine series for f(x): [11]

$$f(x) = \sum_{n=1}^{\infty} a_n \sin \frac{n\pi x}{a} \qquad (3.21)$$

where $$a_n = \frac{2}{a} \int_0^1 f(x') \sin \frac{n\pi x'}{a} dx' \qquad (3.22)$$

For any n, a term of the type:

$$\sin \frac{n\pi x}{a} \quad \sin \frac{n(b-y)\pi}{a} \qquad (3.23)$$

will satisfy certain zero boundary conditions hence this leads us to consider a solution of the form:

$$T = \sum_{n=1}^{\infty} a_n \frac{\left[\sinh \frac{(b-y)n\pi}{a}\right] \sin \left(\frac{n\pi x}{a}\right)}{\sinh \left(\frac{n\pi b}{a}\right)} \qquad (3.24)$$

Boundary conditions determine the exact form of the solution.

3.3.3 THREE-DIMENSIONAL CASE

In this case, the equation is such that the steady-state heat conduction through the system has temperature and heat flow as a function of three spacial coordinates, x, y and z

ie. $$\frac{\partial^2 T}{\partial x^2} + \frac{\partial^2 T}{\partial y^2} + \frac{\partial^2 T}{\partial z^2} = 0$$

This type of equation is solved by making use of double Fourier series ie. a combination of two solutions similar to that of the two-dimensional case. Hence the solution is of the type:

$$T = \sum_{m=1}^{\infty} \sum_{n=1}^{\infty} A_{m,n} \frac{\left[T_1 \sinh \ell (a-x) + T_2 \sinh \ell x\right] \sin \left(\frac{m\pi y}{b}\right) \sin \left(\frac{n\pi z}{c}\right)}{\sinh \ell a} \qquad (3.26)$$

The exact form of the solution will be dictated by the boundary conditions.

3.4 TRANSIENT ANALYSIS

3.4.1 ONE-DIMENSIONAL CASE:

In this case, the equation is such that the heat conduction through the system has temperature and heat flow not only as a function of one spacial coordinate, x, but also as a function of time [11]

ie. $$\frac{\partial^2 T}{\partial x^2} = \frac{1}{\alpha}\frac{\partial T}{\partial t} \quad \text{where} \quad \alpha = \text{thermal diffusivity} \tag{3.27}$$

As again a Fourier analysis suits this type of equation, our solution will be of the form:

$$T = \sum_{n=1}^{\infty} a_n \sin\frac{n\pi x}{\ell} \exp\left[\frac{-\alpha n^2 \pi^2 t}{\ell^2}\right] \tag{3.28}$$

where $$a_n = \frac{2}{\ell}\int_0^1 f(x') \sin\frac{n\pi x'}{\ell}\, dx' \tag{3.29}$$

Boundary conditions determines the exact form of the solution.

3.4.2 TWO-DIMENSIONAL CASE

In this case, the equation is such that the heat conduction through the system has temperature and heat flow not only as a function of two spacial coordinates, but also as a function of time.

ie. $$\frac{\partial^2 T}{\partial x^2} + \frac{\partial^2 T}{\partial y^2} = \frac{1}{\alpha}\frac{\partial T}{\partial t} \tag{3.30}$$

In this case, a double Fourier series is the best solution to the problem, having the form [11]:

$$T = A_{m,n}\sum_{m=0}^{\infty}\sum_{n=0}^{\infty} B(m,n) \exp\left[-\frac{\alpha\pi^2 t}{4} C(m,n)\right] \cos\frac{m\pi x}{a} \cos\frac{n\pi y}{b} \tag{3.31}$$

A, B, C and the correct form of the solution will be established by

the specified boundary conditions.

3.4.3 THREE-DIMENSIONAL CASE

In this case, the equation is such that the heat conduction through the system has temperature and heat flow not only as a function of three spacial variables, but also as a function of time.

ie. $$\frac{\partial^2 T}{\partial x^2} + \frac{\partial^2 T}{\partial y^2} + \frac{\partial^2 T}{\partial z^2} = \frac{1}{\alpha}\frac{\partial T}{\partial t}$$

In this case, a triple Fourier series [11] is the best solution to the problem, having the form:

$$T = A_{m,n,p} \sum_{m=0}^{\infty}\sum_{n=0}^{\infty}\sum_{p=0}^{\infty} B(m,n,p)\ \exp\left[-\frac{\alpha\pi^2 t}{4} C\ (m,n,p)\right] \cos\frac{m\pi x}{a}\ \cos\frac{n\pi y}{b}$$

$$\cos\frac{p\pi z}{c} \qquad (3.33)$$

Boundary conditions determine the exact form of the constants and the solution.

CHAPTER FOUR

INTRODUCTION TO THE FINITE-ELEMENT METHOD

4.1 HISTORY OF THE FINITE-ELEMENT METHOD

Since 1906 continuum problems were being solved by the researchers using the "lattice analogy" method [12] . In this method, the continuum was approximated by a regular mesh of elastic bars, capitalizing on well-known methods for the analysis of framed structures. In 1943, Courant suggested a method to get approximate numerical solutions, this method involving piecewise polynomial interpolation over triangular sub-regions [12]. This was recognised by him as the Rayleigh-Ritz solution of a variational problem and is now known today as the finite-element method. This work by Courant was forgotten until it was independantly developed by engineers.

None of the work done at that time was of any practical use as no computers existed to do the calculations. By the year 1953, stiffness equations in matrix form were being written by engineers and digital computers were solving these equations. In 1956, a classic paper by Turner, Clough, Martin and Topp [12] appeared which, along with other papers, began the explosive development of finite-element methods in engineering. The name "finite-elements" was given to the method in 1960. By 1963, the finite-element method was recognized as a rigorously sound method and became a respectable study area for academicians. Even as late as 1967, finite-elements were being worked with by engineers and mathematicians in apparent ignorance of one another. As an example to show the growth of the finite-element method, ten papers on the subject were published in 1961, 134 in 1966 and 844 in 1971. By the year 1976, the cumulative total of publications exceeded 7000.

4.2 THEORY OF THE FINITE-ELEMENT METHOD

4.2.1 CONCEPT

The basic concept underlying the finite-element method is the principle of "discretization" [13]. The necessity of discretizing, or dividing things into smaller more manageable parts arises from the fundamental limitation of human beings in their ability to see or perceive things surrounding them in the universe in their entirety. Even to see things immediately surrounding us, we must look about

to obtain a jointed mental picture of our surroundings. Usually such jointed views contain an element of error. Discretization implies, therefore, approximation of the real and continuous.

4.2.2 STEPS IN THE FINITE-ELEMENT METHOD

4.2.2.1 Discretizations and Element Confuguration Selection

This step involves subdivision of the body into a suitable number of "small" bodies called finite-elements [13] .
The intersection of the sides of the elements are called nodes or nodal points, and the interfaces between the elements are called nodal lines or nodal planes.

Additional node points can be introduced along the nodal lines as shown in Fig 4.1

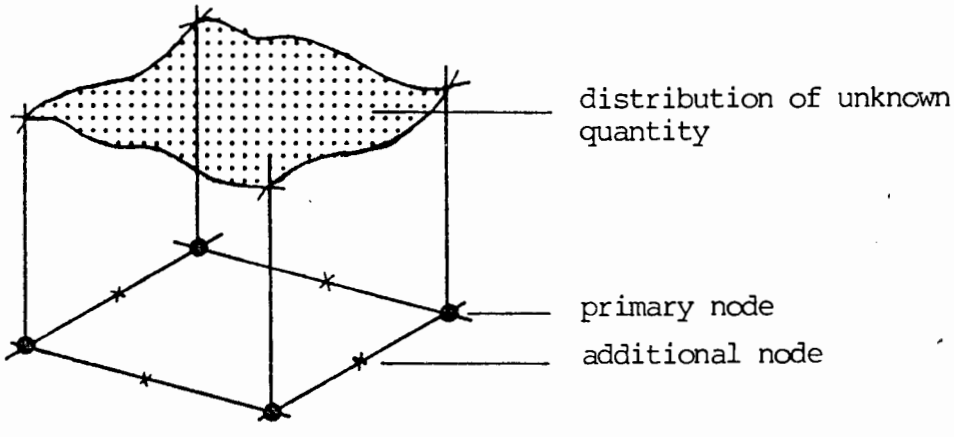

Fig 4.1 Primary and additional nodes

4.2.2.2 Select Approximation Models or Functions

Here we choose a shape for the distribution of the unknown quantity. This unknown quantity can be displacement, stress, velocity or pressure. In our case it is temperature and stress.

4.2.2.3 Definition of Constitutive Relationships

Quantities appearing in the principle must be defined. The constitutive relationship describes the response or effect in a system due to an applied cause. For example, the stress-strain law is one of the most vital parts of finite-element analysis. Unless it is defined to reflect precisely the behavior of the material or system, the result from the analysis can be of very little significance. [13]

4.2.2.4 Derivation of Flement Equations

From availible laws and principals, we obtain equations governing the behavior of the element. The equations are obtained in general terms and can hence be used for all elements in the discretized body.

4.2.2.5 Global Assemblage of Element Equations

Once the element equations are established for a genetic element, we can generate equations recursively for other elements. We then add them together to find global equations. This assembling process is based on the laws of compatibility and continuity. It requires that the body remains continuous. [13]
The boundary conditions are the physical constraints that must exist so that the structure of the body can stand in space uniquely. These conditions are commonly specified in terms of known values of the unknowns on a part of the structure or body.

4.2.2.6 Solve for Primary Unknowns

Gaussian elimination or iterative methods are used

4.2.2.7 Solve for Secondary Unknowns

Often secondary quantities must be computed from the primary quantities.

4.2.8.8 Interpretation of Results

This final and important aim is to reduce the results from the use of the finite-element procedure to a form that can be readily used for analysis and design.

4.3 FINITE-ELEMENT THEORY OF HEAT CONDUCTION

One reason to use finite-elements for a heat transfer analysis is that for a thermal stress analysis to take place, the node point temperatures are needed. [12] .

4.3.1 HEAT EQUATIONS FOR PLANAR HEAT CONDUCTION

The Fourier heat conduction equation is, from Cook [12]

$$q = -k \frac{\partial T}{\partial s} \qquad \text{where} \qquad \begin{aligned} q &= \text{heat flux} \\ s &= \text{direction} \\ T &= \text{temperature} \\ k &= \text{thermal conductivity} \end{aligned} \qquad (4.1)$$

For a thermally orthotropic material, see Fig 4.2

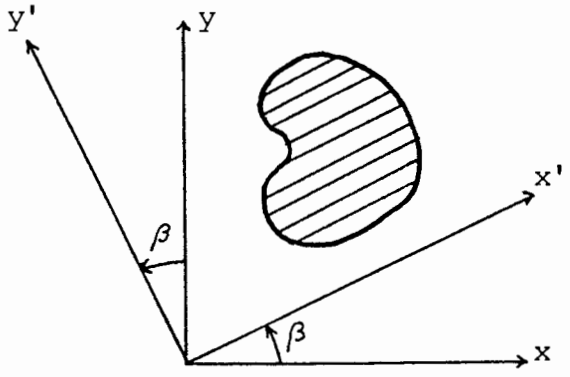

Fig 4.2 Layered material with principal directions x' and y'

Here $\{q_{x'}\ q_{y'}\} = -[k_{x'}\ k_{y'}]\ \{\frac{\partial T}{\partial x'}\ \frac{\partial T}{\partial y'}\}$ (4.2)

where $[k_{x'}\ k_{y'}]$ is a diagonal matrix of principal conductivities

$q_{x'}\ q_{y'}$ are heat fluxes in principal directions.

From the chain rule of differentiation

$$\{\frac{\partial T}{\partial x'}\ \frac{\partial T}{\partial y'}\} = [\Lambda]\ \{\frac{\partial T}{\partial x}\ \frac{\partial T}{\partial y}\} \tag{4.3}$$

where

$$[\Lambda] = \begin{bmatrix} \cos\beta & \sin\beta \\ -\sin\beta & -\cos\beta \end{bmatrix}$$

Heat flux q is a vector and transforms like displacement:

$$\{q_x\ q_y\} = [\Lambda]^T \{q_{x'}\ q_{y'}\} \tag{4.4}$$

Equations (4.2) through (4.4) yield the relation between the x and y direction heat fluxes and their temperature gradients

$$\{q_x\ q_y\} = -[k]\ \{\frac{\partial T}{\partial x}\ \frac{\partial T}{\partial y}\} \tag{4.5}$$

where

$$[k]_{2 \times 2} = \begin{bmatrix} k_x & k_{xy} \\ k_{xy} & k_y \end{bmatrix} = [\Lambda]^T \begin{bmatrix} k_{x'} & 0 \\ 0 & k_{y'} \end{bmatrix} [\Lambda] \tag{4.6}$$

The net flow into a region is inflow minus outflow. This is shown in Fig 4.3

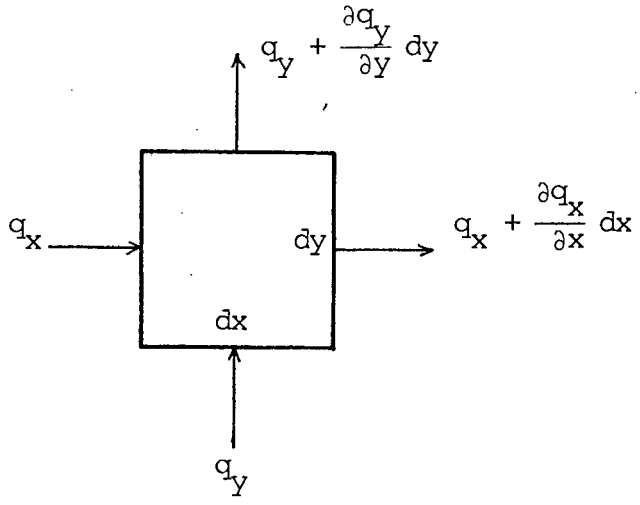

Fig 4.3 Heat Flow through Planar Element

$$[(q_x\, dy + q_y\, dx)\,\tau] - [(q_x + \frac{\partial q_x}{\partial x}\, dx)dy\,\tau] - [(q_y + \frac{\partial q_y}{\partial y}\, dy)dx\,\tau]$$

$$= (-\frac{\partial q_x}{\partial x} - \frac{\partial q_y}{\partial y})\, dx\, dy\, \tau \qquad (4.7)$$

where τ is the constant thickness of the material.

Let Q denote the internally generated heat flow. With equation (4.7) the net inward flow is

$$(Q - \frac{\partial q_x}{\partial x} - \frac{\partial q_y}{\partial y})\, dx\, dy\, \tau \qquad (4.8)$$

This flow produces a time rate of change of stored energy

$$c\rho\, dx\, dy\, \dot{T} \qquad \text{where } \dot{T} = \frac{\partial T}{\partial t} \qquad (4.9)$$

Expressions (4.8) and (4.9) are equated and equation (4.5) is substituted.

Thus

$$\frac{\partial}{\partial x}(k_x \frac{\partial T}{\partial x} + k_{xy} \frac{\partial T}{\partial y}) + \frac{\partial}{\partial y}(k_{xy} \frac{\partial T}{\partial x} + k_y \frac{\partial T}{\partial y}) + Q = \rho c\, \dot{T} \qquad (4.10)$$

In an isotropic and homogeneous medium equation (4.10) becomes:

$$k \left(\frac{\partial^2 T}{\partial x^2} + \frac{\partial^2 T}{\partial y^2} \right) + Q = c\rho \dot{T} \tag{4.11}$$

where $k_{xy} = 0$ $\qquad$ $k_x = k_y = k$ = constant

If in addition we have a steady-state, Laplace's equation results:

$$\frac{\partial^2 T}{\partial x^2} + \frac{\partial^2 T}{\partial y^2} = 0 \tag{4.12}$$

The plane heat conduction problem is the solution if equation (4.10) for $T = T(x, y, t)$ in area A subjected to boundary conditions.
See Fig 4.4

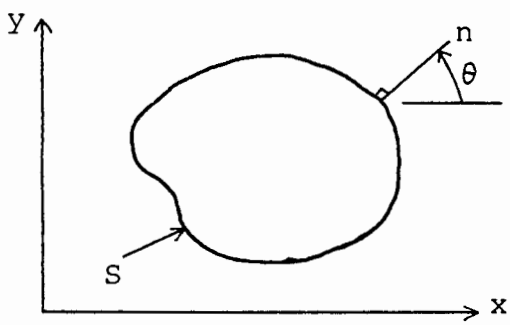

Fig 4.4 Plane Region A with Normal n on boundary S.

A functional Π_T for the problem is

$$\Pi_T = \frac{1}{2} \int \int \left(\left\{ \begin{matrix} \partial T/\partial x \\ \partial T/\partial y \end{matrix} \right\}^T [k] \left\{ \begin{matrix} \partial T/\partial x \\ \partial T/\partial y \end{matrix} \right\} - 2Q T + 2 \rho c T \dot{T} \right) dx\, dy$$

$$+ \int_{S_N} q^* T \, dS + \int_{S_c} \frac{h}{2} (T^2 - 2 T T_\infty) \, dS \tag{4.13}$$

where q^* = normal to boundary

$$= - \left(k_x \frac{\partial T}{\partial X} + k_{xy} \frac{\partial T}{\partial y} \right) \cos\theta - \left(k_{xy} \frac{\partial T}{\partial x} + k_y \frac{\partial T}{\partial y} \right) \sin\theta \tag{4.14}$$

where dS = increment of length on S

At every time, the temperature field must adjust itself so that

$$\delta\Pi = 0 \tag{4.15}$$

4.3.2 FINITE-ELEMENT FORMULATION

The spacial field $T = [N_T] \{T_e\}$ (4.16)

where $[N_T]$ = row vector of interpolation functions

$\{T_e\}$ = nodal degrees of freedom

Temperature gradients are:

$$\{\frac{\partial T}{\partial x} \quad \frac{\partial T}{\partial y}\} = [B_T] \{T_e\} \tag{4.17}$$

where $[B_T] = \{\frac{\partial}{\partial x} \quad \frac{\partial}{\partial y}\} [N_T]$ (4.18)

Also, let Q be defined in terms of nodal values $\{Q_e\}$

$$Q = [N_Q] \{Q_e\}$$

It is convenient, but not necessary, to have $[N_Q] = [N_T]$

We define element matrices as follows:

Let $dV = dx\, dy$ for unit thickness

Hence,

$$[k_T] = \int_V [B_T]^T [k] [B_T] \, dV \qquad \text{(conductivity ht)}$$

$$[^{C}T] = \int_V [N_T]^T [N_T] \quad \rho c \, dV \qquad \text{(specific ht)}$$

$$[h_T] = \int_{S_c} [N_T]^T [N_T] \, h \, dS \qquad \text{(convection ht's)}$$

$$\{r_Q\} = \int_V [N_T]^T [N_Q] \, dV \, \{Q_e\} \tag{4.20}$$

$$\{r_q\} = \int_{S_N} [N_T]^T \, q^* \, dS$$

$$\{r_\infty\} = \int_{S_c} [N_T]^T \, h \, T_\infty \, dS$$

Usually $\{r_q\}$ and $\{r_\infty\}$ are zero for most boundary conditions. $[h_T]$ is non zero for edges where $h \neq 0$ and T_∞ is prescribed.

With the notation of equation (4.20), substitution of equations (4.16) through (4.19) yields the following functional for an element.

$$\Pi_{Te} = \frac{1}{2} \{T_e\}^T ([k_T] + [h_T]) \{T_e\} + \{T_e\}^T ([c_T] \dot{\{T_e\}} - \{r_Q\} - \{r_\infty\} + \{r_q\}) \tag{4.21}$$

By adding the Π_{Te} conditions of the elements, we obtain Π_T for the assembled structure. Assembly implies the expansion of element arrays to global arrays so that $\{T_e\}$ is replaced by $\{T\}$ and $\{K_T\} = \Sigma[k_T]$ and so on. Hence equations that make Π_T stationary are:

$$\left\{ \frac{\partial \Pi}{\partial T} \right\} = 0 \tag{4.22}$$

hence

$$([K_T] + [H_T]) \{T\} + [C_T] \{\dot{T}\} = \{R_Q\} + \{R_\infty\} - \{R_q\} \tag{4.23}$$

The simplest form of (4.23) is

$$[K_T]\{T\} = 0 \tag{4.24}$$

which represents the steady-state conditions without internal heat source or sinks.

4.3.3 THE TRANSIENT THERMAL PROBLEM [12]

For direct integration, equation (4.23) has the form with respect to time,

$$[K]\{T\} + [C_T]\{\dot{T}\} = \{R\} \qquad (4.25)$$

where $\{R\}$ is a known function of time

$[K]$, $[C_T]$ assumed independant of T

An integration scheme is based on the assumption that temperatures $\{T\}_t$ at time t and temperatures $\{T\}_{t+\Delta t}$ at time $t + \Delta t$ have the relationship:

$$\{T\}_{t+\Delta t} = \{T\}_t + \{(1-\beta)\{\dot{T}\}_t + \beta\{\dot{T}\}_{t+\Delta t}\}(\Delta t) \qquad (4.26)$$

Similarly, like Newmarks method, equation (4.26) has a factor which can be chosen. If $\beta = 0$ we have Euler's method. If $\beta = 0{,}5$ we have the trapezoidal rule.

An implicit method can be developed from equations (4.25) and (4.26) as follows:

Write equation (4.25) for time t and then $t + \Delta t$. Multiply the first of these two equations by $(1-\beta)$ and the second by β

$$(1-\beta)\,([K]\{T\}_t + [C_T]\{\dot{T}\}_t) = (1-\beta)\{R\}_t$$

$$\beta([K]\{T\}_{t+\Delta t} + [C_T]\{\dot{T}\}_{t+\Delta t}) = \beta\{R\}_{t+\Delta t} \qquad (4.27)$$

If equations (4.27) are added and equation (4.26) used to eliminate temperature time derivatives, the result is

$$\left(\frac{1}{\Delta t}[C_T] + \beta[K]\right)\{T\}_{t+\Delta t} = \left(\frac{1}{\Delta t}[C_T] - (1-\beta)[K]\right)\{T\}_t + (1-\beta)\{R\}_t + \beta\{R\}_{t+\Delta t} \qquad (4.28)$$

If $\{T\}_0$ at t = 0 is known, equation (4.28) yields $\{T\}_{\Delta t}$.
Using $\{T\}_{\Delta t}$ we find $\{T\}_{2(\Delta t)}$ etc.

Hence, in this way, a temperature history is generated.

If $\beta = 0$ this method becomes explicit.

If Δt remains constant, the coefficient of $\{T\}_{t + \Delta t}$ in equation (4.28) need only be reduced once. We can then solve repeatedly for a series of right-hand sides.

In linear problems, ie. $[K]$ and $[C_T]$ do not depend on T, the stability limit on equation (4.28) is

$$\Delta t_{cr} = \frac{2}{(1 - 2\beta)\lambda_{max}} \tag{4.29}$$

where λ max is the largest eigenvalue of the system:

$$([K] - \lambda [C_T])\ \{\bar{T}\} = 0 \tag{4.30}$$

From equation (4.29), if $\beta = 0$, Δt must not exceed $2/\lambda_{max}$.
The method will be unconditionally stable for $\beta \geq \frac{1}{2}$.
If we have the case of $\beta = \frac{1}{2}$ and we apply the method to heat conduction problems, we call the method the "CRANK-NICOLSEN" method.
If we have Δt greater than $2/\lambda_{max}$ in this Crank-Nicolsen method, undesirable oscillations in response to a step change in the forcing function occur, which can be reduced using a smaller value of β, say $0.67 < \beta < 0.88$.

In a nonlinear problem, $[K]$ and $[C_T]$ in equation (4.25) can be kept unchanged by transferral of all nonlinearities to the right hand side. $\{R\}$ is hence augmented by a temperature dependent vector $\{N\}$. The following terms

$$(1 + \beta)\{N\}_t - \beta\{N\}_{t - \Delta t} \tag{4.31}$$

are added to the right-hand side of equation (4.28). For good stability, accuracy and efficiency in non-linear problems, β should be slightly greater than $\frac{1}{2}$, say 0.55.

4.4 NEED FOR COMPUTER METHODS

From Cook [12] it is concluded that there are plenty of uncertainties in the field of engineering analysis. We are unsure of construction errors, material properties and stiffnesses of connections, apart from others. Loads are also often of uncertain magnitude and distribution and even in a large analysis, only a few of the possible load cases will be analyzed. The structure might not even be used for the purpose intended. All these uncertainties make a mockery of the term "exact" with respect to an analysis but it is important that the analysis should not be so crude or casual, as this would add to the confusion.

In an actual analysis, we build a mathematical model and pose a question about it. If the program works, it answers us, but these answers will still be in terms of the mathermatical model and not the structure. Also, the program will say nothing about buckling, for example, unless we ask, even if the actual mode of failure is buckling. We cannot even presume that the structure is obliged to behave as the computer says it should. The important message here is that computation assists engineering judgement, but must not replace it.

Finally, the use of non-linear analysis techniques has become increasingly more important because it is realized that a large number of problems, when properly stated, are in fact nonlinear and that the understanding of the nonlinear behavior of a system can be essential for an effective design.

CHAPTER FIVE

COMPUTATIONAL IMPLEMENTATION OF THE FINITE-ELEMENT METHOD

5.1 ADINAT (AUTOMATIC DYNAMIC INCREMENTAL NONLINEAR ANALYSIS OF TEMPERATURE)

In recent years, finite-element analysis has become an effective stress analysis tool for structural systems. One such problem is that of the analysis of heat transfer in order to predict the temperatures and stresses in structural systems. In many cases, a heat-transfer analysis can be conducted seperately before stresses are determined, as the thermal stresses do not always affect the distribution of temperatures.

The program ADINAT [14] can be used for general linear and non-linear steady-state and transient heat transfer analysis.

5.1.1 Governing field-equations in ADINAT

Considering a three-dimensional body in steady-state conditions, the governing heat transfer equations are, in differential form

$$\frac{\partial}{\partial x}\left(k_x\frac{\partial\theta}{\partial x}\right) + \frac{\partial\theta}{\partial y}\left(k_y\frac{\partial\theta}{\partial y}\right) + \frac{\partial\theta}{\partial z}\left(k_z\frac{\partial\theta}{\partial z}\right) = -q^B \qquad (5.1)$$

$$\theta|_{S_1} = \theta_e \qquad (5.2)$$

$$k_n \frac{\partial\theta}{\partial n}\Big|_{S_2} = q^s \qquad (5.3)$$

where θ = body temperature

k_x, k_y, k_z = thermal conductivities in x, y and z axes

q^B = rate of heat generated per unit volume

θ_e = environmental temperature of area S_1

q^s = bondary heat flow input of area S_2

k_n = body thermal conductivity normal to surface

Equation (5.1) must hold at all points within the body, whereas equation (5.2) and (5.3) must hold at the surface of the body.

where c = material heat capacity

q_c = part of rate of heat generated, q^B, per unit volume.

Thus, for transient analysis in eq (5.1) and (5.5)

$$q^B = \tilde{q}^B - c\dot{\theta} \tag{5.9}$$

where $\tilde{q}^B$ no longer includes the material heat capacity effect.

5.1.2 Boundary-conditions in ADINAT

5.1.2.1 Temperature conditions

Temperatures can be prescribed at specific points and surfaces of the body, denoted by S_1.

5.1.2.2 Heat-flow conditions

These conditions can be prescribed.

5.1.2.3 Convection boundary conditions

$$q^S = h(\theta_e - \theta^S) \tag{5.10}$$

where h = convection coefficient

5.1.2.4 Radiation bondary conditions

$$q^S = \kappa(\theta_r - \theta^S) \tag{5.11}$$

where θ_r = temperature of external radiation source

κ = coefficient such that:

$$\kappa = h_r (\theta_r^2 + \theta^{S^2}) (\theta_r + \theta^S) \tag{5.12}$$

h_r is determined from the Stefan-Boltzmann constant, the emissivity of the radiant and absorbing materials and the geometric view factors.

5.1.3 Incremental field equations in ADINAT

As in incremental finite-element stress analysis, we assume that the conditions at time t have been calculated and that the temperatures are to be determined for time $t + \Delta t$ where Δt is the time increment. In steady-state or transient analysis using the Euler backward-integration method, the equations to be satisfied at time $t + \Delta t$ are, using eqns (5.5), (5.10), (5.11) and (5.12):

$$\int_V \delta\underline{\theta}^{'T}\, {}^{t+\Delta t}\underline{k}\; {}^{t+\Delta t}\underline{\theta}^{'}\, dV = {}^{t+\Delta t}Q + \int_{S_c} \delta\theta^s\, {}^{t+\Delta t}h\, ({}^{t+\Delta t}\theta^e - {}^{t+\Delta t}\theta^s)\, ds + \int_{S_r} \delta\theta^s\, {}^{t+\Delta t}\kappa\, ({}^{t+\Delta t}\theta_r - {}^{t+\Delta t}\theta^s)\, dS \tag{5.13}$$

where ${}^{t+\Delta t}$ = time at $t + \Delta t$

S_c = surface areas with convection boundaries

S_r = surface areas with radiation boundaries

${}^{t+\Delta t}Q$ = virtual work of external heat flow input to the system at time $t + \Delta t$ and includes heat flow inputs, internal heat generation and heat capacity.

Hence,

$$ {}^{t+\Delta t}Q = \int_{S_2} \delta\theta\, {}^{s}q^{s}\, dS + \int_V \delta\theta\, ({}^{t+\Delta t}\tilde{q}^{B} - {}^{t+\Delta t}c\; {}^{t+\Delta t}\dot{\theta})\, dV \tag{5.14}$$

In linear analysis ${}^{t+\Delta t}\underline{k}$, ${}^{t+\Delta t}h$ and ${}^{t+\Delta t}c$ are constant and radiation boundary conditions are not included.

In nonlinear analysis, eq (5.13) is a nonlinear equation for the temperatures at time t + Δt. The solution is obtained by linearizing equation (5.13) and using the modified Newton-Raphson iteration method. We then solve for i = 1, 2, 3 .... , resulting in:

$$\int_V \delta\underline{\theta}'^T\, {}^{t}\underline{k}\, \Delta\underline{\theta}'^{(i)}\, dV + \int_{S_c} \delta\theta^s\, {}^{t}h\, \Delta\theta^{s(i)}\, dS + \int_{S_r} \delta\theta^s\, {}^{t}\kappa\, \Delta\theta^{s(i)}\, dS$$

$$= {}^{t+\Delta t}Q + \int_{S_c} \delta\theta^s\, {}^{t+\Delta t}h^{(i-1)}\, ({}^{t+\Delta t}\theta_e - {}^{t+\Delta t}\theta^{s(i-1)})\, dS$$

$$+ \int_{S_r} \delta\theta^s\, {}^{t+\Delta t}\kappa\, ({}^{t+\Delta t}\theta_r - {}^{t+\Delta t}\theta^{s\,(i-1)})\, dS$$

$$- \int_V \delta\underline{\theta}'\, {}^{t+\Delta t}\underline{k}^{(i-1)}\, {}^{t+\Delta t}\underline{\theta}'^{\,(i-1)}\, dV \qquad (5.15)$$

where $${}^{t+\Delta t}\theta^{(i)} = {}^{t+\Delta t}\theta^{(i-1)} + \Delta\theta^{(i)} \qquad (5.16)$$

and $${}^{t+\Delta t}h^{(i-1)}$$ $${}^{t+\Delta t}\kappa^{(i-1)}$$ $${}^{t+\Delta t}\underline{k}^{(i-1)}$$ are the convection, radiation and conductivity matrices corresponding to temperature $${}^{t+\Delta t}\theta^{(i-1)}$$

In a transient analysis, $${}^{t+\Delta t}Q$$ is a function of $${}^{t+\Delta t}\theta$$ which must be approximated using a time integration scheme.

5.1.4 Finite-element discretization in ADINAT

In ADINAT, isoparametric finite-element discretization is employed, in which, for an element,

$$x = \sum_{i=1}^{N} h_i\, x_i \quad ; \quad y = \sum_{i=1}^{N} h_i\, y_i \quad ; \quad z = \sum_{i=1}^{N} h_i\, z_i \qquad (5.17)$$

and

$${}^{t+\Delta t}\theta = \sum_{i=1}^{N} h_i\, {}^{t+\Delta t}\theta_i \quad ; \; {}^{t}\theta = \sum_{i=1}^{N} h_i\, {}^{t}\theta_i \; ; \; \Delta\theta = \sum_{i=1}^{N} h_i\, \Delta\theta_i \qquad (5.18)$$

where h_i = element interpolation functions

N = number of nodal points

x_i, y_i, z_i = coordinates of nodal point i

$t+\Delta t_{\theta_i}, t_{\theta_i}, \Delta\theta_i$ = temperature at time $t + \Delta t$, t and temperature increment at node i.

The finite-element incremental heat flow equilibrium equations are hence derived by the substitution of eq (5.17) and (5.18) into eqns (5.14) and (5.15). We only consider a single element as the equilibrium equations of the complete finite-element system are obtained by the assemblage of the individual element matrices obtained from eq (5.14) and (5.15) when equations (5.17) and (5.18) are substituted. Hence from Appendix A [27]

$$(\underline{{}^{t}K}^{k} + \underline{{}^{t}K}^{c} + \underline{{}^{t}K}^{r})\,\underline{\Delta\theta}^{(i)} = \underline{{}^{t+\Delta t}Q} + \underline{{}^{t+\Delta t}Q}^{c(i-1)} + \underline{{}^{t+\Delta t}Q}^{r\,(i-1)} - \underline{{}^{t+\Delta t}Q}^{k\,(i-1)} \qquad (5.19)$$

where $$\underline{{}^{t+\Delta t}\theta}^{(i)} = \underline{{}^{t+\Delta t}\theta}^{(i-1)} + \underline{\Delta\theta}^{(i)} \qquad (5.20)$$

The temperature interpolation matrices $\underline{H}$ and $\underline{H}^{s}$ are constructed directly from the element interpolation functions and the temperature gradient interpolation functions are obtained from the derivatives of the interpolation functions.

Eq (5.19) is the general incremental heat flow equilibrium equation that is valid for linear and nonlinear analysis. In linear analysis, the equation can be used in a more effective form. If the conductivity and convection coefficients are constant ie. $\underline{{}^{t}K}^{k}$ and $\underline{{}^{t}K}^{c}$ are constant matrices, and radiation boundary conditions are excluded, equation (5.19) becomes

$$(\underline{K}^{k} + \underline{K}^{c})\,\underline{{}^{t+\Delta t}\theta} = \underline{{}^{t+\Delta t}Q} + \underline{{}^{t+\Delta t}Q}^{e} \qquad (5.21)$$

where $\underline{K}^c$ and $^{t+\Delta t}\underline{Q}^e$ are defined in Appendix A.

5.1.5 Step-by-step time integration in ADINAT

For transient analysis, a numerical time integration scheme is employed and in ADINAT, a family of one-step methods is used, in which is assumed

$$^{t+\alpha\Delta t}\dot{\underline{\theta}} = (^{t+\Delta t}\underline{\theta} - {}^{t}\underline{\theta}) / \Delta t \tag{5.22}$$

$$^{t+\alpha\Delta t}\underline{\theta} = (1-\alpha)\,{}^{t}\underline{\theta} + \alpha\, {}^{t+\Delta t}\underline{\theta} \tag{5.23}$$

where $0 \leq \alpha \leq 1$

These assumptions correspond to the following time integration schemes

$\alpha = 0$: Euler forward method (explicit)
$\alpha = 1/2$: Trapezoidal rule (implicit)
$\alpha = 1$: Euler backward method (implicit)

The governing heat transfer equations used with Euler backward method have previously been derived.
Since in nonlinear analysis using implicit time integration $^{t+\alpha\Delta t}\underline{\theta}$ is calculated by iteration we use for the assemblage of elements in nonlinear analysis

$$^{t+\alpha\Delta t}\underline{\theta}^{(i)} = {}^{t+\alpha\Delta t}\underline{\theta}^{(i-1)} + \Delta\underline{\theta}^{(i)} \tag{5.24}$$

5.1.6 Program Organization in ADINAT

The solution process in the program ADINAT is divided into 4 phases:

5.1.6.1 Mesh and element data input

The control information and nodal point input data are read by the program. Equation numbers for the active temperature degrees of freedom at each nodal point are established. Initial conditions and element data is read whereas element connection arrays are calculated.

5.1.6.2 Assemblage of constant structure matrices

The linear system conductivity and heat capacity matrices are assembled.

5.1.6.3 Calculation of externally applied heat flow vectors

The complete nodal point heat flow vector at each time step consists of the applied concentrated nodal point heat flow, applied distributed heat flux, internal heat generation, convection and radiation boundary conditions.
In linear heat analysis the complete heat flow vectors for all time steps are calculated before the step-by-step solution.
In a nonlinear analysis, the linear externally applied heat flow vectors established before the step-by-step solution are updated during the step-by-step solution.

5.1.6.4 Step-by-step solution

The solution of eq (5.19) is obtained at all time points.

5.1.7 Types of analyses in ADINAT

5.1.7.1 Linear steady-state analysis

In this analysis, all the element groups are linear. Only the linear system conductivity matrix that includes the contributions due to convection is calculated in the matrix assembly phase. The system conductivity matrix is triangularized before entering the step-by-step phase.

5.1.7.2 Linear transient analysis

In this analysis, all the elements are linear with heat capacity effects included. The heat capacity matrix may be diagonal (lumped analysis) or banded (consistent analysis).

5.1.7.3 Nonlinear steady-state analysis

In this analysis, elements can be linear or non-linear and heat capacity effects are neglected. Before the step-by-step solution, the linear system conductivity matrix was calculated. This matrix is now updated in preselected load steps by the conductivity matrices of the nonlinear convection and radiation boundary conditions to form the current tangent conductivity matrix.
The accuracy of the solution may be increased significantly using heat-flow equilibrium iteration.

5.1.7.4 Nonlinear transient analysis

This analysis is performed in the same way as a nonlinear steady-state analysis, but heat capacity effects are included.
The heat capacity matrix can be constant or a function of temperature.

5.2 ADINA (AUTOMATIC DYNAMIC INCREMENTAL NONLINEAR ANALYSIS)

It has been recognized recently that the ability to perform an effective linear and nonlinear analysis can be an important asset in the study and design of various structures encountered in civil, aeronautical and mechanical engineering. These linear and nonlinear analyses of complex structures have become possible through the use of digital computers operating on discrete representations of the actual structures.

The program ADINA [15] is a computer program for the static and dynamic displacement and stress analysis of solids, structures and fluid-structure systems, performing linear and nonlinear analysis.

5.2.1 Equilibrium equations of structural systems in ADINA

In linear analysis, the governing equilibrium equations are at time $t + \Delta t$:

$$\underline{M}\,{}^{t+\Delta t}\ddot{\underline{U}} + \underline{C}\,{}^{t+\Delta t}\dot{\underline{U}} + \underline{K}\,{}^{t+\Delta t}\underline{U} = {}^{t+\Delta t}\underline{R} \tag{5.25}$$

where
- $\underline{M}$ = constant mass matrix
- $\underline{C}$ = constant damping matrix
- $\underline{K}$ = constant stiffness matrix
- ${}^{t+\Delta t}\underline{R}$ = external load vector applied at time $t + \Delta t$
- ${}^{t+\Delta t}\ddot{\underline{U}}$ = vector of nodal point accelerations at time $t + \Delta t$
- ${}^{t+\Delta t}\dot{\underline{U}}$ = vector of nodal point velocities at time $t + \Delta t$
- ${}^{t+\Delta t}\underline{U}$ = vector of nodal point displacements at time $t + \Delta t$.

These equations are solved in ADINA using implicit time integration, explicit time integration or mode superposition.

In nonlinear analysis the incremental finite-element equilibrium equations are, using implicit time integration:

$$\underline{M}\,{}^{t+\Delta t}\ddot{\underline{U}} + \underline{C}\,{}^{t+\Delta t}\dot{\underline{U}} + {}^{t}\underline{K}\,\underline{U} = {}^{t+\Delta t}\underline{R} - {}^{t}\underline{F} \tag{5.26}$$

where
- ${}^{t}\underline{K}$ = tangent stiffness matrix at time t
- $\underline{U}$ = vector of nodal point displacement increments from time t to time $t + \Delta t$ ie. $\underline{U} = {}^{t+\Delta t}\underline{U} - {}^{t}\underline{U}$
- ${}^{t}F$ = nodal point force vector equivalent to the element stresses at time t.

In explicit time integration,

$$\underline{M}\,{}^{t}\ddot{\underline{U}} + \underline{C}\,{}^{t}\dot{\underline{U}} = {}^{t}\underline{R} - {}^{t}\underline{F} \tag{5.27}$$

Equations (5.25) and (5.26) reduce to the static analysis equations if mass and inertia effects are excluded.

The solution of eq (5.26) yields an approximate displacement increment $\underline{U}$. To improve the solution accuracy and prevent instabilities, equilibrium iteration may be necessary in each or preselected timesteps.

In this case, we condiser the equilibrium equations:

$$\underline{M}\,{}^{t+\Delta t}\ddot{\underline{U}}^{(i)} + \underline{C}\,{}^{t+\Delta t}\dot{\underline{U}}^{(i)} + {}^{t}\underline{K}\Delta\underline{U}^{(i)} = {}^{t+\Delta t}\underline{R} - {}^{t+\Delta t}\underline{F}^{(i-1)} \tag{5.28}$$

where $i = 1, 2, 3 \ldots$

M, C, ${}^{t}K$ and ${}^{t+\Delta t}R$ defined previously

${}^{t+\Delta t}\ddot{\underline{U}}^{(i)}$ = approximation to acceleration obtained in iteration i

${}^{t+\Delta t}\dot{\underline{U}}^{(i)}$ = approximation to velocity obtained in iteration i.

${}^{t+\Delta t}\underline{U}^{(i)} = {}^{t+\Delta t}\underline{U}^{(i-1)} + \Delta\underline{U}^{(i)}$ = approximation to displacement obtained in iteration i.

The first iteration, i = 1 in eq (5.28) corresponds to the solution of eq (5.26) where

$$\begin{aligned} \underline{U}^{(1)} &= \underline{U} \\ {}^{t+\Delta t}\underline{U}^{(0)} &= {}^{t}\underline{U} \\ {}^{t+\Delta t}\ddot{\underline{U}}^{(1)} &= {}^{t+\Delta t}\ddot{\underline{U}} \\ {}^{t+\Delta t}\dot{\underline{U}}^{(1)} &= {}^{t+\Delta t}\dot{\underline{U}} \\ {}^{t+\Delta t}\underline{F}^{(0)} &= {}^{t}\underline{F} \end{aligned} \tag{5.29}$$

The approximations to the velocities and accelerationes ${}^{t+\Delta t}\ddot{\underline{U}}^{(i)}$ and ${}^{t+\Delta t}\dot{\underline{U}}^{(i)}$ respectively, depend on the time integration

scheme used.
The solution scheme used in eq (5.28) corresponds to a modified Newton iteration. In ADINA, covergence can be accelerated using the Aitken or the BFGS method.
In ADINA, the central difference method is used in explicit time integration for statics, whereas the Newmark or Wilson method is used for dynamics.

5.2.2 Element to Structure matrics

The structure matrices are formed by the direct addition of element matrices and vectors

$$\underline{K} = \sum_{m} \underline{K}^{(m)} \tag{5.30}$$

where $\underline{K}^{(m)}$ is the stiffness matrix of the m-th element. Although $\underline{K}^{(m)}$ is of the same order as $\underline{K}$, only those terms in $\underline{K}^{(m)}$ which pertain to the element degrees of freedom are non zero.
In ADINA, either a consistent or lumped mass matrix may be used.

5.2.3 Displacement boundary conditions

If a component of displacement is zero, the corresponding equation is not retained in the structure equilibrium equations and the corresponding element stiffness and mass terms are ignored. To impose a non zero displacement, constraint equations can be specified.

5.2.4 Program Organization in ADINA

The complete solution process in ADINA can be divided into four phases.

5.2.4.1 Mesh and element data input

The control information and nodal point input data are read and generated. The equation numbers for active degrees of freedom at each node, are established and initial conditions are read.

The element data and connection arrays are read, calculated and stored.

5.2.4.2 Assemblage of constant structure matrices

Before the solution of eq (5.28) is performed, the linear structure stiffness, mass and damping matrices are assembled and stored.

5.2.4.3 Load vector calculation

The external load vectors for each time step are calculated and stored.

5.2.4.4 Step-by-step solution

The solution of eq (5.25), (5.26) or (5.27) is obtained at all time points. In addition to the displacement, velocity and acceleration vectors the element stresses are calculated and printed.

CHAPTER SIX

COMPARISON OF THEORY AND FINITE-ELEMENT HEAT ANALYSIS FOR MULTI-DIMENSIONAL PROBLEMS WITH SIMPLE BOUNDARY CONDITIONS

6.1 INTRODUCTION

The aim of this chapter was to verify the accuracy of the finite-element method. Results between a finite-element solution and a theoretical analysis were compared for simple problems with simple boundary conditions. These problems were analysed in steady-state and transient state and consisted of problems in 1-dimension (rod), 2-dimensions (thin plate) and 3-dimensions (solid cube).
In all the analyses, the temperature of the node at the centroid of the structure was required and compared.

Schematically, the problems were as follows for steady state:

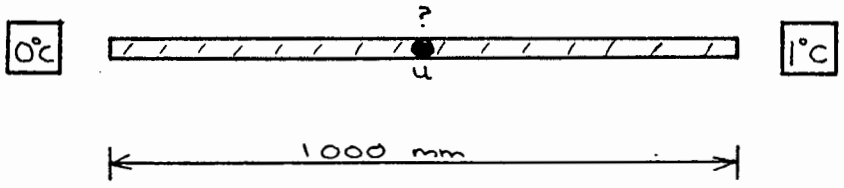

Fig 6.1 1-D rod

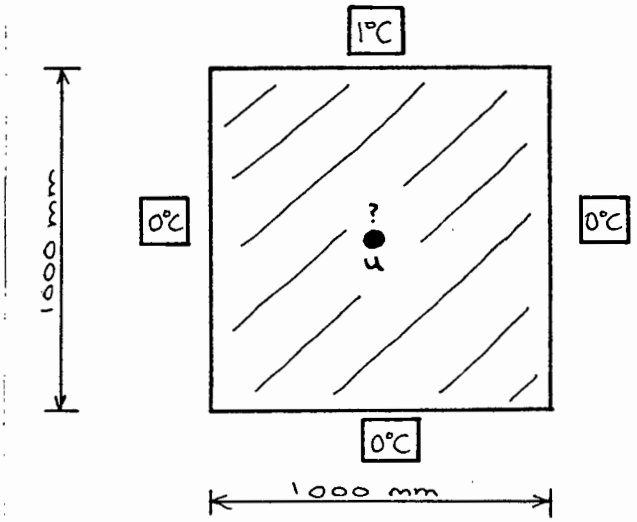

Fig 6.2 2-D plate

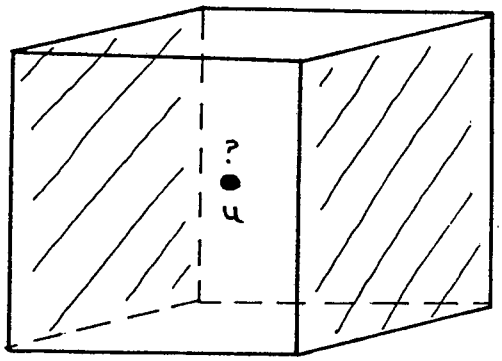

Cube 1000 mm x 1000 mm x 1000 mm
Left hand face has temperature = 0°c
Right hand face has temperature = 1°c
All other faces have temperature = 0°C

Fig 6.3 3-D solid cube

Only a thermal analysis was performed for each of the three cases

6.2 STEADY-STATE ANALYSIS

6.2.1 1-Dimension

The equation to be solved in this analysis is

$$\frac{\partial^2 u}{\partial x^2} = 0 \qquad (6.1)$$

subjected to the boundary conditions:

1) at $x = 0$, $u = u_1$

2) at $x = L$, $u = u_2$

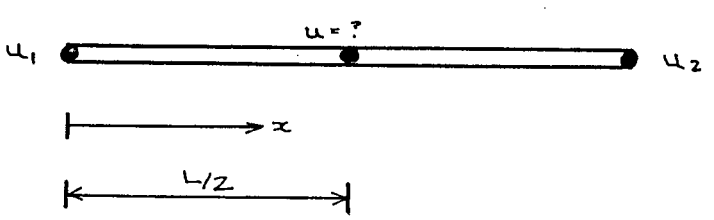

Fig 6.4 1-D bar

By integrating equation (6.1) twice, we get the solution

$$u = Ax + B \qquad (6.2)$$

At $x = 0$, $u = u_1$ therefore $B = u_1$

At $x = L$, $u = u_2$ therefore $A = (u_2 - u_1)/L$

Hence, $$u = \left(\frac{u_2 - u_1}{L}\right) x + u_1 \qquad (6.3)$$

If we set $u_1 = 0$, $u_2 = 1$ and $L = 1$, then

$$u = x \qquad (6.4)$$

Therefore at the centre of the element, ie. at $x = \frac{L}{2}$

we get $$u = 0.5°C \qquad (6.5)$$

Using the ADINAT temperature analysis to check the value obtained in eq (6.5), the following was done:

A finite-element mesh was constructed enabling the temperature at the centre of the bar to be calculated. Two two-noded 1-dimensional heat conduction elements were used.

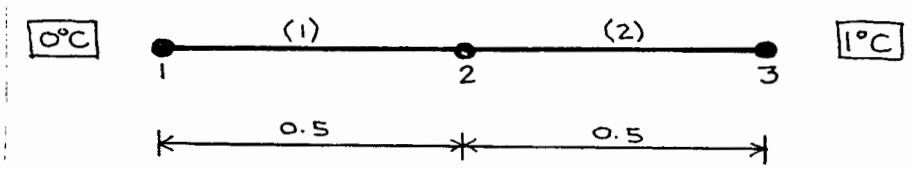

Fig 6.5 1-D finite-element mesh

The linear heat conduction elements were used in conjuction with the constant conductivity and specific heat material model. The program was run with node 1 having a temperature of zero and node 3 having a temperature of 1. The output of the analysis is shown in Table 6.A.

Node i	Temperature
1	0 (°C)
2	0.5
3	1.0

Table 6.A ADINAT temperature output. (1-D case)

This output shows the steady-state temperature of the central node 2 to be 0.5 °C. This is exactly the same as that obtained from the theory (eq (6.5)). Hence we deduce that the theoretical and finite-element solutions agree exactly.

6.2.2 2-DIMENSIONS

The equation to be solved in this analysis is

$$\frac{\partial^2 u}{\partial x^2} + \frac{\partial^2 u}{\partial y^2} = 0 \qquad (6.6)$$

subject to the boundary conditions:

1) As $x \to 0^+$, $u \to 0$ for $0 < y < b$
2) As $x \to a^-$, $u \to 0$ for $0 < y < b$
3) As $y \to 0^+$, $u \to 0$ for $0 < x < a$
4) As $y \to b^-$, $u \to 1$ for $0 < x < a$

This is represented diagramatically as:

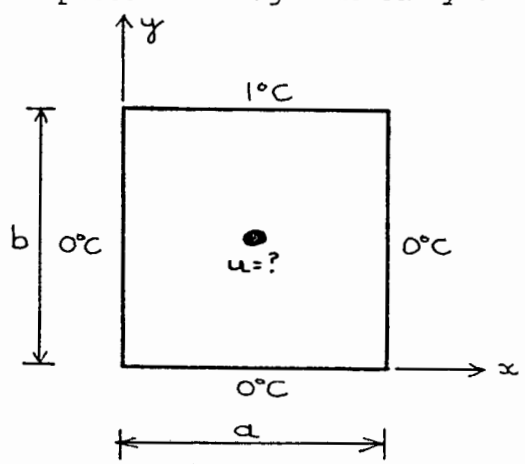

Fig 6.6 2-D plate

Using a Fourier analysis, the solution to equation (6.6) is:

$$u = \frac{4}{\pi} \sum_{k=0}^{\infty} \frac{\sin h\,[(2k+1)\pi y/a]\,\sin\,[(2k+1)\pi x/a]}{(2k+1)\,\sin h\,[(2k+1)\,\pi\, b/a]} \qquad (6.7)$$

By making simplifications, this equation can be greatly reduced. If we let a = b = 1, then

$$u = \frac{4}{\pi} \sum_{k=0}^{\infty} \frac{\sin h\,[(2k+1)\,\pi\, y]\,\sin\,[(2k+1)\,\pi\, x]}{(2k+1)\,\sin h\,[(2k+1)\pi]} \qquad (6.8)$$

At the centre of the domain, $x = y = \frac{1}{2}$ hence,

$$u = \frac{4}{\pi} \sum_{k=0}^{\infty} \frac{\sin h\,[(2k+1)\pi/2]\,\sin\,[(2k+1)\,\pi\,/2]}{(2k+1)\quad \sin h\,[(2k+1)\pi]} \qquad (6.9)$$

Considering the first term in this infinite series ie. k = 0:

$$u\,(\tfrac{1}{2}\,;\,\tfrac{1}{2}) = 0.2536°C \qquad (6.10)$$

Considering the second term in the series ie. k = 1:

$$u\,(\tfrac{1}{2}\,;\,\tfrac{1}{2}) = -0.0038°C \qquad (6.11)$$

Summing the two values in eq (6.10) and eq (6.11) yields

$$u_{CENTRE} = 0.249°C \qquad (6.12)$$

Using ADINAT, a finite-element mesh was constructed enabling the calculation of the temperature at the centre of the domain. As nine-noded conduction elements were not availible, four eight-noded quadrilaterals had to be used. These elements were linear two-dimensional conduction elements. The material model was used here as in the one-dimensional analysis. The mesh is shown in Fig 6.7

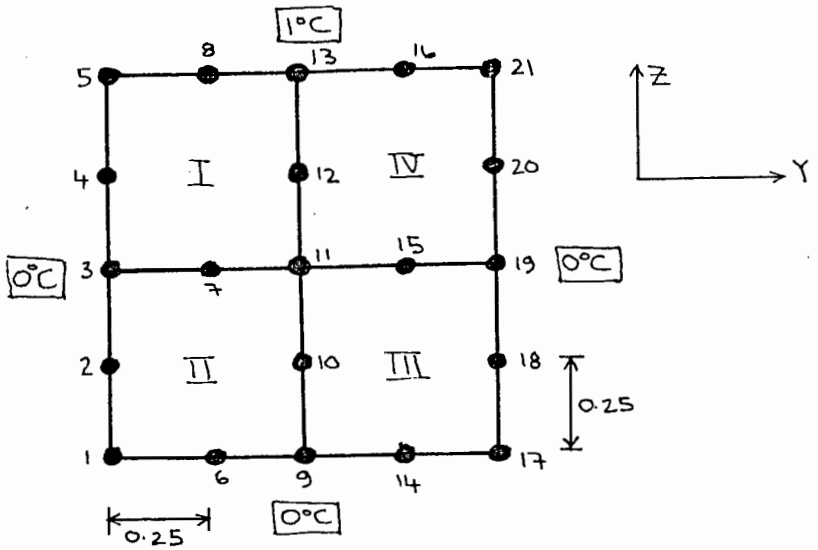

Fig 6.7 2-D finite-element mesh

A slight problem occured in the analysis with regard to the corner nodes 5 and 21 as they lay on the intersection of two conflicting boundary conditions. This problem was run twice. Run 1 consisted of the analysis with nodes 5, 8, 13, 16 and 21 all heated to 1°C with remaining nodes at 0°C. Run 2 consisted of analysing the problem with only nodes 8, 13 and 16 heated to 1°C with the remaining nodes at 0°C.

In order to "smooth-out" the corner boundary conditions, the arithmetic mean of the temperatures of the two runs was taken. In practice, this ammounted to assuming that corner nodes 5 and 21 had an initial temperature of 0.5°C.

Results of the analysis are shown in Table 6.B

Node	Temp (Run 1)	Temp (Run 2)	Temp (Average)
1	0 °C	0	0
2	0	0	0
3	0	0	0
4	0	0	0
5	1.0	0	0.5
6	0	0	0
7	0.212	0.138	0.175
8	1.0	1.0	1.0
9	0	0	0
10	0.062	0.113	0.088
11	0.176	0.323	0.249

Table 6B continued

12	0.662	0.463	0.563
13	1.0	1.0	1.0
14	0	0	0
15	0.212	0.138	0.175
16	1.0	1.0	1.0
17	0	0	0
18	0	0	0
19	0	0	0
20	0	0	0
21	1.0	0	0.5

Table 6B ADINAT temperature output (2D case)

Upon investigation, we can see that the average temperature at steady-state of the central node 11 is 0.249°C.
This is exactly the same as obtained from the theory (eq (6.12)).
Hence, we deduce that the theoretical and finite-element solutions agree exactly.

6.2.3 3-DIMENSIONS

The equation to be solved in this analysis is

$$\frac{\partial^2 u}{\partial x^2} + \frac{\partial^2 u}{\partial y^2} + \frac{\partial^2 u}{\partial z^2} = 0 \qquad (6.13)$$

subject to the boundary conditions:

1) On $x = 0$, temperature = u_1

2) On $x = a$, temperature = u_2

3) On all other faces, the temperature is zero

This is represented schematically in Fig 6.8

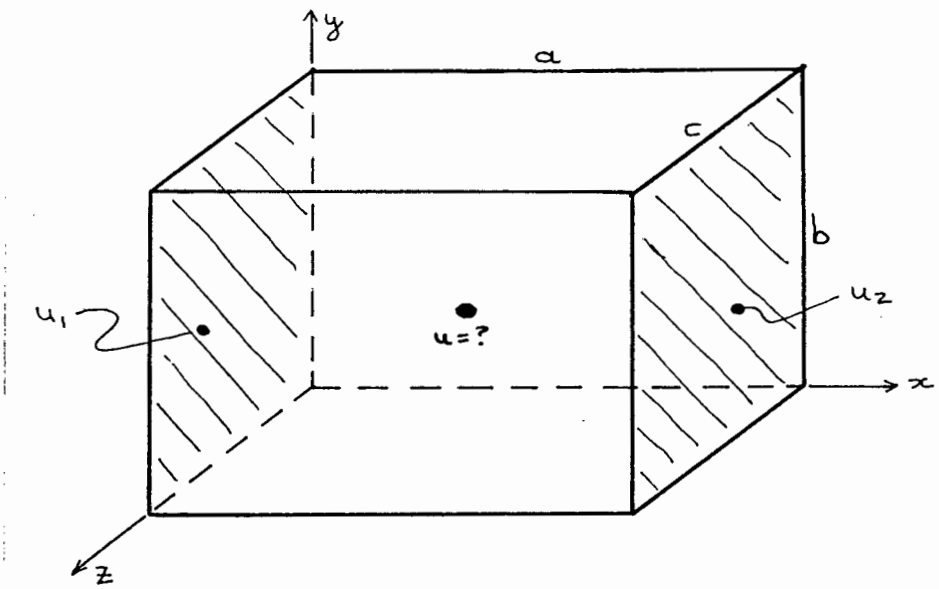

Fig 6.8 3-D solid cube

Using Fourier analysis, the equation (6.13) has as solution:

$$u = \frac{16}{\pi^2} \sum_{p=0}^{\infty} \sum_{q=0}^{\infty} \frac{[u_1 \sin h\ell(a-x) + u_2 \sin h\ell x] \sin [(2p+1)\frac{\pi y}{b}] \sin [(2q+1)\frac{\pi z}{c}]}{(2p+1)\ (2q+1)\ \sinh \ell a}$$

where

$$\ell^2 = \frac{(2p+1)^2\pi^2}{b^2} + \frac{(2q+1)^2\pi^2}{c^2} \qquad (6.14)$$

By making simplifying assumptions, we can reduce the complexity of eq (6.14)

If we let a = b = c = 1, then the coordinates of the centroid are $(\frac{1}{2}; \frac{1}{2}; \frac{1}{2})$. Hence $x = y = z = \frac{1}{2}$. We also let $u_1 = 0$ and $u_2 = 1°C$.

Thus eq (6.14) is reduced to:

$$u = \frac{16}{\pi^2} \sum_{p=0}^{\infty} \sum_{q=0}^{\infty} \frac{\sinh \ell(\frac{1}{2}) \sin [(2p+1)\frac{\pi}{2}] \sin [(2q+1)\frac{\pi}{2}]}{(2p+1)\ (2q+1)\ \sinh \ell}$$

where $\ell^2 = \pi^2 [(2p+1)^2 + (2q+1)^2]$ (6.15)

By inputting combinations of p and q, we can calculate the value of the series. This was done and it was found that only the first three terms were sufficient for convergence, hence p = 0, 1, 2, 3 and q = 0, 1, 2, 3. All the combinations of (p ; q) were input and summed. Summing gave us:

$$u\left(\frac{1}{2};\frac{1}{2};\frac{1}{2}\right) = 0.166°C \qquad (6.16)$$

Using ADINAT, a finite-element mesh was constructed enabling the calculation of the temperature at the centre of the domain. A single 3-dimensional heat conduction element was used with 17 nodes. The material model used was again the same as in the other two analyses. The mesh is shown in Fig 6.9

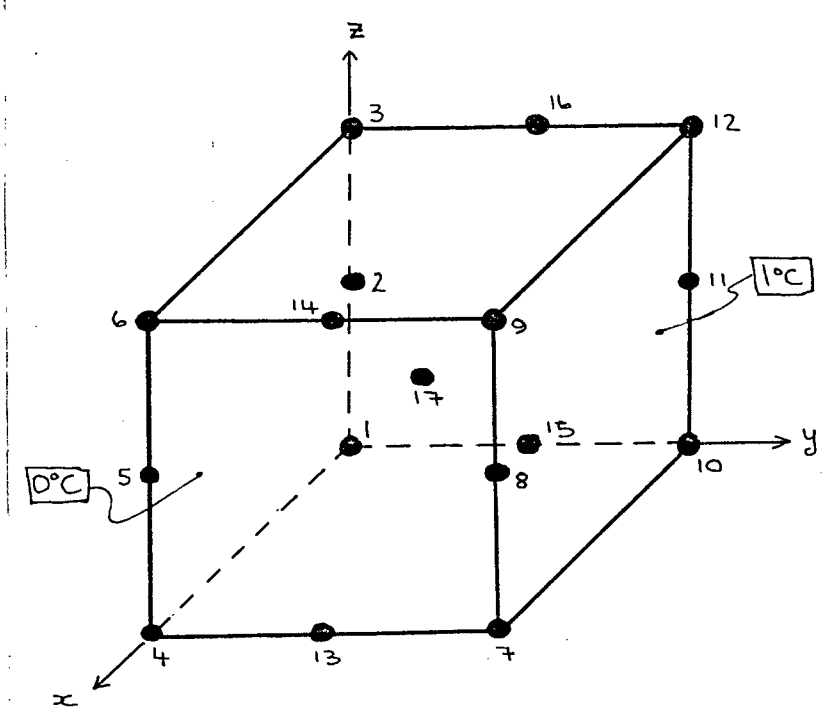

Fig 6.9 3-D finite-element mesh

Again the problem of conflicting boundaries occured with nodes 9, 12, 7 and 10. Again the problem was run twice and averaged. Run 1 consisted of the analysis with nodes 9, 12, 8, 11, 7 and 10 all heated to 1°C with the remaining nodes at 0°C. Run 2 consisted of

analysing the problem with only nodes 8 and 11 heated to 1°C with the remaining nodes at 0°C. In practice, this ammounted to assuming that nodes 9, 12, 7 and 10 were "transition-nodes" with a temperature of 0.5°C.

Results of the analysis are shown in Table 6C

Node	Temp (Run 1)	Temp (Run 2)	Temp (Average)
1	0 °C	0 °C	0 °C
2	0	0	0
3	0	0	0
4	0	0	0
5	0	0	0
6	0	0	0
7	1.0	0	0.5
8	1.0	1.0	1.0
9	1.0	0	0.5
10	1.0	0	0.5
11	1.0	1.0	1.0
12	1.0	0	0.5
13	0	0	0
14	0	0	0
15	0	0	0
16	0	0	0
17	0.260	0.239	0.249

Table 6C ADINAT temperature output (3D case)

Upon investigation, we can see that the average temperature at steady-state of the central node 11 is 0.249°C.

This is not the same as the value obtained in eq (6.16), but the difference can be attributed to the coarseness of the finite-element mesh. If four of these elements were joined together as another cubic mesh and the temperature of the central node obtained from ADINAT, the finite-element solution would definitely be closer to the theoretical value obtained in eq (6.16). This fact, that the more we refine the finite-element mesh the more accurate our answer will be, will be illustrated in section 6.2.1 in the 1-dimensional transient analysis

As a matter of interest, the values obtained in the previous analyses is almost exactly the same as values guessed for each analysis. For example, if in a rod one side is fixed at 0°C and the other end fixed at 1°C, we can guess that the temperature at the centre of the rod is 0.5°C as the heat can only flow in one path. In the case of a plate under similar boundary conditions, the heat can take two paths and if we assume isotropy then we would guess the value at the centre of the plate to be a half of 0.5°C ie. 0.25°C. Similarly in the case of the cube structure, there are three heat paths, hence we expect the central temperature to be one third of 0.5°C ie. 0.166°C. These temperatures are the same as those calculated by theory and apply at steady-state. We are more interested in finding out what happens immediately after the application of the temperature loading, ie. the transient state.

6.3 TRANSIENT ANALYSIS

For the transient analyses, the problems were similar to those in Fig 6.1, 6.2 and 6.3 except that the boundary conditions were changed. In the 1-dimensional case, the rod had an initial temperature of 1°C throughout but at the start of the analysis, the ends of the rod were subjected to a temperature of 0°C. In the 2-dimensional case, the plate had an initial temperature of 1°C throughout, but at the start of the analysis, all four boundaries were fixed at 0°C. In the 3-dimensional case, the cube had an initial temperature of 1°C throughout, but at the start of the analysis, all the surfaces were subjected to a temperature of 0°C. In each case, the variation in temperature with respect to time was monitored for the node at the centre of each mesh.

Only a thermal analysis was performed for each of the cases, using the linear conduction elements with a lumped heat capacity matrix and a constant isotropic conductivity matrix and constant specific heat matrix.

At this point, the timestep choice came into condiseration. In the transient analysis, we were now to consider how the temperature changed at the nodes as the time increased and we had to specify a timestep Δt for use in a time integration scheme. The availible schemes were

the Euler backward method, Euler forward method and the trapezoidal rule. (See ch. 5.1.5). In Bathe [21], it was stated that the Euler forward method would be stable provided that $\Delta t \leq 2/\lambda$ where λ is the maximum eigen-value of the system. Also, the Euler backward method and the trapezoidal rule were both unconditionally stable but the trapezoidal rule was second-order accurate in Δt whereas the Euler backward method was only first-order accurate in Δt. This implied that using $\Delta t = 1$ for the last two methods would give an answer free of numerical instabilities.
Also, it was obvious that using a smaller timestep we could obtain even more accurate answers, but the answers would converge to respective values making extremely small timesteps unnecessary. Some problems investigated in this section were analysed for both the Euler backward and trapezoidal rules and for time steps of $\Delta t = 1$, $\Delta t = .5$ and $\Delta t = .1$

As a check, a frequency analysis was performed for the 2-dimensional case showing that our choice of Δt was in the range of stability.

6.3.1 1-DIMENSION

The equation to be solved is:

$$\frac{\partial^2 u}{\partial x^2} = \frac{1}{\kappa}\frac{\partial u}{\partial t} \quad \text{where} \quad \kappa = \frac{k}{\rho c} \tag{6.17}$$

subject to the boundary conditions:

1) Initial temperature throughout = 1°C
2) At time t = 0, the ends are fixed at 0°C for t 0

These conditions are shown schematically in Fig 6.10

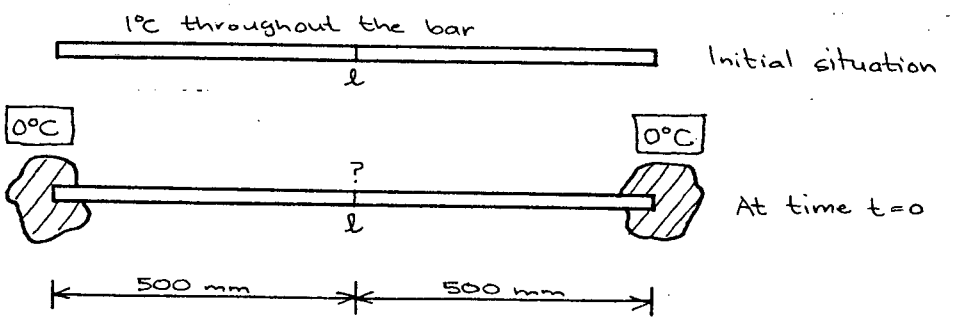

Fig 6.10 Problem boundary conditions

Using Fourier analysis, equation (6.17) has solution

$$u = \frac{4}{\pi} \sum^{\infty} \frac{1}{} \quad \exp\left[\frac{-\kappa(2n+1)^2\pi^2 t}{\ell^2}\right] \quad \sin\frac{(2n+1)\pi x}{\ell} \qquad (6.18)$$

where $\exp(x) = e^x$

Again, this equation (6.18) can be reduced in complexity by making simplificating assumptions. If we let $\kappa = 10\,000$ for rapid convergence, $\ell = 1\,000$ mm and $x = 500$ mm (ie. at the centre of the bar, the equation reduces to:

$$u = \frac{4}{\pi} \sum^{\infty} \frac{1}{(2n+1)} \quad \exp\left[-\frac{(2n+1)^2\pi^2 t}{100}\right] \quad \sin\frac{(2n+1)\pi}{2} \qquad (6.19)$$

If we evaluate eq (6.19) for 3 timesteps ie. t = 0, 1, 2, we get the results shown in Table 6D

	TEMPERATURE (°C)		
n	t = 0	t = 1	t = 2
0	1.2732	1.1536	1.0452
1	-0.4244	-0.1746	-0.0718
2	0.2546	0.0216	0.0018
3	-0.1819	-0.0014	0
4	0.1415	0	0

Table 6D Evaluation of eq (7.19)

At this point, the temperatures for t = 1 and t = 2 have already converged, but the sequence for t = 0 continues.
This series is, in fact, the infinite series

$$\sum \frac{1}{(2n+1)} \qquad (6.20)$$

which sums to $\frac{\pi}{4}$ for an infinite number of terms.

As in eq (6.19) the series is multiplied by the factor $\frac{4}{\pi}$, this summed value for t = 0 becomes 1.0

Hence, the temperature at the central node for n = 0, 1, 2 .... is

$$\begin{aligned} &\text{At } t = 0, \quad u = 1.0000\ ^\circ C \\ &\text{At } t = 1, \quad u = 0.9992\ ^\circ C \\ &\text{At } t = 2, \quad u = 0.9752\ ^\circ C \end{aligned} \tag{6.21}$$

Using ADINAT, this problem was modelled as a bar using two one-dimensional heat conduction elements and the constant conductivity and specific heat material model.
As a first approximation, a 3-noded mesh was used and is shown in Fig 6.11. The implicit Euler backward method of integration was used and a timestep was chosed of $\Delta t = 1$.

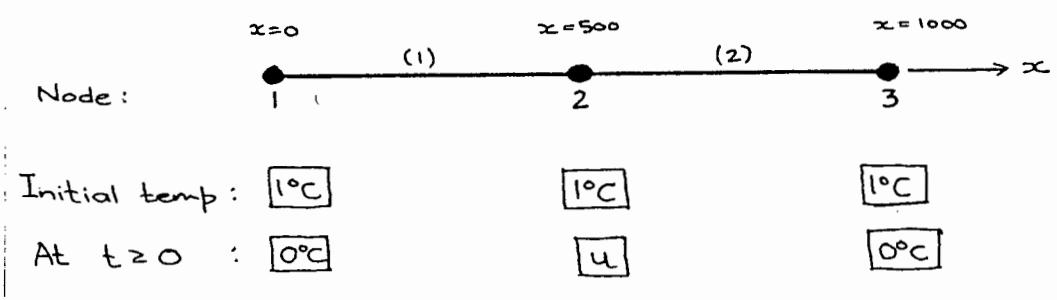

Fig 6.11 1-D transient analysis finite-element mesh

The result of this analysis yielded, at node 2:

$$\begin{aligned} &\text{At } t = 0, \quad u = 1.0000\ ^\circ C \\ &\text{At } t = 1, \quad u = 0.9259\ ^\circ C \\ &\text{At } t = 2, \quad u = 0.8573\ ^\circ C \end{aligned} \tag{6.22}$$

Comparing (6.21) and (6.22) we notice that the ADINAT results decrease more rapidly than the theoretical solutions, which can be attributed to the coarseness of the finite-element mesh. By adding more nodes to the mesh, ie. using more elements, a more refined estimate of the temperature decrease would be obtained. To verify the above statement, the exact problem was run again, but this time four 2-noded elements were used. This 5-noded mesh is shown in Fig 6.12

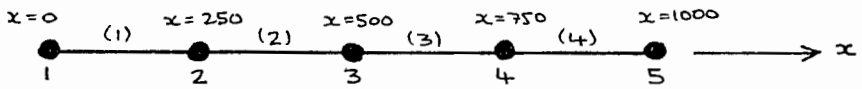

Fig 6.12 Refined 1-D finite-element mesh

The resulting temperatures from this mesh for the central node 3 were:

$$\begin{aligned} &\text{At} \quad t = 0, \quad u = 1.0000\ ^\circ C \\ &\text{At} \quad t = 1, \quad u = 0.9697\ ^\circ C \\ &\text{At} \quad t = 2, \quad u = 0.9225\ ^\circ C \end{aligned} \tag{6.23}$$

Comparing (6.22) and (6.23), we can see that the results from the 5-noded mesh are closer to the theoretical results than the 3-noded mesh, substantiating our previous statement.

For the sake of completeness, the same problem was run again using 17 nodes and still using the Euler backward integration method with a timestep of $\Delta t = 1$. The mesh is shown below:

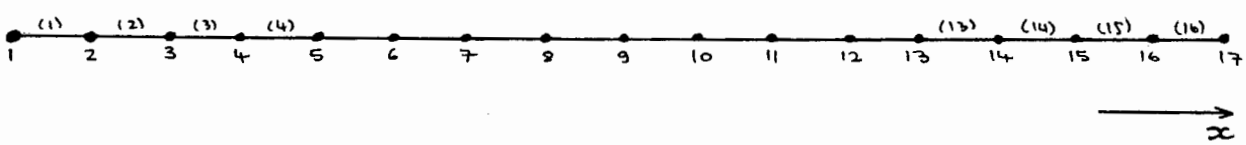

Fig 6.12a Refined 1-D finite-element mesh

The results of this mesh for the central node 9 were:

$$\begin{aligned} &\text{At} \quad t = 0, \quad u = 1.0000\ ^\circ C \\ &\text{At} \quad t = 1, \quad u = 0.9854\ ^\circ C \\ &\text{At} \quad t = 2, \quad u = 0.9506\ ^\circ C \end{aligned} \tag{6.23a}$$

Comparing (6.23 a) and (6.23) we are now even closer to the theoretical values of (6.21).

At this point it was decided to change the integration method from the Euler-backward method to the trapezoidal rule. The same 17-noded 1-D mesh was used with the Trapezoidal rule and a timestep of $\Delta t = 1$. This yielded:

$$\begin{aligned} &\text{At } t = 0, \quad u = 1.0000\ ^\circ C \\ &\text{At } t = 1, \quad u = 0.9958\ ^\circ C \\ &\text{At } t = 2, \quad u = 0.9728\ ^\circ C \end{aligned} \tag{6.23b}$$

Again, running the exact mesh except changing the timestep in the trapezoidal rule to $\Delta t = 0.1$, the following results were obtained:

$$\begin{aligned} &\text{At } t = 0, \quad u = 1.0000\ ^\circ C \\ &\text{At } t = 1, \quad u = 0.9981\ ^\circ C \\ &\text{At } t = 2, \quad u = 0.9716\ ^\circ C \end{aligned} \tag{6.23c}$$

These results are practically exact when compared to the theoretical results (6.21), and supports the theory of finite-element analysis that as we refine a mesh or decrease the timestep, the more accurate our analysis will be.

All these results are shown graphically in Graph G1 and as a percentage error of the theoretical value in Graph G2.

Table 6E below shows results from running the 17-node mesh with Euler and Trapezoidal rule integration each for timesteps of $\Delta t = 1$, $\Delta t = 0.5$ and $\Delta t = 0.1$

Method	Euler backward Integration			Trapezoidal Rule		
Time	t=0 sec	t=1 sec	t=2 sec	t=0 sec	t=1 sec	t=2 sec
Theory	1.0000	0.9992	0.9752	1.0000	0.9992	0.9752
t = 1	1.0000	0.9854	0.9506	1.0000	0.9958	0.9728
t = 0.5	1.0000	0.9911	0.9590	1.0000	0.9973	0.9723
t = 0.1	1.0000	0.9966	0.9685	1.0000	0.9981	0.9716

Table 6E Difference in Integration Methods

Studying this table, we can notice that the trapezoidal rule approached the theoretical solution with a much larger timestep than the Euler backward integration method. The reason for this is that the implicit Euler backward integration method is unconditionally stable and first order accurate in Δt, whereas the Trapezoidal rule is also unconditionally stable but is second order accurate in Δt. [21] This means that the temperature variation of the finite-element model is approximated much better by the Trapezoidal rule and very small timesteps can be avoided if we use this rule, which will ultimately save computer time and cost.

6.3.2 2-DIMENSIONS

The equation to be solved is;

$$\frac{\partial^2 u}{\partial x^2} + \frac{\partial^2 u}{\partial y^2} = \frac{1}{\kappa}\frac{u}{\partial t} \quad \text{where} \quad \kappa = \frac{k}{\rho c} \tag{6.24}$$

subject to the boundary conditions:

1) Initial temperature throughout = 1°C.
2) At the time t = 0, boundaries fixed at 0°C for t > 0

This is shown schematically in Fig 6.13

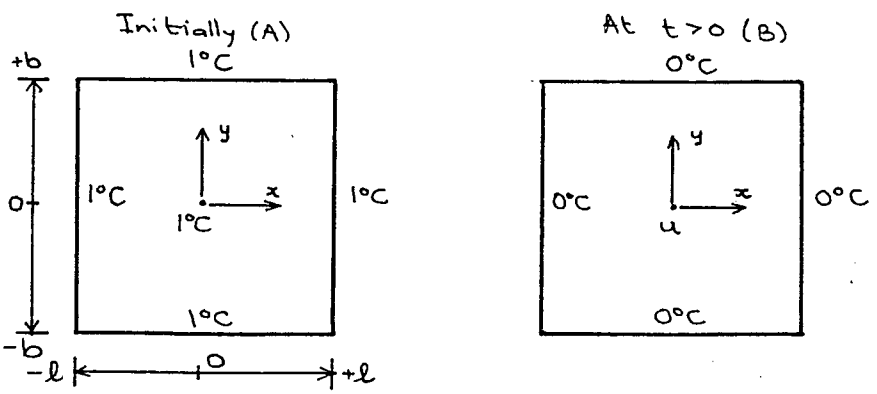

Fig 6.13 (A) 1°C throughout
(B) Boundaries 0°C

Using Fourier analysis, equation (6.24) has solution:

$$u = \frac{16}{\pi^2} \sum_{m=0}^{\infty} \sum_{n=0}^{\infty} \frac{(-1)^{m+n}}{(2m+1)(2n+1)} \exp\left[\frac{-\kappa\pi^2 t}{4}\left\{\frac{(2m+1)^2}{b^2} + \frac{(2n+1)^2}{\ell^2}\right\}\right] x$$

$$\cos\frac{(2n+1)\pi x}{2\ell} \qquad \cos\frac{(2m+1)\pi y}{2b} \qquad (6.25)$$

By having $-\ell < x < \ell$ and $-b < y < b$, this conveniently gives us the coordinates of the centre of the plate as (0;0). This implies that the cosine terms in eq (6.25) all become equal to 1. The equation (6.25) simplifies further by letting κ = 10 000, ℓ = 1 000, b = 1000. Hence

$$u = \frac{16}{\pi} \sum_{m=0}^{\infty} \sum_{n=0}^{\infty} \frac{(-1)^{m+n}}{(2m+1)(2n+1)} \exp\left[\frac{-\pi^2 t}{400}\left\{(2m+1)^2 + (2n+1)^2\right\}\right] \quad (6.26)$$

Evaluating this series, we get the result for the plate centre:

At	t = 0,	u = 1.000°C
At	t = 1,	u = 0.978°C
At	t = 2,	u = 0.942°C

(6.27)

Note that these values are lower than those for the one-dimensional case. This implies that the 2-D system cools faster than the 1-D system. This is logical, as in the 2-D case, more heat can flow out of a particular point (x and y direction) as opposed to the 1-D case (only x direction).

Using ADINAT, this problem was modelled as a thin plate using four eight-noded two-dimensional heat conduction elements with the same material model as used previously. The mesh used is shown in Fig 6.14.

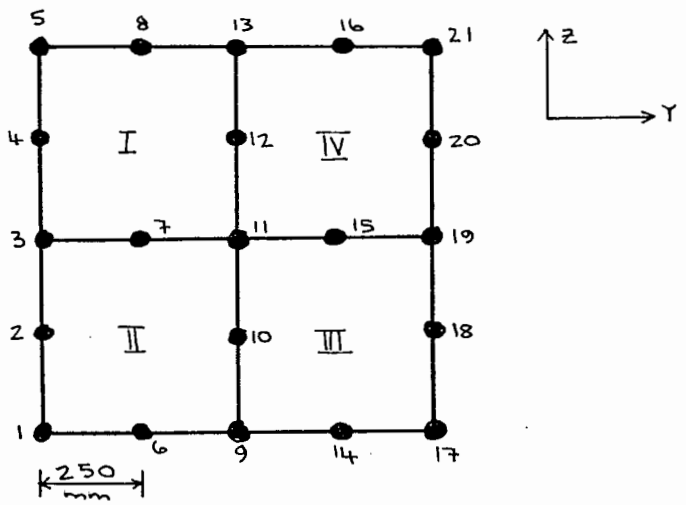

Fig 6.14 2-D mesh for transient analysis

Initially, all nodes had a temperature of 1°C. At the start of the analysis, the four boundaries were fixed at 0°C with only interior nodes 7, 10, 11, 12 and 15 free to vary. Our main interest was the variation of temperature at central node 11.

Results of this analysis yielded, at node 11:

$$\begin{aligned} &\text{At} \quad t = 0, \quad u = 1.000°C \\ &\text{At} \quad t = 1, \quad u = 1.0060°C \\ &\text{At} \quad t = 2, \quad u = 0.9497°C \end{aligned} \tag{6.28}$$

Comparing equations (6.27) and (6.28) we see that the results for $t = 0$ and $t = 2$ are very close to the theoretical solution. At $t = 1$ though, the temperature appears to have become warmer instead of cooler, which due to the impossibility of this occuring in practice, can only be attributed to numerical instability.
In order to investigate this "warming" effect, the 2-D problem was run again using a more refined mesh with Euler backward integration and a timestep of $\Delta t = 1$.
The mesh is shown in Fig 6.14a.

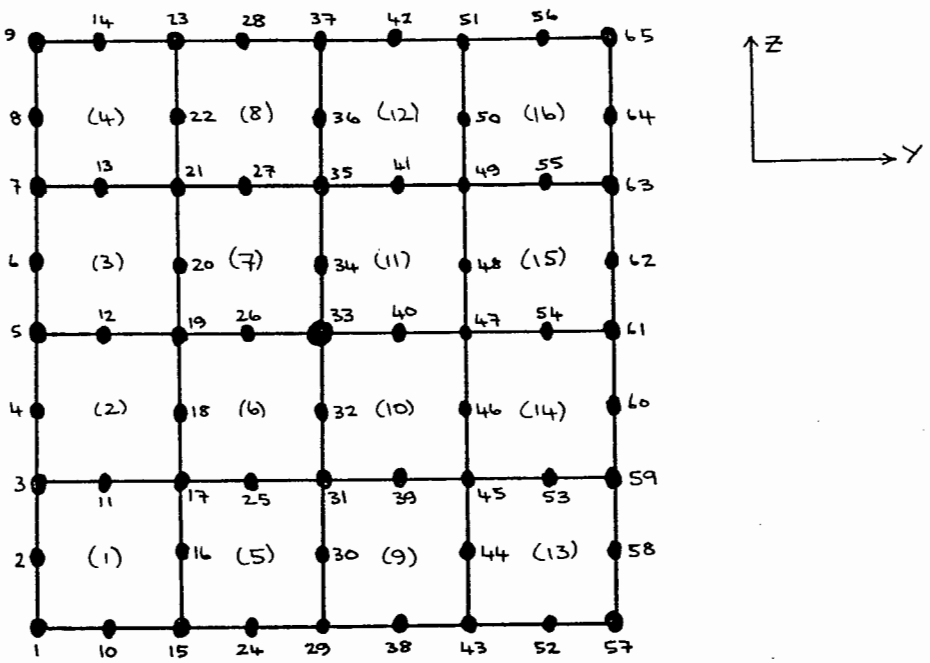

Fig 6.14a 2-D refined mesh

The results for node 33 were:

$$\begin{aligned} &\text{At} \quad t = 0, \quad u = 1.0000°C \\ &\text{At} \quad t = 1, \quad u = 0.9361°C \\ &\text{At} \quad t = 2, \quad u = 0.8673°C \end{aligned} \qquad (6.28a)$$

In spite of extensive mesh refining, these values above were the closest values obtained to the theoretical solution. These results are shown graphically in Graph G3 and as a percentage error of the theoretical value in Graph G4.

6.3.3 3-DIMENSIONS

The equation to be solved is:

$$\frac{\partial^2 u}{\partial x^2} + \frac{\partial^2 u}{\partial y^2} + \frac{\partial^2 u}{\partial z^2} = \frac{1}{\kappa}\frac{\partial u}{\partial t} \quad \text{where } \kappa = \frac{k}{\rho c} \qquad (6.29)$$

subject to the boundary conditions:

1) Initial temperature throughout = 1°C
2) Surface temperature = 0°C for $t > 0$

The problem is shown schematically in Fig 6.15

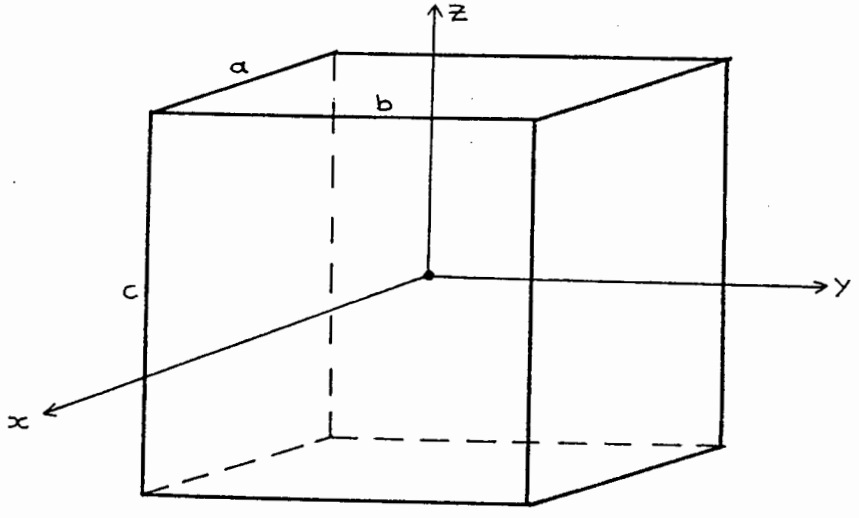

Fig 6.15 3-D representation of problem

Using Fourier analysis, the solution to eq (6.29) is:

$$u = \frac{64}{\pi} \sum_{\ell=0}^{\infty} \sum_{m=0}^{\infty} \sum_{n=0}^{\infty} \frac{(-1)^{\ell+m+n}}{(2\ell+1)(2m+1)(2n+1)} \cos \frac{(2\ell+1)\pi x}{2a} \times \cos \frac{(2m+1)\pi y}{2b} \times \cos \frac{(2n+1)\pi z}{2c} \times e^{-\alpha t} \qquad (6.30)$$

where $\alpha = \frac{\kappa\pi^2}{4} \left[\frac{(2\ell+1)^2}{a^2} + \frac{(2m+1)^2}{b^2} + \frac{(2n+1)^2}{c^2} \right]$

By having $-a < x < a$, $-b < y < b$ and $-c < z < c$, this conveniently give us the coordinates of the centroid of the cube as (0;0;0). This implies again that all the cosine terms in eq (6.30) become equal to 1. The equation (6.30) simplifies further by letting κ = 10 000, a = 1 000, b = 1 000, c = 1 000. Hence

$$u = \frac{64}{\pi} \sum_{\ell=0}^{\infty} \sum_{m=0}^{\infty} \sum_{n=0}^{\infty} \frac{(-1)^{\ell+m+n}}{(2\ell+1)(2m+1)(2n+1)} \quad e^{-\alpha t}$$

where

$$\alpha = \frac{\pi^2}{400} [(2\ell+1)^2 + (2m+1)^2 + (2n+1)^2] \qquad (6.31)$$

Evaluating this series, we get the results for the cube centroid.

$$\begin{aligned} &\text{At} \quad t = 0, \quad u = 1.000°C \\ &\text{At} \quad t = 1, \quad u = 0.967°C \\ &\text{At} \quad t = 2, \quad u = 0.915°C \end{aligned} \qquad (6.32)$$

Using ADINAT, this problem was modelled as a cubic structure using a single 17-noded 3-dimensional heat conduction element with the same material model as used previously.
The mesh is shown in Fig 6.16. The Euler backward integration method was used with a timestep $\Delta t = 1$

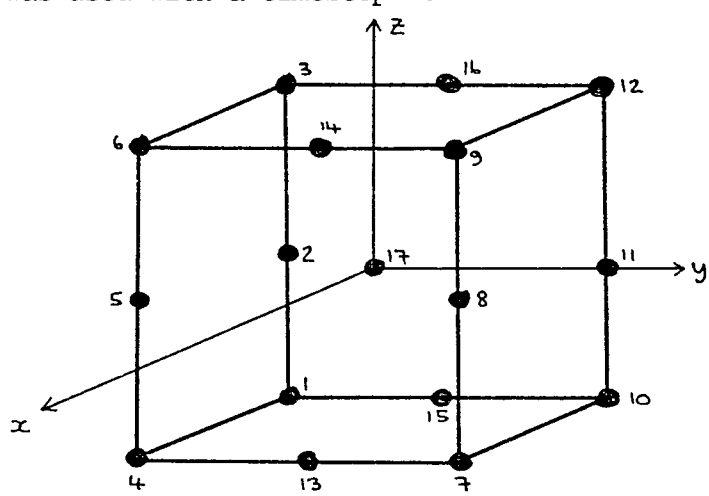

Fig 6.16 3-D finite-element mesh (17 nodes)

The results from this mesh were, for node 17:

$$\begin{aligned} &\text{At} \quad t = 0, \quad u = 1.000°C \\ &\text{At} \quad t = 1, \quad u = 0.652°C \\ &\text{At} \quad t = 2, \quad u = 0.424°C \end{aligned} \qquad (6.33)$$

Again, by comparing the results of eq (6.32) and (6.33) we see that the finite-element model temperatures decrease very much more quickly than the theoretical solution, again due to the coarseness of the 3-dimensional mesh. This principle was discussed and verified in the 1-dimensional transient analysis case, Section 6.3.1.

On the topic of "coarseness of a mesh", the coarser a finite-element mesh, the more error exists in its solution. This can be understood, for example, if we concentrate on the results of the 3-dimensional transient analysis. The theoretical solution was based on the boundary condition that the "surface" temperatures were fixed at 0°C. This surface comprised of an area 1 000 mm x 1 000 mm. The finite-element solution which was to represent this area comprised of 6 or 8 single nodes. This means, in theoretical terms, that each node was to model the behaviour of an area 408 mm x 408 mm or 350 mm x 350 mm respectively. This is quite a tall order and we can, at best only expect an approximate answer. More accurate answers would have been obtained if, say, 27 elements consisting of 27 nodes each could have been used. This idea is prohibited by the amount of input data.
It was deceided however, for completeness, to run the problem again using a 21 noded mesh as shown below:

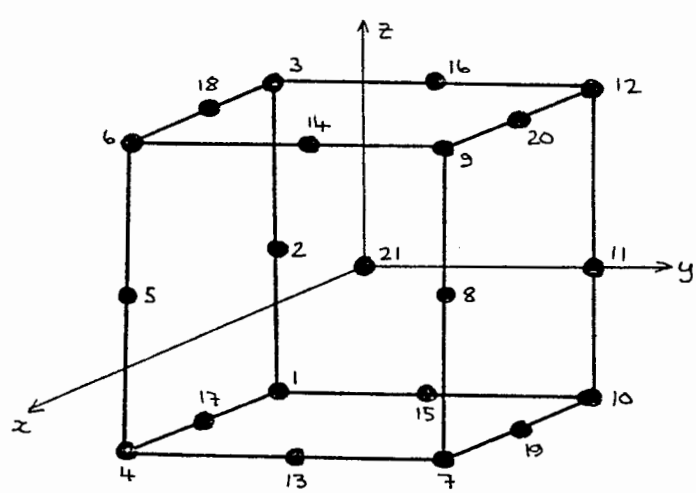

Fig 6.17 21 noded mesh

The results of this mesh for the central node 21 were:

$$\begin{aligned} &\text{At} \quad t = 0, \quad u = 1.0000°C \\ &\text{At} \quad t = 1, \quad u = 0.6030°C \\ &\text{At} \quad t = 2, \quad u \ 0 \ 0.3624°C \end{aligned} \tag{6.34}$$

Comparing (6.34) and (6.33), it was noticed that the addition of more nodes gave a worse result contrary to the finite-element theory. This indicated that the original mesh used could have been unstable in terms of the problem. The problem was refined further using 3 elements identical to Fig 6.17, joined together, hence still providing a node at the centroid. This mesh is shown in Fig 6.17a below.

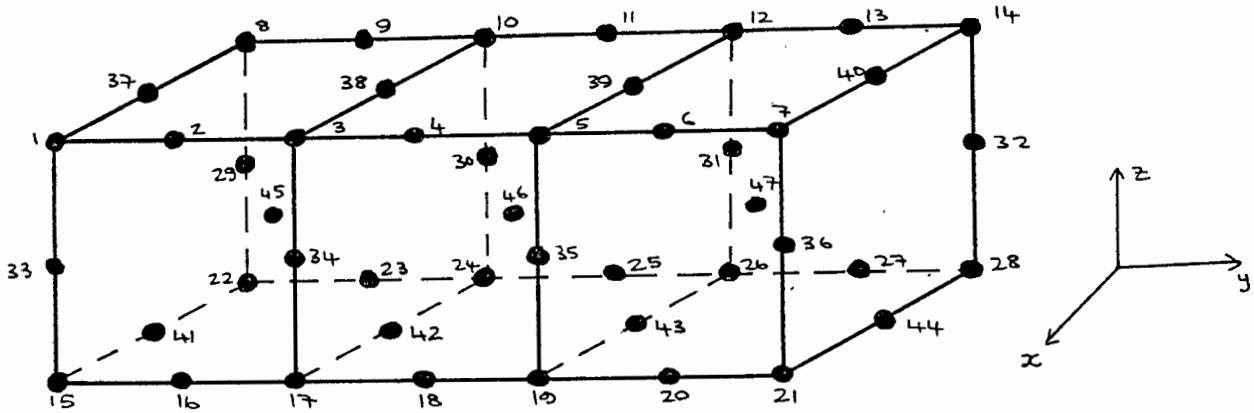

Fig 6.17a 47-noded mesh

The resulting temperatures of central node 46 were as follows:

$$\begin{aligned} &\text{At} \quad t = 0, \quad u = 1.0000°C \\ &\text{At} \quad t = 1, \quad u = 0.2950°C \\ &\text{At} \quad t = 2, \quad u = 0.0861°C \end{aligned} \tag{6.35}$$

Comparison between (6.34) and (6.35) showed that something was wrong. We were refining the mesh but our error was increasing . The necessity of the central node in each element was questioned, and it was thought that this extra node at the centroid could be causing numerical problems. The problem was rerun using 8 eight-noded brick elements as shown in Fig 6.17b.

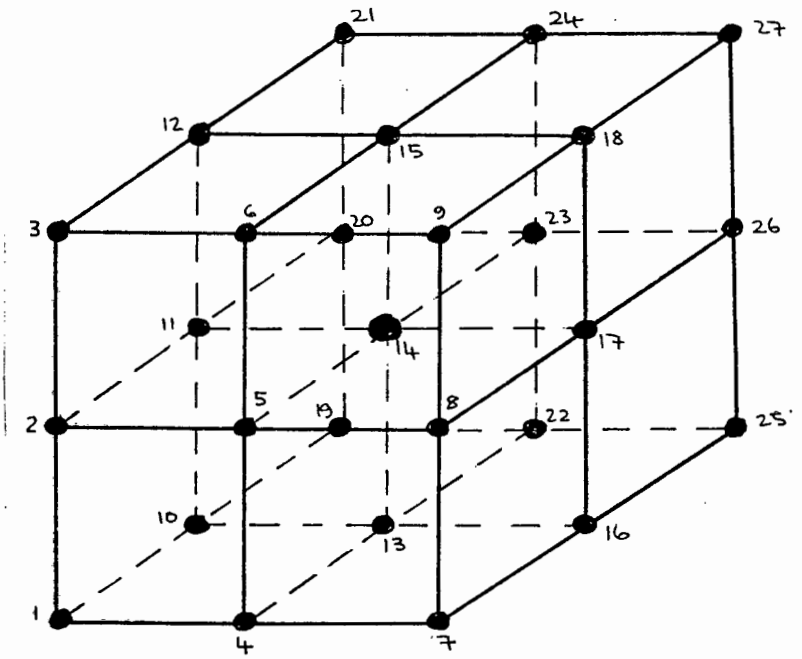

Fig 6.17b 8 eight-noded 3D elements

Using Euler backward integration with a timestep $\Delta t = 1$, the following results were obtained:

$$\begin{aligned} &\text{At } t = 0, \quad u = 1.000°C \\ &\text{At } t = 1, \quad u = 0.904°C \\ &\text{At } t = 2, \quad u = 0.817°C \end{aligned} \tag{6.36}$$

As these results from (6.36) were still relatively far from the exact solution, the mesh was once again refined a final time, as shown in Fig 6.17c.

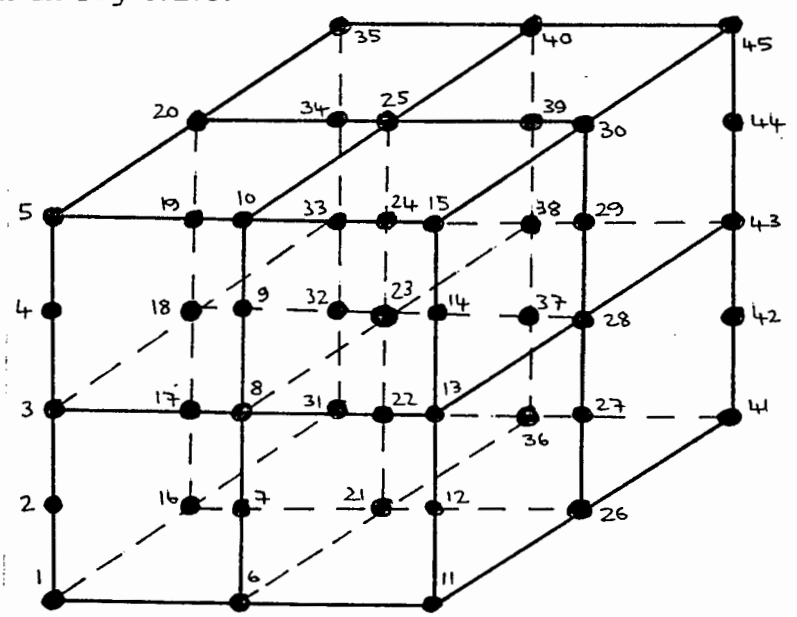

Fig 6.17c
45 noded mesh

Using Euler backward integration with a timestep of $\Delta t = 1$, the following results were obtained for the temperature of node 23:

$$\begin{aligned} &\text{At } t = 0, \quad u = 1.0000°C \\ &\text{At } t = 1, \quad u = 0.9328°C \\ &\text{At } t = 2, \quad u = 0.8598°C \end{aligned} \tag{6.37}$$

Using Trapezoidal integration with $\Delta t = 1$ yielded

$$\begin{aligned} &\text{At } t = 0, \quad u = 1.0000°C \\ &\text{At } t = 1, \quad u = 0.9372°C \\ &\text{At } t = 2, \quad u = 0.8623°C \end{aligned} \tag{6.38}$$

These results are shown graphically in Graph G5 and as a percentage error of the theoretical value in Graph G6.

For examination of this 3-dimensional transient analysis accentuated the fact that although results would be output for any input, the correct modelling of a particular problem is essential and can only be undertaken with a comprehensive knowledge of finite-element theory. In our case, the effect of a central node in the centre of the element seemed to cause numerical problems which were rectified as shown as this node was removed, even though a central node was allowable in the User Manual of ADINAT [14].

TIME AFTER SOLUTION START

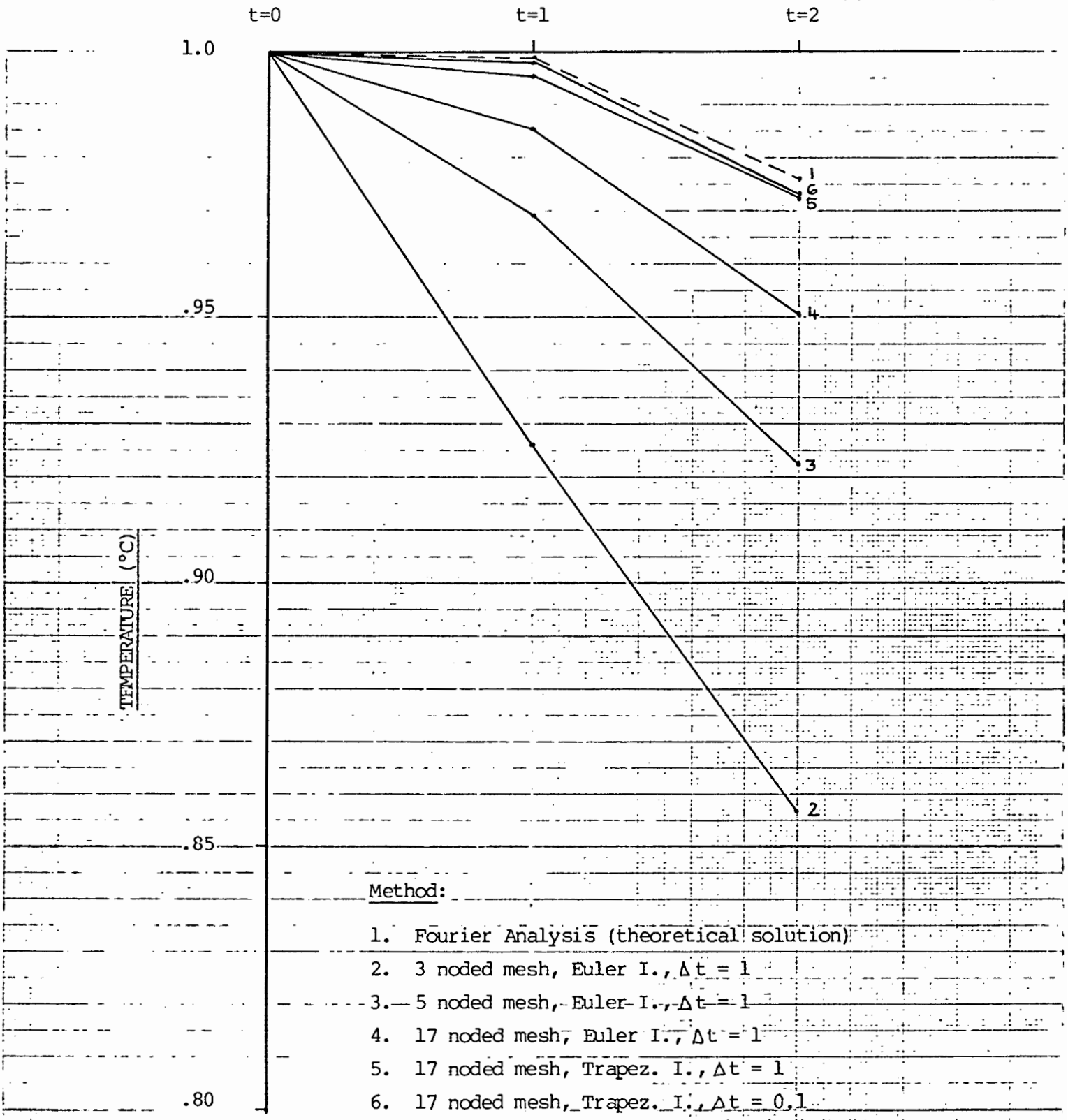

Method:

1. Fourier Analysis (theoretical solution)
2. 3 noded mesh, Euler I., $\Delta t = 1$
3. 5 noded mesh, Euler I., $\Delta t = 1$
4. 17 noded mesh, Euler I., $\Delta t = 1$
5. 17 noded mesh, Trapez. I., $\Delta t = 1$
6. 17 noded mesh, Trapez. I., $\Delta t = 0.1$

Graph G1 1-D Transient Analysis Results Comparison

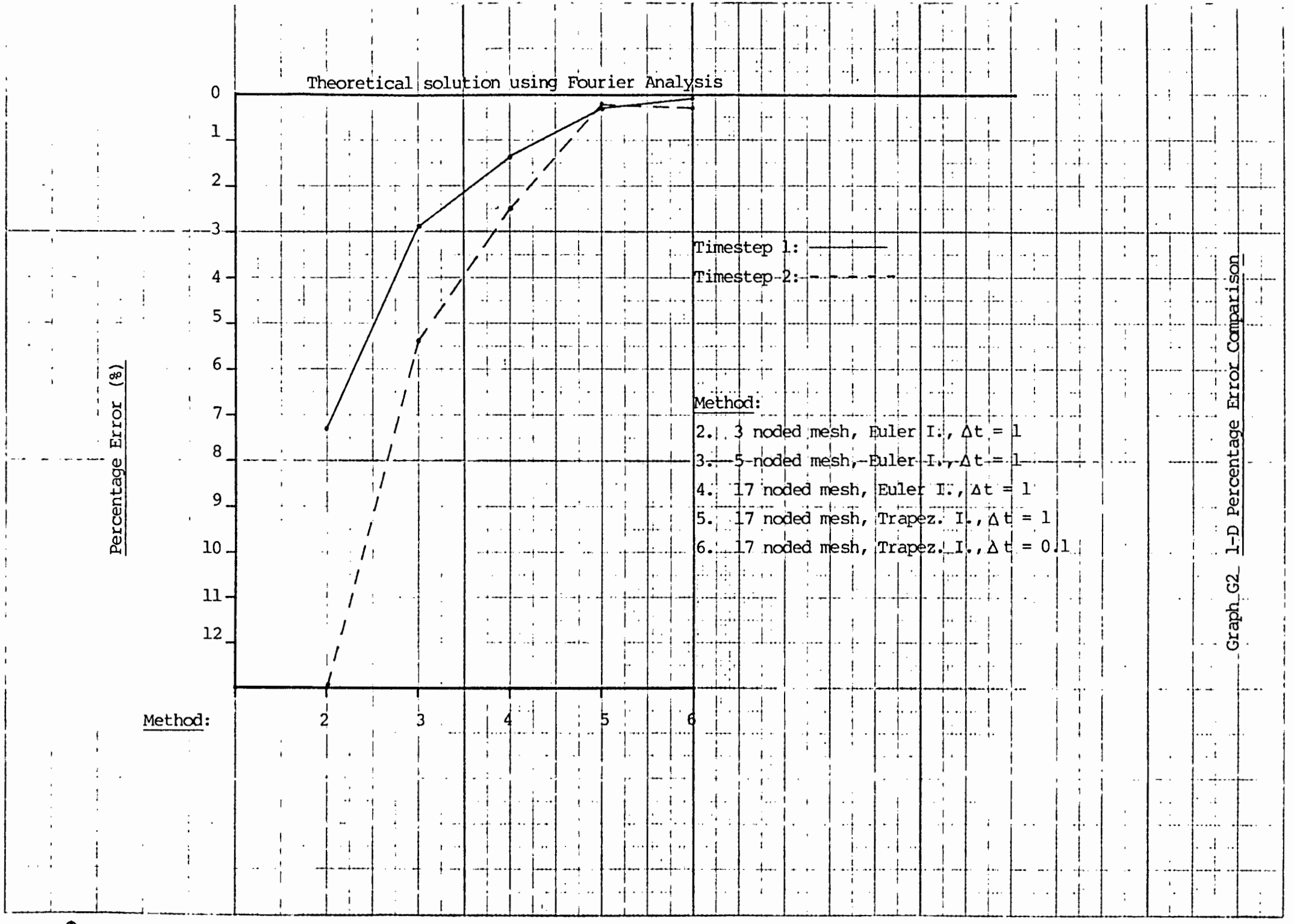

Graph G2 1-D Percentage Error Comparison

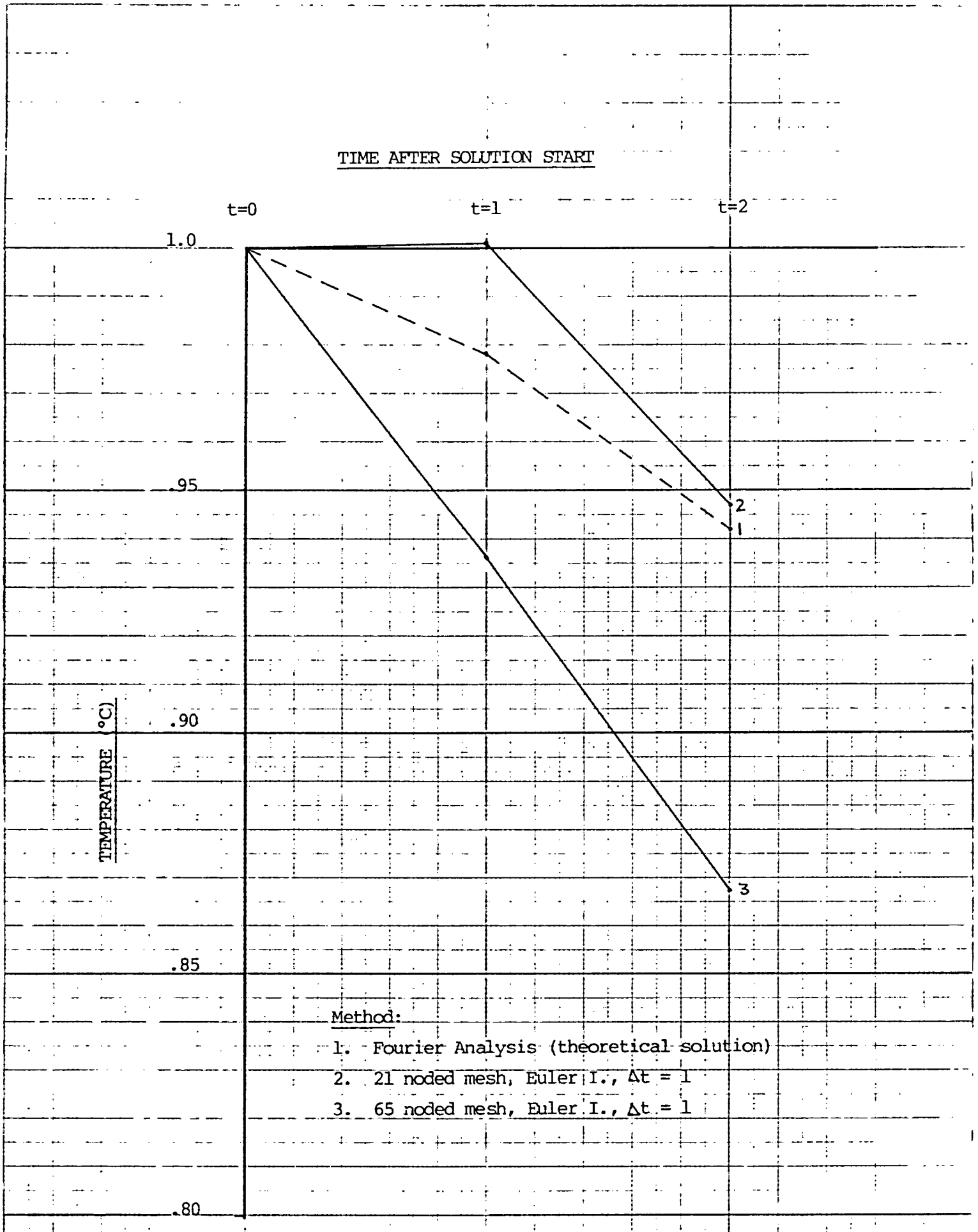

Method:

1. Fourier Analysis (theoretical solution)
2. 21 noded mesh, Euler I., $\Delta t = 1$
3. 65 noded mesh, Euler I., $\Delta t = 1$

Graph G3 2-D Transient Analysis Results Comparison

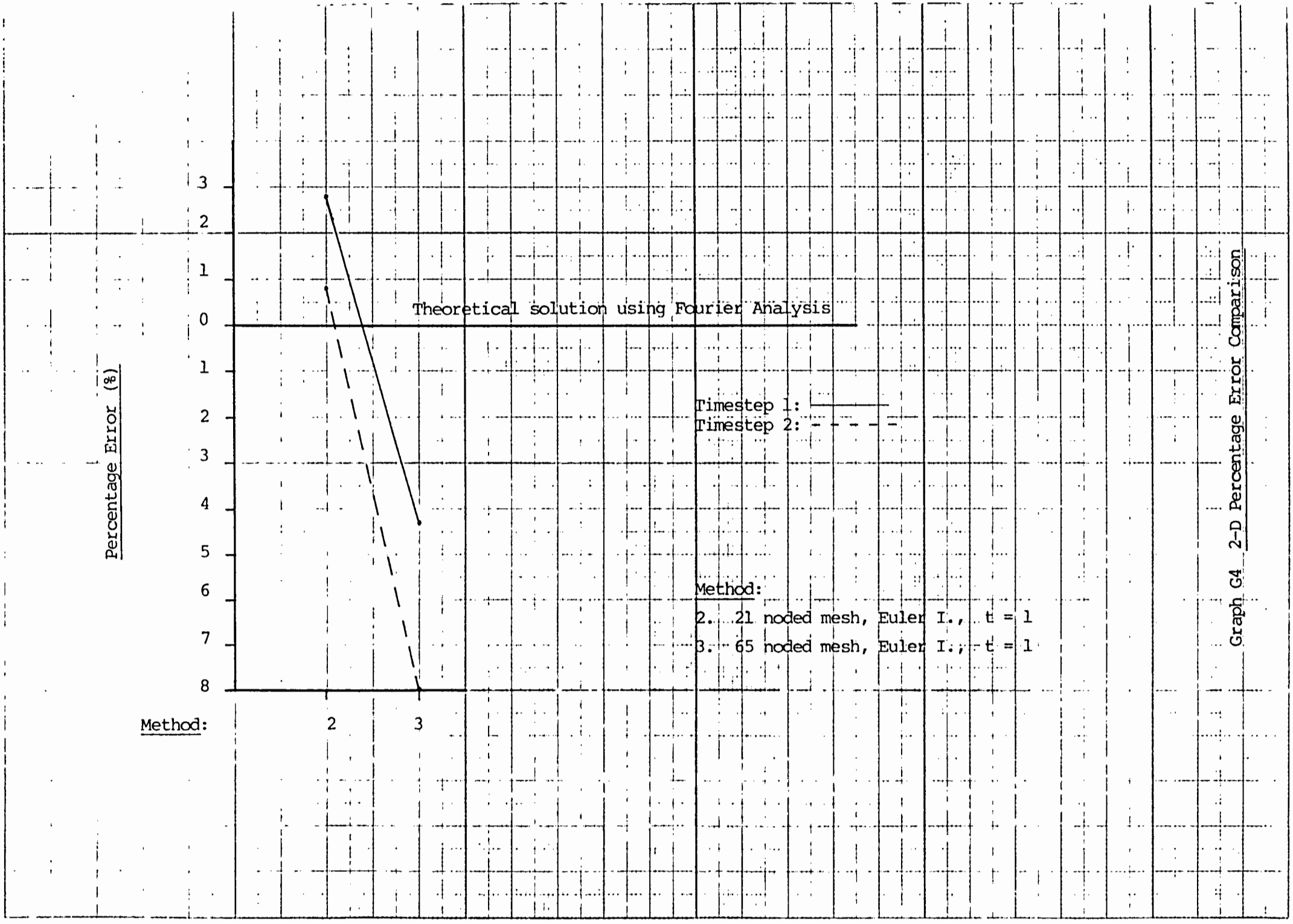
Graph G4 2-D Percentage Error Comparison
Percentage Error (%)
3
2
1
0
1
2
3
4
5
6
7
8
Theoretical solution using Fourier Analysis
Timestep 1:
Timestep 2:
Method:
2. 21 noded mesh, Euler I., t = 1
3. 65 noded mesh, Euler I., t = 1
Method:
2
3

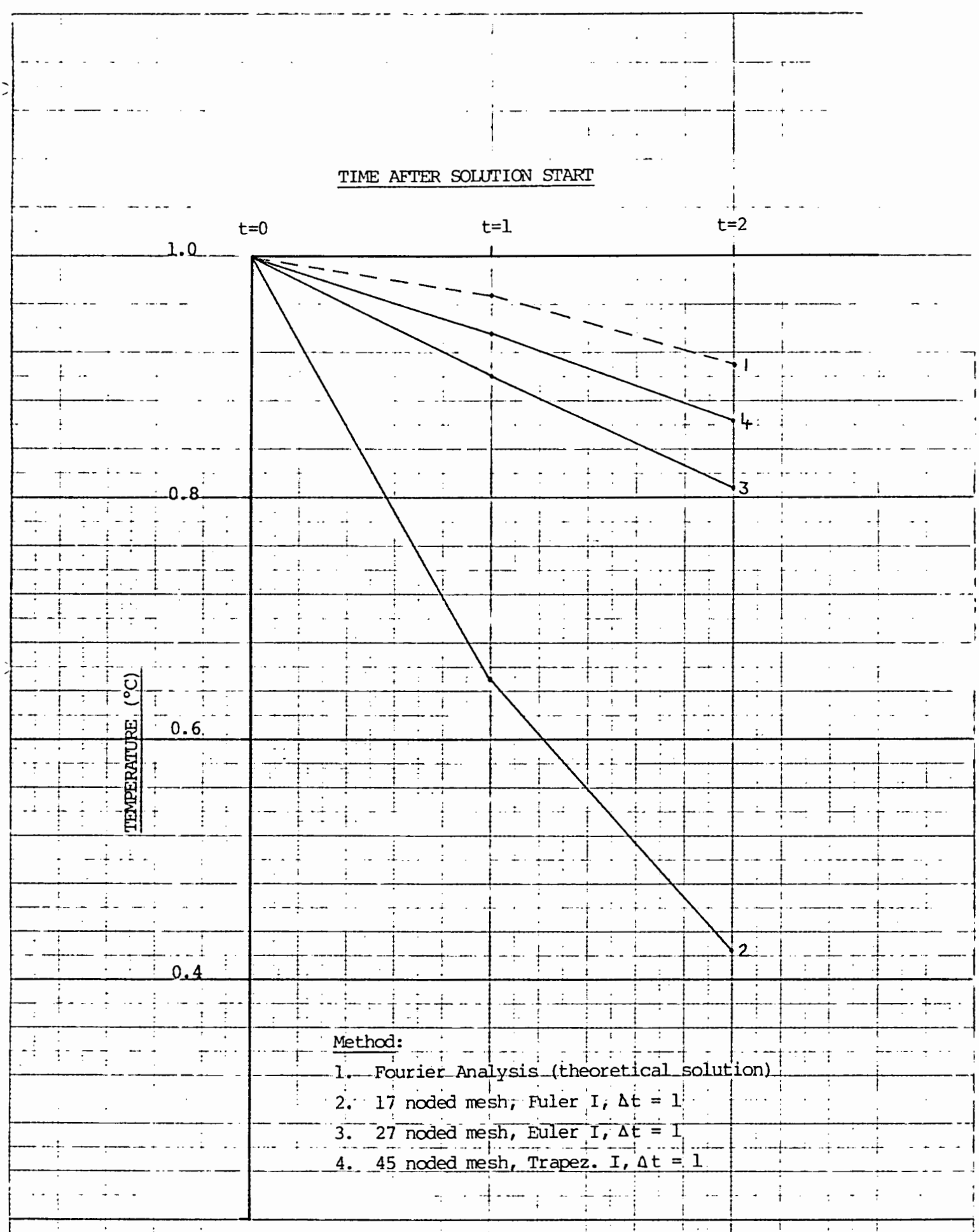

Graph G5 3-D Transient Analysis Results Comparison

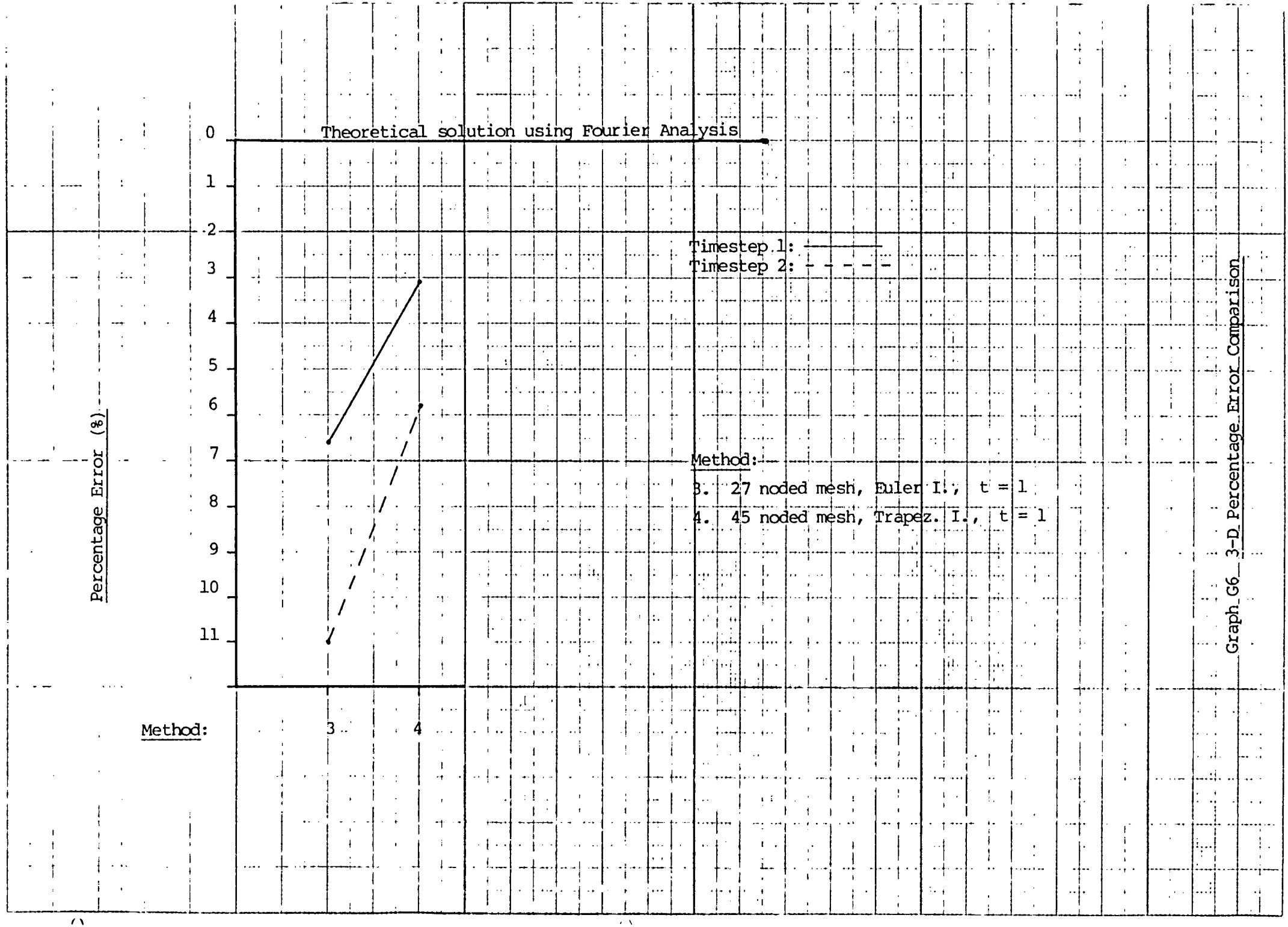

Graph G6 3-D Percentage Error Comparison

CHAPTER SEVEN

MATHEMATICAL ANALYSIS OF HEAT FLOW IN WELDMENTS

7.1 INTRODUCTION

Complex thermal cycles in the weldment are produced by the heat supplied by a welding arc, causing thermal stress and resulting in residual stress and distortion. These problems can only be analyzed once the heat flow during the welding operation is fully understood. Analysis has shown that accuracy is high when dealing with changes in temperature reasonably far from the welding arc, but this accuracy, in general, drops when analyzing temperature changes in the heat-affected-zone and weld metal.

7.2 GENERATION OF WELDING ARC HEAT

The main source of heat generated is the heat generated by the electric power of the welding arc, H, where

$$H = VI \text{ (Watts)} \tag{7.1}$$

and V = arc voltage (volts)
I = arc current (amps)

Other sources are the heat generated by chemical reactions in the electrode coating, arc atmosphere and molten pool as well as heat caused by the transformation of the metal.

7.3 DISSIPATION OF THE WELDING HEAT

The generated heat from the welding arc either dissipates into the workpiece by thermal conduction, dissipates into the electrode by thermal conduction or dissipates into the surrounding atmosphere by radiation from the arc and workpiece.

7.4 SIMPLE SOLUTIONS FOR HEAT FLOW ANALYSIS IN WELDMENTS

7.4.1 TEMPERATURE DISTRIBUTIONS IN QUASI-STATIONARY STATE [3]

Fig 7.1 shows the temperature distribution in a plate when a weld bead is being laid on the surface using a moving coordinate (w, x, y) moving at the same speed as the welding arc, where

$$w = x - vt \qquad (7.2)$$

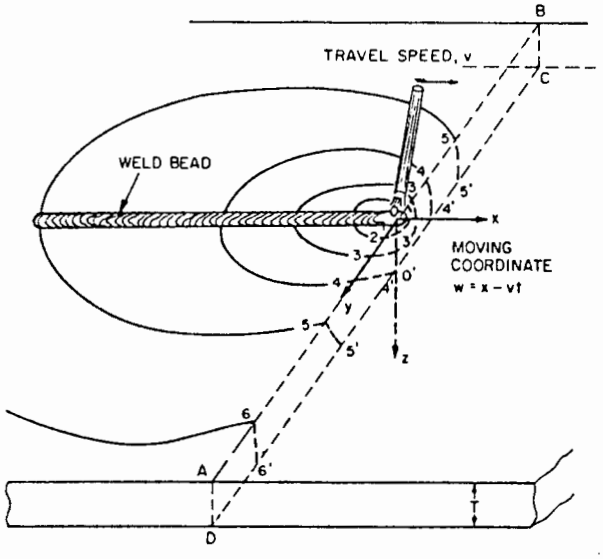

Fig 7.2 Plate temperature distribution during weld

The conduction equation

$$\frac{\partial^2\theta}{\partial x^2} + \frac{\partial^2\theta}{\partial y^2} + \frac{\partial^2\theta}{\partial z^2} = \frac{1}{\kappa}\frac{\partial\theta}{\partial t} \qquad (7.3)$$

can also be expressed as follows:

Because the temperature undergoes no change in the new system and

$$w = x - vt \qquad (7.2)$$

$$\frac{\partial w}{\partial x} = 1 \qquad \frac{\partial w}{\partial t} = -v \qquad (7.3a)$$

Hence $$\frac{\partial\theta}{\partial x} = \frac{\partial\theta}{\partial w}\frac{\partial w}{\partial x} = \frac{\partial\theta}{\partial w} \qquad (7.4)$$

and similarly $$\frac{\partial^2\theta}{\partial x^2} = \frac{\partial^2\theta}{\partial w^2} \qquad (7.5)$$

The relationship between $\left(\frac{\partial\theta}{\partial t}\right)$ for the fixed coordinate and the moving coordinate ie. $\left(\frac{\partial\theta}{\partial t}\right)_{FC}$ and $\left(\frac{\partial\theta}{\partial t}\right)_{MC}$ is

$$\left(\frac{\partial\theta}{\partial t}\right)_{FC} = \left(\frac{\partial\theta}{\partial t}\right)_{MC} + \frac{\partial\theta}{\partial w}\frac{\partial w}{\partial t}$$

$$= \left(\frac{\partial\theta}{\partial t}\right)_{MC} - v\left(\frac{\partial\theta}{\partial w}\right) \qquad (7.6)$$

In the quasi-stationery state,

$$\left(\frac{\partial\theta}{\partial t}\right)_{MC} = 0 \qquad (7.7)$$

Hence eq (7.3) can be expressed as:

$$\frac{\partial^2\theta}{\partial w^2} + \frac{\partial^2\theta}{\partial y^2} + \frac{\partial^2\theta}{\partial z^2} = -\frac{v}{\kappa}\left(\frac{\partial\theta}{\partial w}\right) \qquad (7.8)$$

Now we have θ as a function of position (w, y, z) only.
We can handle eq (7.8) more easily by replacing it with the following expression:

$$\theta = \theta_o + \exp\left[-\left(\frac{v}{2\kappa}\right)w\right]\phi(w, y, z) \qquad (7.9)$$

where θ_o= initial temperature

$\phi(w, y, z)$ = function to be found

If we put eq (7.9) into (7.8), we find

$$\frac{\partial^2\phi}{\partial w^2} + \frac{\partial^2\phi}{\partial y^2} + \frac{\partial^2\phi}{\partial z^2} - \left(\frac{v}{2\kappa}\right)^2\phi = 0 \qquad (7.10)$$

This expression can be solved for special cases.

7.4.1.1 <u>3-D, semi-infinite plate</u>

This applies when a bead weld is deposited on the surface of a

large, thick plate ($T \to \infty$ in Fig 7.2).
The following conditions must be satisfied by the solution of eq (7.8):

1) The heat flux through the surface of the hemisphere drawn around the source must tend to the value of the total heat Q delivered to the plate as the radius of the sphere tends to zero. If R is the radius of the sphere, then

$$\lim_{R \to 0} \left(-2\pi R^2 \lambda \frac{\partial \theta}{\partial R}\right) = Q_p$$

where $R = \sqrt{w^2 + y^2 + z^2}$ (7.11)

λ = thermal conductivity

2) There is no heat transmission from the plate to the surrounding atmosphere, heat loss through the surface being negligible ie.

$$\frac{\partial \theta}{\partial z} = 0 \quad \text{for } z = 0 \text{ and } R \neq 0 \qquad (7.12)$$

3) At a very large distance from the source, the temperature of the plate remains unchanged. If the distance is assumed infinite, then

$$\theta = \theta_o \quad \text{for } R = \infty \qquad (7.13)$$

The solution satisfying the previous three conditions is then:

$$\theta - \theta_o = \frac{Q_p}{2\pi\lambda} e^{-(v/2\kappa)w} \left[\frac{e^{-(v/2\kappa)R}}{R} \right] \qquad (7.14)$$

7.4.1.2 3-D, finite Thickness

The temperature distribution in a plate of finite thickness T can be obtained from solution (7.14) by neglecting radiation from the surface

The surface condition is thus

$$\frac{\partial \theta}{\partial z} = 0 \quad \text{for} \quad z = 0 \text{ and } z = T \tag{7.15}$$

The solution is obtained by adding an infinite series to eq (7.14). Hence

$$\theta - \theta_o = \frac{Q}{2\pi\lambda} \; e^{-(v/2\kappa)w} \; \left[\frac{e^{-(v/2\kappa)R}}{R} + \sum_{n=1}^{\infty} \left(\frac{e^{-(v/2\kappa)R_n}}{R_n} + \frac{e^{-(v/2\kappa)R'_n}}{R'_n} \right) \right] \tag{7.16}$$

where $R_n = \sqrt{w^2 + y^2 + (2nT - z)^2}$ and

$$R'_n = \sqrt{w^2 + y^2 + (2nT + z)^2} \tag{7.17}$$

7.4.1.3 2-D, Infinite Plate

The change in temperature caused by a line source of intensity

$$q = \frac{Q}{T} \tag{7.18}$$

which moves along the x - axis of an infinite plate is given by:

$$\theta - \theta_o = \frac{q}{2\pi\lambda} \; e^{-(v/2\kappa)w} \; K_o \left(\frac{v}{2\kappa} r\right) \tag{7.19}$$

where $r = \sqrt{w^2 + y^2}$

and $K_o(z)$ is the modified Bessel Function,

$$K_o(z) = \int_{-1}^{\infty} \frac{e^{-zt}}{\sqrt{t^2 - 1}} \, dt \; \sim \sqrt{\frac{\pi}{2z}} \, e^{-z} \text{ for large } (z) \tag{7.20}$$

7.4.1.4 2-D, Infinite Plate

If the plate breadth is 2B, the plate edge condition is:

$$\frac{\partial \theta}{\partial y} = 0 \quad \text{for } y = \pm B$$

The solution can be obtained by adding an infinte series to eq (7.21).

7.4.2 TEMPERATURE DISTRIBUTION IN THE NON-STATIONARY STATE [3]

Fig 7.3 shows the coordinates in the z-dimensional heat flow due to welding.

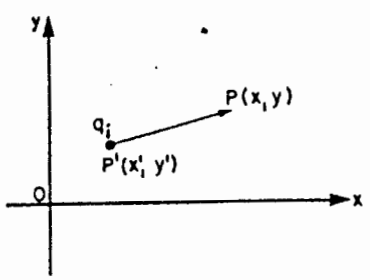

a. Instantaneous Heat Source at P'(x', y')

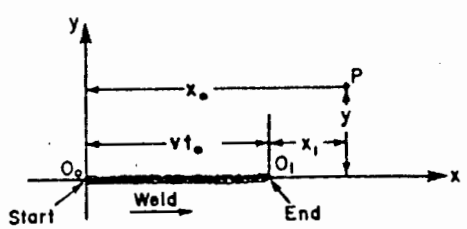

b. Welding Along the X-axis from O_0 to O_1 for a Distance vt_0

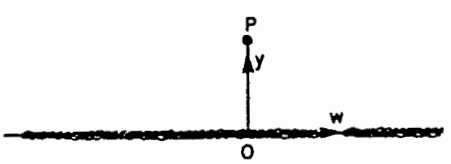

c. Quasi-stationary State

Fig 7.3 2-D heat flow coordinates due to welding

If at time t' an instantaneous line source q_i' occurs at P' (x', y') on an infinite plate (shown Fig 7.3a) and is then extinguished, the temperature change at P(x,y) at time T is given by:

$$\theta - \theta_o = \frac{e^{-[(x-x')^2 + (y-y')^2 / 4\kappa (t-t')]}}{4\pi\kappa(t-t')} \frac{q_i}{\rho c} \qquad (7.22)$$

Using eq (7.22), the temperature change due to a moving point source can be obtained. Fig (7.3b) shows a line source of intensity q initiating at a point 0_o and moving along the x - axis at a constant velocity v for a period t_o. It is then extinguished at point 0_1. The temperature change θ at point P at time t_1 after the heat source has been extinguished is:

$$\theta - \theta_o = \int_o^{t_o} \frac{e^{-[(x-vt)^2 + y^2] / 4\kappa (t_o + t_1 - t)}}{4\kappa\pi (t_o + t_1 - t)} \frac{q}{\rho c} \, dt \qquad (7.23)$$

This equation can be expressed as follows:

$$\theta - \theta_o = \frac{q}{4\pi\lambda} \, e^{-(v/2\kappa) w} \int_a^b \frac{e^{-\zeta - (\gamma^2/\zeta)}}{\zeta} \, d\zeta$$

where

$$a = (v^2/4\kappa) \, t_1 \qquad (7.24)$$

$$b = (v^2/4\kappa) \, (t_0 + t_1)$$

$$w = x - v \, (t_0 + t_1)$$

$$r^2 = \left(\frac{v}{4\kappa}\right)^2 (w^2 + y^2) \qquad (7.25)$$

Eq (7.25) represents a two-dimensional heat flow general solution

when laying a straight weld bead. If we assume welding continues from $t_0 = -\infty$ to $+\infty$, from eq (7.24) we obtain the temperature distribution in the quasi-stationary state as:

$$\theta - \theta_o = \frac{q}{4\pi\lambda} \; e^{-(V/2\kappa)\, w} \int_{-\infty}^{\infty} \frac{e^{-\zeta - (\gamma^2/\zeta)}}{\zeta} \, d\zeta$$

$$= \frac{q}{2\pi\lambda} \; e^{-(V/2\kappa)w} \; K_o \, (V/2\kappa \; r) \qquad (7.26)$$

In eq (8.26), the origin of the moving coordinate (w, y) is taken as shown in Fig 7.3c. ie. t = 0 when the heat source passes point 0. Note that eq (7.26) is the same as eq (7.19).

CHAPTER EIGHT

MATHEMATICAL THEORY OF RESIDUAL THERMAL STRESS

8.1 INTRODUCTION

Upon uniform heating, a material will expand uniformly and no thermal stresses will be produced. If the material undergoes uneven heating, thermal stresses will be produced. When unevenly distributed non-elastic strains such as plastic strains exist, residual stresses are also produced. The fundamental two-dimensional plane-stress ($\sigma_z = 0$) relationships in a residual stress-field are discussed in Section 8.2.

8.2 FUNDAMENTAL RELATIONSHIPS IN 2-DIMENSIONAL STRESS FIELD [3]

Strains are composed of elastic and non-elastic strains, ie.

$$\begin{aligned} \varepsilon_x &= \varepsilon'_x + \varepsilon_x'' \\ \varepsilon_y &= \varepsilon'_y + \varepsilon_y'' \\ \gamma_{xy} &= \gamma'_{xy} + \gamma_{xy}'' \end{aligned} \qquad (8.1)$$

where ε_i = components of total strain

ε_i' = components of elastic strain

ε_i'' = components of non-elastic strain (thermal, plastic)

Note that for thermal stress,

$$\varepsilon_x'' = \varepsilon_y'' = \alpha\Delta T$$

$$\gamma_{xy}'' = 0$$

where α = coefficient of linear expansion

ΔT = change in temperature from initial temperature

The Hooke's Law relationship holds between stress and elastic strain (Recall eq (2.3)): Hence,

$$\varepsilon_x' = \frac{1}{E}(\sigma_x - \nu\sigma_y)$$

$$\varepsilon_y' = \frac{1}{E}(\sigma_y - \nu\sigma_x) \qquad (8.2)$$

$$\gamma_{xy}' = \frac{1}{G}\tau_{xy}$$

The stress must satisfy the equilibrium conditions:

$$\frac{\partial\sigma_x}{\partial x} + \frac{\partial\tau_{xy}}{\partial y} = 0$$

$$\frac{\partial\tau_{xy}}{\partial x} + \frac{\partial\sigma_y}{\partial y} = 0 \qquad (8.3)$$

The total strain must also satisfy the compatibility condition:

$$\left(\frac{\partial^2\varepsilon_x'}{\partial y^2} + \frac{\partial^2\varepsilon_y'}{\partial x^2} - \frac{\partial^2\gamma_{xy}'}{\partial x\,\partial y}\right) + \left(\frac{\partial^2\varepsilon_x''}{\partial y^2} + \frac{\partial^2\varepsilon_y''}{\partial x^2} - \frac{\partial^2\gamma_{xy}''}{\partial x\,\partial y}\right) = 0 \qquad (8.4)$$

In the above equations, residual stresses will exist when the value of R, determined by the non-elastic strains, is not zero. ie.

$$R = -\left(\frac{\partial^2\varepsilon_x''}{\partial y^2} + \frac{\partial^2\varepsilon_y''}{\partial x^2} - \frac{\partial^2\gamma_{xy}''}{\partial x\,\partial y}\right) \qquad (8.5)$$

This R is the cause of the residual stresses and is termed "incompatibility".

Findings from mathematical analyses [3] have shown that:

1. Residual stresses in a body cannot be calculated by measuring the stress change taking place when an external load is applied to the body. Hence, the body is always cut to determine the residual stresses.

2. Residual stresses can be calculated from eq (8.2) when the elastic strain components are determined. However, the components of non-elastic strains, the cause of residual stress, cannot be calculated without knowledge of the formation history of the residual stress.

8.3 MATHEMATICAL ANALYSIS [3]

Many studies have been made to calculate the stress components σ_x, σ_y and τ_{xy} from knowing the non-elastic strains ε_x'', ε_y'' and γ_{xy}'' distributed under certain boundary conditions. Masubuchi developed a particular solution for stress calculation due to incompatibility distributed in a plate.

Airy's stress function is defined as $F(x,y)$ where

$$\sigma_x = \frac{\partial^2 F}{\partial y^2}$$

$$\sigma_y = \frac{\partial^2 F}{\partial x^2} \qquad (8.6)$$

$$\tau_{xy} = -\frac{\partial^2 F}{\partial x \partial y}$$

By introducing this function, the equilibrium condition, eq (8.3) can be satisfied. Strain components can be expressed from eq (8.2) as follows:

$$\varepsilon_x' = \frac{1}{E}\left(\frac{\partial^2 F}{\partial y^2} - \nu\frac{\partial^2 F}{\partial x^2}\right)$$

$$\varepsilon_y' = \frac{1}{E}\left(\frac{\partial^2 F}{\partial x^2} - \nu\frac{\partial^2 F}{\partial y^2}\right) \qquad (8.7)$$

$$\gamma_{xy}' = \frac{2(1+\nu)}{E}\frac{\partial^2 F}{\partial x \partial y}$$

From eq (8.5):

$$\frac{1}{E}\left(\frac{\partial^4 F}{\partial x^4} + 2\,\frac{\partial^4 F}{\partial x^2 \partial y^2} + \frac{\partial^4 F}{\partial y^4}\right) = R(x,y) \qquad (8.8)$$

Equation (8.8) can also be written as:

$$\left(\frac{\partial^2}{\partial x^2} + \frac{\partial^2}{\partial y^2}\right)^2 F(x,y) = E.R(x,y) \qquad (8.9)$$

The function $F(x,y) = F_1(x,y) + F_2(x,y)$ (8.10)

where $F_1(x,y)$ is a solution of

$$\left(\frac{\partial^2}{\partial x^2} + \frac{\partial^2}{\partial y^2}\right)^2 F_1(x,y) = 0 \qquad (8.11)$$

and $F_2(x,y)$ is a particular solution of eq (8.9)

The solution of eq (8.11) is generally called a "biharmonic" function which can be expressed as the combination of two "harmonic" functions.

CHAPTER NINE

LITERATURE SURVEY

(EXAMPLES OF WORK DONE IN THIS FIELD)

9.1 FINITE-ELEMENT CALCULATION OF RESIDUAL STRESSES IN WELDS

This research was done by J.K. Hepworth of the Central Electricity Generating Board, Marchwood Engineering Laboratories, Marchwood, Southampton SO5 5ZB [16]

9.1.1 SUMMARY

As the molten weld metal in welds begin to cool, residual stresses are generated. The surrounding parent metal experiences a thermal cycle and stresses are also generated from this action. In this research, a suite of finite-element programs were used to compute the residual stresses generated by a simple bead weld on a ferritic steel pipe. Apart from other approximations made, the austenitic-ferritic phase change effect was taken into account. The computed results for two different welding heat inputs were compared with a low alloy ferritic steel pipe weld made using the submerged arc welding process.

9.1.2 INTRODUCTION

When structural components are joined by welding, the critical region determining the life of the structure is usually the weld itself. The reason for this is that the weld metal and the heat-affected-zone (HAZ) often have inferior properties to those of the parent metal and it is here that defects of various types can occur. In addition, residual stresses generated during welding will act on the weld. These stresses can have the magnitude of the yield stress and even after treatment, aimed at relieving the stresses, can still be the largest stresses acting on the weld. Thus, if a welded component is to operate at high temperatures, the residual stresses may dictate the creep crack growth rate. It is therefore very important to be able to know how the welding procedure can affect the residual stresses present to a weld.

In the terms of residual stress measurement, the current experimental procedure is the semi-destructive and time consuming method, the centre hole-drilling method. With this method, it is virtually impossible to repeat a measurement in exactly the same place. Also, only surface measurements can be obtained and considerable problems are presented

with the determination of through-thickness stress distributions needed for a fracture mechanics assessment. The alternative approach is to calculate the residual stress, which should give the stress throughout the material.

9.1.3 METHOD OF CALCULATION

Residual stress calculation is a non-linear thermo-mechanical problem. Initialy a thermal analysis of the weld is performed to obtain the temperature distribution as a function of time. These temperatures are then used in a thermal transient elastic-plastic analysis of the weld. In this research, the BERSAFE suite of finite-element programs were used to obtain solutions.

9.1.3.1 Thermal Analysis

This work aimed to study the effect of various temperature distributions on the residual stresses produced by differing welding procedures. A number of drastic assumptions were made to simplify the thermal analysis; for example, the heat flow was treated as if it were axisymmetric, neglecting all heat transfer in the hoop direction. In submerged arc welding where the welding speed is fairly high, this is a reasonable approximation.

A major problem in welding thermal analysis is the melting and re-solidification of the weld pool and the attendant latent heat effects. Also, the heat transfer process in the molten weld pool and the solid will differ as convection and stirring are important. The enhancing of the specific heat over a range of temperature around the melting point represented the effect of latent heat, whereas the increased heat transfer rates in the weld pool were approximated by an increased thermal conductivity. Although these approximations do not represent the weld pool accurately, it is adequate as it is in the later part of the thermal cycle that residual stresses build up, when the temperatures are much lower.

The mesh for the thermal analysis is shown is Fig 9.1.

A high level of mesh refinement was required near the heated region, but this yielded too many elements to be used in the subsequent stress analysis. Hence, temperature data was transferred to a simpler mesh

for the stress analysis part of the calculation, as shown in Fig 9.2

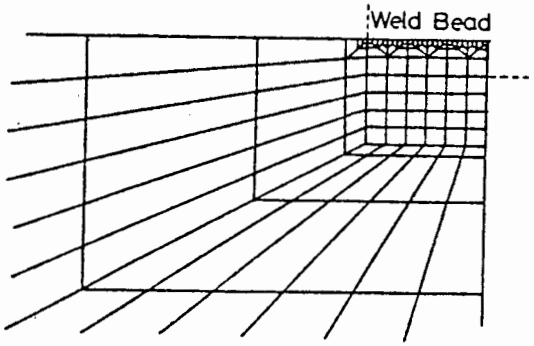

Fig 9.1 Thermal Analysis Mesh

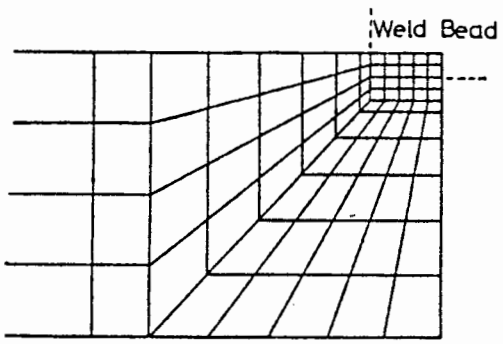

Fig 9.2 Stress Analysis Mesh

9.1.3.2 Stress Analysis

As the pipe weld was taken as axisymmetric, this meant that the assumption was made that all the weld metal was not being progressively laid around the pipes, but was being deposited all at the same time. Other assumptions were made to deal with the high temperature portion of the thermal cycle. At temperatures greater than 800°C, convergence problems in the analysis were caused by the low yield stress and extensive yielding. This high deformation at low stress was removed

from the calculation by allowing no thermal expansion above 800°C as it had little effect on the final residual stress. It was then assumed that the weld was heated instantaneously to a certain temperature distribution after solidification of the weld pool. The initial temperature distributions for the stress analysis are shown in Fig 9.3 for two seperate heat inputs.

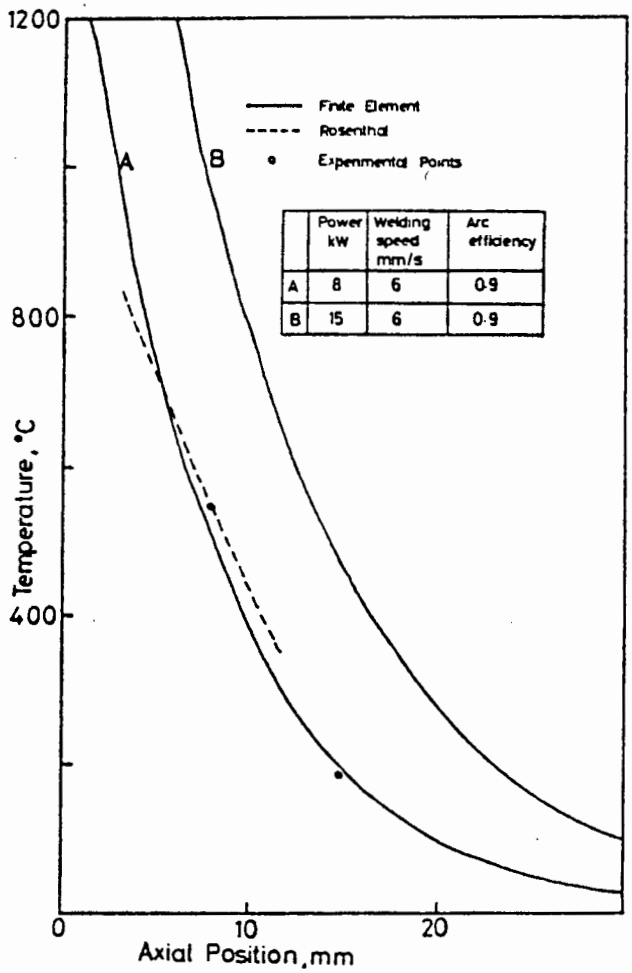

Fig 9.3 Initial Temperature Distributions

Residual stresses were then obtained by following the cooling of the weld. The insensitivity of the final residual stresses to the choice of time of the starting temperature distribution was shown by tests, provided that peak temperatures of less than 800°C were observed. Creep was also not taken account of. Many restarts were needed to

ensure good representation of the temperature dependant mechanical properties during thermal transient analysis with large temperature changes.

9.1.4 CALCULATION RESULTS

Calculations were performed on a pipe with outer radius of 250 mm and wall thickness of 30 mm.

Outer surface profiles of temperature for the start of the stress analysis are shown in Fig 9.3. This figure also shows the results of an approximate analytical solution by Rosenthal at a corresponding time after the passage of the arc. Reasonable agreement is obtained. Also shown are two experimental measures of temperature from a single layer bead on pipe weld under comparable conditions with the first set of conditions. The results of the stress calculations are shown in Figures 9.4, 9.5 and 9.6 for the first case

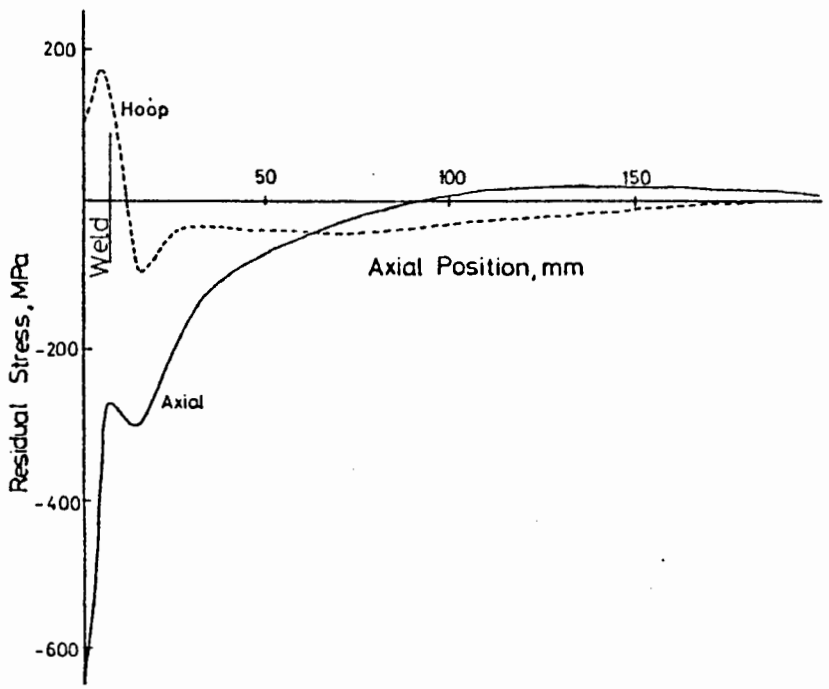

Fig 9.4 Residual Stress Distribution on Outer Surface

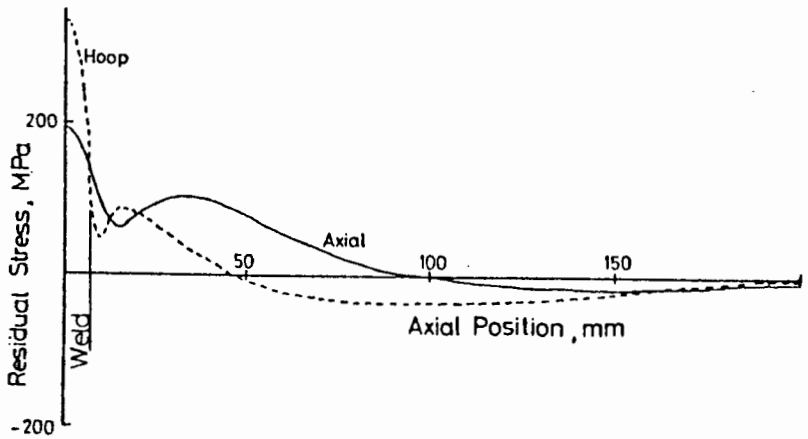

Fig 9.5 Residual Stress Distribution on Pipe Bore

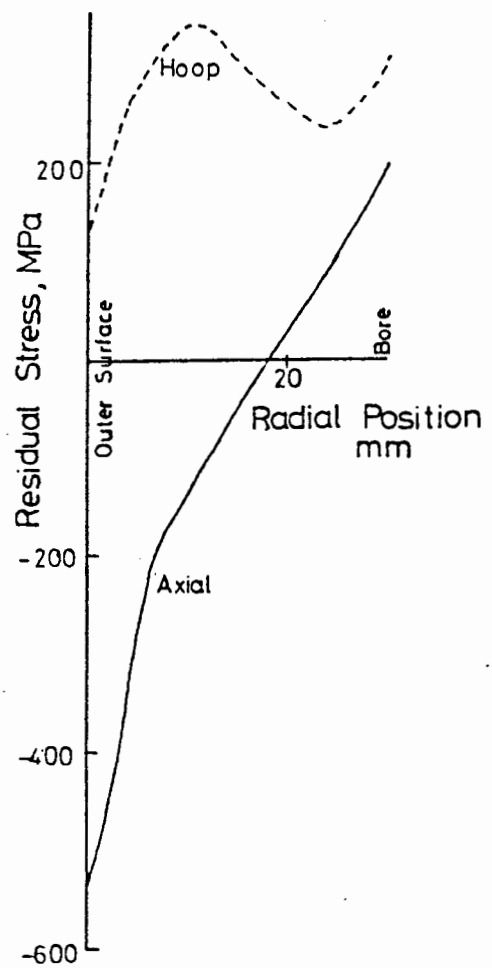

Fig 9.6 Residual Stress Distribution through the Pipe Wall

Fig 9.7 shows the calculated stress distribution along the outer surface for the second case, which also shows some residual stress experimental measurements.

9.1.5 DISCUSSION

The agreement between the analytical results and the finite element results for temperature distribution is good, considering the differences between the two approaches and the multitude of approximations used. Also, in the finite element calculation, the thermal properties varied as a function of temperature and the heat source was of a finite width. None of these factors were taken account of in the analytical solution.

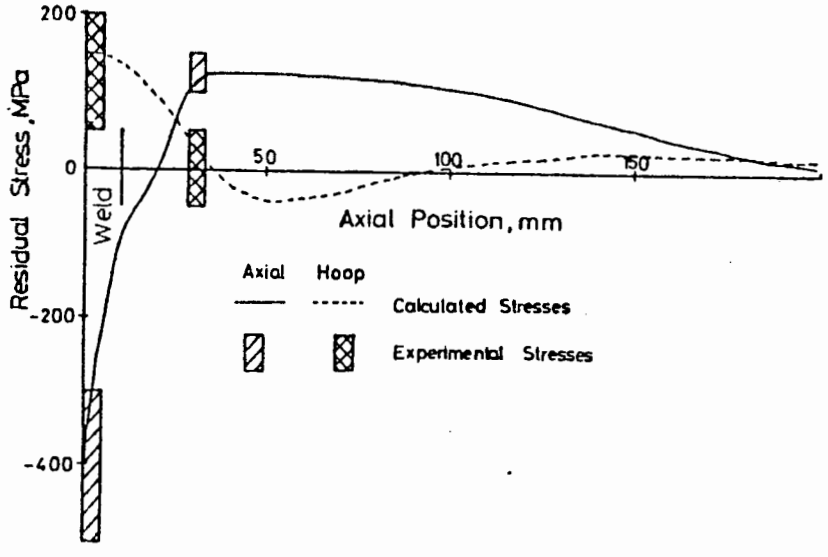

Fig 9.7 Residual Stress Distribution along the Outer Surface of the Pipe for a High Heat Input Weld

In Fig 9.7, computed results are compared with experimental measurements made under comparable conditions on a submerged arc weld. Experimental results are shown as areas enclosing a number of measured values due to the variability of the residual stress data. The agreement is reasonable, as the general magnitude and trend is

similar. Variations found in the experimental data in the weld metal are much larger than can be accounted for by measurement errors. These variations arise due to the rapid variation of residual stresses in ferritic weld metals and computation cannot simulate this, as the factors causing it have not been modelled.
Examining the axial stress distribution across the wall in Fig. 9.6, this shows that the analysis is not exact, as equilibrium requirements that no net axial force should exist across the section, are not satisfied completely. Comparison of the stresses for the two temperature distributions in Fig 9.4 and 9.7 shows that the stresses in the weld metal are roughly similar.

9.1.7 CONCLUSIONS

A fairly straight forward finite-element program can model the thermo-mechanical history of a simple weld bead. The residual stress distribution results agree with those obtained experimentally on similar welds. This kind of approach can be extended to more complex welds and to study the effect of input parameter variation more fully.

9.2 ANALYSIS OF THERMAL STRESSES AND METAL MOVEMENT BY COMPUTOR METHODS DURING WELDING

This research, termed the "Battelle program", was done in a study for the G.C. Marshall Space Flight Centre, NASA by Masubuchi and entailed the development of computer programs for the calculation of thermal stress in bead-on-plate welding. This work is described in "Analysis of Welded Structures" by Masubuchi [3] .

9.2.1 SUMMARY OF THEORY

Fig 9.8 shows a schematic representation of temperature and stress changes during the process of welding.
In Fig 9.8a, a bead-on-plate weld is being made along x-axis. The arc, presently located at the origin o, is moving at a speed v.

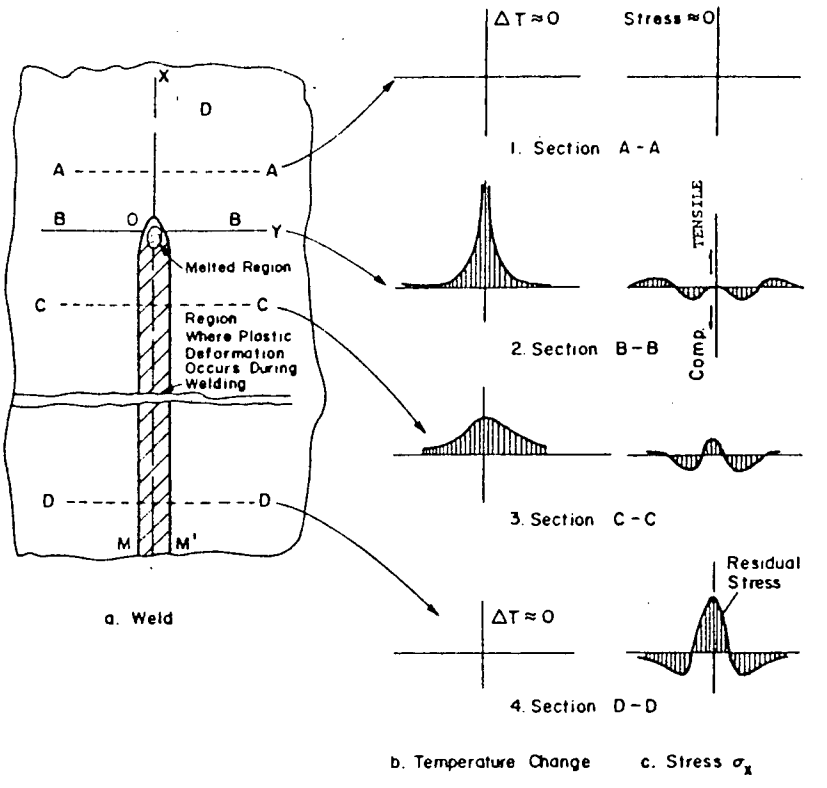

Fig 9.8 Temperature and Stress Change during Welding

In Fig 9.8b, the temperature distribution is shown at several cross-sections. At section A-A, which is ahead of the weld, the temperature change is almost zero. At section B-B, which crosses the weld arc, the temperature change is very rapid. At section C-C, some distance behind the arc, the distribution of temperature change is less that at C-C. At section D-D, far from the arc, the temperature change is again almost zero.

In Fig 9.8c, the thermal stresses due to welding are shown at the cross-sections. At section A-A, the stresses are almost zero. At section B-B, compression and tension occur due to the expansion of areas restrained by the surrounding metal where the temperatures are lower. The stress under the arc is close to zero as molten metal will not support a load. At section C-C, since the weld metal and base metal near the weld have cooled, they contract and cause tensile stresses. Further from the weld, they change to compressive stresses. At section D-D, high residual tensile stresses remain near the weld whereas

compressive stresses remain in region far from the weld.
The shaded area in Fig 9.8a shows where plastic deformation occurs during the weld thermal cycle. The egg-shaped region near the origin o indicates where the metal is molten. Outside the shaded region, the remaining area remains elastic during the weld thermal cycle.

9.2.2 THE BATTELLE PROGRAM

In the Battelle study, the temperature distribution around the moving arc was calculated using eg. (7.19). When the stresses were calculated, it was assumed that the changes in stress in the x-direction were much less than the changes in stress in the y-direction, from Fig. (9.8).
From the following equilibrium equations,

$$\frac{\partial \sigma_x}{\partial x} + \frac{\partial \tau_{xy}}{\partial y} = 0$$

$$\frac{\partial \tau_{xy}}{\partial x} + \frac{\partial \sigma_y}{\partial y} = 0$$

One could assume that the longitudinal stress σ_x, is a function of y only and also that σ_y and τ_{xy} are zero.

The field was divided into a series of transverse strips of width h_o as shown in Fig 9.9

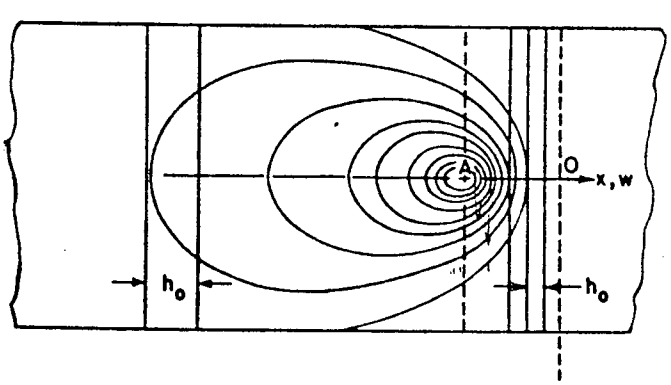

Fig 9.9 Stress Field divided into Transverse Stripes

The time intervals represented by the strip width were to be short so that the temperature and thermal stress for each increment could be treated as a constant.
Narrow strips were used in areas near the arc as this was where the greatest temperature changes would occur.

The calculation began on a strip a certain distance ahead of the welding arc where the temperature change was negligible and the stresses purely elastic. Time zero was fixed on the strip. Stresses in the strip crossing the origin o, were calculated based on elasticity theory. Stresses in the second strip were calculated by adding stresses caused by the increment in temperature. Analysis was made whether or not plastic deformation had taken place. It was also assumed that the stresses at a given point did not exceed the yield stress of the material at the temperature of that point. Similar analyses were calculated step-by-step in the following strips.
In this way, the stress distribution of the entire field was determined.

9.2.3 RESULTS OF THE BATTELLE PROBLEM

The results of an example are shown in Figures (9.10) through (9.13). In this example, the following conditions prevailed:

1. Material - aluminium alloy
2. Thickness - 1/4 inch (6.4 mm)
3. Plate width - 8 inches (200 mm)
4. Welding current - 254 ampere
5. Arc voltage - 10 volts
6. Arc travel speed - 14 inches per minute
7. Arc efficiency - 80%

Fig 9.10 shows the change in temperature along the weld centre-line (y=0), y = 1 inch (25 mm), and y = 4 inches (100 mm).
Time is represented along the horizontal axis and temperature along the vertical axis. The arc is located at t = 9 seconds. Each of the curves shows the thermal cycle at a point some distance from the weld.

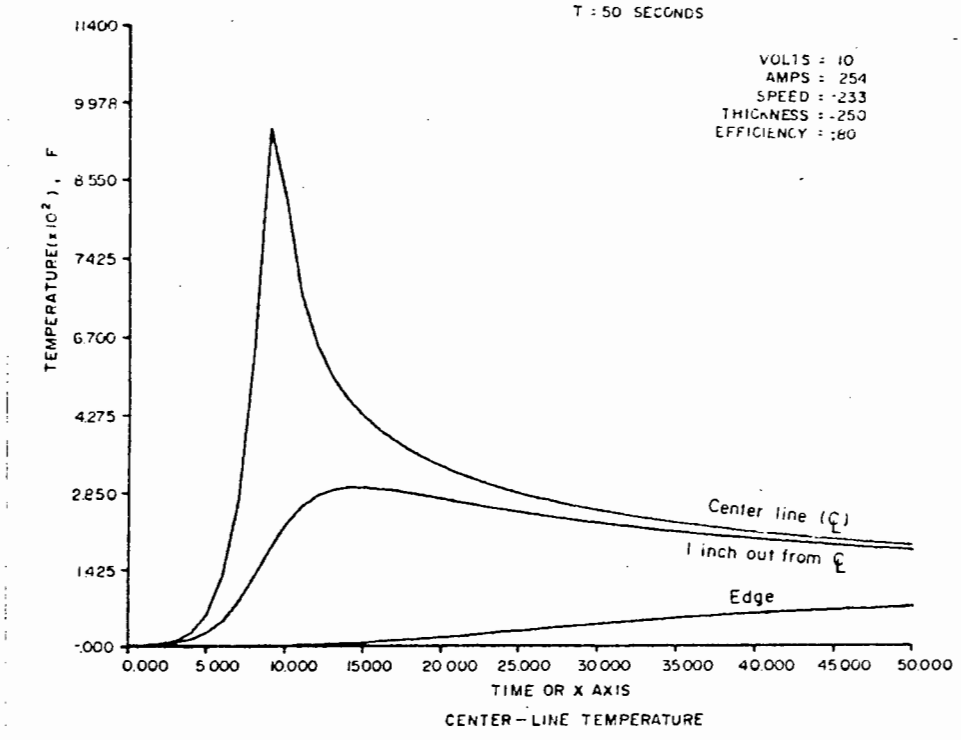

Fig 9.10 Temperature Change along 3 Longitudinal Lines

Fig 9.11 shows the isotherm pattern around the arc.
The longitudinal x-coordinate is again the time scale.

Figure 9.12 shows the changes in stress along y = 0,1 and 4 inches (0,25 and 100 mm). On the centreline, the stresses are in compression areas ahead of the arc. As the arc approaches the point, the absolute value of the compressive stress increases first and then decreases. At the point directly under the arc, we have zero stress. When the areas behind the arc cool, the stresses become tensile

Figure 9.13 shows the isostress pattern around the arc. Of interest is the horse-shoe shaped region formed by the compressive stresses extending ahead of the arc and continuing along both sides.

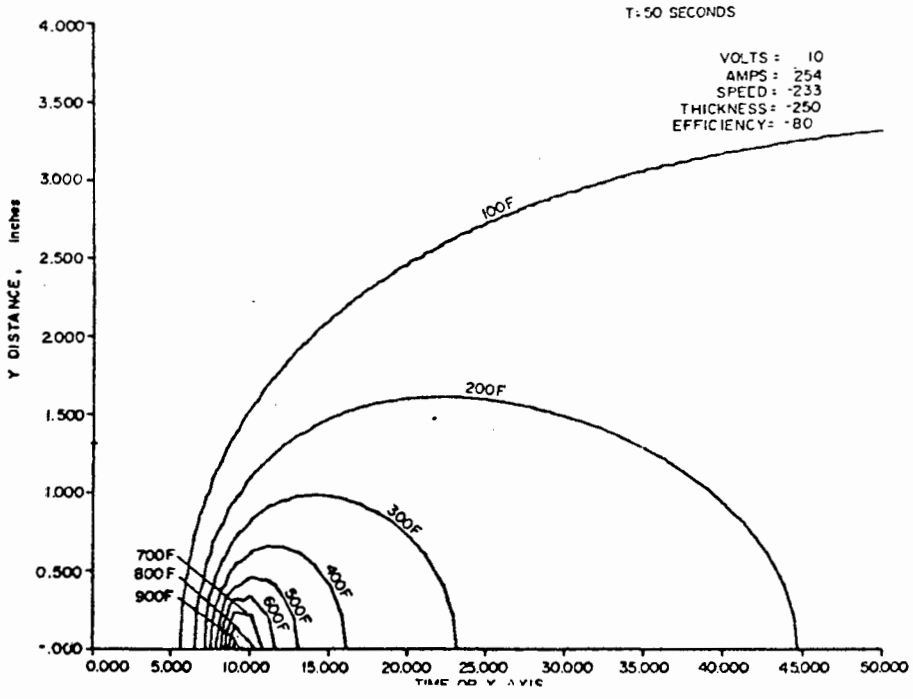

Fig 9.11 Isotherm Pattern around the Moving Arc

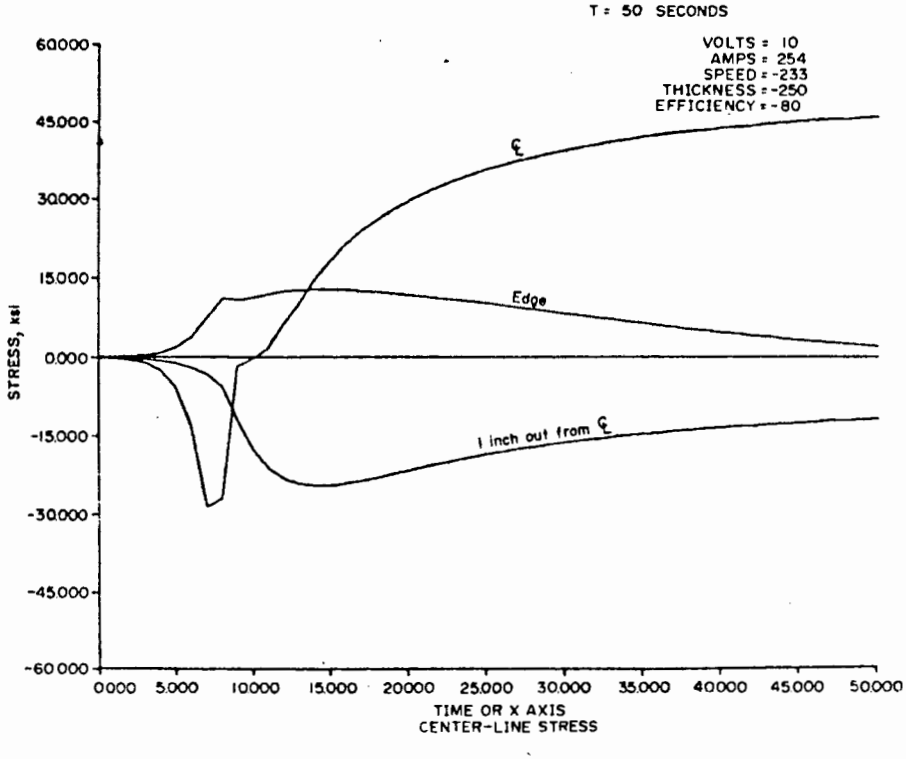

Fig 9.12 Stress Changes along 3 Longitudinal Lines

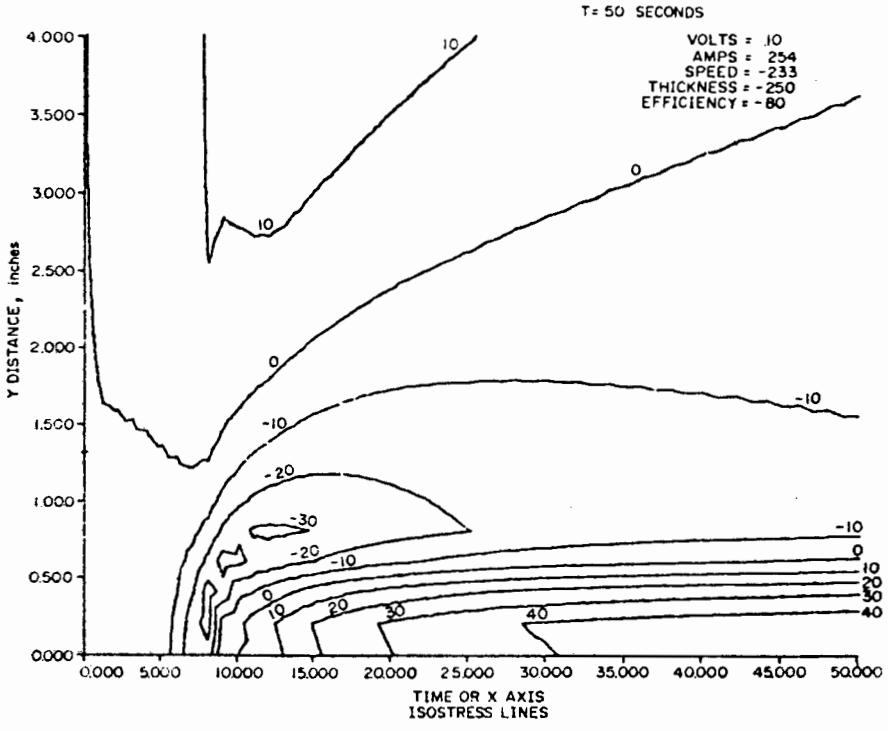

Fig 9.13 Isostress Pattern around the Moving Arc

CHAPTER TEN

MULTI-DIMENSIONAL COARSE WELD SIMULATION WITH HEAT AND STRESS ANALYSIS

10.1 INTRODUCTION

The aim of this chapter was to introduce for the first time the effect of a weld on a structure. A coarse mesh was used in this preliminary investigation. The idea was simply to apply an instantaneous heat load of 1000°C, representing the weld, along a predecided boundary, leaving remaining areas at room temperature, 20°C. The properties of the weld area were assumed to be identical to those of the rest of the structure. The word "coarse" was used as the heat load showed no characteristics of an actual weld except for the high temperature. In addition, the thermo-elastic material model from ADINAT was used, which takes no effects of plasticity into account.

The problems considered were the following:

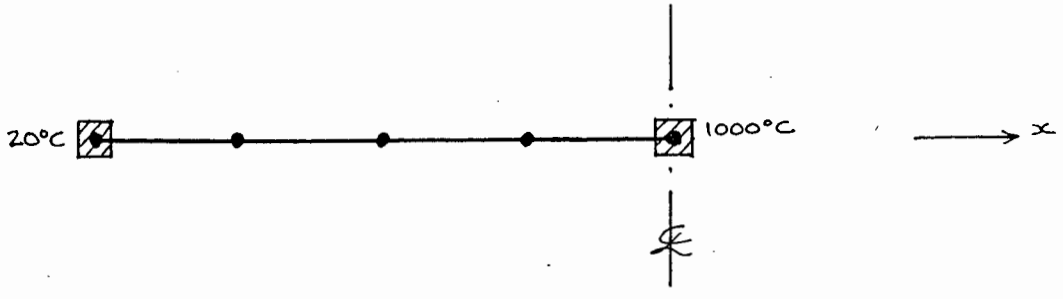

Fig 10.1 1-Dimensional Rod

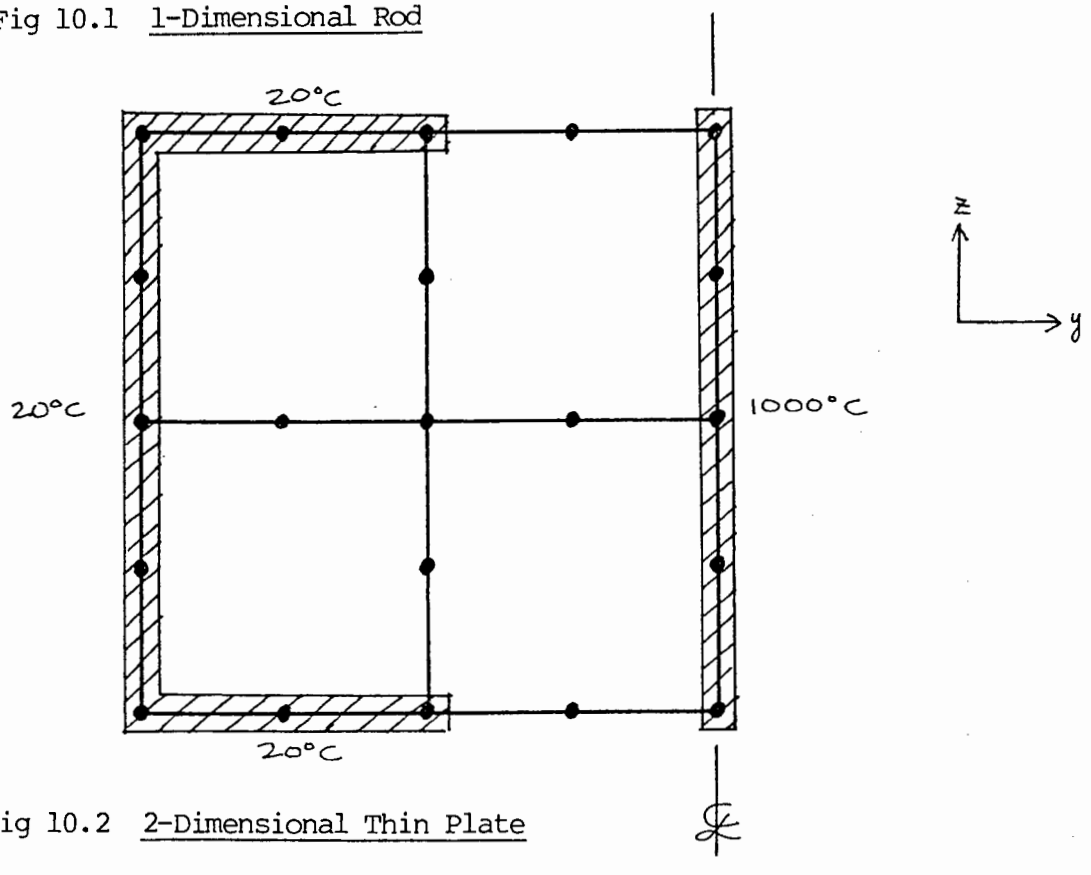

Fig 10.2 2-Dimensional Thin Plate

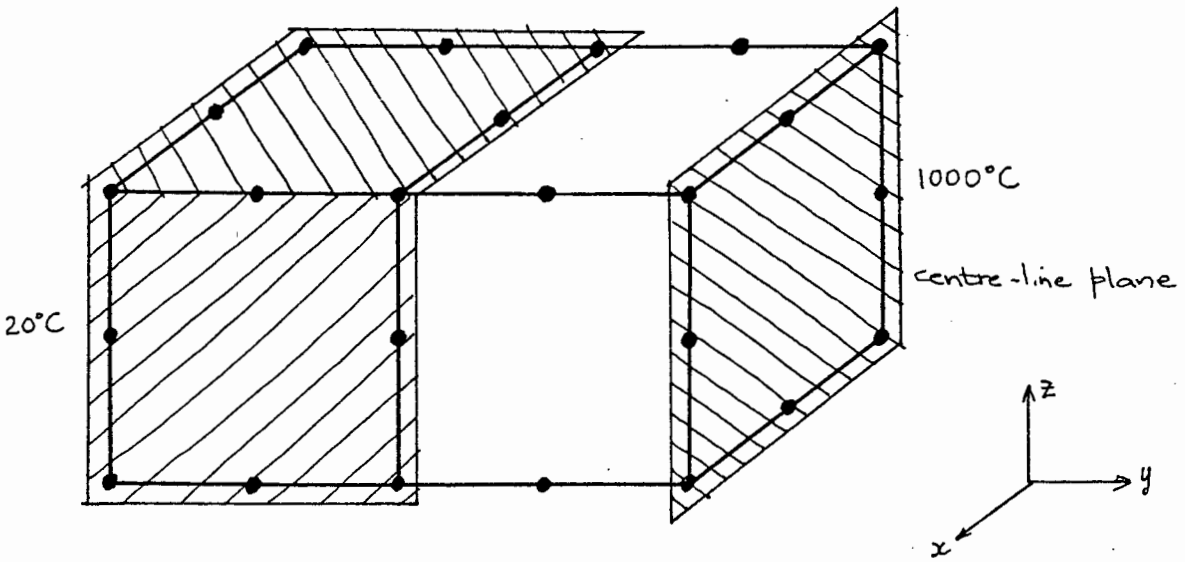

Fig 10.3 3-Dimensional Thick Plate

Initially, the ADINAT program was run to generate the temperature distribution throughout the mesh due to the instantaneous heat load. These results were input to ADINA which calculated the stresses due to the calculated temperature distribution. This was done for the steady-state.

The problems are symmetrical, the centre-lines being shown in Fig (10.1), (10.2) and (10.3) hence only half of the mesh was analyzed.

10.2 STEADY-STATE ANALYSIS

10.2.1 1-Dimensional Rod

The finite-element mesh is shown in Fig 10.4

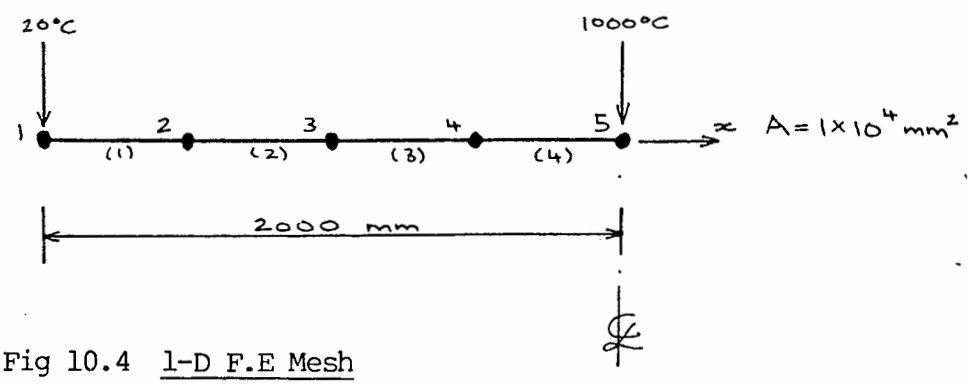

Fig 10.4 1-D F.E Mesh

The heat load was applied at node 5, being the centre of the 4 000 mm long rod. This problem corresponds to welding two equidiameter rods together. The cross-sectional area of the rod was taken as 10 000 mm^2 as this corresponded to a plate being 1 000 mm in width and having a thickness of 10 mm (See 2-dimensional case).
This area also corresponds to a bar of radius approximately 55 mm. Linear one-dimension heat conduction elements were used with a realistic thermal conductivity for steel of 52 J/m.s.°C. The resulting temperature distribution at steady-state is shown in Table 10A

Node	Temp (°C)
1	20
2	265
3	510
4	755
5	1 000

TABLE 10A Temperature Distribution due to Weld "Heat Load"

This linear temperature distribution was input into ADINA. The following displacements and stresses were obtained:

Node	Displacement (mm)	Stress (MPa)
1	0	-1462
2	-3.04	-1462
3	-4.39	-1462
4	-3.49	-1462
5	0	

TABLE 10B Output of Adina

The stresses apply to elements 1, 2, 3 and 4.

As node 5 lay on the centre-line, an x-displacement was prevented. All the free nodes displaced an average of about 4 mm to the left,

away from the weld and because node 1 was fixed against displacement in the x-direction, the rod was put into compression by this movement. This compressive stress had a value of -1462 MPa throughout the rod, this value being the average of a higher and lower value at the Gauss points on each element. Note that these values are all at steady-state.

10.2.2 2-Dimensionsal Thin Plate

The finite-element mesh is shown in Fig 10.5

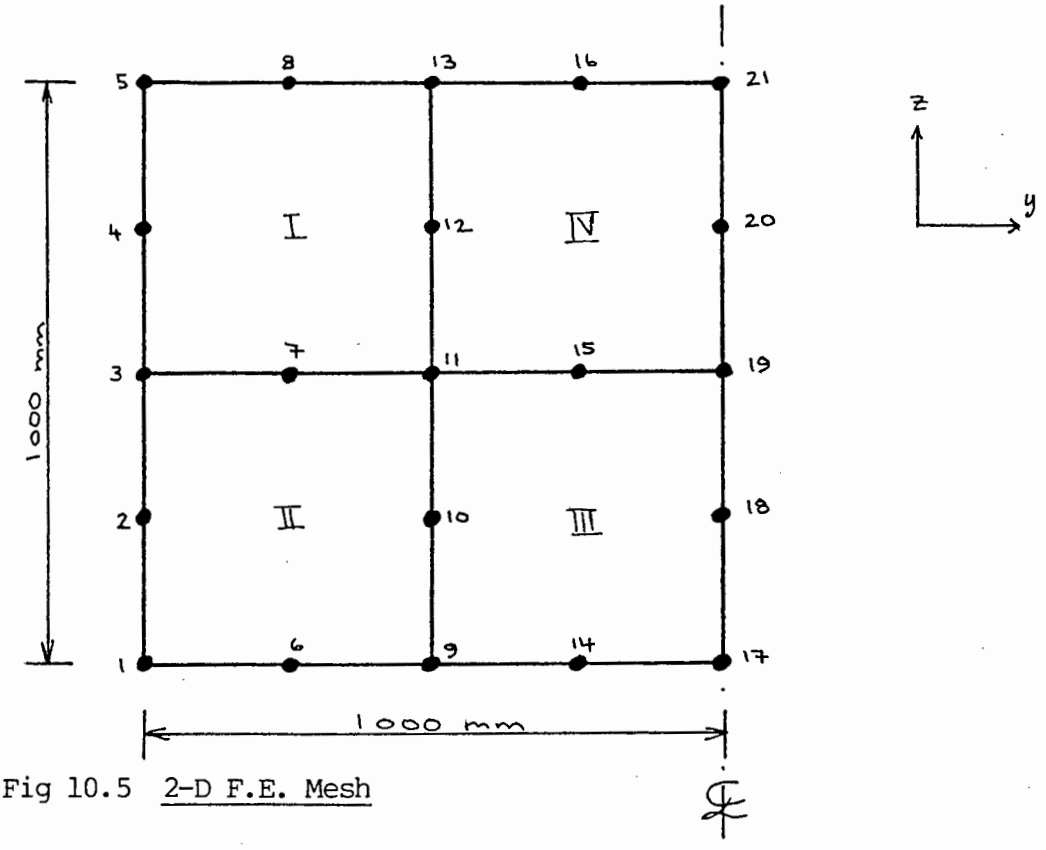

Fig 10.5 2-D F.E. Mesh

The heat load, representing a weld in a thin plate 2 000 mm long and 1 000 mm wide, being 10 mm thick, was applied to nodes 17, 18, 19, 20 and 21, the value of the temperature being 1 000°C. Boundary nodes 13, 8, 5, 4, 3, 2, 1, 6, 9 were fixed at room temperature, ie. 20°C. Internal nodes 7, 10, 11 and 12 were allowed to attain their own steady-state temperatures. The same applied to nodes 14, 15 and 16 alongside the weld. This was done in order to simulate a pseudo-heat-affected-zone.

Linear two-dimensional heat conduction elements were used in ADINAT with a realistic thermal conductivity of 52 J/m.s.°C. The resulting

steady-state temperature distribution is shown in Table 10C:

Node	Temp (°C)	Node	Temp (°C)
1	20	12	296.6
2	20	13	20
3	20	14	579.4
4	20	15	625.7
5	20	16	579.4
6	20	17	1000
7	149.6	18	1000
8	20	19	1000
9	20	20	1000
10	296.6	21	1000
11	390.3	-	-

TABLE 10C Temperature Distribution from ADINAT

The temperature distribution along the horizontal centre-line of the finite-element mesh is shown in Graph G5.
The temperature distribution from Table 10C was input into ADINA.
The following displacements and stresses were obtained:

Node	y-disp(mm)	z-disp(mm)	Node	y-disp(mm)	z-disp(mm)
1	0	0	12	-1.84	1.97
2	0	0	13	-3.61	3.25
3	0	0	14	-3.27	-6.61
4	0	0	15	-1.39	0
5	0	0	16	-3.27	6.61
6	-1.97	-1.28	17	0	-8.93
7	-0.92	0	18	0	-4.40
8	-1.97	1.28	19	0	0
9	-3.61	-3.25	20	0	4.40
10	-1.84	-1.97	21	0	8.93
11	-1.69	0			

TABLE 10D Displacements in 2-D plate from ADINA

Considering the y-displacements, we can see that they are all negative which implies a steady-state displacement to the left. Interior nodes 6, 8, 10, 11, 12 and 15 displace approximately 2 mm to the left whereas nodes on the boundary eg. nodes 9, 13, 14 and 16 displace approximately 3.5 mm to the left. Hence it appears that the centre portion of the plate lags the edges of the plate as it displaces leftwards. See Graph G6.

Considering the z-displacements, they are symmetrical about the line joining nodes 3 and 19. As we progress towards the weld, these displacements increase, especially along the plate edge. As nodes 1 to 5 are restrained from z-displacement and the fact that nodes 17 to 21 are not, the displacement is pronounced along the line of nodes 17 to 21. See Graph G6.

Considering the stresses involves the evaluation thereof at the positions called the "Gauss Points". As we used 3 x 3 integration in our 2-dimensional solid plane-stress element in conjunction with the thermo-elastic material model in ADINA, we will have as output, stresses evaluated at 9 "Gauss Points" in each element. The Gauss points are shown in Fig 10.6

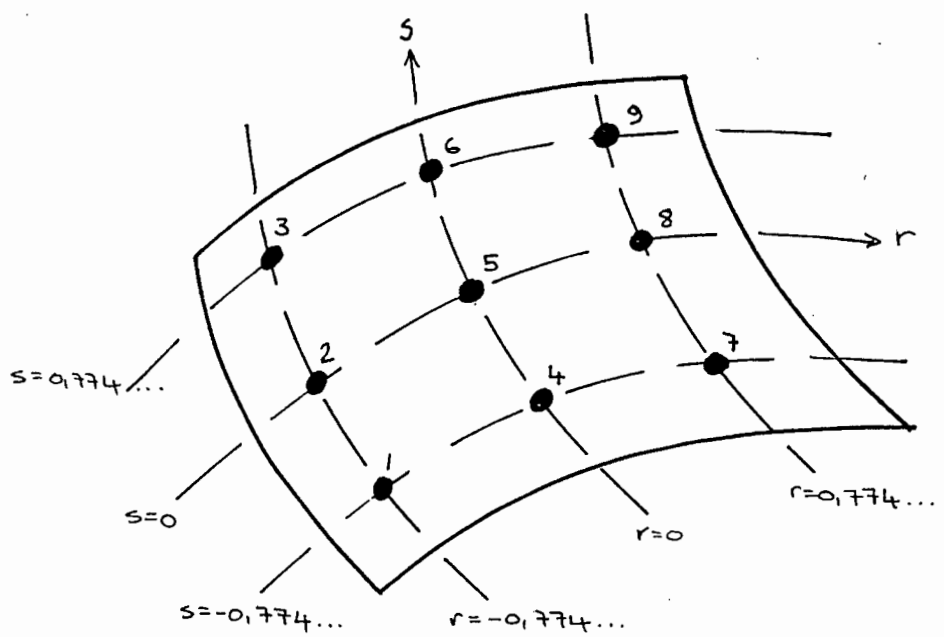

Fig 10.6 Position of 3 x 3 Gauss Points [28]

From ADINA, we are interested in the stresses σ_{yy} and σ_{zz}. Using the above, we can represent these stresses schematically as in Fig 10.7 and Fig 10.8

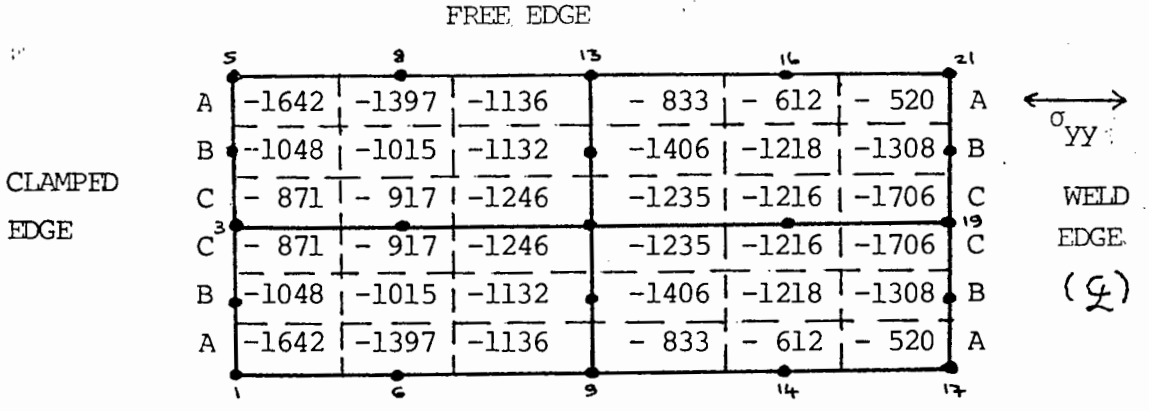

Fig 10.7 Schematic representation of σ_{yy} (MPa) at Gauss Points

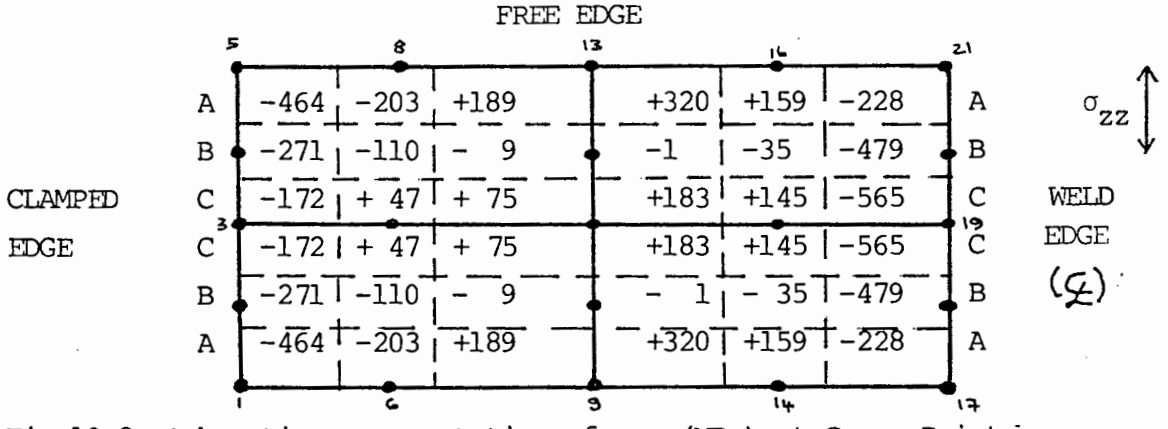

Fig 10.8 Schematic representation of σ_{zz} (MPa) at Gauss Points

10.2.2.1 σ_{yy} distribution in longitudinal plate direction

On analyzing σ_{yy} in Fig 10.7 we see that the stresses are all compressive and are symmetrical about the longitudinal centre-line of the plate ie. the line joining nodes 3 and 19. Due to symmetry, we will only discuss the stresses above the longitudinal centre line, in which 3 distinct areas are defined:

1. Area C-C, being the Gauss point adjacent to the longitudinal centre-line (Gauss point 1,4 and 7 for elements I and IV).

2. Area A-A, being the Gauss points adjacent to the free edge (Gauss points 3, 6 and 9 for elements I and IV).

3. Area B-B, being the Gauss points in the area between the abovementioned two areas (Gauss points 2, 5 and 8 for elements I and IV).

In area C-C, we see that the stresses decrease from right to left whereas in area A-A the stresses decrease from left to right. The stresses in area B-B are variable, having a minimum value at the centre of each element. These stresses are shown in Graph G7. It is thus evident that the centre area of the plate has the highest stress state at the weld, whereas the free edge areas have their highest state of stress at the clamped edge.

10.2.2.2 σ_{yy} distribution in transverse plate direction

In this direction, the stress distribution varies from concave-up at the side with the clamped edge to concave-down at the edge of the weld. This distribution is shown in Graph G8 for 3 lines, being

1. Clamped edge
2. Welded edge
3. Midway between these two

10.2.2.3 σ_{zz} distribution in longitudinal direction

On analyzing σ_{zz} in Fig 10.8 we see that the stresses are compressive and tensile. These values of stress are very much lower than those for σ_{yy}, and are also symmetrical about the longitudinal centre-line of the plate. The 3 areas defined in section 10.2.2.1 are used again. In all 3 areas, we have compressive stresses at the weld and the clamped edge. These stresses are shown in Graph G9.

10.2.2.4 σ_{zz} distribution in transverse direction

From Fig 10.8, the stress distribution is similar in shape to the σ_{yy} transverse distribution being concave-up at the side with the clamped edge to concave-down at the edge with the weld. Even the stresses in area B-B are similar in shape to those in area B-B for σ_{yy}. In fact, Graphs 8 and 10 agree very well, except for scale factor where the σ_{yy} distribution has a greater spread than the σ_{zz} distribution.

10.2.2.5 Discussion

The fact that the changes in stress in the z-direction (σ_{zz}) is much less than the changes in stress in the y-direction (σ_{yy}), both longitudinally and transversely, ties up with the assumption made by Masubuchi [3] where in section 9.2.2 it is stated that changes in stress parallel to the weld were assumed much less than changes in stress perpendicular to the weld direction.

From Graph G7, as we move away from the longitudinal plate centre line transversally, the stresses at the side having the weld decrease whereas the stresses at the clamped edge increase.

From Graph G8, as we move away from the welded edge towards the clamped edge, longitudinally, the stresses on the longitudinal centre-line decrease whereas the stress along the free edge increases.

From Graph G9, the same happens as in Graph G7.

From Graph G10, as we move longitudinally away from the welded edge, the stresses decrease to a low point midway between the welded and clamped edges, but then increase again as we move towards the clamped edge.

10.2.3 3- Dimensional Thick Plate

Although this analysis was carried out in full, it was not included in this thesis due to the complexity of the output. Two three-dimensional 21-noded brick elements were used with 3 x 3 Gaussian Integration, ammounting to 27 Gauss-points per element, a total of 54 Gauss-points. Because of the excessive quantity of stress output (6 stresses per Gauss-point), trends could not easily be followed. As this experiment served only as an illustration it was neglected here.

10.3 THICK-TO-THIN ELEMENT CONNECTION

In all the previous analyses, the elements were all assumed to have constant thickness ie. constant cross-sectional area. This is not always the case.
As can be expected from a thermal and stress analysis, there are a great number of parameters that can be varied. In the ADINAT program, for example, we have the choice of nodal temperatures being prescribed of free to obtain their own temperature; we have the choice of one, two or three-dimensional conduction elements; we have the choice of a linear or a nonlinear analysis, steady-state or transient.
In the ADINA program we have the choice of fixing boundary conditions; we have a wide choice of element type; we have a choice of thirteen material models; we have a choice of a linear or nonlinear analysis. As we can vary any one of these choices independently, this can lead to a multitude of solutions to different problems. Also, all this freedom of choice can add to the confusion of selecting a certain problem and varying parameters in a logical fashion as to obtain progressive and realistic results of the solution.

The basic problem to be analysed in this section is the joining together of two elements, whether they are bars (1-dimension), plates (2-dimensions) or solid structures (3-dimensions). We are particularly interested in the thick-to thin bar stress analysis under steady-state or transient conditions. Initially this connection will be straight one, but can later be varied to accomodate a right-angle joint or even a hollow box structure.

10.3.1 Straight connection in 1-Dimension

10.3.1.1 Steady-state analysis

A steady-state analysis was performed first, the purpose of this being that it could be a guide to a later transient analysis, which would have to approach the steady-state solution as the time increased.

The problem considered here was the connection of two bars, one thick (A = 25 000 mm^2) and one thin (A = 5 000 mm^2). This is shown in Fig 10.9. The thick bar's area was reduced in steps of 5 000 mm^2 until the case of the uniform bar (both areas equal to 5 000 mm^2) was reached. This was done to show up any trends in the stresses or displacements.

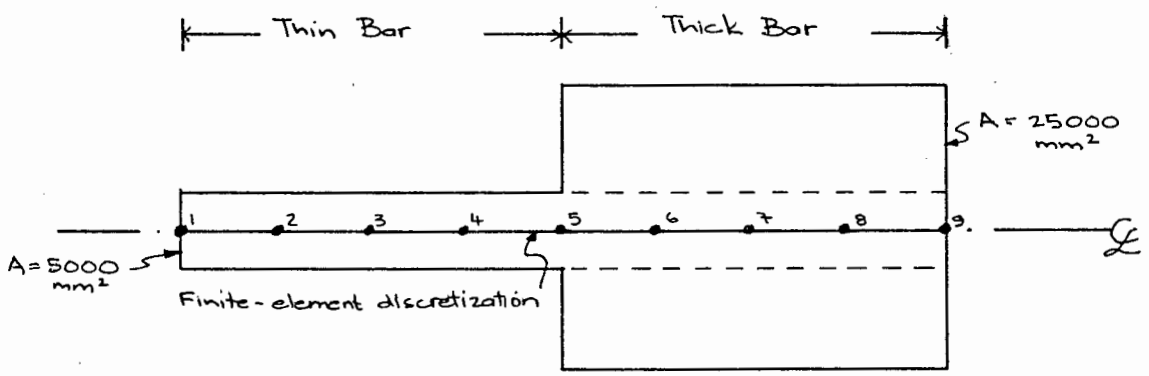

Fig 10.9 Illustration of Problem

1-Dimensional heat conduction linear elements were used in conjunction with the constant conductivity and constant specific heat material model ("Model 1") in the ADINAT case. The two boundary nodes were fixed at 20°C with the central node being fixed at 1 000°C, representing the weld. It was assumed that the weld metal and the parent bar metal have identical properties. The finite-element mesh took the form as shown in Fig 10.10:

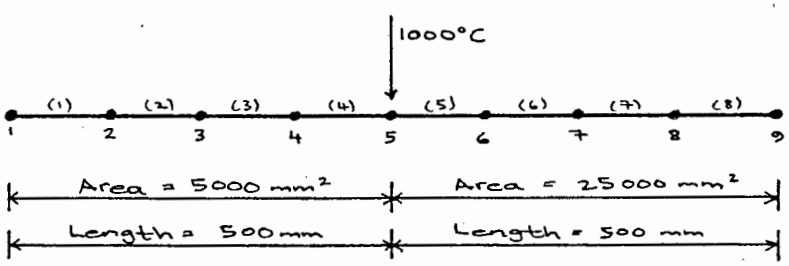

Fig 10.10 Mesh for the Thermal Analysis

The results of the ADINAT thermal analysis were, as shown in Table 10E

Node i	Temperature (°C)
1	20
2	265
3	510
4	755
5	1 000
6	755
7	510
8	265
9	20

TABLE 10E

These results were then input to ADINA, whose stress analysis mesh was identical to that of ADINAT and is shown in Fig 10.11. In the stress analysis, linear one-dimensional elements were used in conjunction with the non-linear isotropic thermo-elastic model ("Model"3). Nodes 1 and 9 were fixed against displacement with the rest of the nodes free to displace axially. Two point integration was used in the Gauss quadrature formulae, as two-noded elements were being used. The stress analysis mesh for ADINA is shown in Fig 10.11

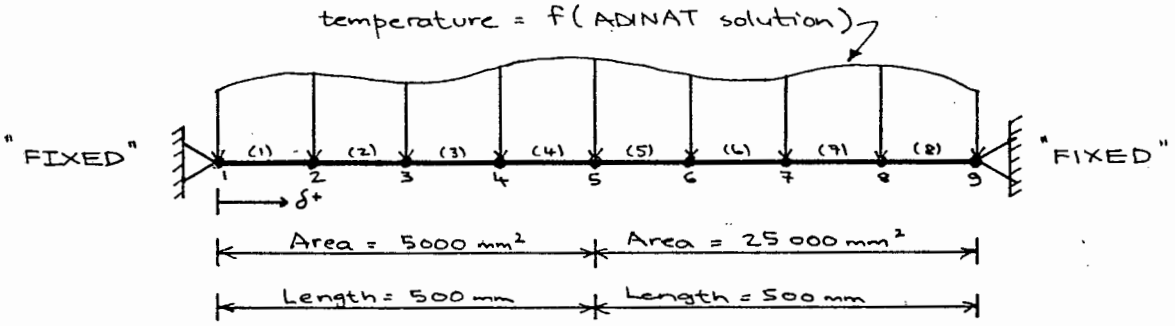

Fig 10.11 Mesh for the Stress Analysis

The displacement results for the problem is shown in Table 10F

Node i	Displacement
1	0
2	-1.42
3	-2.47
4	-3.00
5	-2.92
6	-1.25
7	-0.27
8	0.11
9	0

TABLE 10F

This shows that at the steady-state, the nodes 1 to 7 have all moved towards the left-hand side of the structure, whereas node 8 has moved fractionally to the right hand side, probably influenced by the fixity of adjacent node 9. The largest displacements occur on the side of the thinner bar near the centre. The corresponding displacements on the thicker bar are less than those of the thinner bar. This supports the theory that a thinner object will displace to a greater degree than a thicker object upon heating.

Upon examining the stresses, we find a difference between the stresses at the two "Gauss points" in each element. If these two stresses are averaged, we get a value of stress on the element. These stresses are shown in Table 10G

Element	Stress (MPa)
1	-2435
2	-2437
3	-2438
4	-2438
5	- 487
6	- 487
7	- 487
8	- 487

TABLE 10G

These results show that a much higher compressive stress exists in the thinner bar that that in the thicker one. This is expected due to the large area difference. The stress values also appear roughly constant in each bar. It must be remembered though that this condition will only arise after a long time has expired ie. at steady-state.

For the sake of completeness, this problem was run 5 times, varying the thickness of the right hand bar, the cross-sectional area varying from 5 000 mm^2 to 25 000 mm^2 in steps of 5 000 mm^2. The result of the temperature analysis are shown in Table 10H and the results of the stress analysis shown in Table 10I. Note that the left-hand half of the structure remains throughout with an area of 5 000 mm^2.

Thick bar area	A=5 000mm^2	A=10 000	A=15 000	A=20 000	A=25 000
Node i	Displ δ (mm)	Displ δ (mm)	Displ δ (mm)	Displ δ (mm)	Displ δ (mm)
1	0	0	0	0	0
2	-0.76	-1.09	-1.25	-1.35	-1.42
3	-1.10	-1.78	-2.13	-2.33	-2.47
4	-0.87	-1.94	-2.47	-2.79	-3.00
5	0	-1.45	-2.19	-2.62	-2.92
6	0.87	-0.19	-0.72	-1.03	-1.25
7	1.10	0.41	0.07	-0.14	-0.27
8	0.76	0.43	0.27	0.18	0.11
9	0	0	0	0	0

TABLE 10H Displacements for different area cases

This procedure was repeated for the stresses and yielded table 10I (overleaf).

Examining the results presented in Table 10H, we can see that in terms of the thermal analysis, the displacements in the uniform bar case are perfectly symmetrical about the central node 5. (The uniform bar case where both bars have equal cross-sectional area = 5 000 mm^2). This was expected, though, as the temperature loading was symmetrical. Also, as the difference in the joint cross-sectional

area increases, the displacements increase. This occurs predominantly in the thin bar portion of the structure. However, in the thick bar section, the displacements decrease (see node 8) or change direction (nodes 6 and 7). From these displacements, it seems that in the steady-state, the structure has been pulled over slightly to the left. Thic can be attributed to the high compressive stresses in the thin bar, being 5 times larger than the compressive stresses in the thick bar.

Thick bar area	A=5000mm^2	A=10 000	A=15 000	A=20 000	A=25 000
Element	Stress(MPa)	Stress(MPa)	Stress(MPa)	Stress(MPa)	Stress(MPa)
1	-1463	-1950	-2194	-2340	-2435
2	-1462	-1949	-2193	-2330	-2437
3	-1462	-1950	-2194	-2340	-2438
4	-1462	-1950	-2194	-2340	-2438
5	-1462	- 975	- 731	- 585	- 487
6	-1462	- 975	- 731	- 585	- 487
7	-1462	- 975	- 731	- 585	- 487
8	-1462	- 975	- 731	- 585	- 487

TABLE 10I Stresses for different area cases

Examining the results presented in Table 10I, we can see that in terms of the stress analysis, the stresses are constant throughout the structure in the uniform bar case, as is to be expected. As the difference in cross-sectional area increases at the joint, the stresses in the thin bar increase almost two fold whereas the stresses in the thick bar decrease by a factor of 3.

It must be stated again that all these results will occur at the steady-state ie. after a long time and the weld has been allowed to cool. In our case, we are far more interested in what happens as soon as the weld is created and how the cooling induces the residual stresses. This can only be done using a transient analysis with a suitable time step, which was not attempted here, keeping the finite-element model the same. It must be remembered also that as a check, the transient analysis will tend to the steady-state analysis as time progresses.

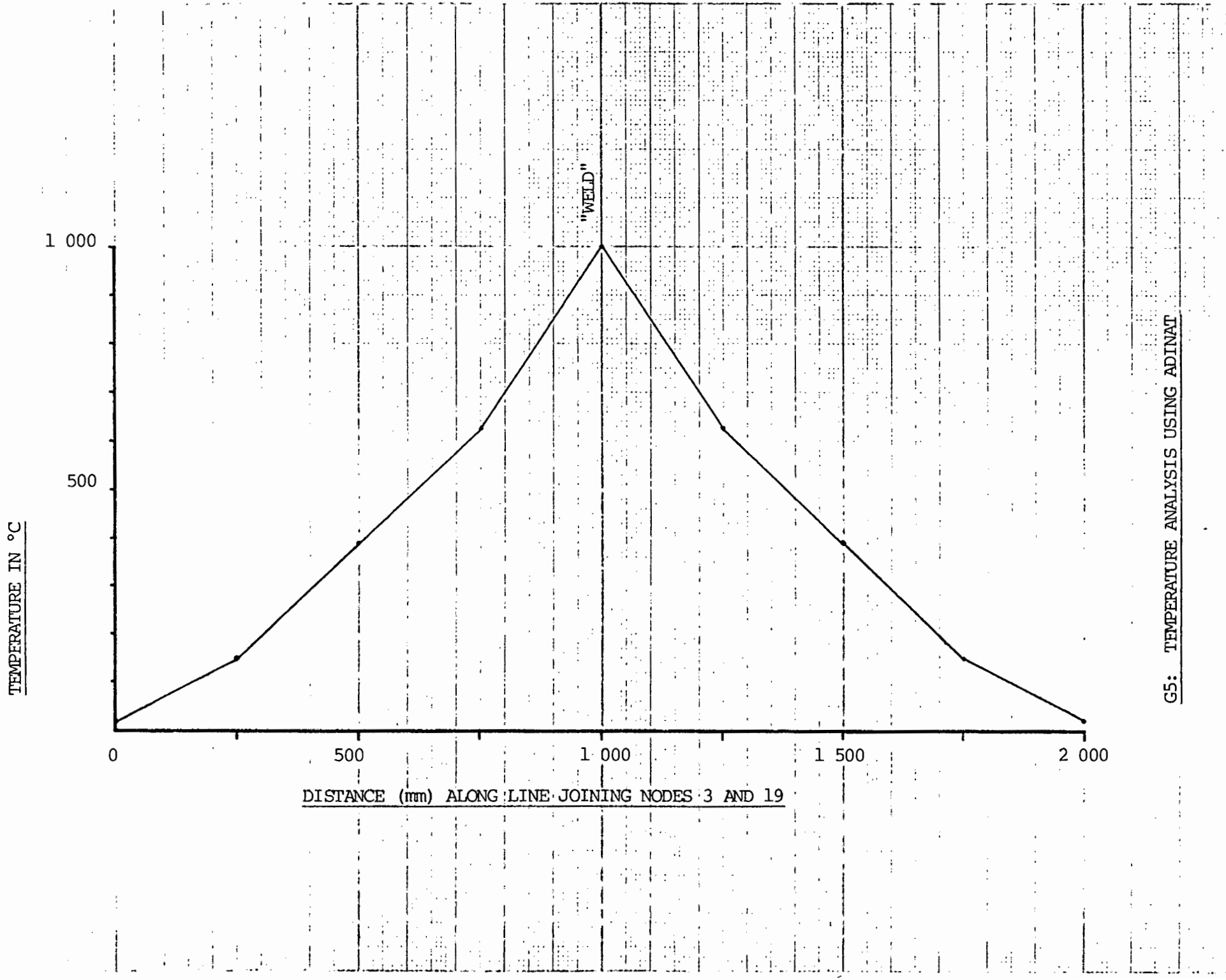

G5: TEMPERATURE ANALYSIS USING ADINAT

Scale for displacements

2 mm on graph

= 1 mm on plate

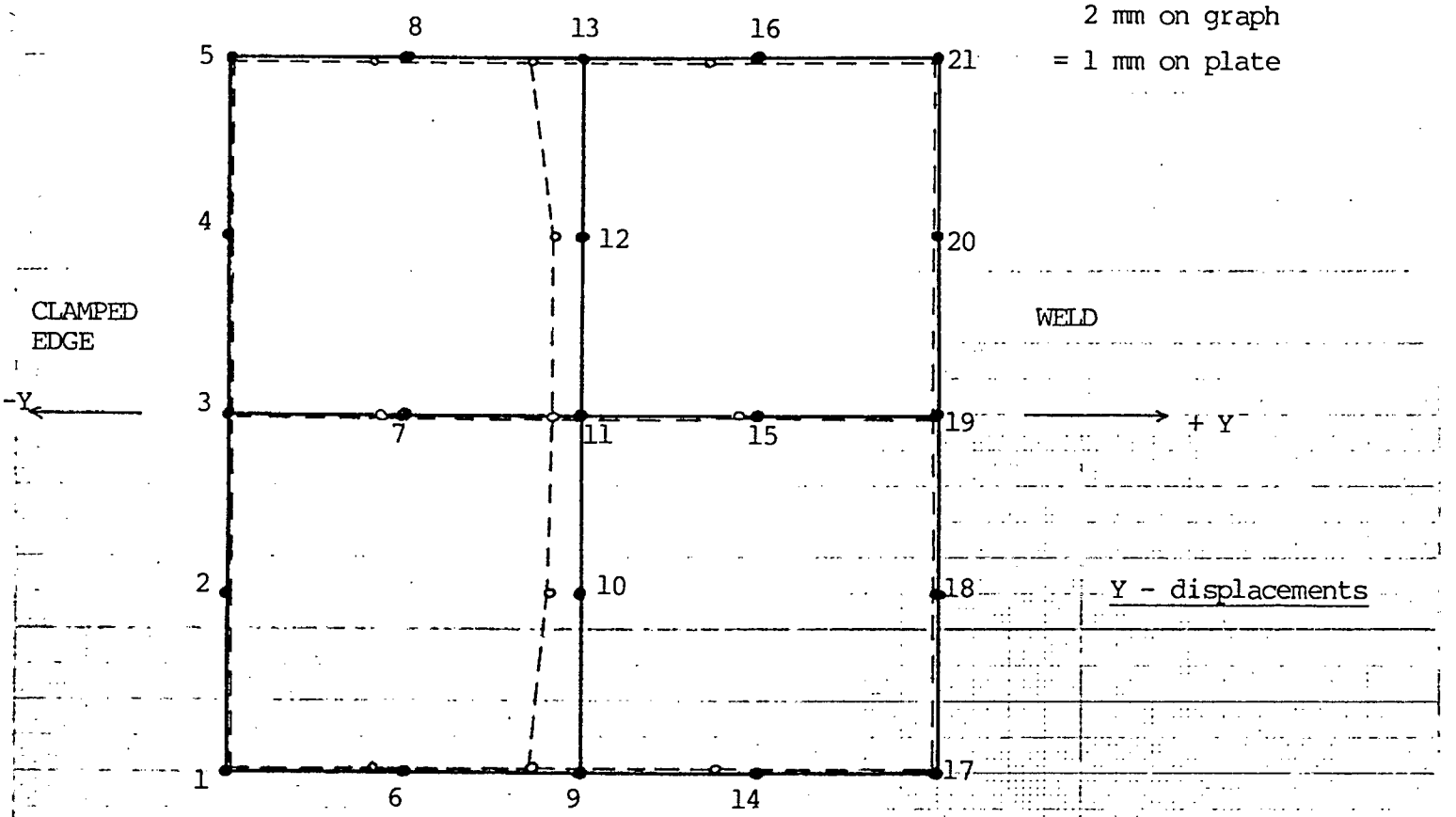

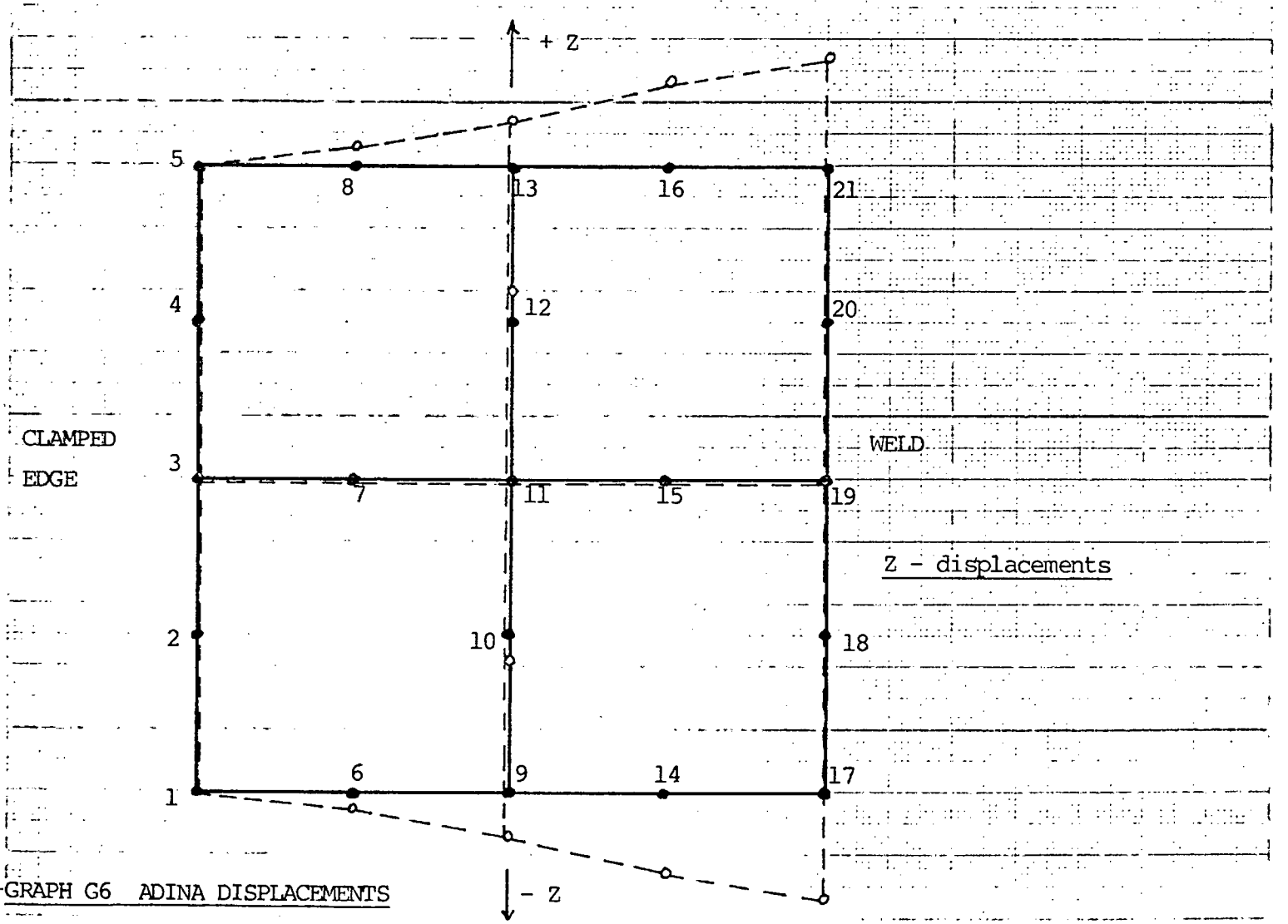

GRAPH G6 ADINA DISPLACEMENTS

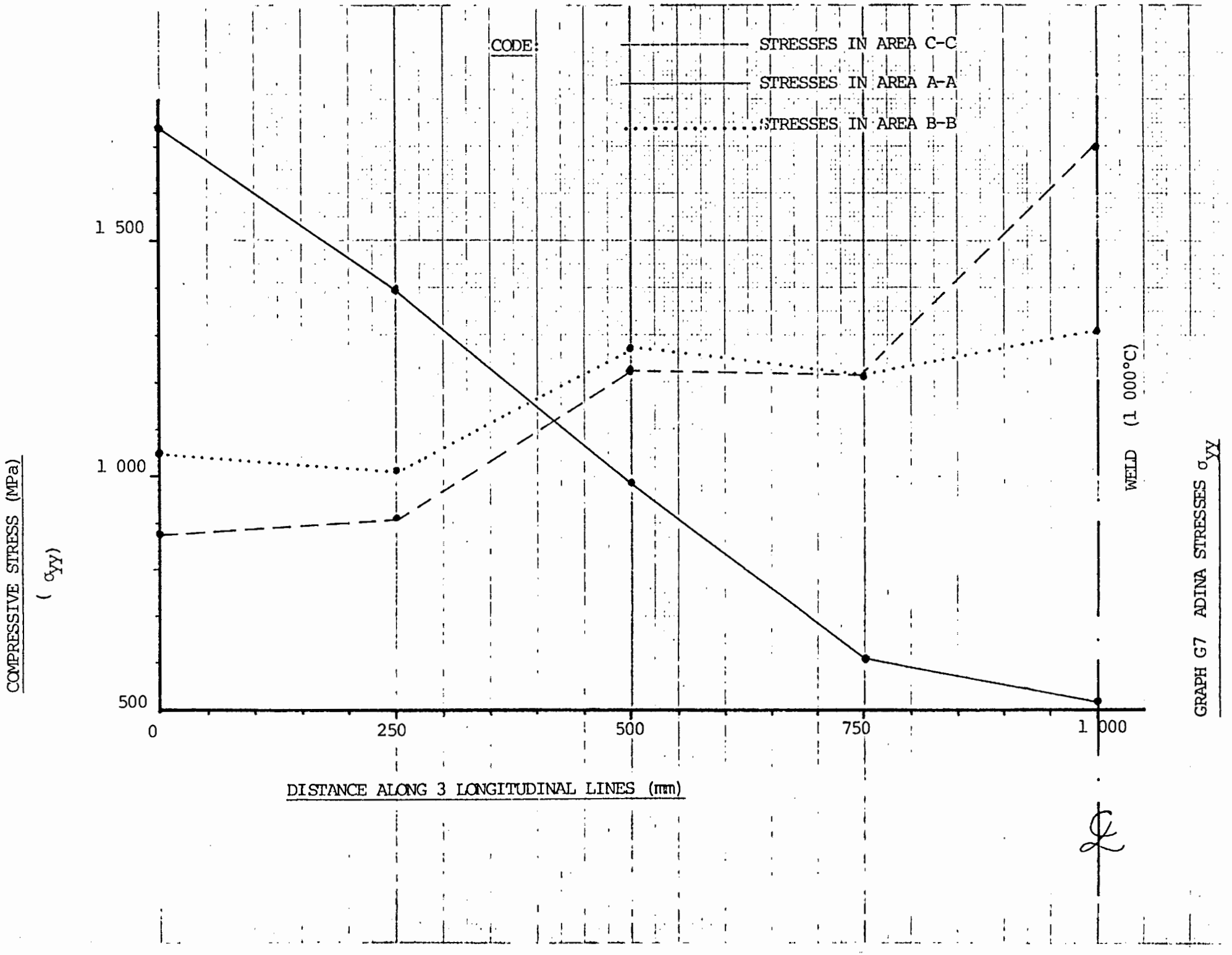
CODE:
STRESSES IN AREA C-C
STRESSES IN AREA A-A
STRESSES IN AREA B-B
1 500
1 000
500
0
250
500
750
1 000
WELD (1 000°C)
COMPRESSIVE STRESS (MPa)
(σyy)
DISTANCE ALONG 3 LONGITUDINAL LINES (mm)
GRAPH G7 ADINA STRESSES σyy

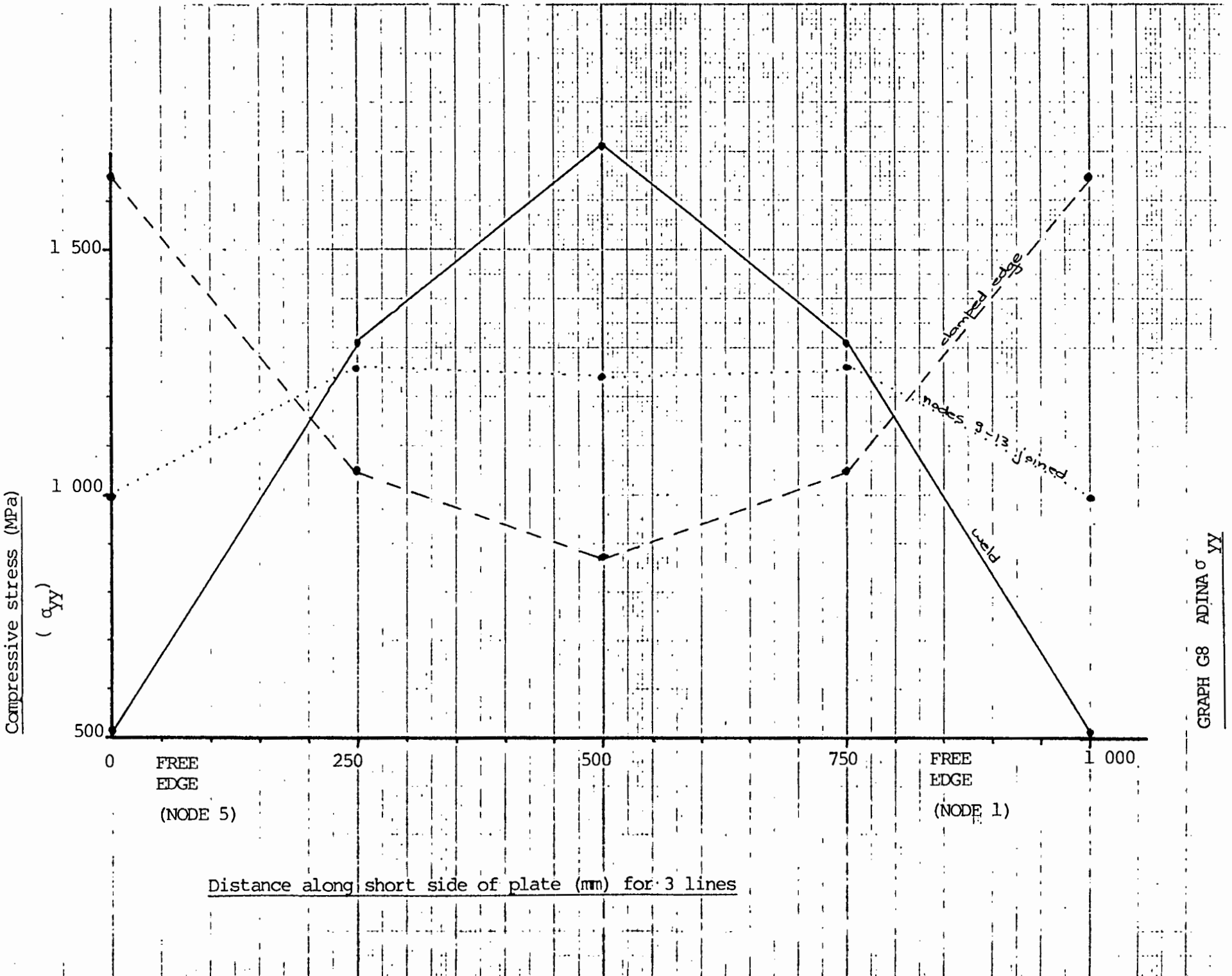
1 500
1 000
500
Compressive stress (MPa)
(σ_{yy})
0
FREE EDGE
(NODE 5)
250
500
750
FREE EDGE
(NODE 1)
1 000
Distance along short side of plate (mm) for 3 lines
clamped edge
nodes 9-13 joined
weld
GRAPH G8 ADINA σ_{yy}

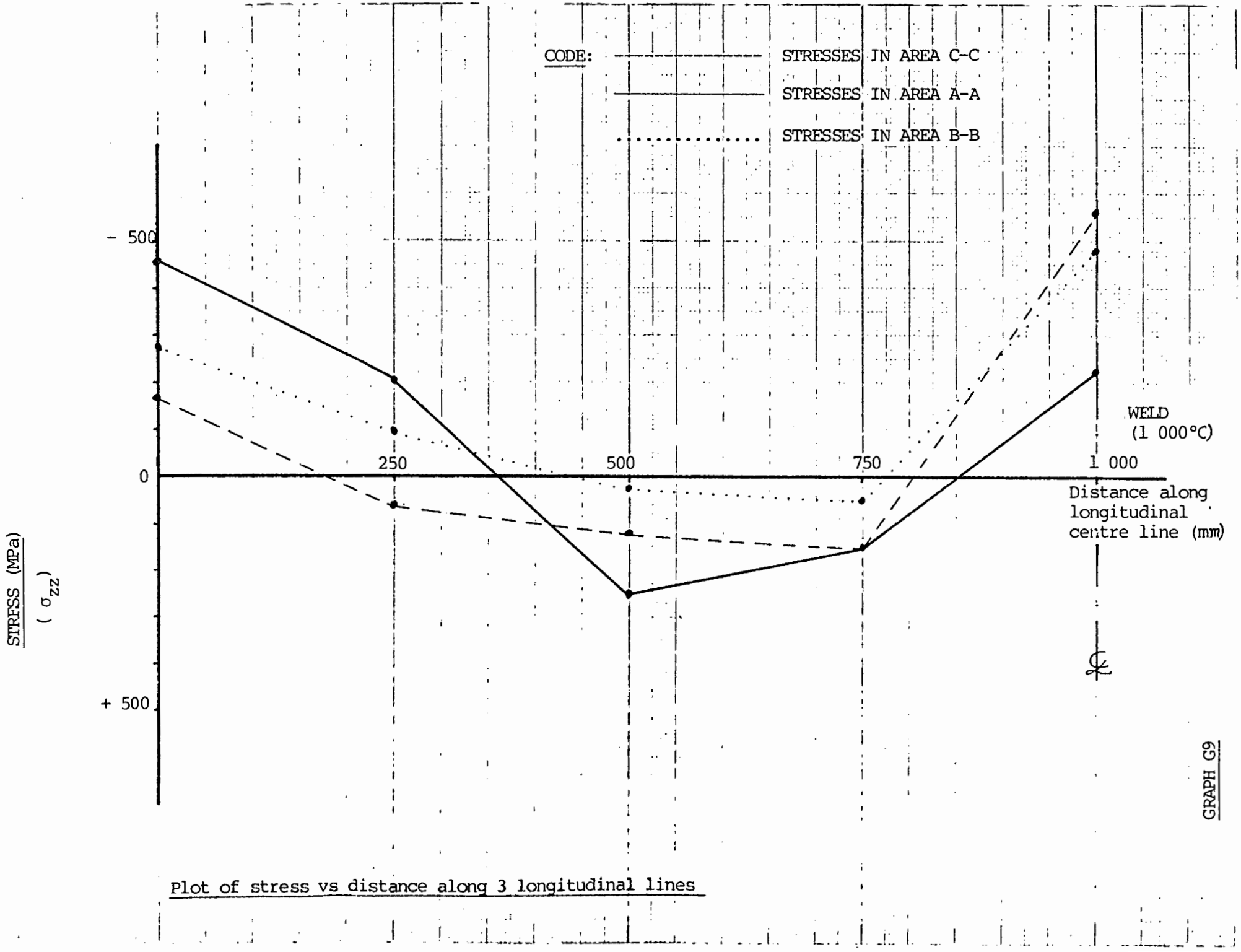

Plot of stress vs distance along 3 longitudinal lines

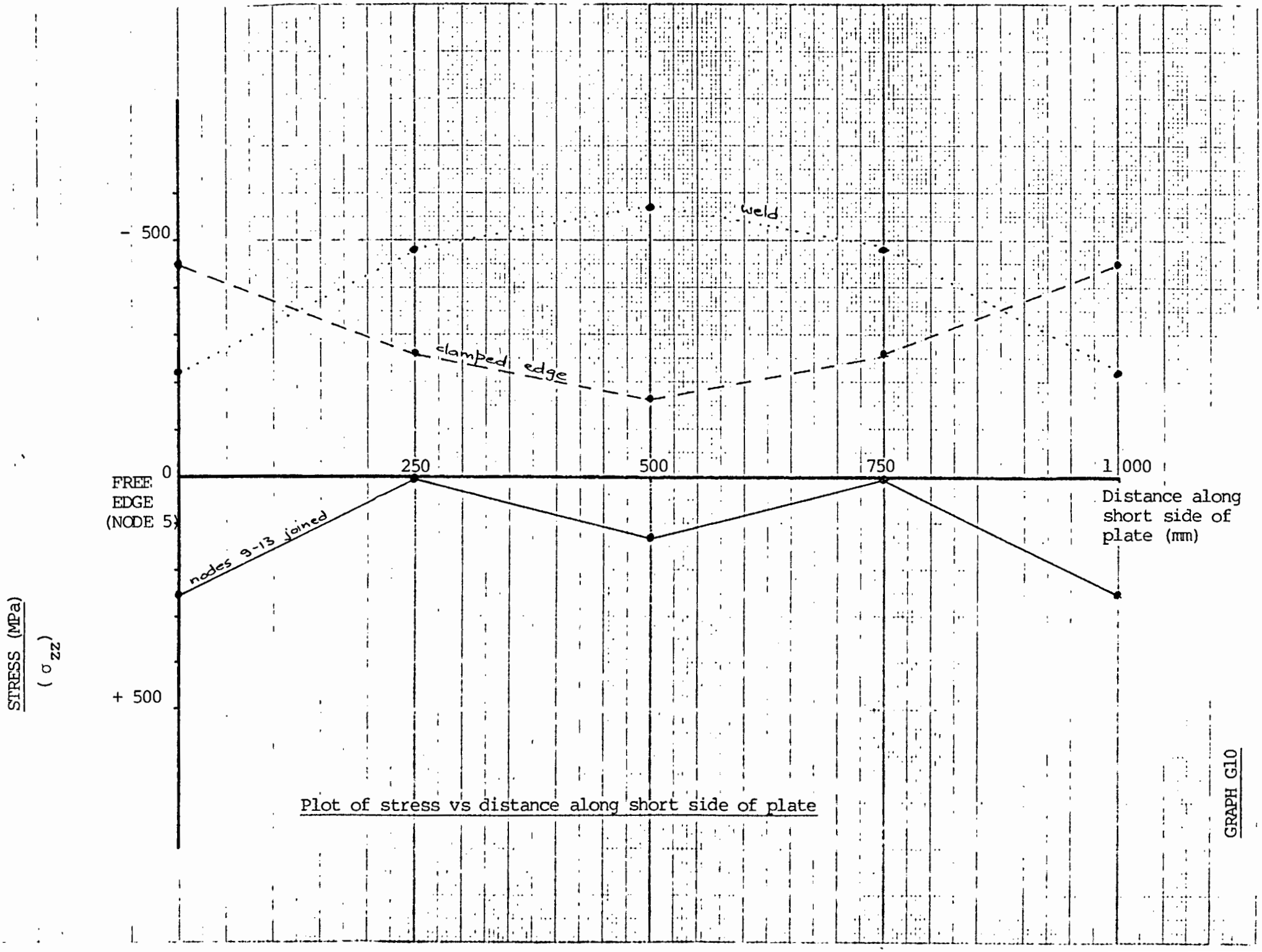

Plot of stress vs distance along short side of plate

GRAPH G10

CHAPTER ELEVEN

EXPERIMENTAL INVESTIGATION INTO THE TRANSIENT TEMPERATURE DISTRIBUTION IN THE PLATE

Apart from investigating the history and theory of welding, heat conduction and thermal stress and the verification of the analytical and finite-element compatibility, another major aim of this research was to try and predict the temperature and stress distribution set up over a certain time period during the process of welding, given a minimum amount of temperature information about the weld. This temperature information would ideally be a typical heating-cooling curve that would describe the thermal behavior of any point in the weld area.

This logical prediction process will be described in the following three chapters and is set out as shown below:

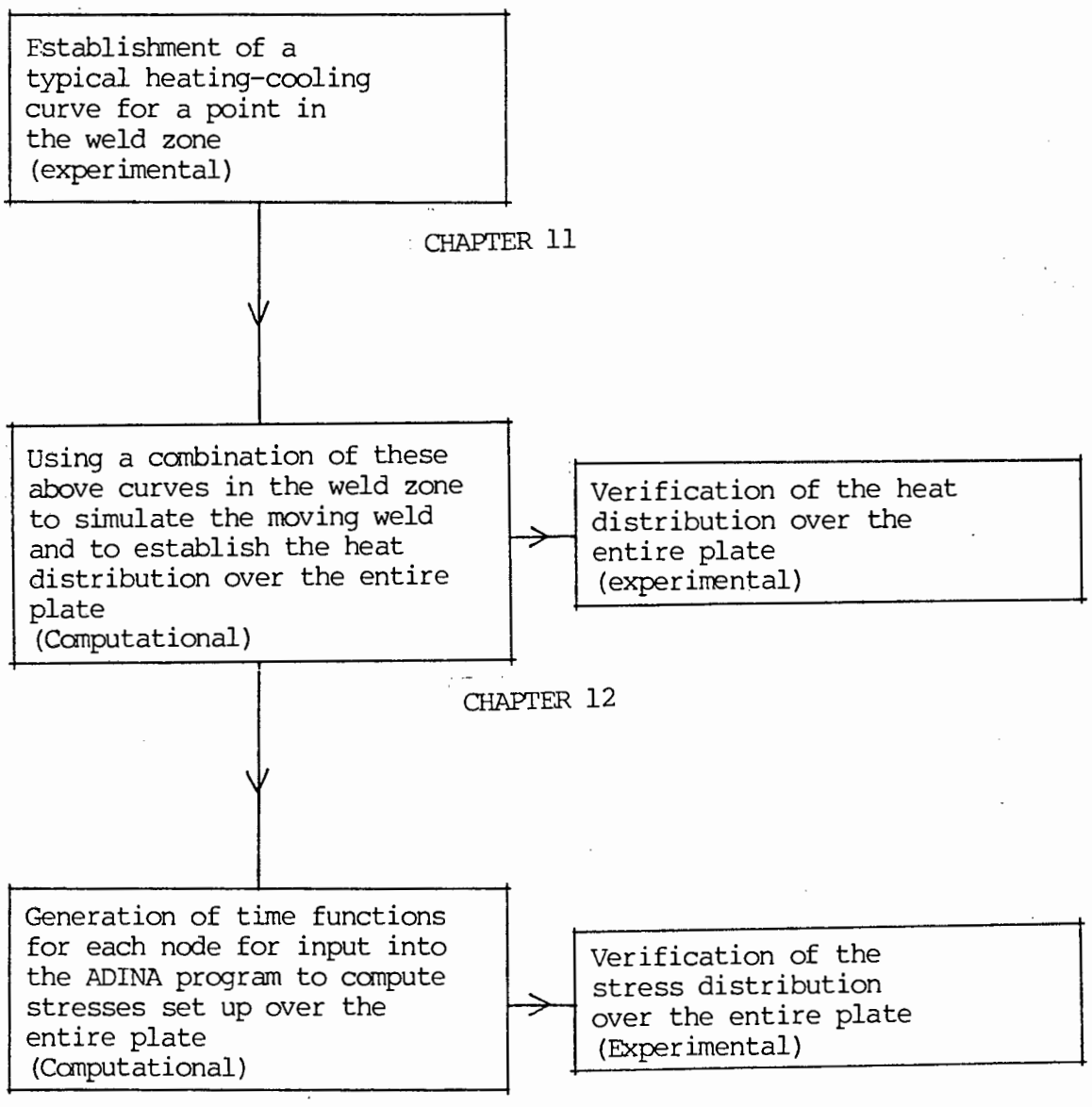

11.1 TEMPERATURE MEASUREMENT

The invention of the thermometer is credited to Galileo in the year 1592. [17] This consisted of a long thin glass tube suspended in an alcohol-filled open container. Heating and cooling caused the liquid to move up and down the tube. This thermometer was a poor indicator as barometric pressure affected the level of liquid in the tube, which also had no scale.

In the early 1700's Gabriel Fahrenheit produced accurate mercury thermometers. His fixed low point on the thermometer was obtained when measuring a mixture of ice water and salt and he called this point "zero degrees". The high point was the temperature of human blood and this was labelled "96" degrees.

Around 1742, Anders Celsius proposed that the high and low points be fixed as the boiling point of water and the melting point of ice, respectively. Zero was chosen as the boiling point and 100 degrees as the melting point. Later, these end points were reversed. In 1948 this scale was officially changed in the Celsius scale.

In the early nineteenth century, William Thomson (Lord Kelvin) developed his universal thermodynamic scale based on the coefficient of expansion of an ideal gas. He created the concept of absolute zero and this scale is the standard for modern thermometry.

The Rankine scale (°R), named after early thermodynamicist W V M Rankine, is just the Fahrenheit equivalent of the Kelvin Scale.

Conversion equations for these four temperature scales are:

$$
\begin{aligned}
°C &= \frac{5}{9}\ (°F - 32) \\
°F &= \frac{9}{5}\ °C + 32 \\
K &= °C + 273.15 \\
°R &= °F + 459.67
\end{aligned}
\qquad (11.1)
$$

As temperatures cannot be manipulated mathematically as easily as length and time, we have to rely on easily observed and consistent

temperatures established by physical phenomena. The International Practical Temperature Scale (IPTS), revised in 1968, is based on such physical phenomena and establishes eleven reference temperatures. This is shown in Fig 11.1

IPTS-68 REFERENCE TEMPERATURES

EQUILIBRIUM POINT	K	°C
Triple Point of Hydrogen	13.81	-259.34
Liquid-Vapor Phase of Hydrogen at 25/76 Std Atmosphere	17.042	-256.108
Boiling Point of Hydrogen	20.28	-252.87
Boiling Point of Neon	27.102	-246.048
Triple Point of Oxygen	54.361	-218.789
Boiling Point of Oxygen	90.188	-182.962
Triple Point of Water	273.16	.01
Boiling Point of Water	373.15	100
Freezing Point of Zinc	692.73	419.58
Freezing Point of Silver	1235.08	961.93
Freezing Point of Gold	1337.58	1064.43

Fig 11.1 IPTS-68 Reference Temperatures

As only these temperatures are availible to us as fixed reference temperatures, instruments must be used to interpolate between these fixed points. Some of the instruments used to interpolate accurately between the reference points can be fairly exotic, complicated and expensive to use in any practical situation. The choice of instrumentation (temperature transducer) for our research requirements were limited to four types:

i) thermocouples
ii) resistance-temperature detectors (RTD's)
iii) thermistors
iv) integrated-circuit sensors.

Due to the nature of welding plates and the measuring of the high temperatures resulting, the thermistor and integrated-circuit sensor were rejected as choices as their temperature range was too limited [17]. In the case of the RTD, disadvantages were that this method was slow and expensive. Also a current source was required and the RTD would undergo self-heating. Hence, a simple thermocouple was chosen

as the transducer. Even though the thermocouple is the least sensitive and least stable of the four transducers, it is self-powered, rugged, simple, inexpensive, can have a wide temperature range and can take on a wide variety of forms. As our welding temperature range was between room temperature and that of molten metal, this was the obvious choice.

11.2 THERMOCOUPLE THEORY

11.2.1 INTRODUCTION

In 1822, Thomas Seebeck discovered that if two electrical conductors of differing materials were joined forming a circuit (See Fig 11.2), it was found that small e.m.f.'s (e_1 and e_2) were generated at the junctions, provided the two junctions were at different temperatures (θ_1 and θ_2) [18]. The algebraic sum of these e.m.f's caused a current (i) to flow. The resultant e.m.f. for any particular pair of metals having the junctions at particular temperatures is independant of the size of the conductors, the contact areas or the method of joining.

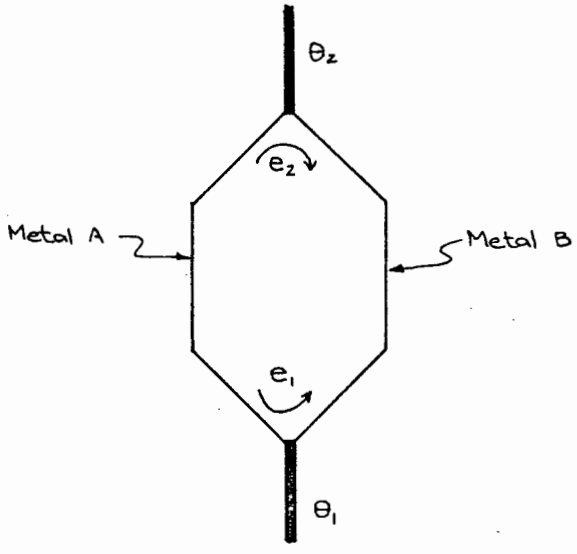

Fig 11.2 Structure of a thermocouple

If this circuit is broken at the centre, the net open circuit voltage, called the Seebeck voltage, is a function of the composition of the two metals and the junction temperature. For small changes in temperature, the Seebeck voltage is linearly proportional to temperature (See Fig 11.3):

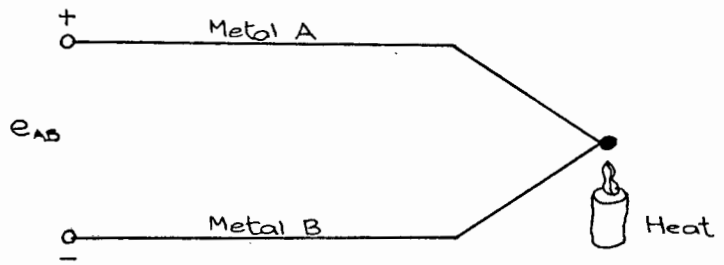

Fig 11.3 e_{AB} = Seebeck Voltage

Hence,

$$e_{AB} = \alpha T \quad \text{where } \alpha = \text{Seebeck coeffient} \qquad (11.2)$$

11.2.2 Measurement of thermocouple voltage

As a voltmeter has to be connected to the thermocouple, we cannot measure the Seebeck voltage directly as the voltmeter leads create a new thermoelectric circuit. As an example, we shall examine connecting a voltmeter across a copper-constantan thermocouple (See Fig 11.4) [17]

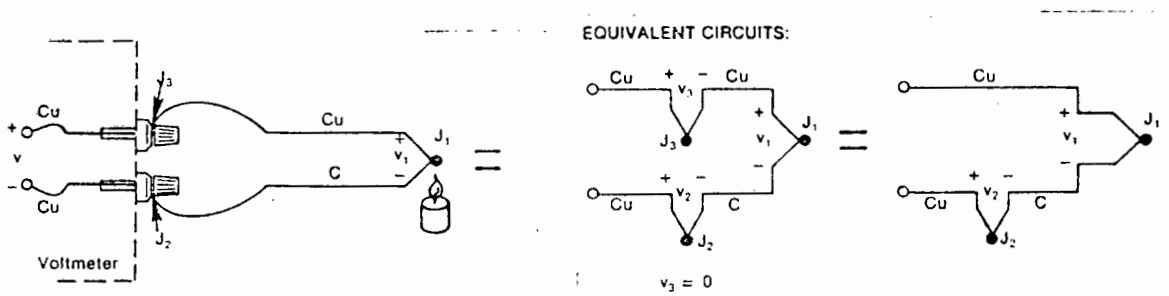

Fig 11.4 Measuring junction voltage

In this case we wish the voltmeter to read only V_1 but because we have connected a voltmeter into the circuit to measure the output at the junction J_1 we have created another two junctions, J_2 and J_3. J_3, being a Cu-Cu junction creates no thermal e.m.f, hence $V_3 = 0$, but J_2 is a copper-constantan junction which will add an emf (V_2) in opposition to V_1. Thus the resultant voltmeter reading V is proportional to the difference in temperature between J_2 and J_1. This implies that the temperature at J_1 cannot be found without knowing the temperature of J_2.

One way to solve this problem is if the junction V_2 is physically inserted into an ice-bath, forcing its temperature to be 0°C. This junction is then referred to as the "reference junction". Since both the terminals of the voltmeter are copper-copper, no thermal emf is created and the reading on the voltmeter V is proportional to the difference between J_1 and J_2. (See Fig 11.5)

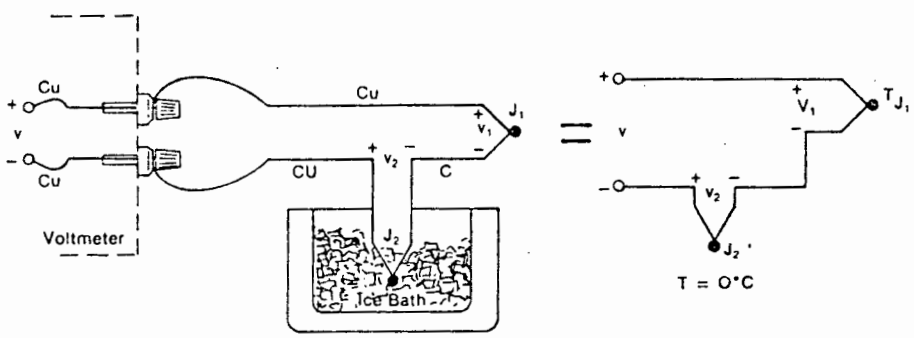

Fig 11.5 External Reference Junction

From Fig 11.5,

$$V = (V_1 - V_2) \simeq \alpha (t_{J1} - t_{J2}) \qquad (11.3)$$

where t_{Ji} = absolute temp (°K)

If we specify T_{J1} in °C

$$T_{J1}\ (°C) + 273.15 = t_{J1}\ (°K) \tag{11.4}$$

then V becomes

$$V = V_1 - V_2 = \alpha\left[(T_{J1} + 273.15) - (T_{J2} + 273.15)\right]$$

$$= \alpha\left[T_{J1} - T_{J2}\right] \tag{11.5}$$

$$= \alpha\left[T_{J1} - 0\right]$$

Hence,

$$V = \alpha T_{J1} \tag{11.6}$$

This derivation emphasizes that ice-bath junction output V_2 is not zero volts, but is a function of absolute temperature. We have now referenced the reading V to 0°C by adding the voltage of the ice-point reference junction. Now it is possible to use standard tables to convert from voltage V to temperature T_{J1}.

In practice, this "physical" ice-bath can be eliminated by replacing it with an isothermal block [17].

11.2.3 Voltage to temperature conversion

Output voltages for the more common thermocouples have been plotted as a function of temperature (Fig 11.6), but unfortunately the temp - vs - voltage relationship of a thermocouple is not linear. By examining the variations in Seebeck coefficient (Fig 11.7), it is evident that using a constant scale factor would not only limit the temperature range of the system, but would also restrict the accuracy. It would be more accurate to read the voltage and convert this to a temperature using standard thermocouple conversion

tables [19] (See Appendix B). These table values could be stored but this implies a massive amount of storage and memory. A more practical approach is to approximate the table values using a power series polynomial:

$$T = a_0 + a_1 x + a_2 x^2 + a_3 x^3 + ... a_n x^n \qquad (11.7)$$

where T = temperature
x = thermocouple voltage
a = polynomial coefficients
n = maximum order of polynomial.

As n increases, so does the accuracy of the polynomial

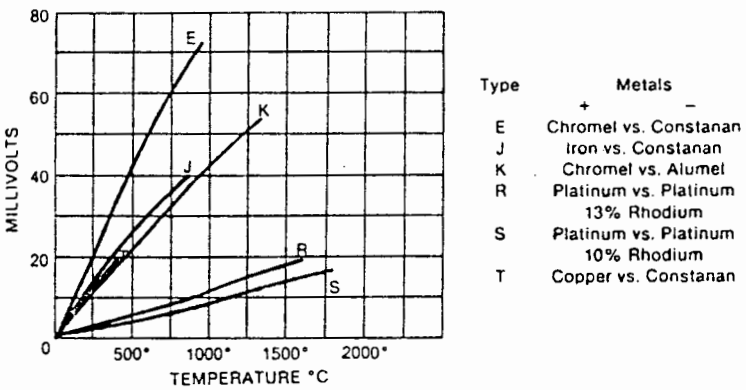

Fig 11.6 Thermocouple temp vs voltage

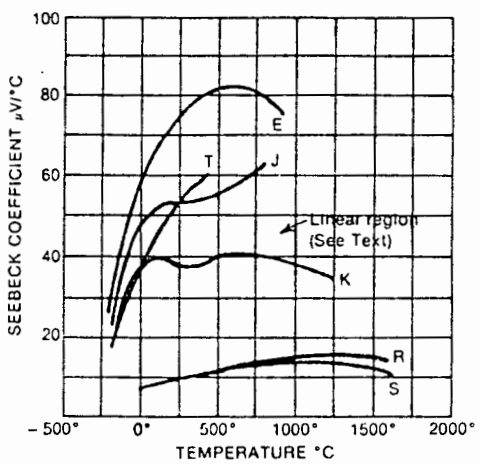

Fig 11.7 Seebeck coefficient vs temperature

Fig 11.8 shows the values of the polynomial coefficients for each type of thermocouple

	TYPE E	TYPE J	TYPE K	TYPE R	TYPE S	TYPE T
	Nickel-10% Chromium(+) Versus Constantan(-)	Iron(+) Versus Constantan(-)	Nickel-10% Chromium(+) Versus Nickel-5%(-) (Aluminum Silicon)	Platinum-13% Rhodium(+) Versus Platinum(-)	Platinum-10% Rhodium(+) Versus Platinum(-)	Copper(+) Versus Constantan(-)
	- 100°C to 1000°C* ± 0 5°C 9th order	0°C to 760°C* ± 0 1°C 5th order	0°C to 1370° C* ± 0 7°C 8th order	0°C to 1000°C* ± 0 5°C 8th order	0°C to 1750°C* ± 1°C 9th order	- 160°C to 400°C* ± 0 5°C 7th order
a_0	0 104967248	- 0 048868252	0 226584602	0 263632917	0 927763167	0 100860910
a_1	17189 45282	19873 14503	24152 10900	179075 491	169526 5150	25727.94369
a_2	- 282639 0850	- 218614.5353	67233 4248	- 48840341 37	- 31568363 94	- 767345 8295
a_3	12695339 5	11569199 78	2210340 682	1 90002E + 10	8990730663	78025595 81
a_4	- 448703084 6	- 264917531 4	- 860963914 9	- 4 82704E + 12	- 1 63565E + 12	- 9247486589
a_5	1 10866E + 10	2018441314	4 83506E + 10	7 62091E + 14	1 88027E + 14	6 97688E + 11
a_6	- 1 76807E + 11		- 1 18452E + 12	- 7.20026E + 16	- 1 37241E + 16	- 2 66192E + 13
a_7	1.71842E + 12		1.38690E + 13	3.71496E + 18	6 17501E + 17	3 94078E + 14
a_8	- 9 19278E + 12		- 6 33708E + 13	- 8 03104E + 19	- 1 56105E + 19	
a_9	2 06132E + 13				1 69535E + 20	

TEMPERATURE CONVERSION EQUATION: $T = a_0 + a_1 x + a_2 x^2 + \ldots + a_n x^n$

NESTED POLYNOMIAL FORM: $T = a_0 + x(a_1 + x(a_2 + x(a_3 + x(a_4 + a_5 x))))$ (5th order)

Fig 11.8 NBS Polynomial coefficients

11.3 CHOICE OF SUITABLE THERMOCOUPLE

Basically, six types of thermocouple exist:

Type E: Chromel (+) vs Constantan (-)
J Iron (+) vs Constantan (-)
K Chromel (+) vs Alumel (-)
R Platinum (+) vs Platinum (-) 13% Rhodium
S Platinum (+) vs Platinum (-) 10% Rhodium
T Copper (+) vs Constantan (-)

Fig 11.9 shows the characteristics and temperature ranges of these thermocouples. [18]

	Base-metal couples				Rare-metal couples		
Positive wire	Copper	Iron	Chromel 90% Cr, 10% Ni	Chromel	Platinum 90% rhodium 10%	Tungsten 95% rhenium 5%	Rhodium iridium
Negative wire	Constantan 40% Ni, 60% Cu approx.	Constantan	Alumel 94% Ni, 2% Al. + Si and Mn	Constantan	Platinum	Tungsten 72% rhenium 26%	Iridium
Temperature range (°C)	−250 to +400	−200 to +850	−200 to +1100	−200 to +850	0 to +1400	0 to +2600	0 to +2100
Spot maximum (°C)	500	1100	1300	1100	1650		
Characteristics	Resists oxidising and reducing atmospheres up to 350°C. Requires protection from acid fumes.	Low cost. Corrodes in the presence of moisture, oxygen, and sulphur-bearing gases. Suitable for reducing atmospheres.	Resistant to oxidising but not to reducing atmospheres. Susceptible to attack by carbon-bearing gases, sulphur, and cyanide fumes.	Suitable for oxidising but not for reducing atmospheres, carbon-bearing gases, and cyanide fumes. High e.m.f.	Low e.m.f. Good resistance to oxidising atmospheres, poor with reducing atmospheres. Calibration is affected by metallic vapours and contact with metallic oxides.	For use in non-oxidising atmospheres only. The 5% rhenium arm is brittle at room temperatures	Similar to platinum rhodium platinum.

Fig 11.9 Industrial thermocouple ranges and characteristics

Due to the nature of our research, involving high temperatures, the Chromel-Alumel thermocouple (type K) was chosen. It was inexpensive, being a base-metal thermocouple and suitable for our temperature range. The only other thermocouples that could do the job were the rare-metal couples which had unfavourable characteristics eg. brittleness at room temperature. In the research done by Masubuchi [3] , which also entailed the temperature measurement during the welding process, Type K Chromel-Alumel thermocouples were also used. Hence the thermocouple choice was concluded. The next problem was to decide on a choice of thermocouple hardware. The different types of construction are shown in Fig 11.10.

For the sake of simplicity and cost, it was initially decided to use the exposed-junction type thermocouple. Also from Fig 11.10 it is seen that this type of thermocouple provides the fastest response.

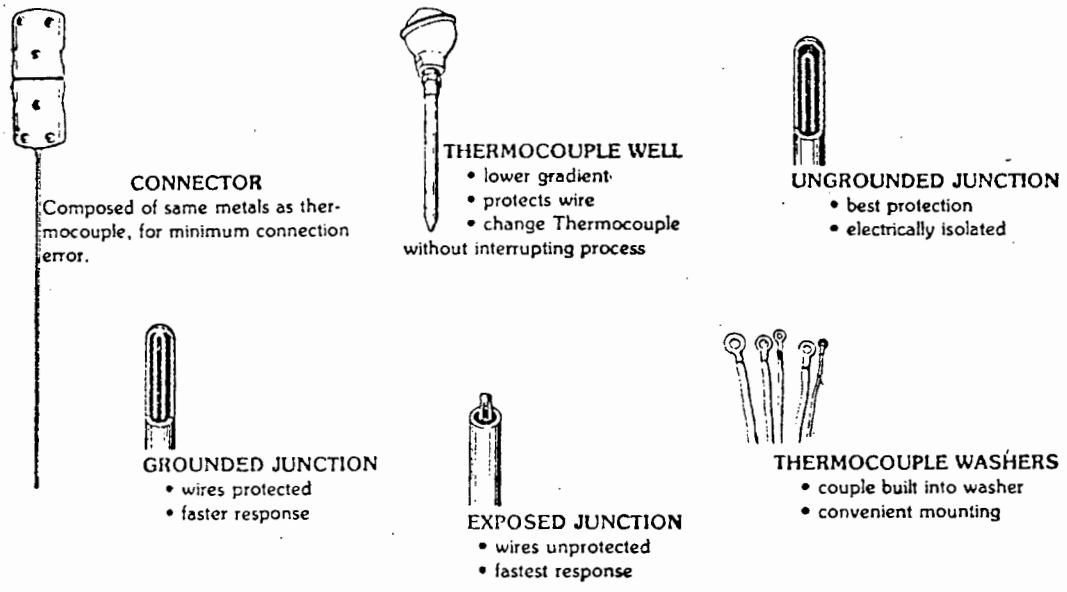

Fig 11.10 Thermocouple Hardware

This requirement is essential if previous research in this field is examined in respect that temperature during heating in welding increases extremely rapidly. As holes were going to be drilled from underneath the plate (See section 11.4) and the thermocouple was to be placed into these small holes, the connector and thermocouple well type hardware were rejected. It was finally decided to use the exposed-junction type thermocouple for these above reasons.

11.4 EXPERIMENTAL SETUP

An arc-welded bead was laid on a mild-steel steel plate 12 mm thick, 145 mm wide and 350 mm long. The weld electrode used was an E6013 Vitemax type (mild steel rod with rutile flux) 4 mm in diameter. The weld was made with an arc current of 170 A and a desired travel speed of 150 mm / minute

Small holes 5 mm in diameter were drilled normal to the surface from the back side to a predetermined depth and were slotted to accept the shape of the thermocouple insulator. A chromel-alumel thermocouple, 1,5 mm in diameter was inserted into the holes provided and locked in position using small aluminium angle brackets and screws (For fixing diagram see Appendix B).

The hot junction of the thermocouple was flattened slightly so that it could rest up against the top of the hole and cover a certain surface area. Hence the thermocouple could measure the temperature of the weld at a predetermined depth into the metal. The coated electrode was fed by a manual welding machine and the bead was laid across the centre of the specimen. The other end of the thermocouple was connected to the Hewlett-Packard 3054 DL Data Logger which was connected to an HP-85 computer which controlled the experiment. Fig 11.11 shows the experimentation setup diagramatically:

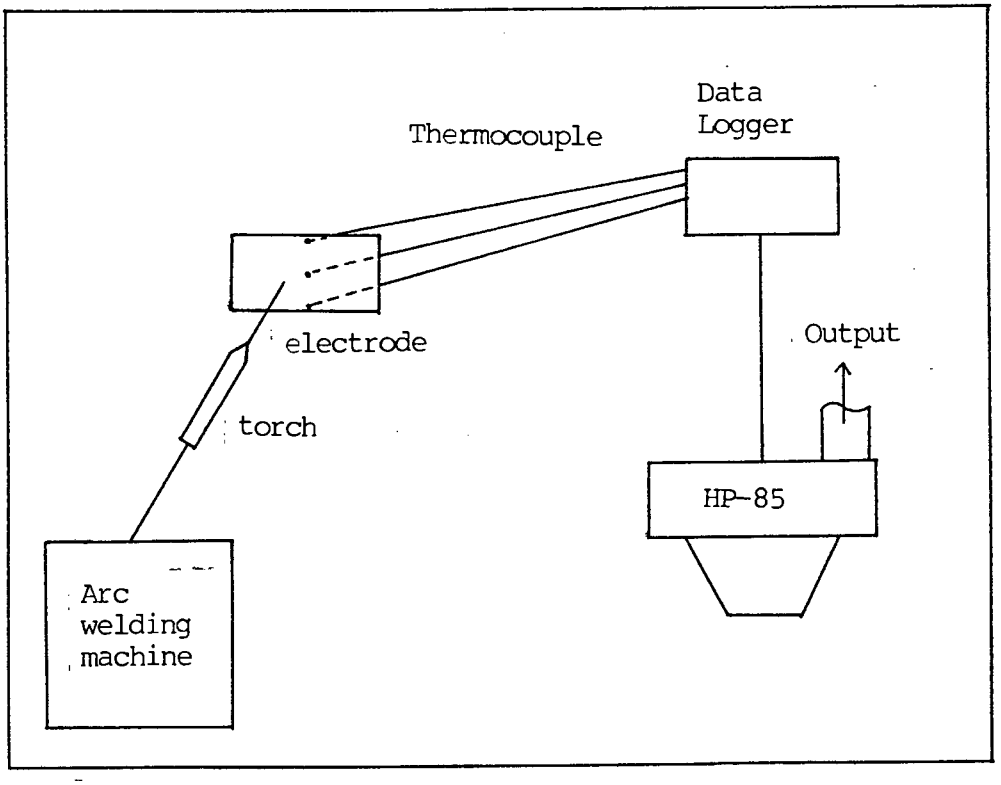

Fig 11.11 Experiment setup

The plan view of each experiment remained identical. See Fig 11.12

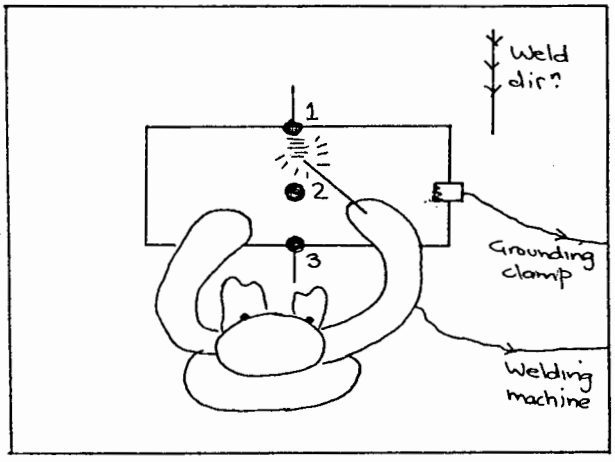

Fig 11.12 Plan view of experiment

Welding began over thermocouple 1 and ended over thermocouple 3. On the thermocouple card in the HP Data Logger, each thermocouple was linked to a channel which monitored the voltages continuously of that specific thermocouple only. They were connected as follows: (See table 11.1)

Thermocouple	Channel	Colour Code
1	6	Black
2	8	Green
3	9	Double red

Table 11.1
Colour Coding

The colour code was of use only to distinguish which thermocouples were monitoring which channels. It was designated by personal choice and has no other bearing in the experiment. [See Documentation Worksheets, Appendix B] . Two programs were used to log the data and will be explained at a later stage.

11.5 DESCRIPTION OF EXPERIMENTS AND RESULTS

Three experiments were conducted and will be described in detail.

11.5.1 Experiment "TEST"

In this experiment, 3 thermocouples were placed across the centre of the width of the plate, being equally spaced. See Fig 11.13

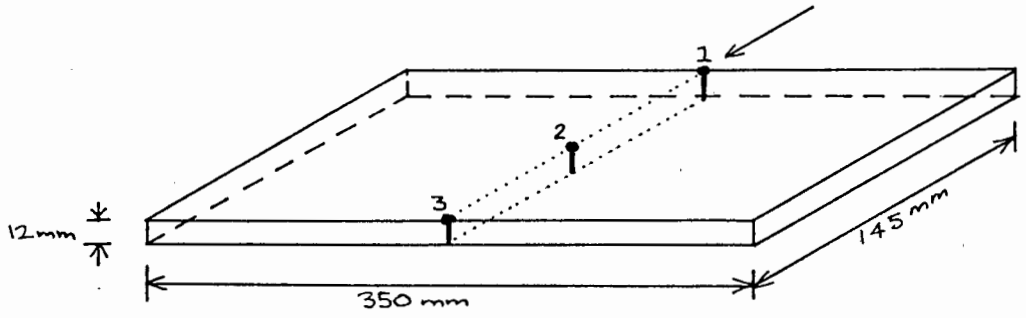

Fig 11.13 Schematic experimental set-up

A weld bead was laid, begining over thermocouple 1 and ending over thermocouple 3. The speed of the arc was to be 150 mm/min hence the experiment was to be of duration 60 seconds.
From underneath, the holes which contained the thermocouples were drilled to within 4 mm of the top of the plate. (ie. hole depth of 8 mm). The software used to gather data was the Hewlett-Packard Level 1 program. (3054 DL System Cartridge Level 1)

11.5.2 RESULTS OF "TEST"

As welding began, it was noticed that the temperature ouput became negative. This was caused by the thermocouple wires being connected incorrectly in the data logger. The experiment was stopped for a period of about 20 minutes while this fault was corrected. At the time of stoppage, the welding arc was about halfway between thermocouples 1 and 2. Upon recommencement of the welding, it was noticed that the plate had cooled considerably. Welding continued at a somewhat faster rate (approximately 225 mm/min). The results are shown on Graph 11A. By examining this graph carefully we can observe:

1. Thermocouple 1, which gave out a negative initial temperature on first attempt, cooled down to about 30°C during the stoppage. As welding continued from the point where it had previously stopped, thermocouple 1 did not receive direct heat again and for the rest of the experiment it just increased slightly due to conduction

through the plate. Thermocouples 2 and 3 on the otherhand showed slight rises as the welding arc approached and good cooling curves as the arc departed, but the sampling time was too large to pick up the high peaks as the weld passed directly overhead. These peaks, shown dotted on the graph, were not verified by the program. Attempts to decrease the time taken to scan the thermocouples failed as we were already using the lowest possible scan time. An undersirable feature of the Hewlett-Packard program used was that the results were printed as the experiment was running, using excessive time to record the scan, format it and print, before scanning again. The actual time between two consecutive scannings was about 8 seconds. [See output in Appendix B.]

In conclusion, it was decided to run this experiment again, but monitoring the voltages with a different program which could log the data more rapidly. It was also noted that the shape of the temperature-time curves compared favourably to that obtained by Masubuchi [3] in a similar type of experiment, shown in Fig 11.14, although the high peaks were not evident from the output data

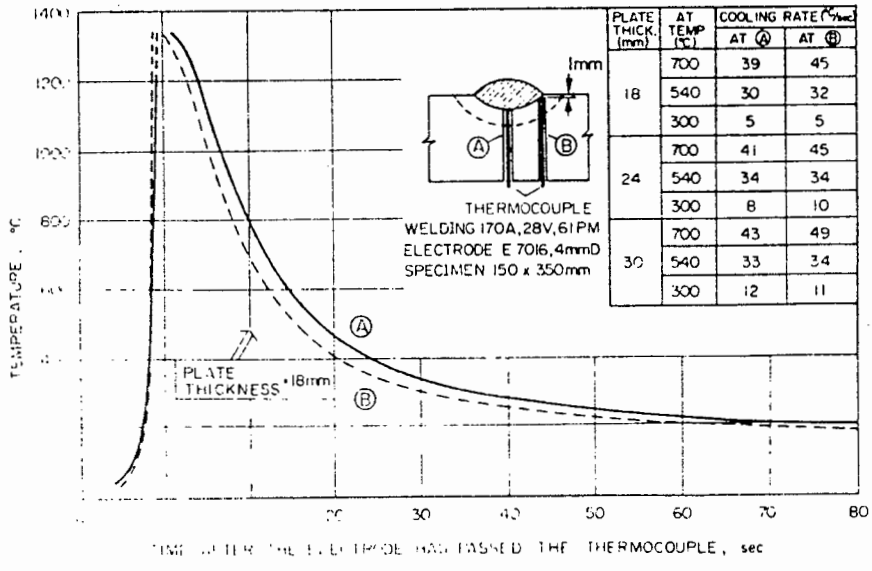

Fig 11.14 Temperature-time curve from Masubuchi [3]

11.5.3 EXPERIMENTAL "RUN 1"

This experiment was identical in all respects to experiment "TEST" except that a different program was used to record the temperature data from the welding operation. The program used was a modified version of an original "fast-scanning" program, developed by A Brink (See Acknowledgements). The capabilities of this program (See Appendix B) was that it could log data continuously and would store and print only after the experiment was completed. Because of this feature, it could scan all three thermocouples in about 0.3 sec, compared to 8 seconds in the case of the Hewlett-Packard program. The new program was certain to reflect the rapid peak temperature as the welding arc passed over each thermocouple.

11.5.4 RESULTS OF "RUN 1"

The results of this experiment are shown on Graph 11B. By examining this graph, we can note:

1. The travel speed turned out faster than desired since the peak temperatures are experienced at 20 sec and 40 sec, giving an arc travel speed of 225 mm/min.

2. Only thermocouple 3 exhibited a high peak temperature ($\pm$ 1000°C).

The curves can be explained as follows:
As the welding begins, the welding arc is directly above thermocouple 1 and immediately begins to move away, hence this thermocouple is not given enough time to reach the arc temperature. Also, due to the fact that we are measuring the temperature 4 mm below the surface of the plate, an accurately high temperature might not be reached. Thermocouple 2 reaches a higher temperature ($\simeq$600°C) as does thermocouple 3 ($\simeq$1000°C). Still, these might not be the correct temperatures of the weld due to the thickness of the plate above the thermocouples. In cooling, the curves decrease to a temperature of between 150 and 250 °C, irrespective of the peak temperature.

In conclusion, we can deduce that the curves are showing a consistent shape and have consistent characteristics, except that we are not picking up the peak weld temperatures of around 1100°C. The 4 mm of plate between the top of the plate and the thermocouple could be excessive. It would be advisable to run the experiment again with a smaller plate thickness between thermocouple and the top of the plate, say 0.5 mm.

11.5.5 EXPERIMENT "RUN 2"

This experiment was identical to experiment "RUN 1" except that the holes for the thermocouples were drilled deeper. Out of a plate thickness of 12 mm, the depths of the holes were 11.5 mm, leaving a 0.5 wafer-thin thickness of plate between the top of the plate and the thermocouple. The thermocouples were now certain to pick up the peak weld temperatures. It was also expected that the thermocouples would be destroyed (or at least non-reusable) as the weld penetration would be greater than o.5 mm.

11.5.6 RESULTS OF "RUN 2"

The results of this experiment are shown on Graph 11C. In this "RUN 2", the arc travel speed of 150 mm/min was maintained with the peak temperatures occuring at 0, 30 and 60 seconds. All 3 thermocouples recorded peak temperatures of about 1300°C. If the output is examined, it will be seen that the temperatures in excess of 1300°C were recprded but are not reliable. These temperatures were denoted with a negative sign in the output. The reason for this was that the approximation polynomial used to convert from voltage to temperature does not match the standard tables above 1500°C. 17 The exact shape of this polynomial was plotted and is shown in Graph 11D. As the voltage exceeds 70 mV, the polynomial curves back on itself and progresses into the negative temperature region. When this occurs, it is shown as dotted on Graph 11C. Again on cooling, the curves level out at a steady temperature of about 200 to 300°C, irrespective of the peak. Also, for the first time, all 3 curves had essentially the same shape and same peak value.

On examination of the thermocouples, they appeared burnt and fixed rigidly to the plate. They could not be removed or re-used. [For sample output, see Appendix B].

In conclusion, it appeared that the 0,5 mm plate thickness above the thermocouples gave reasonable temperatures and if the experiments were to be repeated, it should be done as done in "RUN 2".

11.6 CONCLUSION

It was concluded that the results of "RUN 2" were representative of the real behaviour of the temperature distribution due to the weld. The resluts of thermocouple 1 of "RUN 2" were dotted alongside the result obtained by Masubuchi [3] for a similar experiment. This is shown in Graph 11E. The correlation between the two curves is extremely good, considering the superior equipment and instrumentation used by Masubuvhi.

It is finally concluded that if a heat curve is to be input to ADINAT and the ADINA stress-analysis program in order to calculate a stress distribution, the resul obtained from thermocouple 1 in "RUN 2" is an acceptable approximation of the real thermal behaviour due to a weld bead being laid on a mild-steel plate.

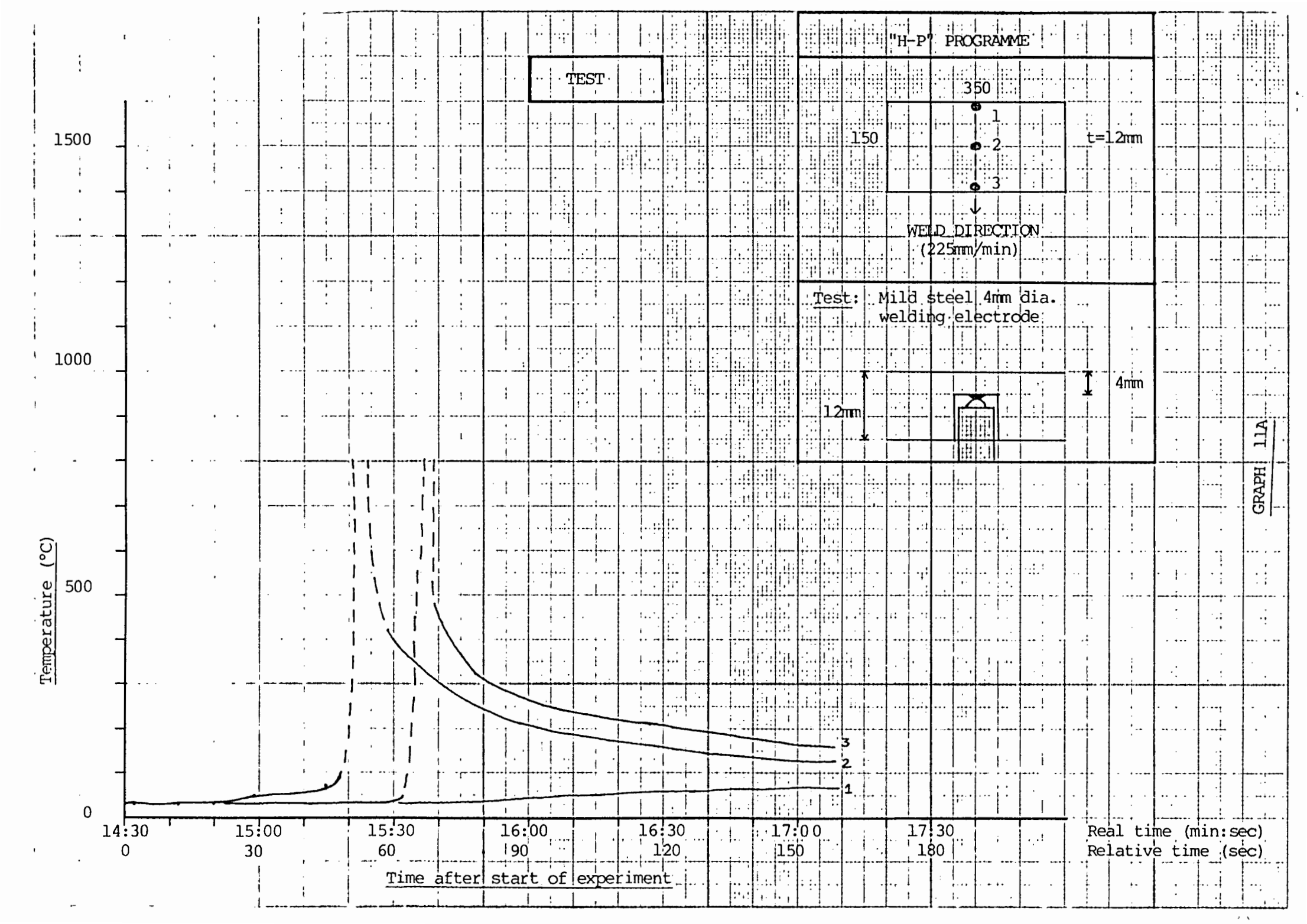
TEST
"H-P" PROGRAMME
350
1
2
3
150
t=12mm
WELD DIRECTION
(225mm/min)
Test: Mild steel 4mm dia.
welding electrode
12mm
4mm
GRAPH 11A
Temperature (°C)
1500
1000
500
0
14:30
15:00
15:30
16:00
16:30
17:00
17:30
0
30
60
90
120
150
180
Real time (min:sec)
Relative time (sec)
Time after start of experiment

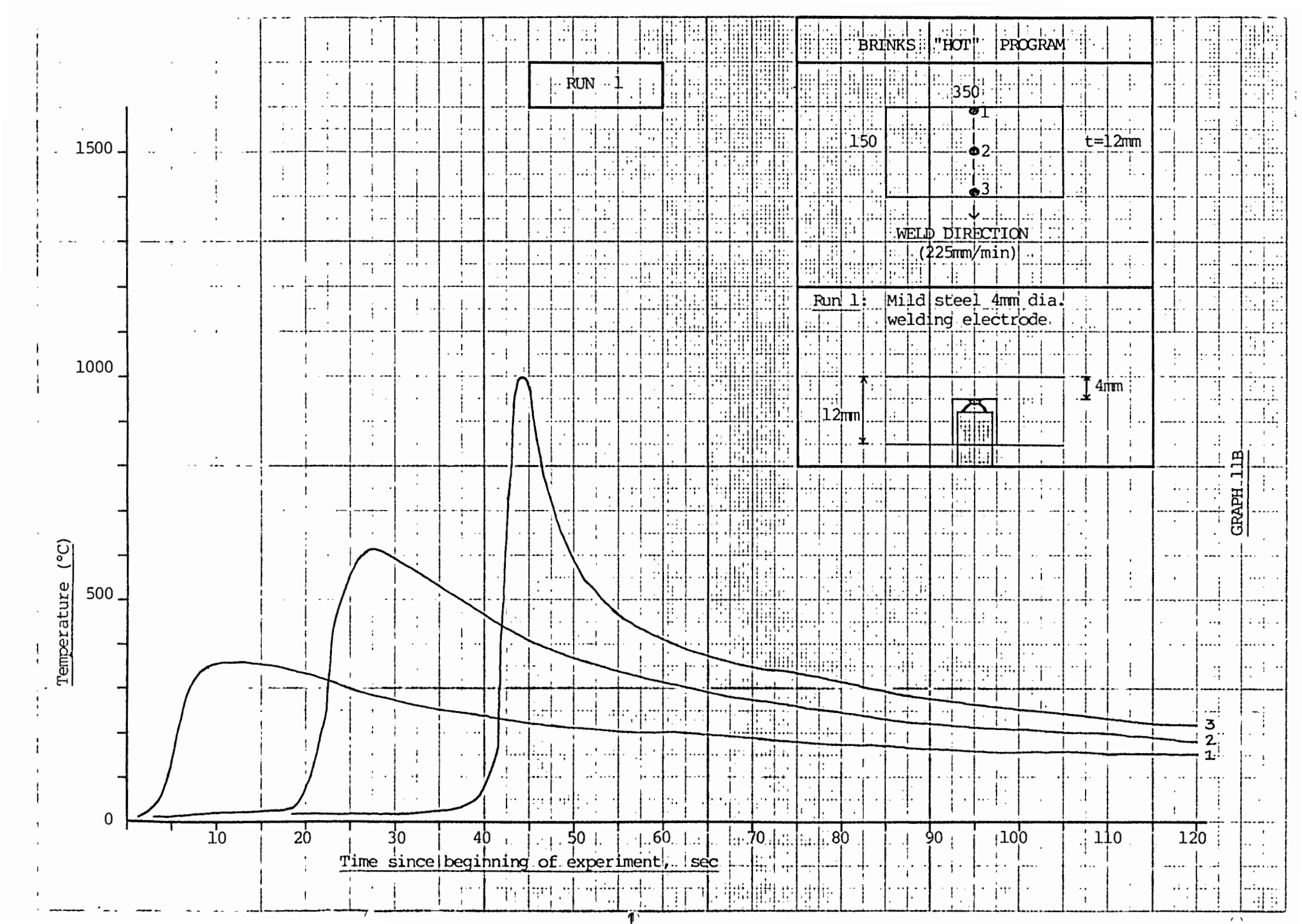
RUN 1
BRINKS "HOT" PROGRAM
350
150
t=12mm
1
2
3
WELD DIRECTION
(225mm/min)
Run 1: Mild steel 4mm dia.
welding electrode.
12mm
4mm
1500
1000
500
0
Temperature (°C)
10
20
30
40
50
60
70
80
90
100
110
120
Time since beginning of experiment, sec
3
2
1
GRAPH 11B

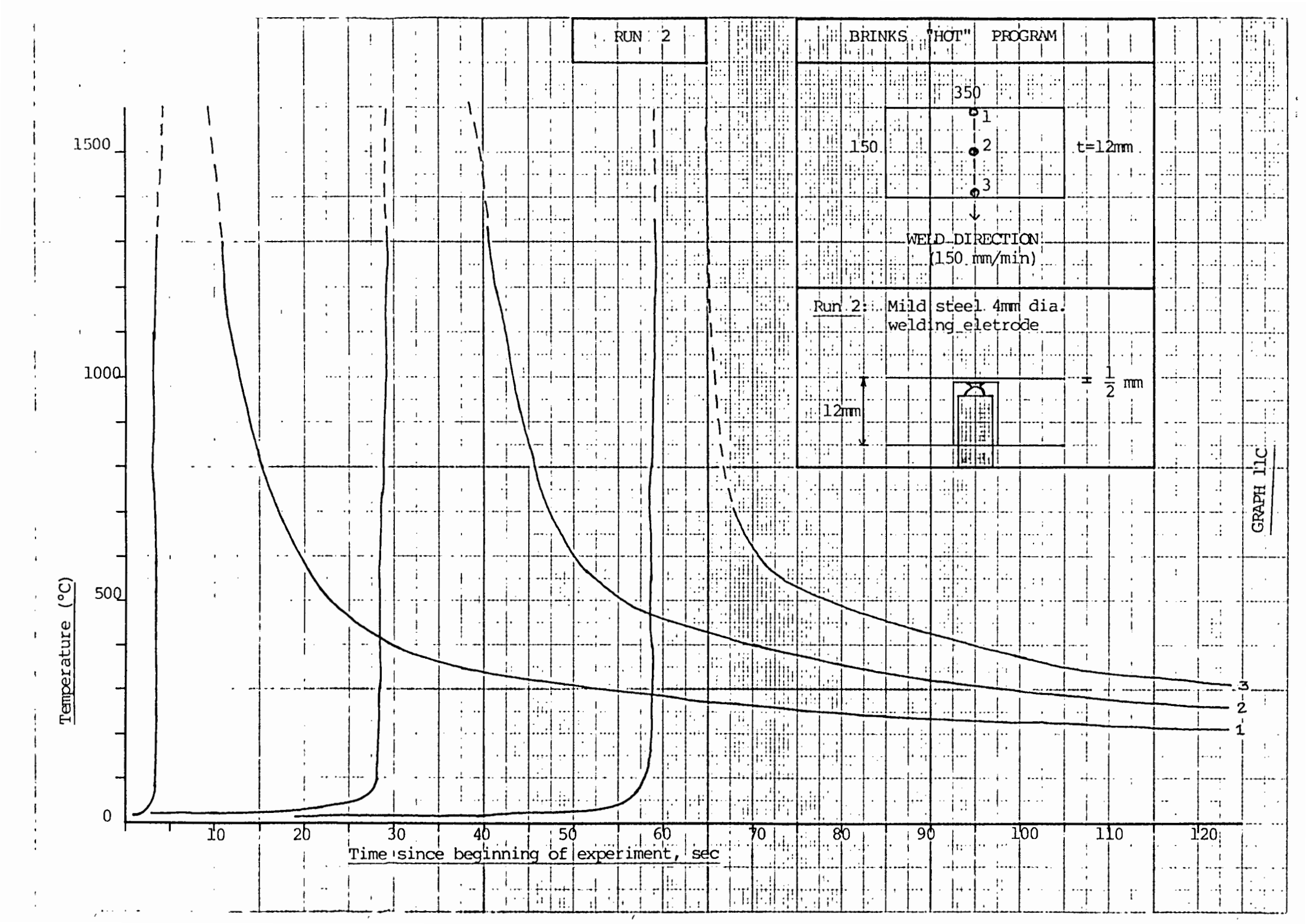
RUN 2
BRINKS "HOT" PROGRAM
350
150
1
2
3
t=12mm
WELD DIRECTION
(150 mm/min)
Run 2: Mild steel 4mm dia.
welding eletrode
12mm
± 1/2 mm
1500
1000
500
0
Temperature (°C)
10
20
30
40
50
60
70
80
90
100
110
120
Time since beginning of experiment, sec
1
2
3
GRAPH 11C

$$f(x) = a_0 + a_1x + a_2x^2 + a_3x^3 + a_4x^4 + a_5x^5 + a_6x^6 + a_7x^7 + a_8x^8$$

a_0 = 0.226584602	a_5 = 4.83506 E+10
a_1 = 24152.10900	a_6 = -1.18452 E+12
a_2 = 67233.4248	a_7 = 1.38690 E+13
a_3 = 2210340.682	a_8 = -6.33708 E+13
a_4 = -860963914.9	

APPROXIATION POLYNOMIAL FOR TEMPERATURE-VOLTAGE RELATIONSHIP FOR K-TYPE THERMOCOUPLE

X - - - - - - X TABLES

f(x), x in mV

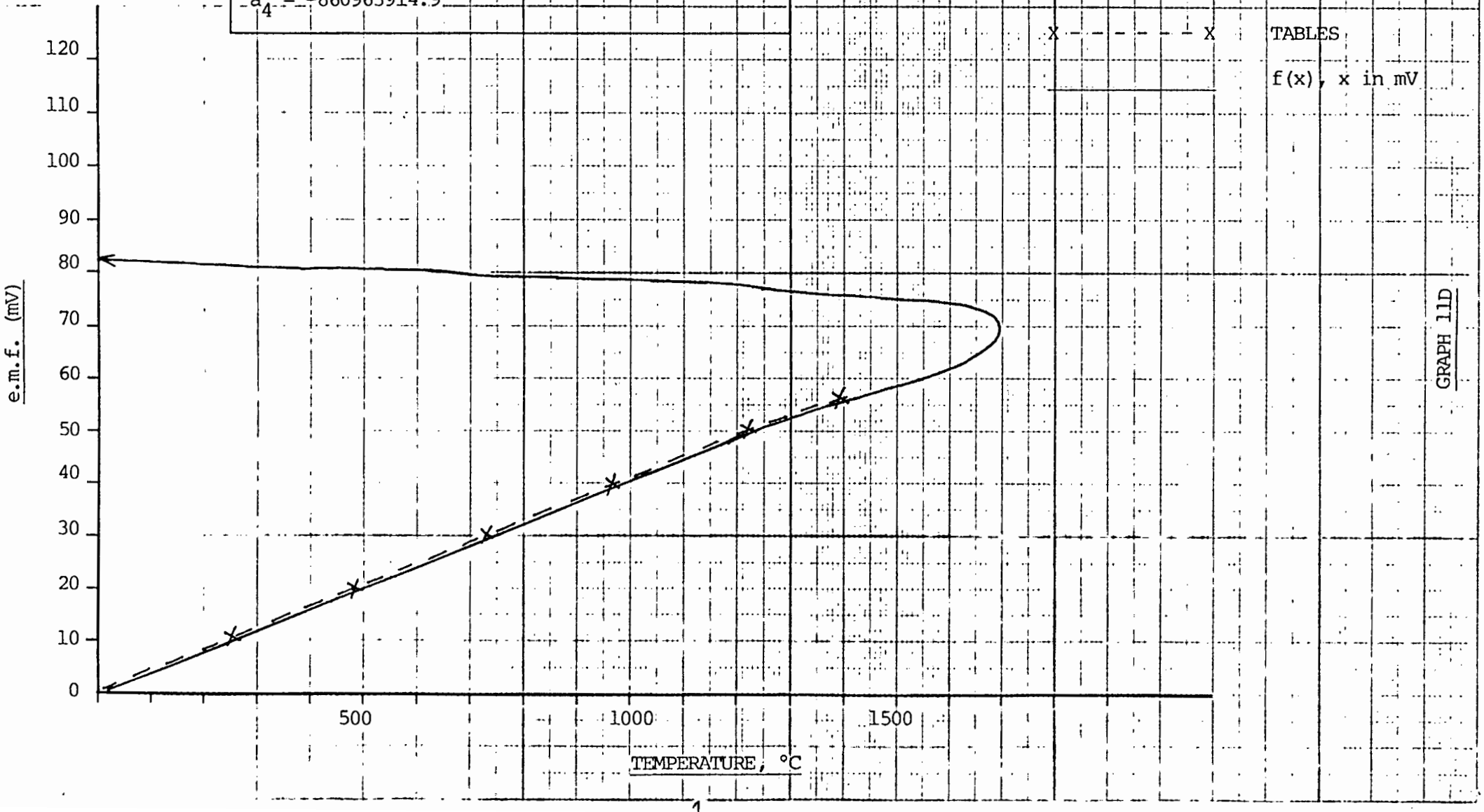

GRAPH 11D

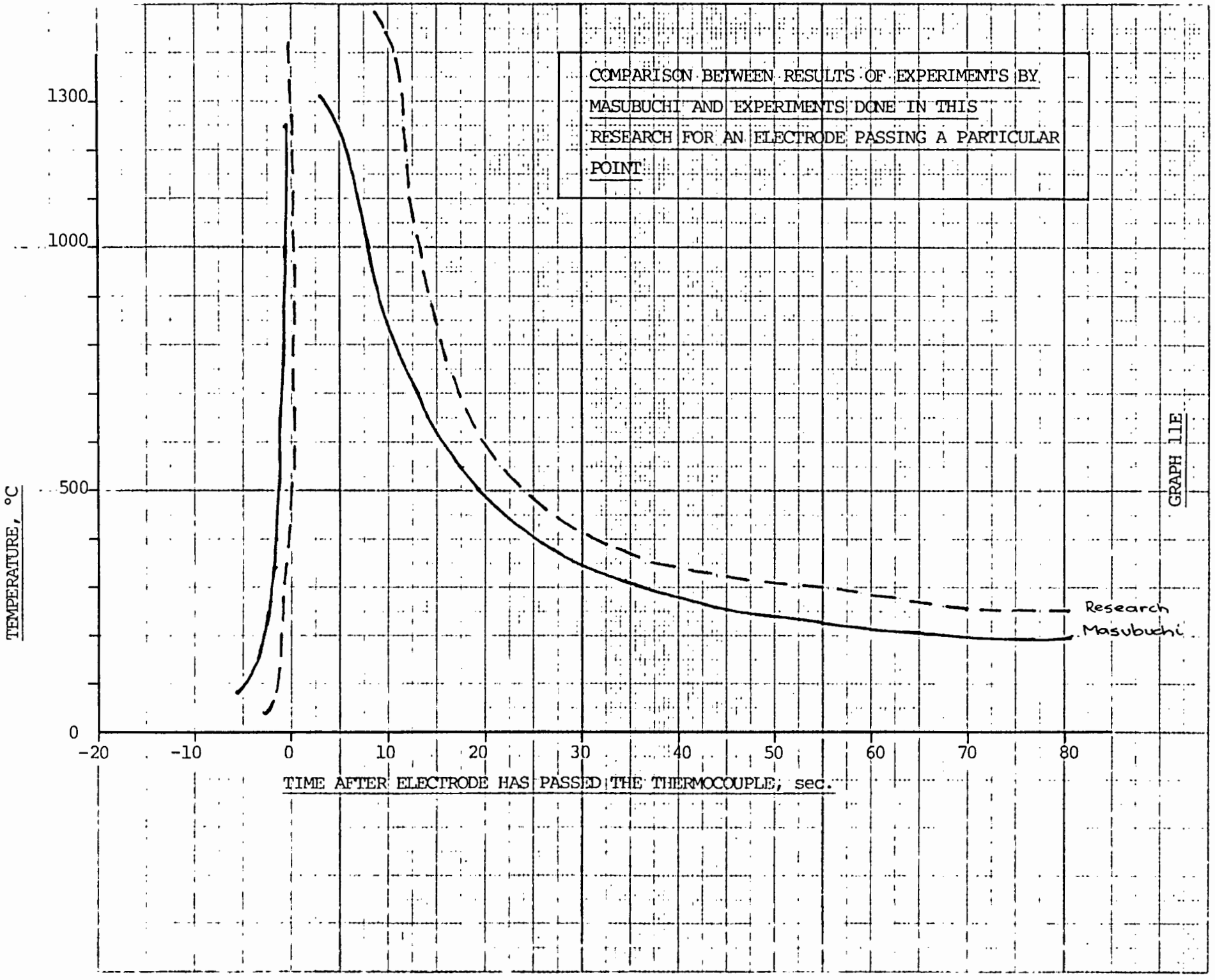
COMPARISON BETWEEN RESULTS OF EXPERIMENTS BY MASUBUCHI AND EXPERIMENTS DONE IN THIS RESEARCH FOR AN ELECTRODE PASSING A PARTICULAR POINT
GRAPH 11E
TEMPERATURE, °C
1300
1000
500
0
-20
-10
0
10
20
30
40
50
60
70
80
TIME AFTER ELECTRODE HAS PASSED THE THERMOCOUPLE, sec.
Research
Masubuchi

12.1 COMPUTATIONAL INVESTIGATION

12.1.1 INTRODUCTION

In the previous chapter, we concluded with the statement that the curve obtained from "RUN 2", shown in Graph 11E, was an acceptable approximation to the real thermal behavior of a particular point due to a weld bead being laid over it on a mild-steel plate. So far, we had only measured the thermal distribution in the weld zone. In order to examine the stresses set up by the weld, it would be necessary to know the temperature distribution over the entire plate. It was therefore necessary to discretize the curve obtained in Graph 11E so that it could be input as a time-function curve to the finite-element model of our plate.
ADINAT was used to model the plate.

12.2 DISCRETISATION OF "STANDARD" HEAT CURVE

In order to perform a temperature analysis using ADINAT, the heat input to the model must be of the form of a time function, where the temperature is defined as a function of time. This function would be input for each node along the weld path with the peak temperature arriving at times corresponding to the arrival of the actual weld at the nodes. The remaining nodes would be free to reach their own transient temperatures.
The "standard" heat curve from Graph 11E is shown in Graph 12A alongside the discretised version of the graph to be used in ADINAT.

12.3 ADINAT MODEL

In order to ensure a high level of accuracy, the finite-element model representing half of our plate consisted of eight 8-noded two dimensional conduction elements and is shown in Fig 12.1
The ADINAT program was executed twice, performing a linear analysis as well as a non-linear analysis. These analyses differed only in the material model specification and will be discussed in detail.

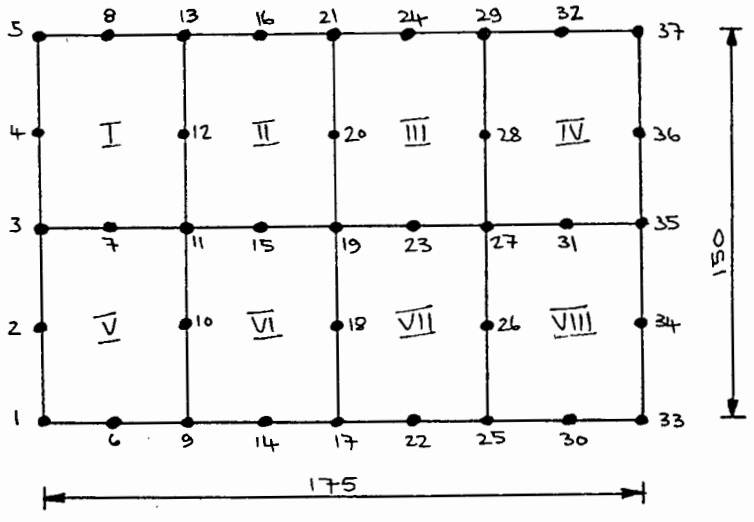

Fig 12.1 Finite-element model of half of plate

12.3.1 LINEAR TRANSIENT ANALYSIS

This analysis modelled the "half-plate" using eight 8-noded two-dimensional solid linear conduction elements (see Fig 12.1) with a lumped specific heat matrix. The time integration method used was the Euler backward method and the program was run as a transient analysis for 120 steps with a timestep of $\Delta t = 1$ second. The initial condition specified was that before welding commenced, the entire plate was at room temperature (20°C). The discretized heat curve shown in Graph 12A was input to nodes 1 to 5 with peak heat arrival times of 0, 15, 30, 45 and 60 seconds respectively. This is shown for nodes 1, 3 and 5 in Graph 12B. The time-functions were input as decimal fractions of the peak temperature, 1300°C, with a function scaling multiplier of this value ie. 650° was input as 0.5 which would later be multiplied by the scaling factor. In connection with the elements used, planar conditions were assumed and the Gauss quadrature numerical integration order used was two. The thickness of the element was 12 mm. The material model used was the constant isotropic conductivity and constant specific heat model ("Model 1"); the conductivity value for mild steel was taken as $k = 45$ W/m°C and the specific heat per unit volume was

taken as c = 460 J/kg°C [9] . The density of mild steel was taken as ρ = 7850 kg/m^3.

12.3.2 NON-LINEAR TRANSIENT ANALYSIS

This analysis modelled the "half-plate" using eight 8-noded two dimensional solid non-linear conduction elements (see Fig 12.1). All the other details are identical to those mentioned in the linear transient analysis, except for the material model. In this case, the material model used was the temperature dependant isotropic conductivity and constant specific heat model ("Model 3"). The variation of conductivity over a specified temperature range was input together with a constant specific heat. This is shown in Fig 12.2

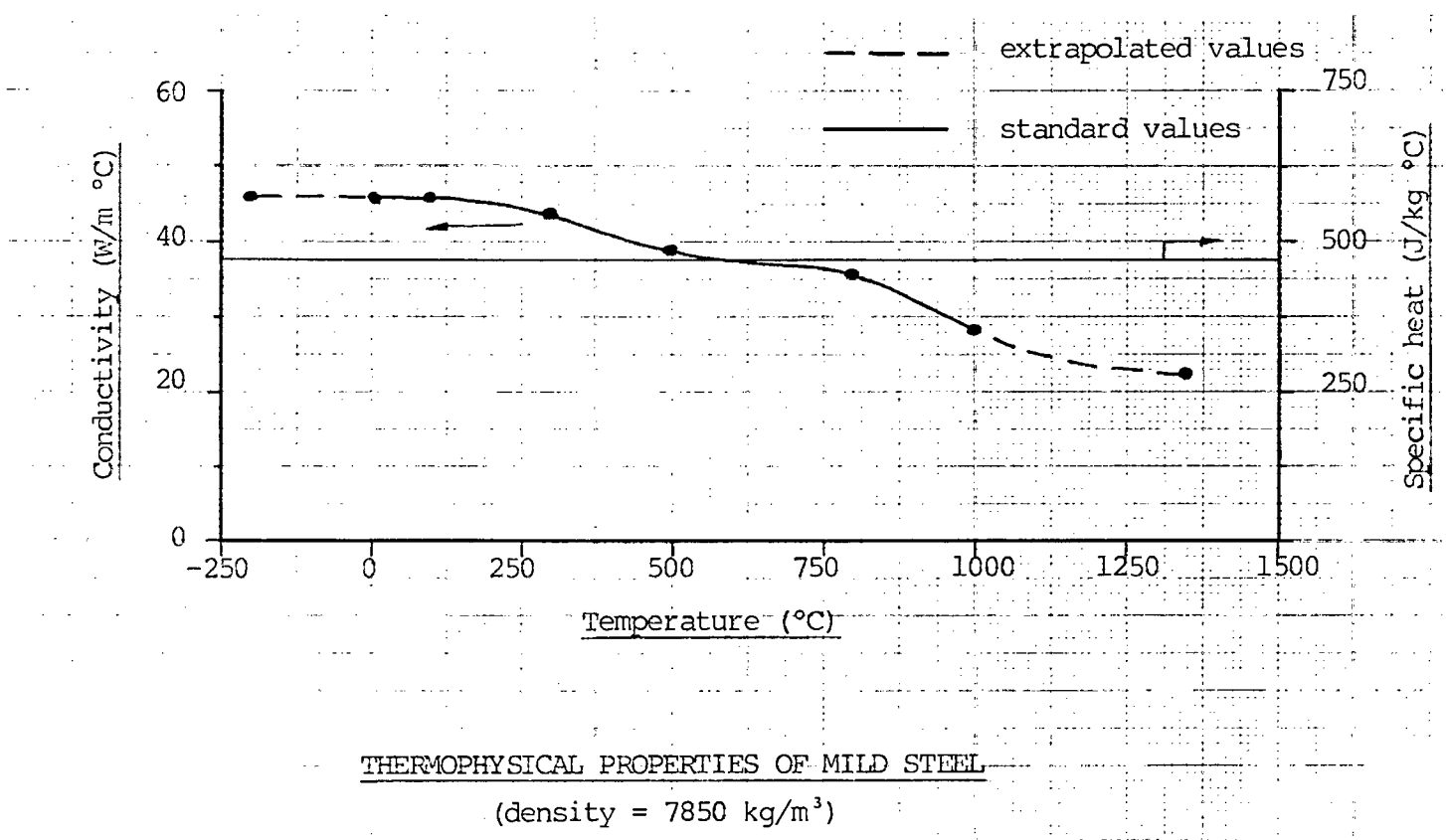

Fig 12.2 Conductivity variation

The values used in constructing Fig 12.2 were obtained from tables in reference on Heat Transfer [9, 22, 23, 24] . The extrapolated values were input to accomodate any anomaly in temperature due to numerical instability which could cause a negative temperature. This point will be discussed later in section 12.5.5

12.4 RESULTS OF ADINAT

The program was executed and yielded a temperature history with respect to time for each of the 37 nodes over a time period of 120 seconds. As the discussion of the response of 37 nodes would be very time consuming, it was decided to consider only 13 nodes, their positions as shown in Fig 12.3 Another reason for choosing 13 nodes will be explained in Chapter 13.4.1

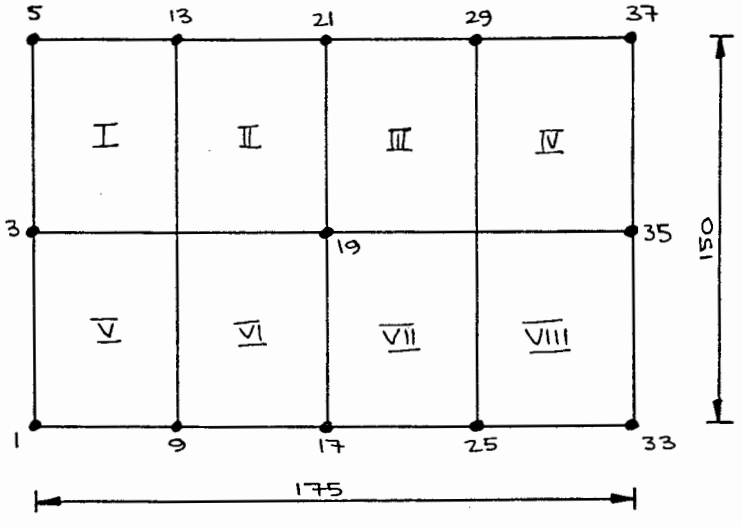

Fig 12.3 13 nodes considered in output

The complete graphical output for the above thirteen nodes can be found in Appendix C.

Of the 13 nodes in Fig 12.3, four were chosed for an in-depth evaluation, being nodes 9, 13, 19 and 35. Nodes 9 and 13 were chosen as they were close to the weld, node 19 was exactly at the centre of the plate-half and node 35 was the central node of a group of nodes furthest away from the weld on the edge of the plate.

The responses of the 4 nodes for both the linear and non-linear models are shown in Graph 12C and 12D.

As mentioned previously, the welding process began directly above node 1 and progressed at a rate of 150 mm/minute towards node 5. After this 60 second weld, the plate was analysed for a further 60 seconds as the weld cooled. Therefore, the entire experiment took 120 seconds.

12.5 DISCUSSION OF RESULTS FROM ADINAT

12.5.1 NODE 9

As this node is the closest node to the point where the weld was initiated, we would expect it to heat up the earliest. This is evident from Graph 12C where node 9 starts heating up at about t = 24 sec. At this time, all the other nodes (13, 19 and 35) are still at room temperature.
Both the linear and non-linear analyses show an irregularity at t = 30 sec., which can only be attributed to a numerical instability in the mathematical model. If the beginning and end of this irregularity is joined, a smooth curve results. Of interest is also the fact that even though a temperature of about 1300°C is being input to the plate only 44 mm away, the temperature 120 seconds later is a maximum of only 153°C.

12.5.2 NODE 13

As this node is the closest node to the point where the weld is terminated, we would expect it to heat up much later than node 9. ie. as the weld approaches node 5. This is evident from Graph 12C where node 13 only starts heating up at about t = 52 sec. By this time, all the nodes, with the exception of node 35, have begun to warm up. As before, both the linear and non-linear analyses show an irregularity, but this time it occurs later, peaking at t = 60 sec. This, again, can only be attributed to numerical instability. Also, joining the beginning and end of this irregularity

results in a smooth curve. As before, it is noted that the temperature does not seem to flow through the plate as quickly as one would expect.

12.5.3 NODE 19

This node is positioned exactly in the centre of the half-plate being modelled. Graph 12D shows the response of this node, which increases slowly from room temperature to a temperature of only ± 60°C after a full two minutes. Again, contrary to the belief that heat would flow rapidly through the plate, this node being at the centre shows that the heat flows at a much slower rate than expected. The nonlinear and linear analyses agree almost perfectly, the maximum difference between the two curves being 4°C.

12.5.4 NODE 35

This node, being 175 mm away from the weld, hardly reacts at all to the high input temperature of the weld. It remains at room temperature throughout the two minutes analysis, increasing from 20°C to 23°C after two minutes.

12.5.5 LOWER LIMIT OF CURVES

In section 12.3.2 it is explained that negative temperatures could exist from numerical instabilties. This indeed occurs for node 9 at time t = 10 sec. and for node 13 at t= 40 sec. for both linear and non-linear analysis. In fact, before these times, the curves actually cool below 20°C, become negative and then heat up again to room temperature before heating up to a much higher temperature. Where this has occured, the curve has purposely been left at room temperature, as by definition, if heat is input to a plate at 20°C, the temperature of the plate should increase, not decrease. (See Fig 12.3a.) This "assumed" room temperature value was essential to the workings of the finite-element model.

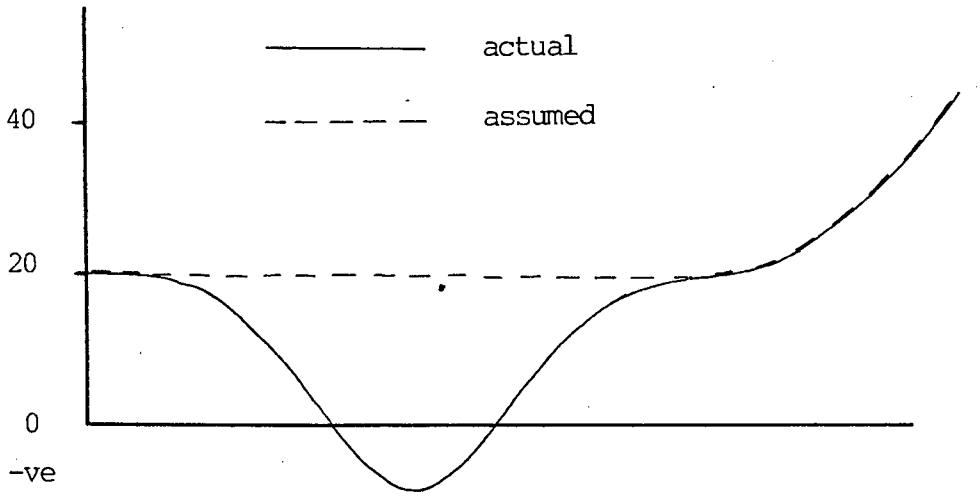

Fig 12.3a Overriding of temperatures below 20°C

12.6 EXPERIMENTAL VERIFICATION OF THE HEAT DISTRIBUTION THROUGH THE ENTIRE PLATE

12.6.1 EXPERIMENTAL SET-UP

The experimental set-up was identical to that used in Chapter 11 to determine the heat response in the weld zone. However, in this case, two thermocouples were attached to the plate away from the weld zone (See Experimental Documentation Worksheets in Appendix C). Two experiments were performed and will be described as "RUN 3" and "RUN 4".

12.6.2 RUN 3

In this experiment, the two thermocouples were placed in positions as shown in Fig 12.4 and the plate was welded, as in Chapter 11, from A to B.

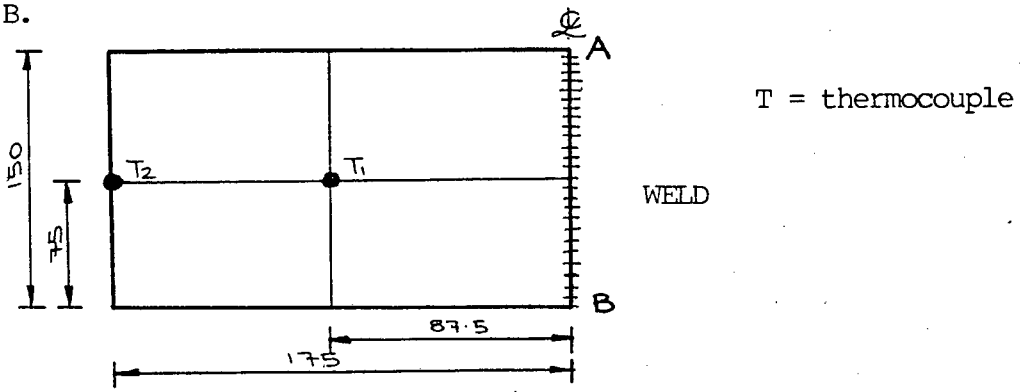

Fig 12.4 Positions of thermocouples for RUN 3

These thermocouples 1 and 2 were to correspond to the thermal response of nodes 19 and 35 of the finite-element mesh in Fig 12.1, respectively.
This experiment was performed twice and in both cases the output from the thermocouples agreed perfectly.

12.6.3 RUN 4

In this experiment, the two thermocouples were placed in positions as shown in Fig 12.5 and the plate was welded from A to B.

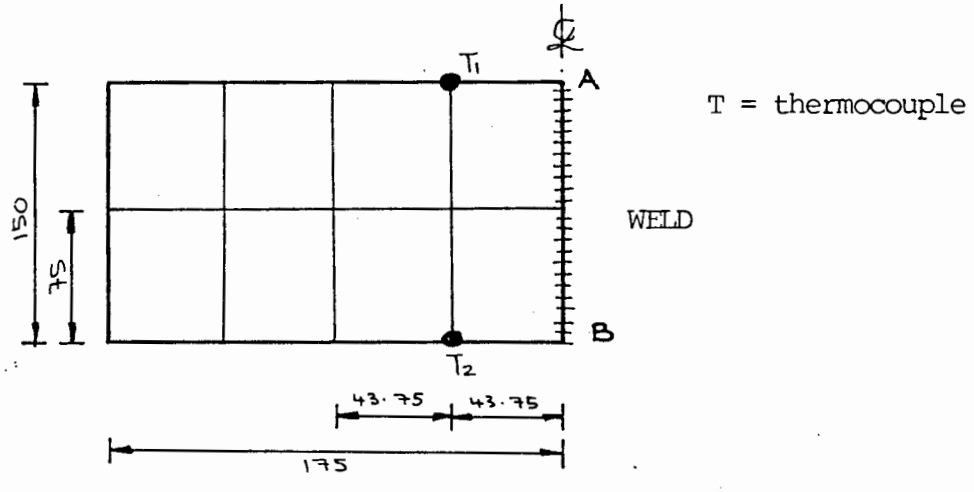

Fig 12.5 Positions of thermocouples for RUN 4

These thermocouples 1 and 2 were to correspond to the thermal response of nodes 9 and 13 of the finite-element mesh in Fig 12.1, respectively.
This experiment was also performed twice and again in both cases the output from the thermocouples agreed perfectly.

12.6.4 RESULTS OF WELDING EXPERIMENT

Each thermocouple yielded a temperature history with respect to time over the 120 second time period. These results are shown in Graph 12E and 12F.

12.6.5 COMPARISON BETWEEN HEAT DISTRIBUTION FROM ADINAT AND HEAT DISTRIBUTION FROM WELDING EXPERIMENT

Graphs 12G and 12H show the heat curves obtained from ADINAT and the welding experiment. The curves are plotted on the same system of axes and each graph has 3 curves: a linear ADINAT curve, a non-linear ADINA curve and an experimentally measured curve.

From the graphs we can see that the results predicted by ADINAT and by our welding experiment agree exceptionally well. In each case, the measured curve is smooth, exhibiting no evidence of the peculiar "hump" attributed to numerical instability in section 12.5. In the case of each of the four nodes under consideration, the non-linear model has a lower temperature value that the linear one. This is attributed to the fact that as the temperature increases, the thermal conductivity decreases, as shown in Fig 12.2. If we were to ignore the "humps" in the graphs for nodes 9 and 13 and join the points where the "humps" begin and end, a smooth curve would result which would compare even more favourably with the curve measured by experiment.

12.7 CONCLUSION

From the results obtained in Graphs 12G and 12H, it is concluded that the finite-element modelling using ADINAT approximates the actual thermal distribution in the plate very accurately. ie. so far, with only a minimum amount of knowledge of the weld being used, we have been able to predict what would happen in reality to an accurate degree. This correlation also verifies the fact that the heat input by the welding arc of temperature 1300°C does not travel through the plate at a rapid rate, but is conducted much slower that was expected before the welding experiments were attempted. A clue to this behavior of slow conduction was evident in Graph 11C of Chapter 11. In this graph, as the welding arc progresses along the weld line, it can be seen that hardly any heat generated by the extremely hot welding arc moves ahead of the arc. Examining the response of node 2 in Graph 11C shows that the thermocouple only

starts to feel the intense heat of the arc approximately 2 seconds before the arc is directly above it. This time-delay is approximately the same for both nodes 1 and 3. This implies that the heat spread from the arc is generated only backwards and sideways. (See Fig 12.6).

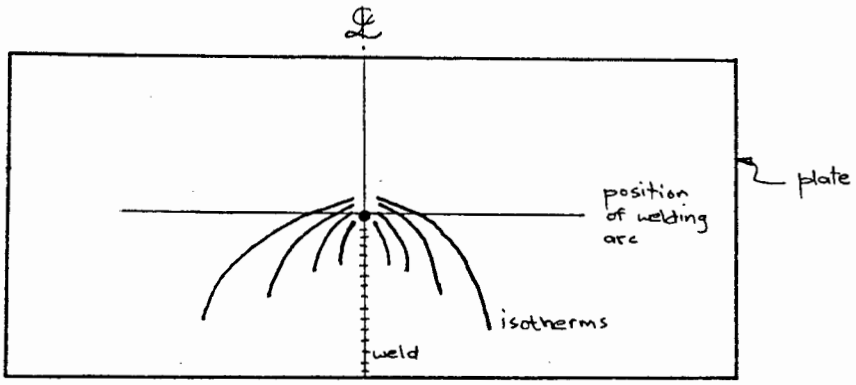

Fig 12.6 Schematic heat spread from arc

In final conclusion, as the curves predicted by ADINAT are an acceptably accurate approximation of the real thermal distribution through the plate, they can be discretised into the form of time functions and input into the program ADINA in order to predict the transient stress distribution throughout the plate.
This step will be performed in the following chapter.

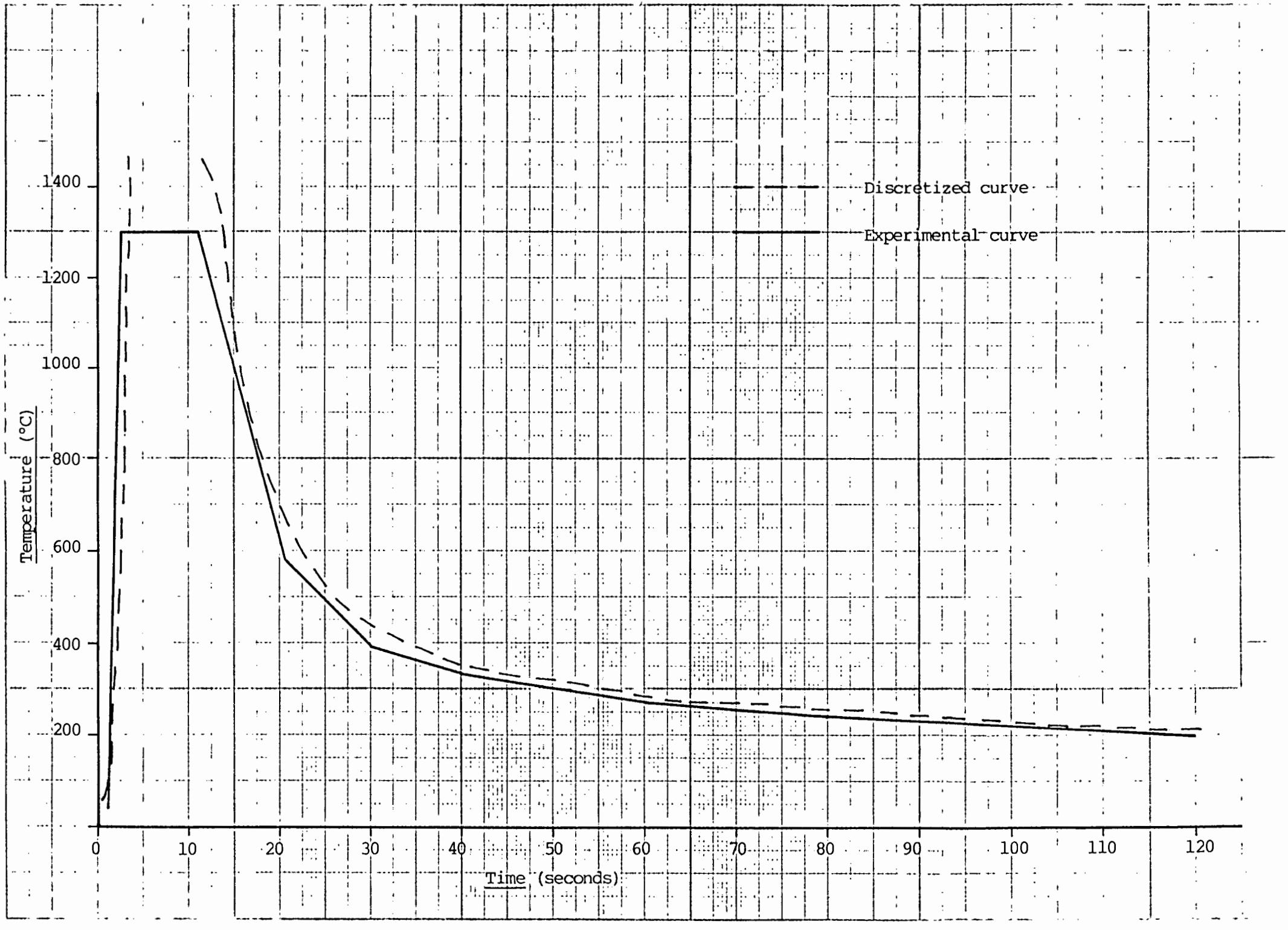

GRAPH 12A Discretized heat curve

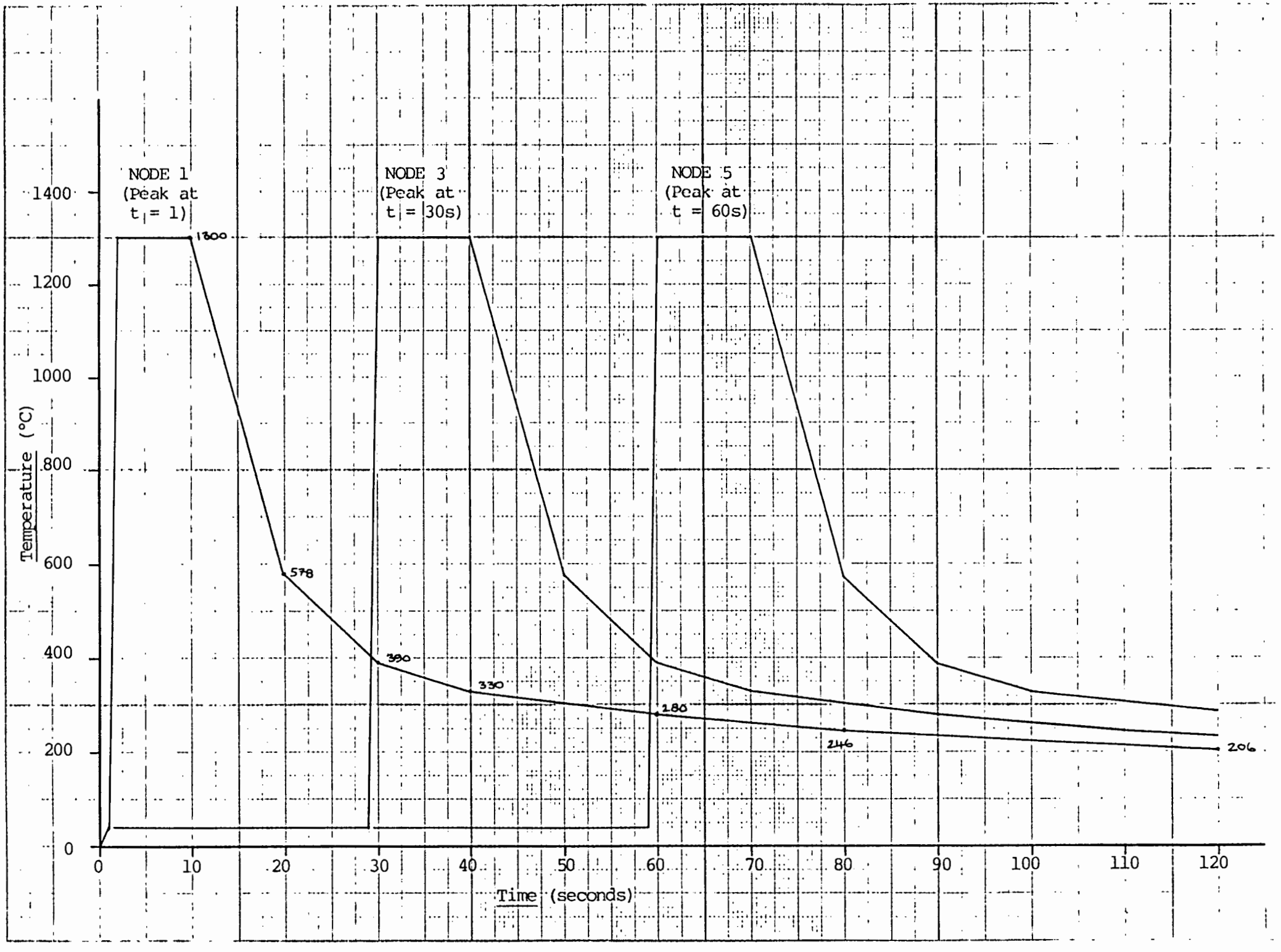

GRAPH 12R Standard heat curve arrival times

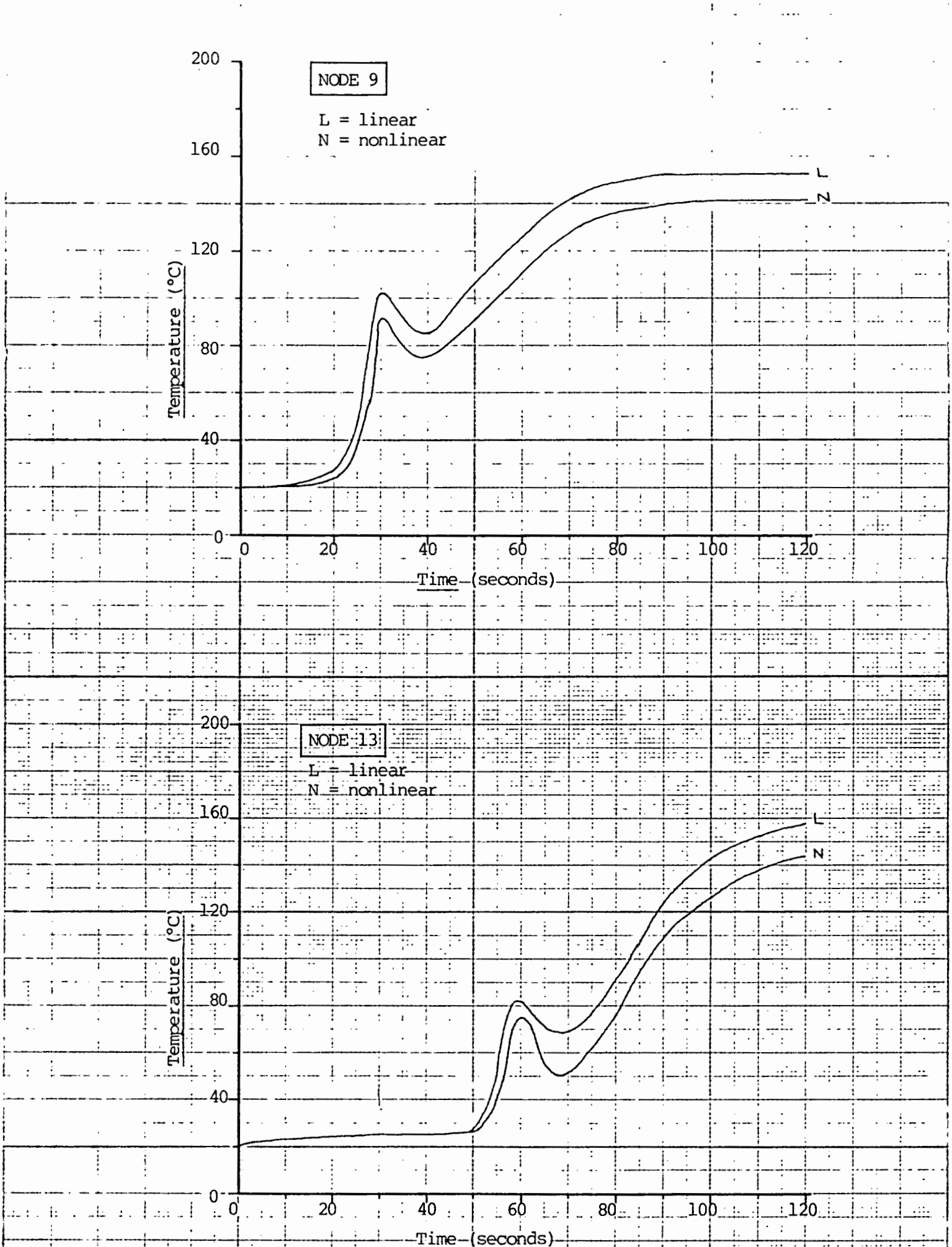

GRAPH 12C Output from ADINAT

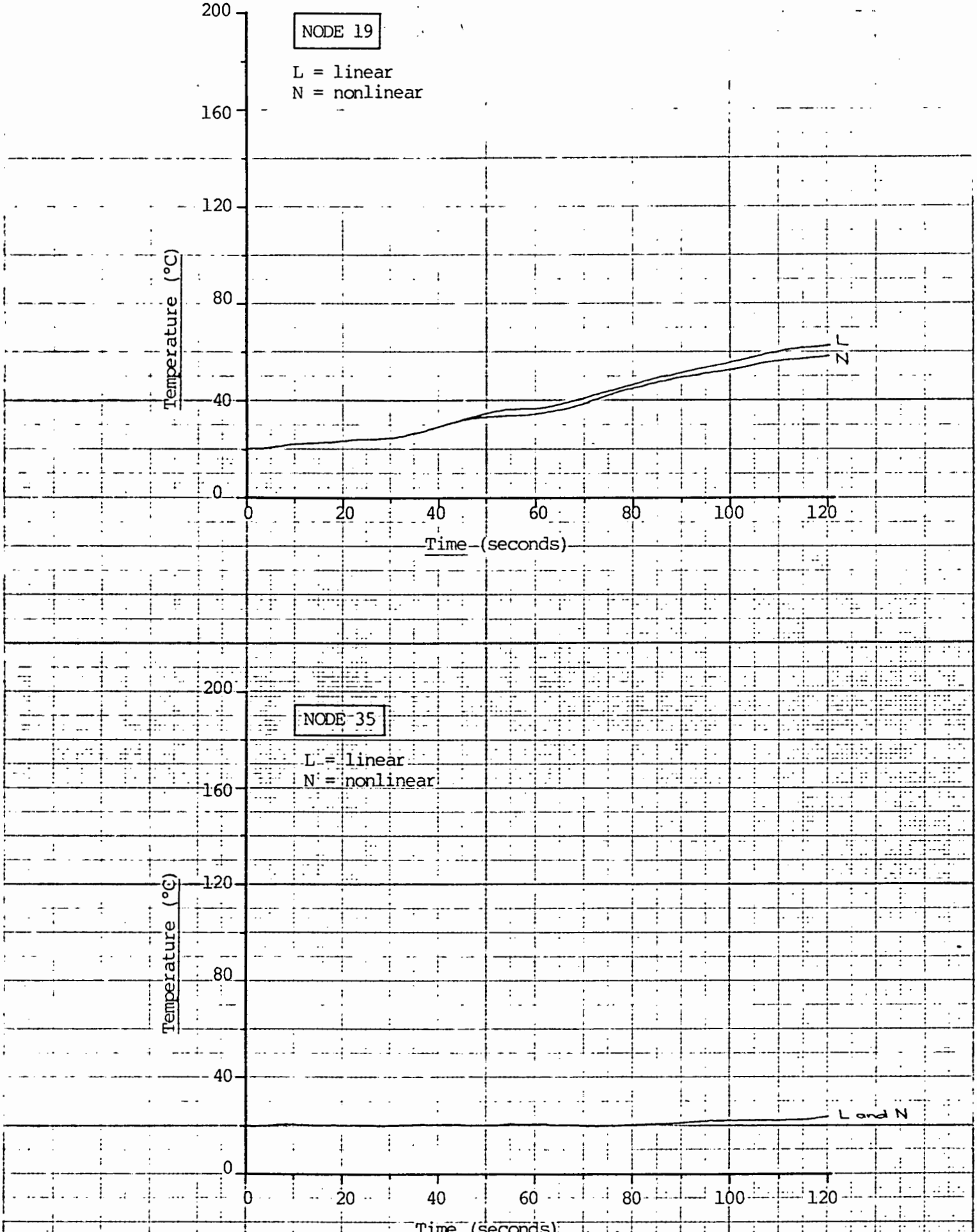

GRAPH 12D Output from ADINAT

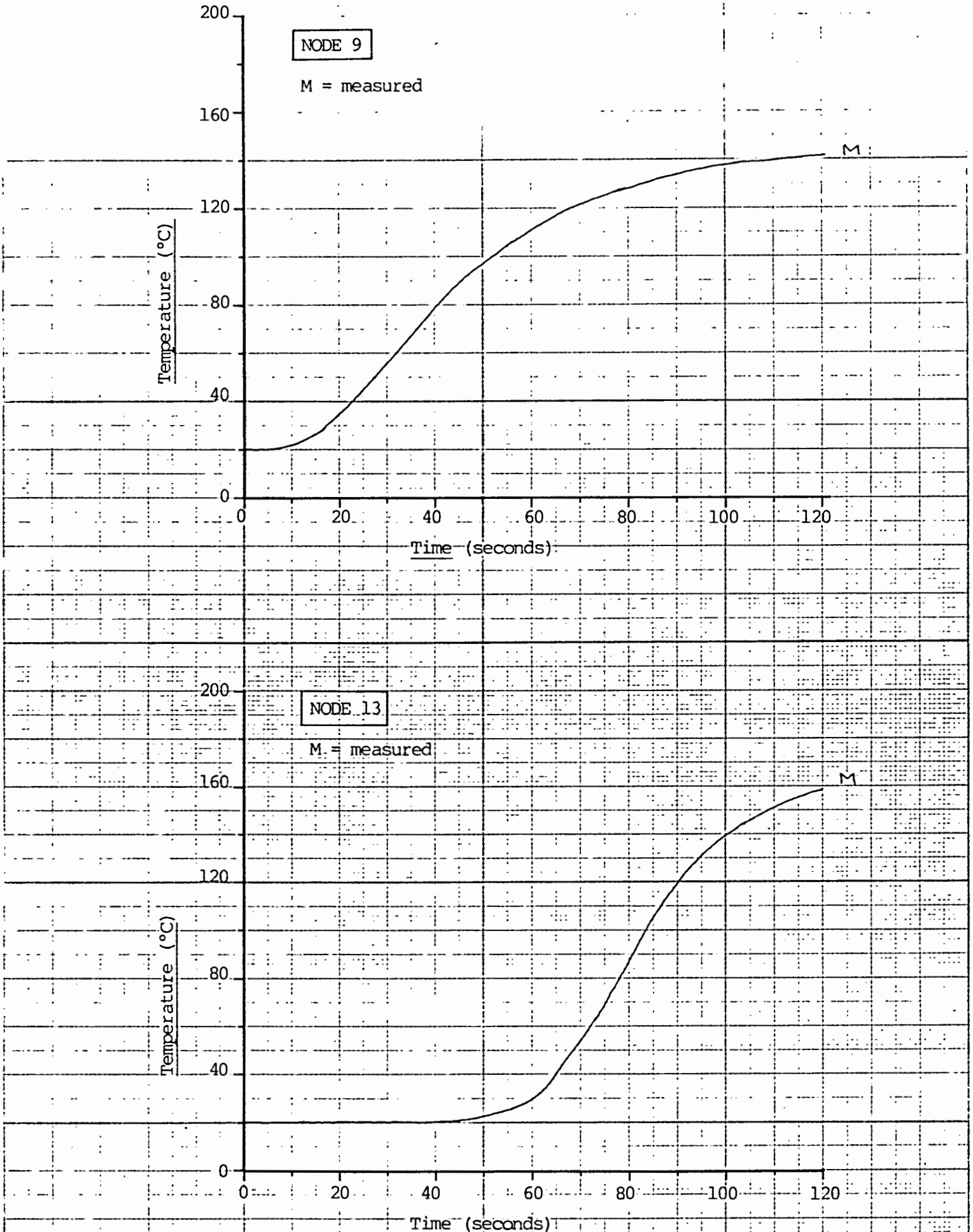

GRAPH 12E Output from welding experiment

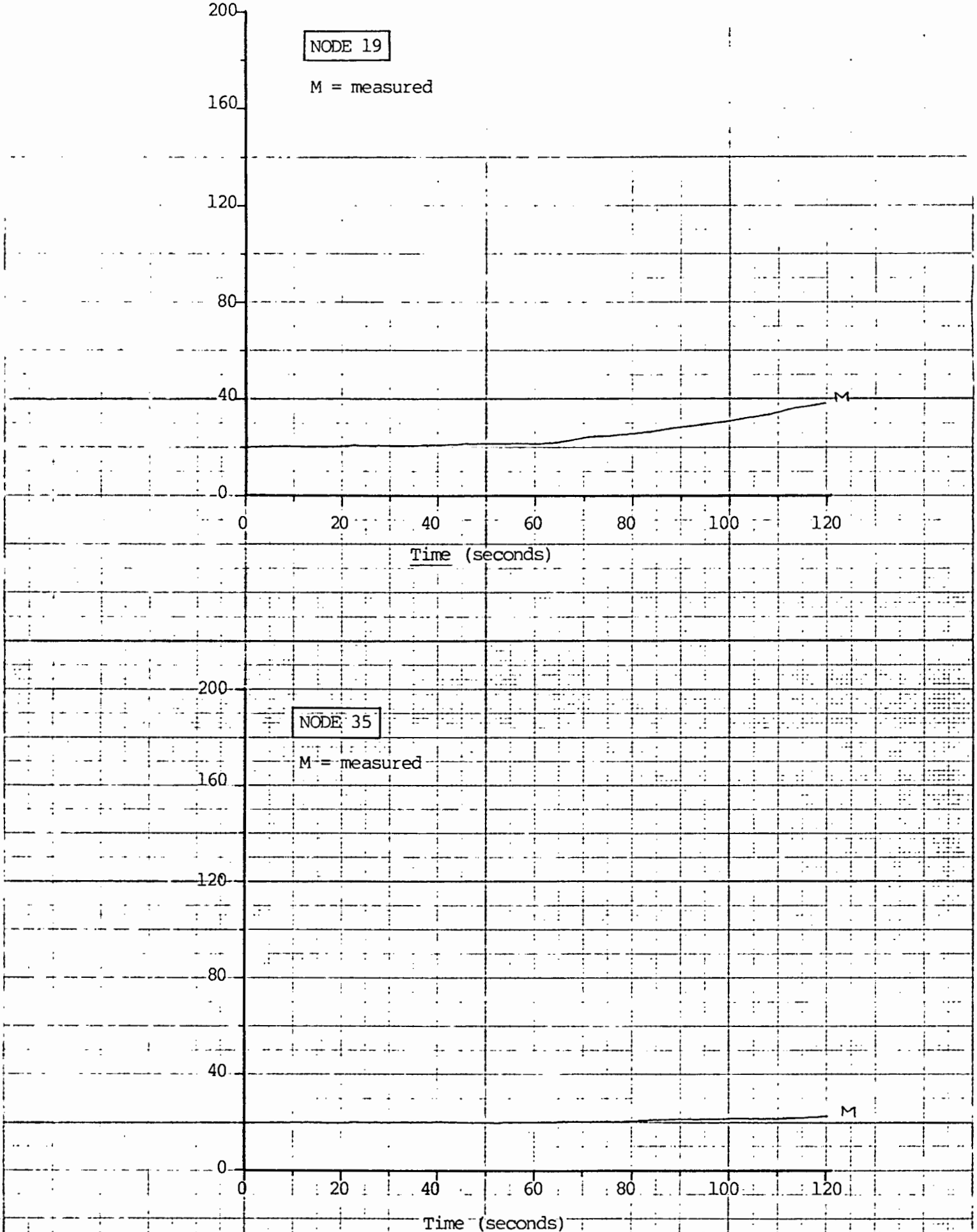

GRAPH 12 F Output from welding experiment

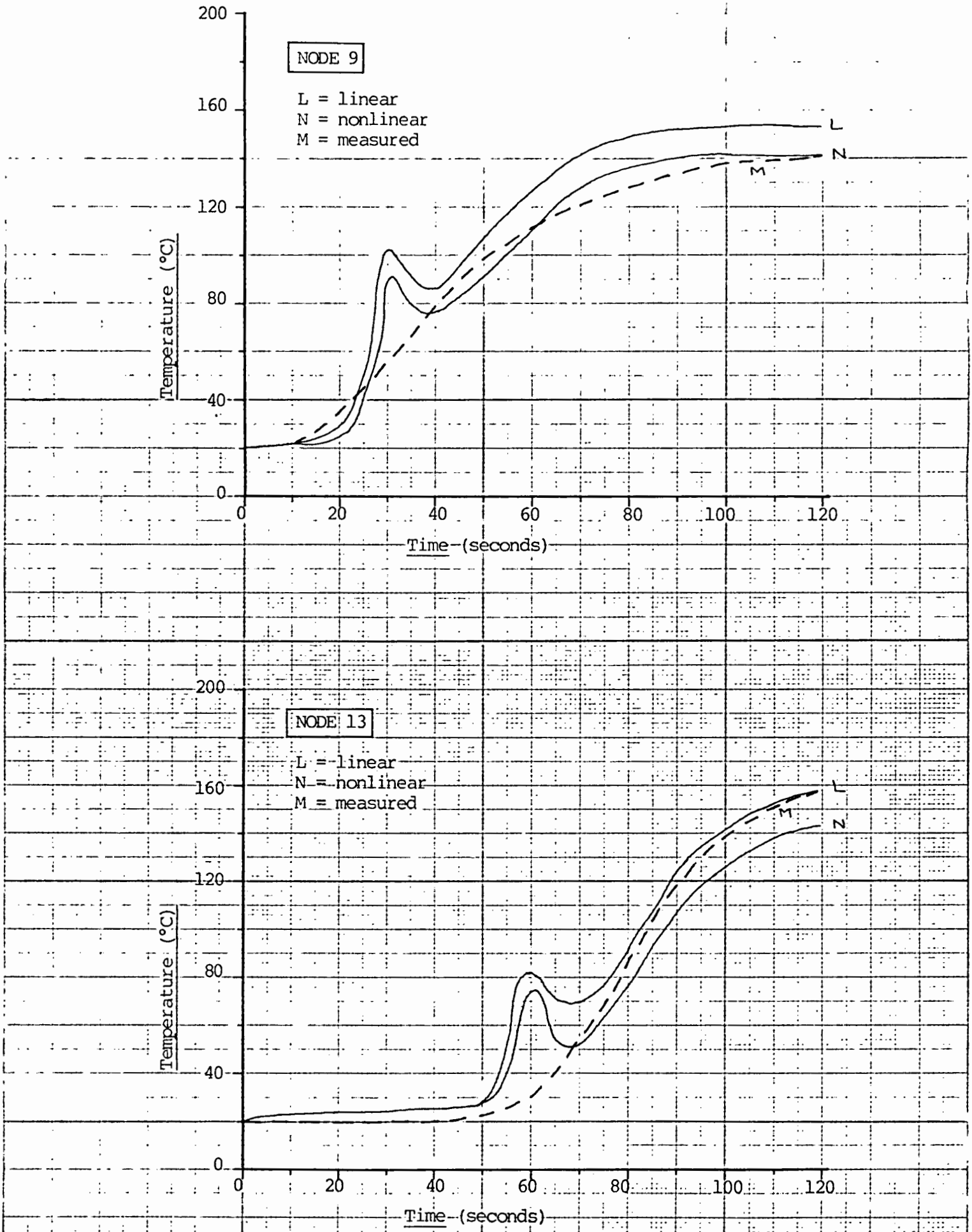

GRAPH 12G Comparison of heat curves

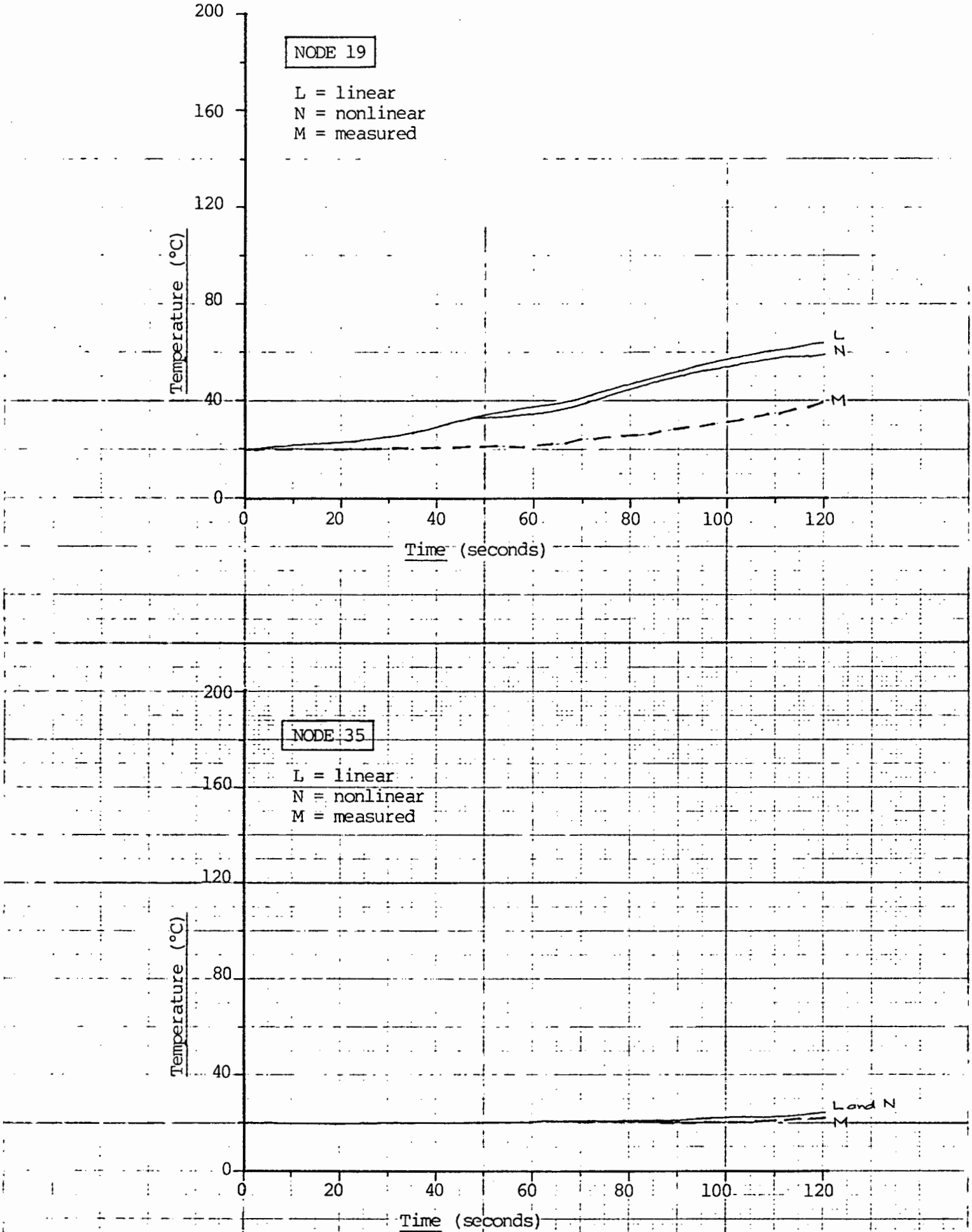

GRAPH 12H. Comparison of heat curves

CHAPTER THIRTEEN

EXPERIMENTAL AND COMPUTATIONAL INVESTIGATION INTO THE STRESS DISTRIBUTION OVER THE PLATE

13.1 INTRODUCTION TO STRESS MEASUREMENTS

As the stress in a material cannot be measured directly, it has to be calculated from other parameters which can be measured. Hence, measured strains along with other material properties are used to calculate the stress condition in a body. These strain measurement methods include mechanical, acoustic, optical and electrical methods [25]

If, as in Fig 13.1, an axial force is applied to a body, the body will elongate. This elongation is termed "strain" and is denoted by the symbol ε (See chapter 2).
This is the strain that would be measured by a strain gauge and is written in equation form as:

$$\varepsilon = \Delta L/L \qquad (13.1)$$

where ΔL = change in length
L = length

Since practical strain values are so small, they are often expressed as microstrain ($\mu\varepsilon$) which is $\varepsilon \times 10^6$

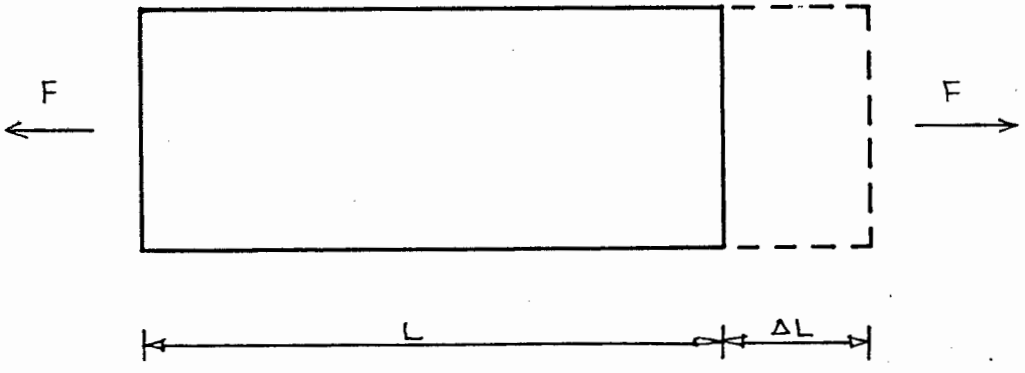

Fig 13.1 Strained body

If, as in Fig 13.2, a uniaxial force acts on a body and is uniformly distributed over a cross-sectional area A, then we have the equation

$$\sigma = F/A \qquad (13.2)$$

where σ = stress

F = force

A = cross-sectional area

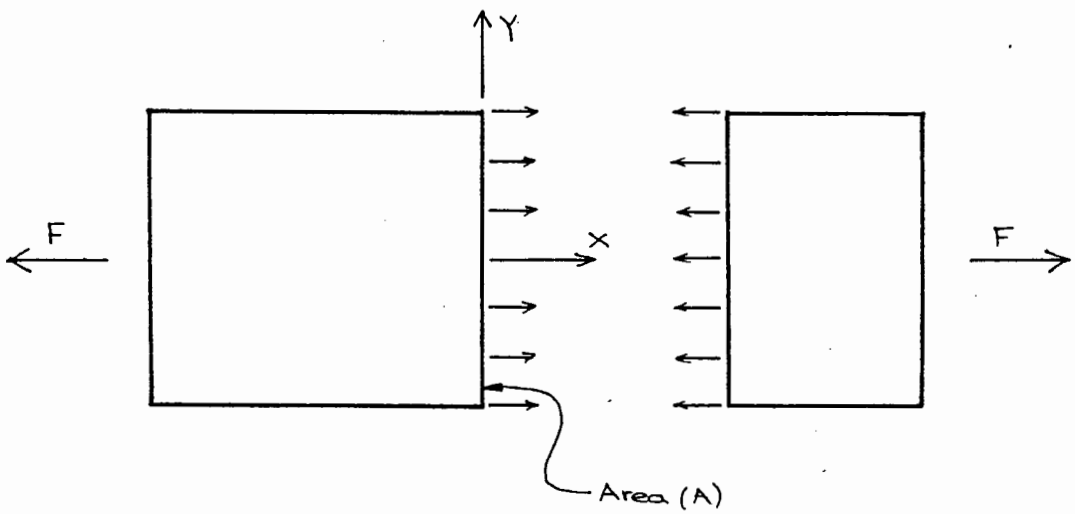

Fig 13.2 Stressed body

As in Chapter 2, stress and strain are related through Young's Modulus, E.

$$E = \sigma/\varepsilon \qquad (13.3)$$

13.2 CHOICE OF STRAIN MEASUREMENT DEVICE

A mechanical device, the Huggenberger tensometer, was considered but was disregarded as a continuous record of strain over the test interval could not be obtained. The gauge would have to be read continuously in the flashing light of a welding arc approximately 22mm away from the arc which was undesirable.

An optical method, the Moiré method, was investigated but rejected due to its delicacy and complexity.

The Brittle-coating method was investigated as well, whereby a brittle laquer would be applied to the test object and would crack

in the regions of highest strain. This investigation was discontinued as getting good data from this method was described as "as much art as science". [25]

This narrowed the choice down to electrical devices, the final choice being the bonded electrical resistance strain gauge.

13.3 THE BONDED ELECTRICAL RESISTANCE STRAIN GAUGE

13.3.1 Background

The principle upon which electrical resistance strain gauge measurement is based was discovered in 1856 by Lord Kelvin, who loaded iron and copper wires in tension, noting that their resistance increased with the strain applied to the wire. [26] In addition he also discovered that the iron wire showed a greater increase in resistance than the copper wire, even though they were both subjected to the same strain. As the final development, Kelvin used a Wheatstone bridge to measure the change in resistance and in this famous experiment, three vital facts emerged:

(1) The resistance of the wire changes as a function of strain.

(2) Different materials have different sensitivities.

(3) The Wheatstone bridge can be used to measure the resistance changes accurately.

Today, the bonded foil strain gauge monitored by a Wheatstone bridge is a highly accurate measuring system whereby precise results for surface strains are obtained using simple methods and inexpensive guages and instrumentation.

13.4 SUMMARY OF THE THEORY OF STRAIN MEASUREMENT USING ELETRICAL STRAIN GAUGES

13.4.1 Gauge Factor

When a conductor is strained, it will undergo a change in electrical resistance. The measure of this resistance change with strain is called the gauge factor, GF, defined as the ratio of the fractional change in resistance to the fractional change in length along the gauge axis. This factor is dimensionless.

$$GF = \frac{\Delta R/R}{\Delta L/L} = \frac{\Delta R/R}{\varepsilon} \qquad (13.4)$$

where ΔR = change in gauge resistance

R = gauge resistance

13.4.2 Wheatstone Bridge

Figure 13.3 shows the Wheatstone bridge circuit

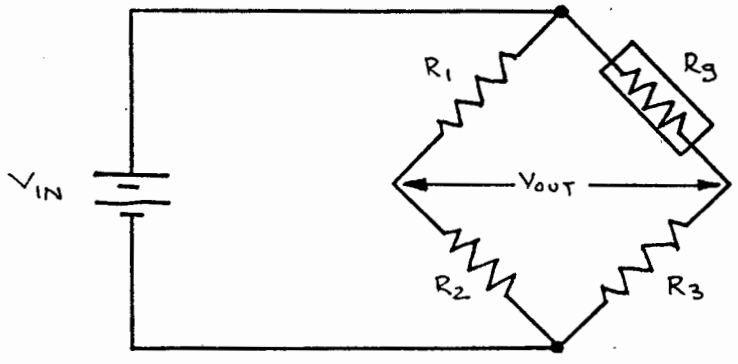

Fig 13.3 Wheatstone bridge circuit

V_{IN} is the input voltage to the bridge, R_g is the resistance of the strain gauges R_1, R_2, R_3 are the resistances of the bridge completion resistors.

V_{OUT} is the bridge output voltage.

The relationship between V_{IN}, R_1, R_2, R_3, R_g and V_{OUT} is:

$$\frac{V_{OUT}}{V_{IN}} = \left[\frac{R_3}{R_3+R_g} - \frac{R_2}{R_1+R_2} \right] \tag{13.5}$$

which holds for both the strained and unstrained condition.

By defining the unstrained value of the gauge resistance as R_g and the change due to strain as ΔR_g, the strained value of the gauge resistance is $(R_g + \Delta R_g)$.

Hence, we define a term Vr as the difference of the ratios of V_{OUT} to V_{IN} from the unstrained state to the strained state:

$$Vr = \left[\left(\frac{V_{OUT}}{V_{IN}} \right)_{\text{strained}} - \left(\frac{V_{OUT}}{V_{IN}} \right)_{\text{unstrained}} \right] \tag{13.6}$$

If we substitute the resistor values corresponding to the two (V_{OUT}/V_{IN}) terms into equation (13.6), we get an equation for $\Delta R_g/R_g$:

$$\frac{\Delta R_g}{R_g} = \frac{-4Vr}{1+2\,Vr} \tag{13.7}$$

13.4.3 Conversion from voltage to strain

If we recall equation (13.4), we have

$$GF = \frac{\Delta R_g/R_g}{\varepsilon} \tag{13.8}$$

and if we combine equation (13.8) with equation (13.7) we get an equation for strain in terms of Vr and GF:

$$\varepsilon = \frac{-4\,Vr}{GF(1+2Vr)} \tag{13.9}$$

In the case of equation (13.9) this is the strain equation for a "quarter-bridge" configuration ie. only one of the four branches of the bridge has a varying resistance.

In the case of a "half-bridge" configuration, the strain equation is as follows:

$$\varepsilon = \frac{-4\ Vr}{GF\left[(1+\nu) - 2\ Vr\ (\nu-1)\right]} \qquad (13.10)$$

Equation (13.10) was the one used in our experiment as in addition to the measuring gauge, a dummy gauge was also used in the Wheatstone bridge.

13.5 COMPUTATIONAL INVESTIGATION

13.5.1 Introduction

It is possible to link temperature analyses of ADINAT with the stress analyses of ADINA via a linking tape. This is described fully in the user manuals for each respective program under the section "MASTER CONTROL CARDS".
This link implies that if we perform a transient thermal analysis on a finite-element mesh, the output of this analysis would be stored on tape and automatically fed into the stress analysis program. This is highly desirable in a transient analysis involving many nodes and many timesteps.

Unfortunately, after many attempts, it was not possible to activate the linking tape due to an error in the source code of the University of Cape Town version of ADINA. This implied that if a large transient analysis were to be performed, the output from each timestep would have to be input manually into ADINA to yield the stresses at each timestep. This operation would have to be performed, in our case, at least 120 times, if 120 timesteps were to be used ie. we would need to perform 120 separate computer runs to obtain the stresses for 120 timesteps. This unfavourable state of affairs would be extremely time consuming

and tedious.

To counter this setback and to ensure the completion of this research, an alternative method was devised whereby the output for a particular node at each timestep could be plotted and a time-function constructed for that node in this way. Instead of a linking tape, each node would have its own time function for the duration of the experiment. This procedure is shown schematically in Fig 13.4

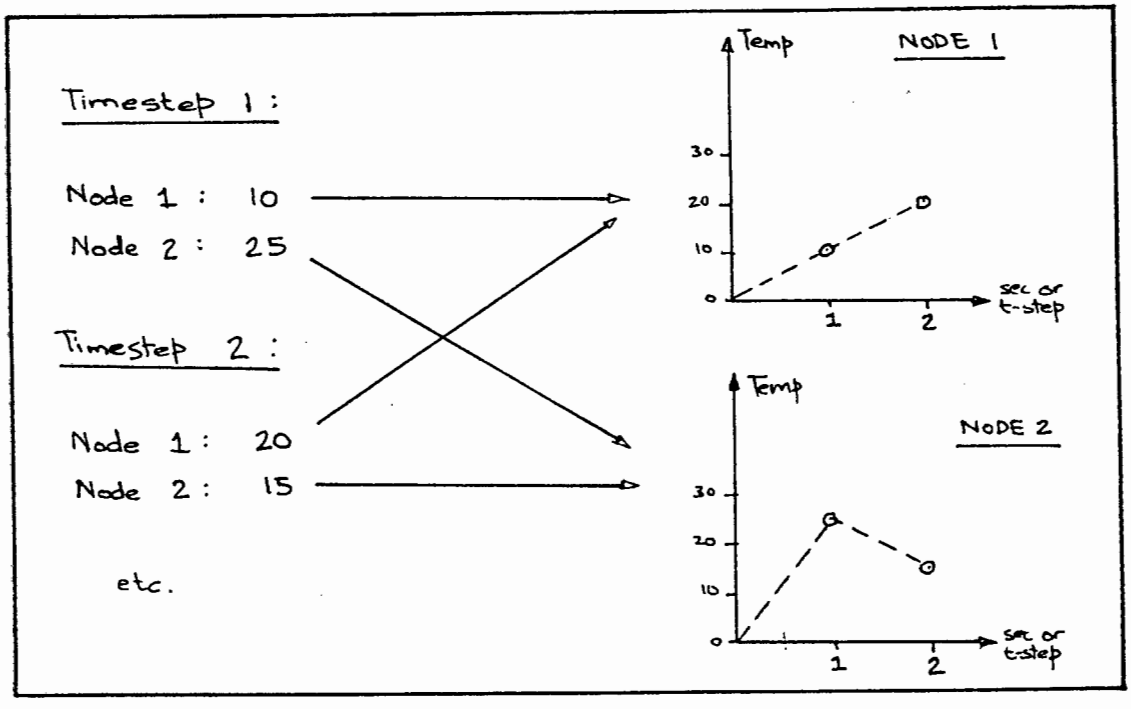

Fig 13.4 "Time-function method"

If these time functions are executed simultaneously, its effect would be identical to that obtained by using the values of timesteps 1, 2 and 3 each in three seperate analyses.

This "time-function method" was used in our analysis which involved 13 nodal points (hence 13 time-fuctions) and 120 timesteps of duration one second each. This would yield the stresses for all 120 timesteps in one single computer run. This method places a restriction on the number of nodes to be used, as the construction of time functions for too many nodes would also be very time consuming.

It is for this reason that only 13 nodes were chosen from ADINAT, hence only 13 time functions.

13.5.2 ADINA model

As in chapter 12, the curves obtained from the ADINAT temperature analysis for the 13 nodes of our finite-element mesh had to be linearly discretised in order to be input as time functions into ADINA (See Appendix D). The curves used were the ones obtained from the nonlinear analysis.

Two non-linear eight-noded two dimensional solid isoparametric elements were used to model half of our plate, having identical dimensions as the plate used in chapter 12. Fig 13.5 shows this mesh.

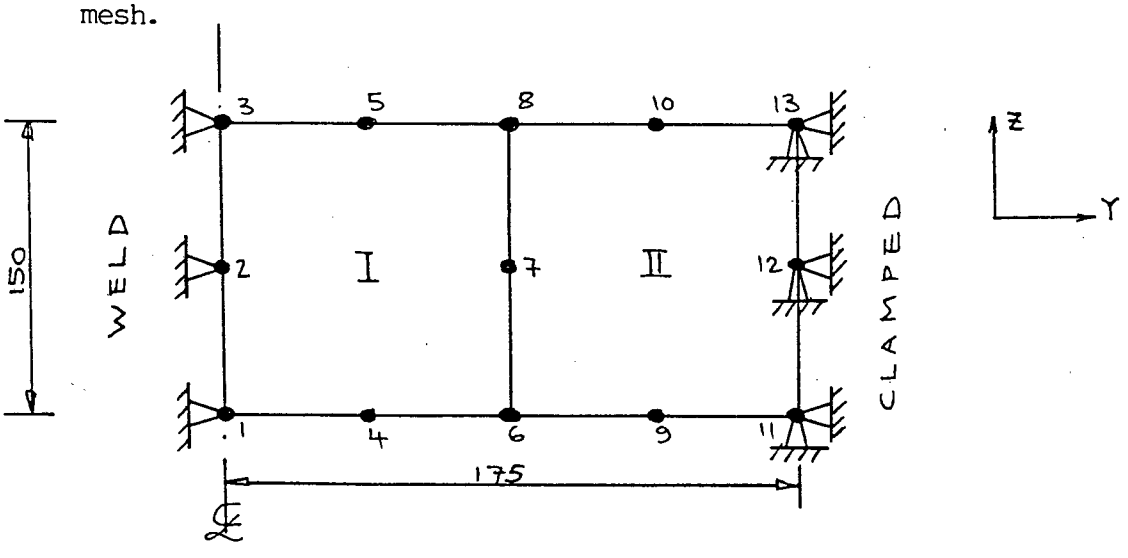

Fig 13.5 ADINA mesh representing half of plate

Nodes 1, 2 and 3, lying on the weld line, were restrained against moving in the Y-direction as they lay on the centre-line of the plate. Nodes 11, 12 and 13 were restrained against moving in both the Y and Z direction as in the experiment being modelled, this edge was fully clamped (welded onto another piece of metal). The experiment will be described later in more detail.
The remaining nodes were free to displace in both the Y and Z directions. As mentioned previously, 13 time-functions were input, one for each node. The initial condition of the plate was that at the start of the analysis, the temperature at each point on the

plate was 20°C (room temperature). The material model used was the thermo-elastic-plastic, von Mises yield condition with isotropic hardening model ("Model 10"). The numerical integration order to be used in the Gauss quadrature formulae was chosen as 2, yielding four Gauss point stresses per element, as shown in Fig 13.6

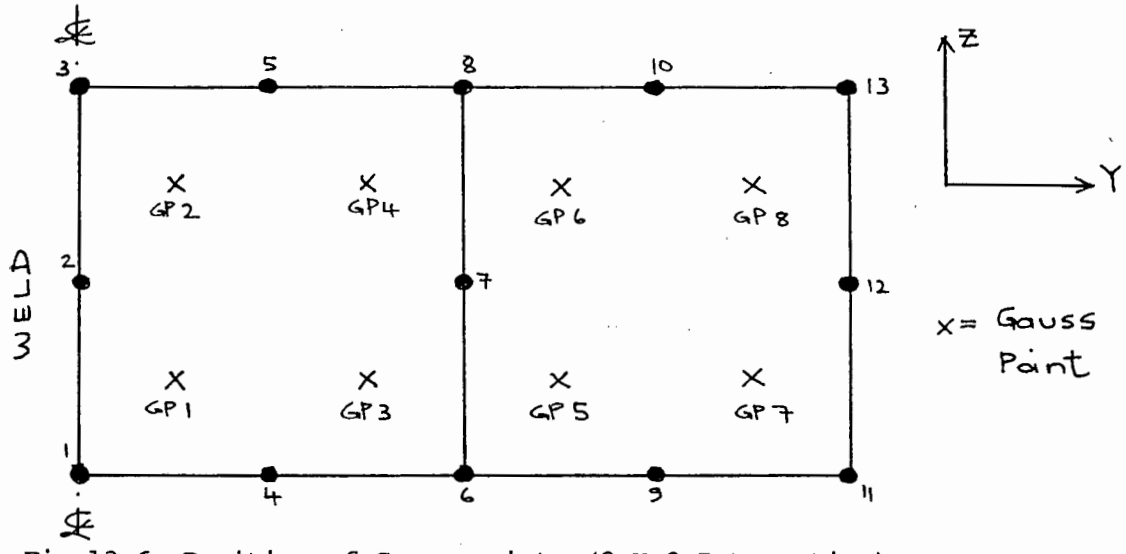

Fig 13.6 Position of Gauss points (2 X 2 Integration)

In the material model used, the changes in the material constants with respect to temperature are shown in Table 13.1

Temperature (°C)	E(MPa)	ν	σ_y(MPa)	E_T	α
-500	$.21 \times 10^6$	.3	$.25 \times 10^3$	0	$.11 \times 10^{-4}$
20	$.21 \times 10^6$	.3	$.25 \times 10^3$	0	$.11 \times 10^{-4}$
600	$.154 \times 10^6$	.3	$.86 \times 10^2$	0	$.11 \times 10^{-4}$
1310	$.154 \times 10^6$	.3	$.86 \times 10^2$	0	$.11 \times 10^{-4}$

TABLE 13.1 Material Property Changes

Most references [28, 29] gave a variation of properties over the range of temperature 20°C to 600°C. To cater for numerical instabilities in the finite-element method (as encountered previously), the lowest temperature considered was -500°C but the properties at this temperature were assumed to be identical to those at 20°C. In effect, this fixed 20°C as the lowest possible

temperature, which is what we defined initially. The same procedure was assumed for the highest temperature of 1310°C whose properties were assumed identical to those at 600°C.

The creep law was ignored as no loading was being applied in addition to the thermal load.

13.5.3 Results from ADINA

It was decided only to consider stresses perpendicular to the weld ie. in the Y-Y direction. Also, only 4 Gauss points were investigated. These were GP1, GP2, GP7 and GP8 as shown in Fig 13.6 The output from this computer run is shown in Graph 13A and is tabulated in Appendix D.

Examining Graph 13A, it is first noticed that the output for Gauss points 2 and 8 are identical. The same applies to Gauss points 1 and 7. This does not appear logical as these Gauss point pairs are far from each other on test plate (See Fig 13.6), where GP1 and 2 are situated adjacent to the weld whereas GP7 and 8 are furthest from the weld. Identical behavior is hence not expected. Inspection of the Gauss point temperatures revealed high negative temperatures of the order of 190°C as output by ADINA. Clearly this is impossible as the lowest temperature input on any time function was 20°C. In addition, a tensile stress of about 280 MPa was not expected, even at GP1.

A logical expectation for GP1 was for it to go into compression immediately after welding had commenced, even though this would only occur very briefly. Cooling would then occur causing contraction of the weld, forcing GP1 into tension.
During this time, the backing material would be heating up and expanding, which could then cause GP1 to go back into compression. Finally, cooling would occur with the possibility of yet another cycle which would reduce the compressive stresses. (See Chapter 2)

This above behavior did not occur for GP1 in this analysis. (See Graph 13A) Because of this, it was decided to investigate the stressed behavior of the plate experimentally.

13.6 EXPERIMENTAL VERIFICATION OF THE STRESS DISTRIBUTION THROUGH THE PLATE

13.6.1 Experimental set-up

An arc-welded bead was again laid on a mild-steel plate 12mm thick, 145mm wide and 350mm long, as in Chapter 11. The weld electrode used was the E6013 Vitemax type with a diameter of 4mm. The arc current used was 170A and the desired arc travel speed was 150mm/min. Fig 13.7 shows the complete experimental set-up.

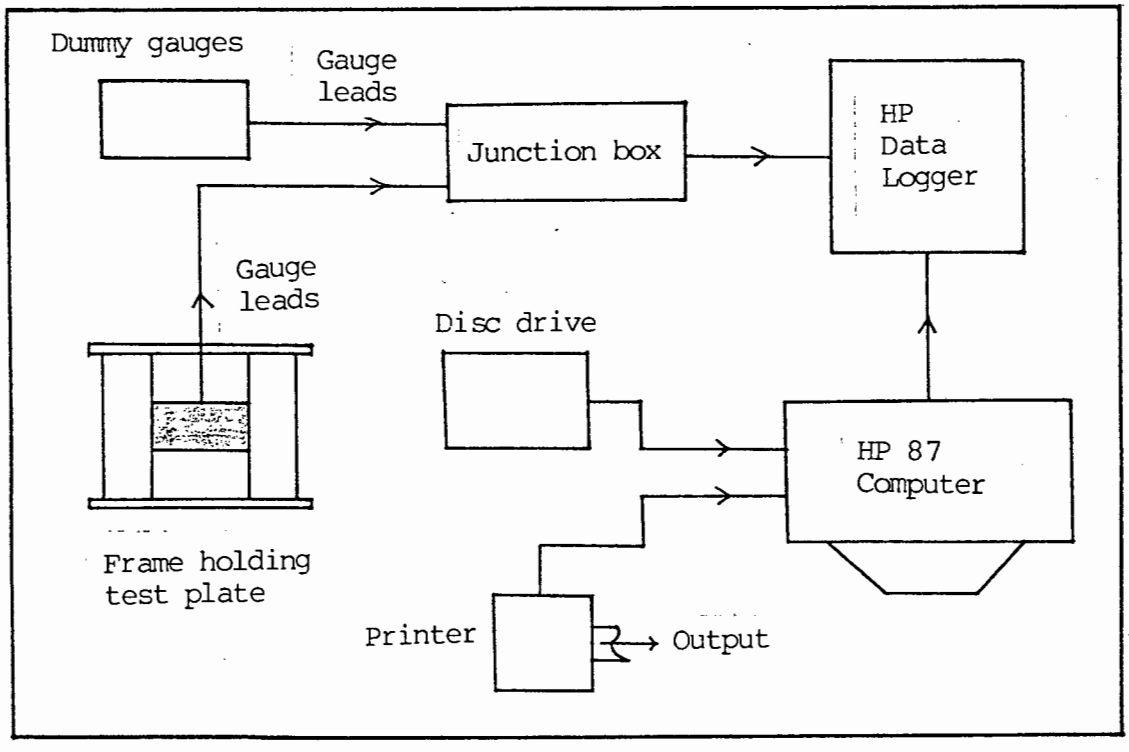

Fig 13.7 Experimental set-up

Two additional plates 270 x 150 x 12mm were welded to the ends of our test plate to approximate the fully clamped edge boundary condition and these two plates were in turn welded to two thick plates 680 x 150 x 40mm. This provided a rigid frame effecting the boundary conditions. This frame is shown in Fig 13.8.

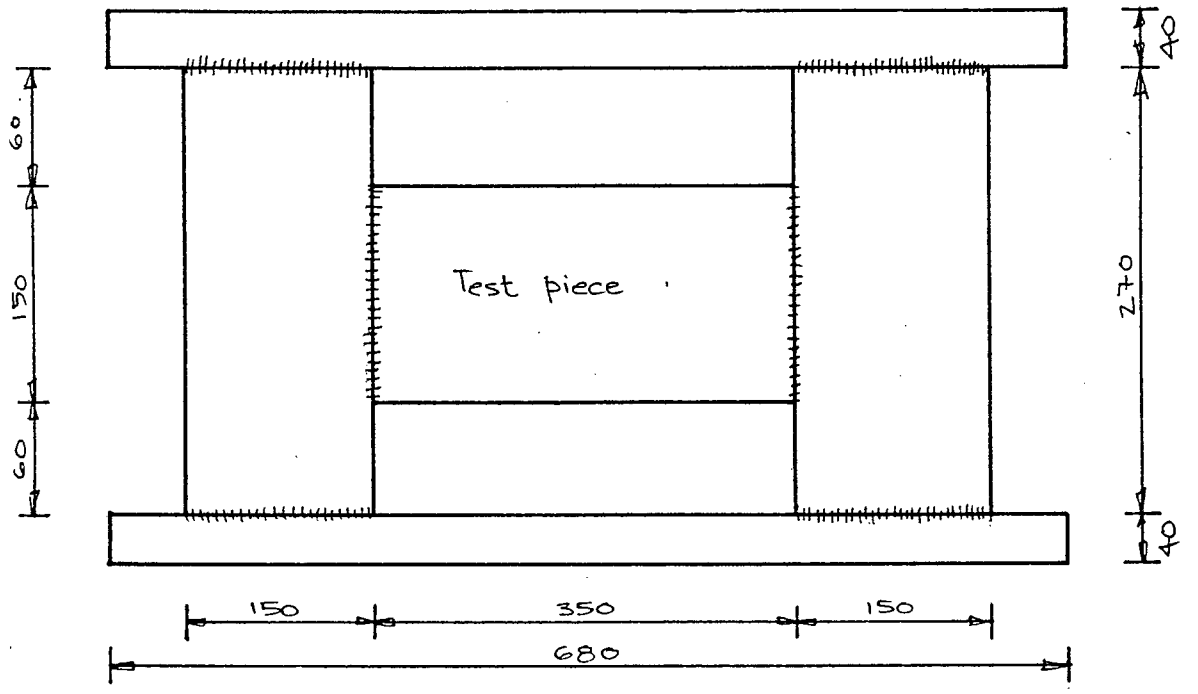

Fig 13.8 Frame to hold test plate

This frame was deemed acceptable, as it was discovered in Chapter 12 that during the 120 second welding time, the ends of the test plate remained cold. This ensured that no heat would be lost into the frame. Detailed sketches of this frame can be found in Appendix D.

In order to measure the strains due to the welding process, 4 special high temperature foil strain gauges were bonded to the test plate at specific Gauss points (See Fig 13.9).

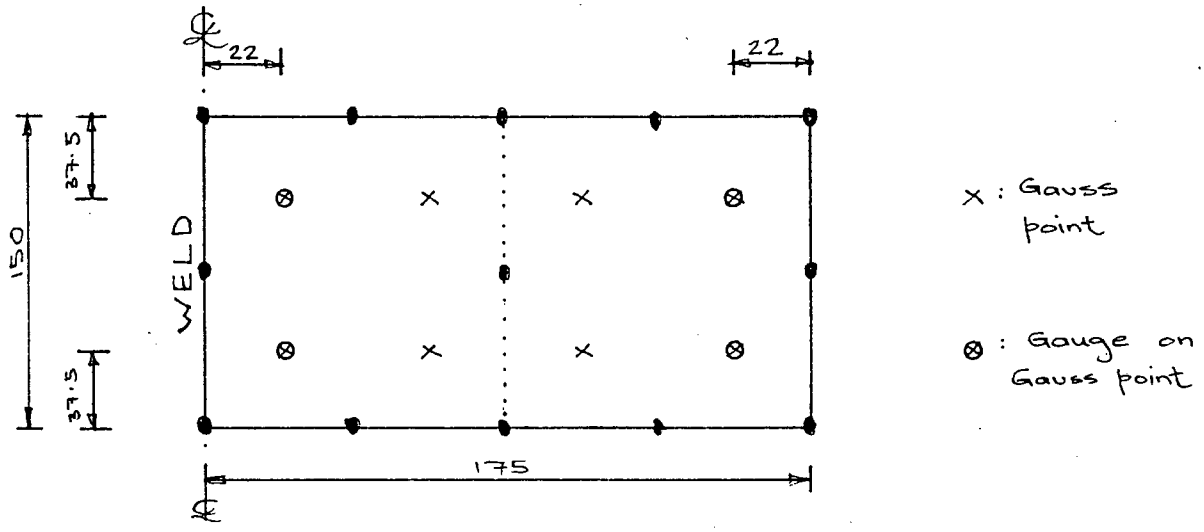

Fig 13.9 Position of Gauges

The gauges used were Kyowa Type KFA-5-C1-(11,16) with a silicone bonding adhesive SC-22. The adhesive curing process entailed heating the gauge on the metal using the following modified manufacturers recommendations:

1 hr at 80°C
2 hrs at 130°C
5 hrs at 200°C

An additional 4 gauges were bonded to a similar loose piece of plate, following the same curing process The gauges on this additional plate acted as dummy gauges, essential to the Wheatstone bridge theory. (See Chapter 13.4.3).

As the wires on the strain gauge were extremely fragile, copper lead wires could not be soldered directly onto them. The strain gauge-copper lead joint was effected using small terminals, bonded to the metal plate. This is shown in Fig 13.10

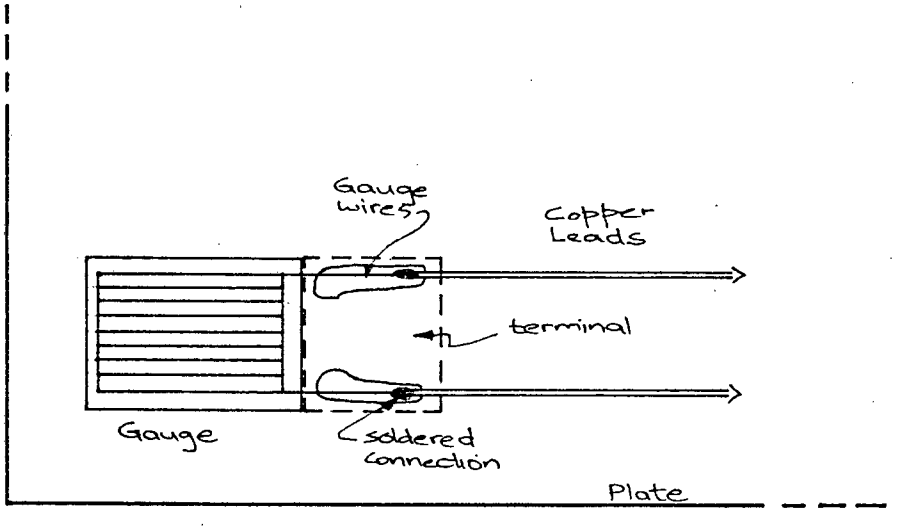

Fig 13.10 Copper lead connection

Small jack plugs were connected to the other ends of all the copper leads. All these leads met at a single junction box which was connected to the Strain Gauge Card in the Hewlett-Packard Data Logger. This data logger was driven by an HP87 computer using software written for it by A. Lloyd [27]. This software

provided the strain records for each of the 4 strain gauges on the test plate.

As mentioned before, in Chapter 13.5.3, the gauges were aligned with the Y-Y axis as we were only interested in the stresses in this direction. The experiment was run for 20 scans, taking 4 strain readings per scan. The time lapse between consecutive scans was approximately 10 seconds, hence any sudden changes in stress during this time lapse could not be monitored.

13.6.2 Results of the experiment

The output from the Data Logger for the stress at the Gauss points is shown in Graph 13B and is tabulated in Appendix D.

Examination of Graph 13B shows four distinctly seperate graphs of the stress at each of the Gauss points.

13.6.2.1 Gauss Point 1, (GP1)

In the case of GP1 in Graph 13B, it appears that the stress is tensile immediately as the experiment is initiated. This tensile stress increases with time and peaks at about 140 MPa at t = 60 sec. This is the time at which the heat source is removed from the plate. From this point, the tensile stress decreases steadily. After t = 120 sec, the stress has reduced to about 120 MPa. Although the experiment ends at this time t = 120 sec it was decided to let the logger scan for a full 1403 seconds (23 minutes) to enable a steady-state stress to be recorded. In the case of GP1, the stress reduced from 120 MPa at t = 120 sec to a steady-state stress of about 42 MPa after 23 minutes.

The tensile behavior of this Gauss Point did not follow our logical expectation, that is, to go initially into compression for a brief period before becoming tensile. An explaination for GP1 in Graph 13B showing an initial tension could be the fact that the strain gauges were only scanned every ten seconds by the data logging program. This time limit is built into the data logger

scanning program [27] and could not be altered. This implied that if any inital brief compressive stress at GP1 had actually occured, it would not have been detected during the first scan.

Further discussion of the following Gauss points assumes non-detection of the initial brief compressive phase.

13.6.2.2 Gauss Point 2, (GP2)

Graph 13B shows the behavior of GP2 to be similar in shape to that of GP1, shifted by about 30 seconds on the time scale. Initially GP2 shows a small compressive stress of about -2 MPa for the first 30 seconds. Between t = 30 and t = 45 seconds, a small anomaly is recorded, peaking at t = 40 seconds with a compressive stress of 7 MPa. After t = 45 seconds, the stress graph of GP2 becomes tensile and peaks at t = 110 seconds with a tensile stress of about 140 MPa. As for GP1, GP2 decreases to a steady-state stress of 52 MPa after 23 minutes.

As the heat flows into the plate at the start of the weld, tension occurs in the backing material, as mentioned in 13.6.2.1. At GP2, situated near the other edge of the plate, compression will occur, to resist the initial tension in the area of GP1 which is flowing outward. As the weld approaches GP2, this compression will reach a maximum value before becoming tensile as the area containing GP2 becomes the "backing material". Hence, as the weld approaches closely to GP2 (t = 45 seconds), we have the same situation as when the welding experiment began, approaching GP1 at t = 0 seconds. This is also evident from Graph 13B.

13.6.2.3 Gauss Point 7 (GP7)

The circumstances surrounding GP7 are similar to those of GP2, with an initial compressive stress resulting for the same reasons as those for GP2. This compressive stress resists the tensile stresses from GP1. After t = 40 seconds, the stress at GP7 becomes tensile, even though only 19 MPa for the duration of the

experiment. This stress increases steadily to a steady-state stress of 32 MPa after 23 minutes.

13.6.2.4 Gauss Point 8, (GP8)

In order to balance the initial stresses set-up in the plate, with GP2 and GP7 being compressive initially, we would expect GP8 to be initially tensile. This is indeed the case as shown in Graph 13B. This tensile stress increases to 19 MPa at t = 50 seconds, reduces slightly to about 13 MPa for the duration of the experiment and increases to a steady-state stress of 36 MPa.

In the cases of GP7 and GP8, the stresses for the duration of all the experiment are much lower than the stresses at GP1 and GP2. This is due to GP7 and GP8 being significantly remote from the weld, whose heat only reaches the outer Gauss points at a late stage.

Also of interest are the steady-state stresses for each Gauss point. After 23 minutes, the stress at each Gauss point is constant at a value between 32 MPa and 52 MPa.

The high stresses of GP1 and GP2 reduce to values in this range, whereas the low stresses of GP7 and GP8 increase to values in the abovementioned range. Taking an average value of 42 MPa, this implies that after 23 minutes, the entire plate is in a state of tensile stress of magnitude 42 MPa. This stress is hence locked into the plate at room temperature.

Fig 13.11 shows the stress setup in the plate during the cooling of the weld.

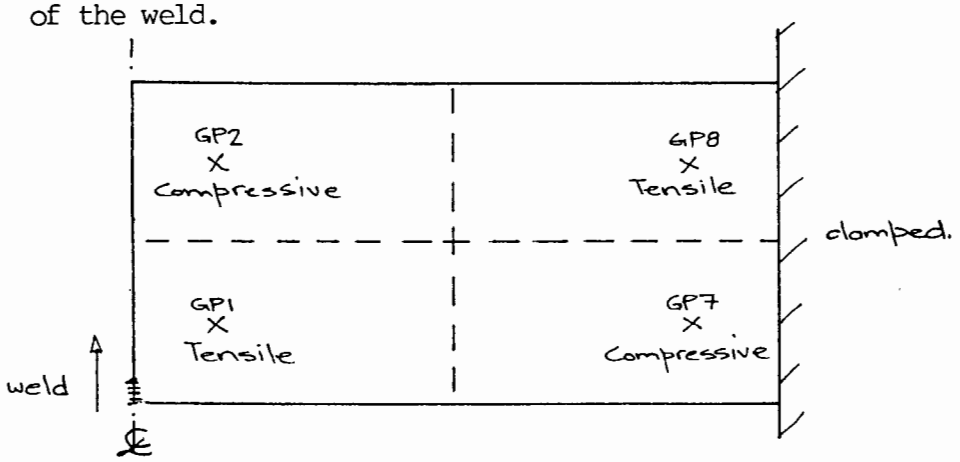

Fig 13.11 Stresses setup during cooling

Fig 13.11 shows that as cooling of the weld occurs causing a tensile stress at GP1, GP2 and GP7 are put into compression with GP8 being forced into tension. The total effect of this set-up can be interpreted as an attempted anticlockwise rotation about the centre of the plate.

After the initial compression at GP1, we could treat the initial cooling action there as a force, F. This is shown in Fig 13.12.
As the heat reduces at the weld, contraction occurs causing tension at GP1. In addition, heat is flowing into the backing material causing it to expand. GP1 is therefore undergoing tension.

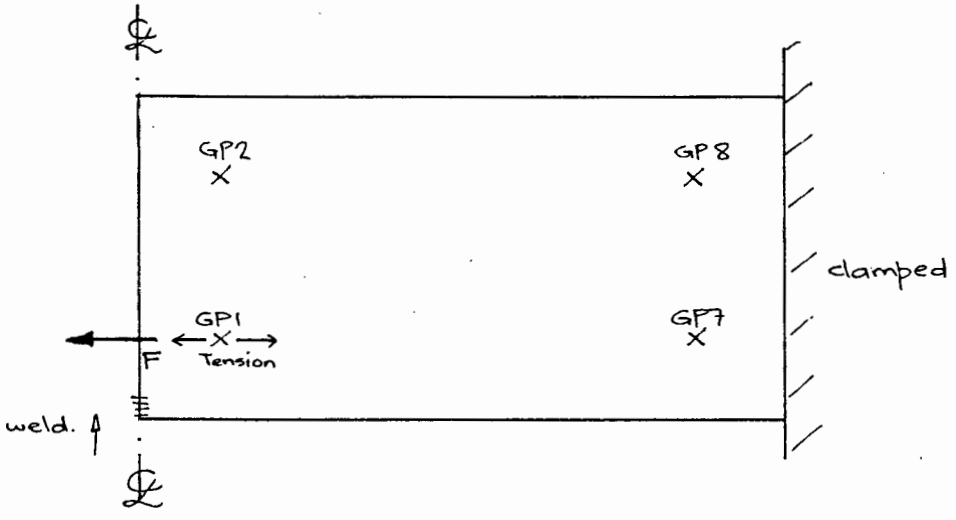

Fig 13.12 Force implication

This force F would indeed cause compression at GP7 and GP2 with tension occuring at GP8. This agrees with our previously made deductions.

We can hence conclude that the experimental stresses obtained and described in section 13.6 are reasonable and can be explained logically. This is not the case with the stresses obtained from ADINA. In order to improve what was thought to be a sufficiently accurate finite-element model, it was decided to increase the number of elements in our mesh, providing a finer mesh and hence a more accurate model.

13.7 REINVESTIGATION INTO ADINA STRESSES

Fig 13.13 shows the mesh used in this analysis.

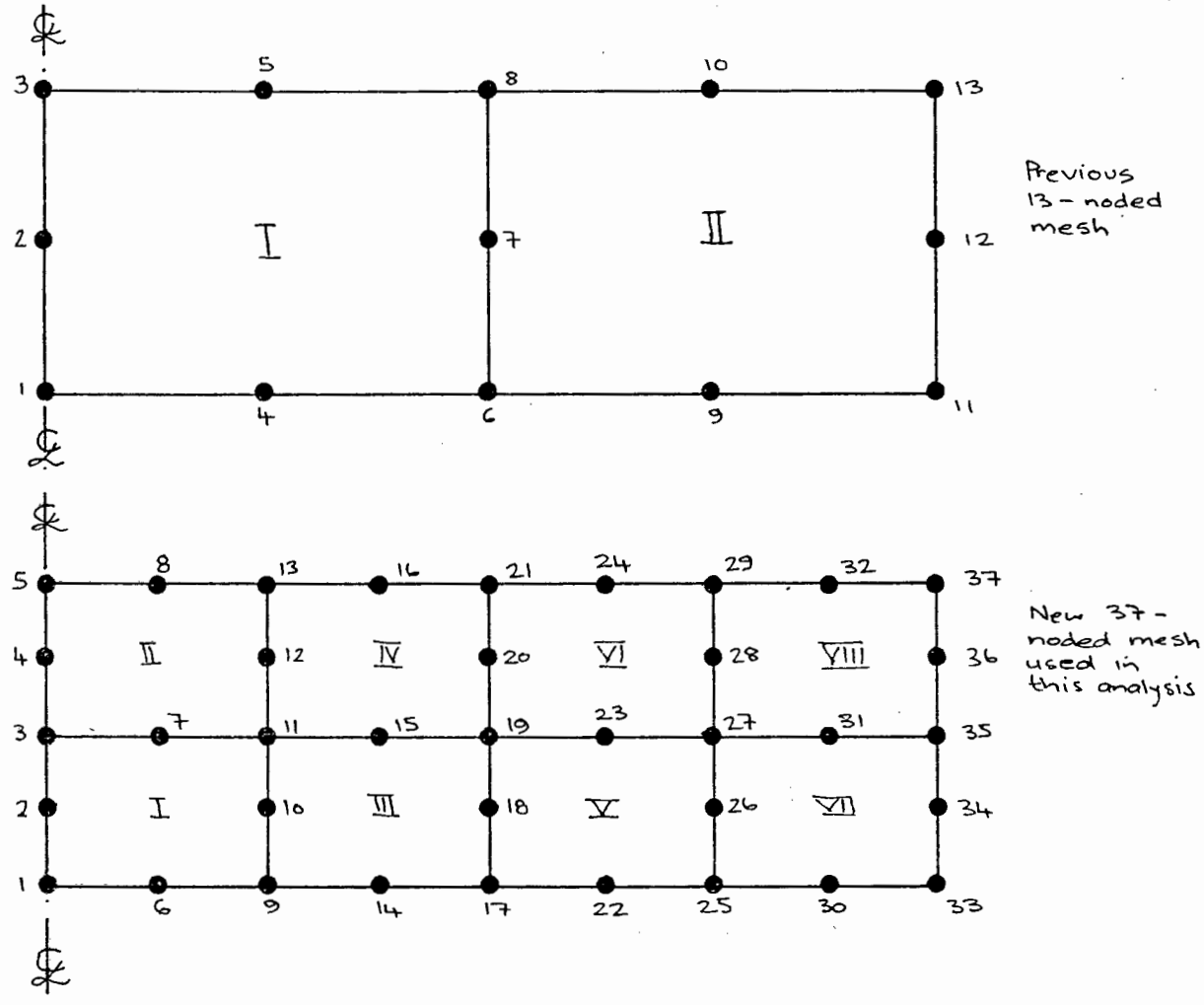

Fig 13.13 Comparison of finite-element meshes

In this model, 37 curves obtained from a transient ADINAT run had to be discretized and input to ADINA in the form of 37 time functions. Eight non-linear eight-noded two dimensional solid isoparametric elements were used in this analysis. The dimensions and boundary conditions remained as for the 13-noded analysis. In this case, as there were two elements now across the width of the plate, more nodes lay along the weld line and clamped edge lines. Nodes 1, 2, 3, 4 and 5 lay along the weld line whereas nodes 33, 34, 35, 36 and 37 lay along the clamped edge line. The material model used was "Model 10", as before. The numerical integration order used in

the Gauss quadrature formulae was upgraded to 3, in order to coincide Gauss points exactly where they had been in the previous 13-noded analysis. The Gauss points are shown in Fig 13.14.

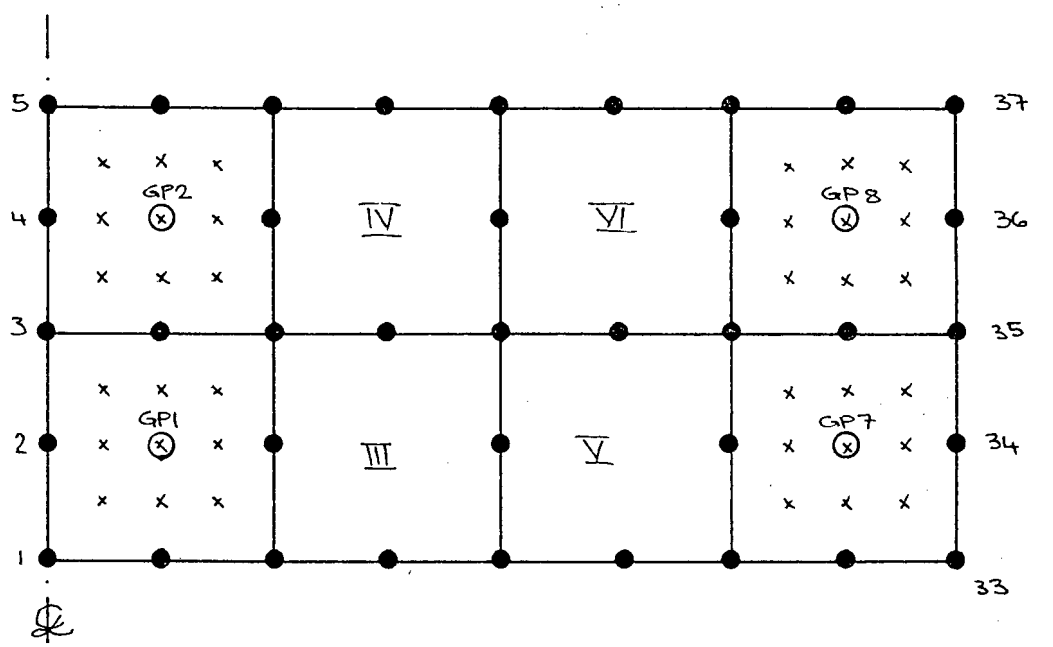

Fig 13.14 Position of Gauss Points

The Gauss points in Fig 13.14 have been named as in the 13-noded analysis to enable comparisions to be made. In fact, the new Gauss points corresponding to the positions of the Gauss points used in the 13-noded analysis are as follows:

Gauss Point	13 noded analysis	37 noded analysis
GP1	Element 1 Gauss Point 1	Element 1 Gauss Point 5
GP2	Element 1 Gauss Point 2	Element 2 Gauss Point 5
GP3	Element 2 Gauss Point 1	Element 7 Gauss Point 5
GP4	Element 2 Gauss Point 2	Element 8 Gauss Point 5

TABLE 13.2 Relationship between Gauss Points in Two Analyses

The BFGS matrix update method was used as the equilibrium iteration method instead of the modified Newton iteration.
Also, the stiffness matrix was reformed at every step in our analysis. Because of this, the analysis was run for only 70 seconds.

13.7.1 Results from the 37-noded ADINA analysis

Graph 13C shows the resulting stresses for each Gauss point. The tabulated output can be found in Appendix D.

Examination of Graph 13C revealed that our refined mesh analysis did not approach the results from Graph 13B, but it did seem to improve on the results from our 13-node analysis, shown in Graph A. Once again we were plagued by negative temperatures at Gauss points which were physically impossible but output numerically, even though all the temperature input was greater than 20°C.
Graph 13C also shows more cyclic stress behavior than 13B or 13A which could occur in terms of welding stress behavior as mentioned in Chapter 2 and Chapter 13.5.3.
In addition, as the weld is initiated, all the Gauss points seem to go into compression immediately and all become tensile between t = 24 seconds and t = 29 seconds. This again seems probable but was not detected by our experiment.
Although this analysis seems more logical than the 13-noded one, all other attemps to obtain stress results from the finite-element analysis, which were closer to those obtained by measurement, failed.

13.8 CONCLUSIONS

In terms of our experiment, it was highly unfortunate that a breakdown in the circuitry of the data logger enabled only one experiment to be performed. By anticipating the fact that something could go wrong at that critical state, the whole experiment was set up carefully, ensuring that all variables were monitored and controlled at every event. For example, the high-temperature strain gauge resistance were checked after exposing them to the atmosphere, before being cemented onto the test plate, after the curing process and after the copper lead wires had been attached to them.

Once connected to the data logger, the strain output was checked against calculated strains for a simple bending test. Hence it was logical to accept the stress results from this experiment as being the best approximation to the real stress behavior of the plate.

In terms of our computer analyses, we were plagued by negative output temperatures at the Gauss points, which cast doubts over the accuracy of the analyses. Even though the input data had been checked extensively and only positive temperatures had been input, high negative temperatures occcured at the Gauss points which could not be explained nor got rid of, even though the finite-element mesh was refined. In fact, even when the material model was changed to the thermo-elastic model ("Model 3") in an investigational run, the negative Gauss point temperatures existed again.

It was finally concluded that if comparisons between the finite-element method and reality were to be made at a later stage, a more detailed and extensive investigation into the mathematical and finite-element theory of the ADINA material model used ("model 10") should be attempted.

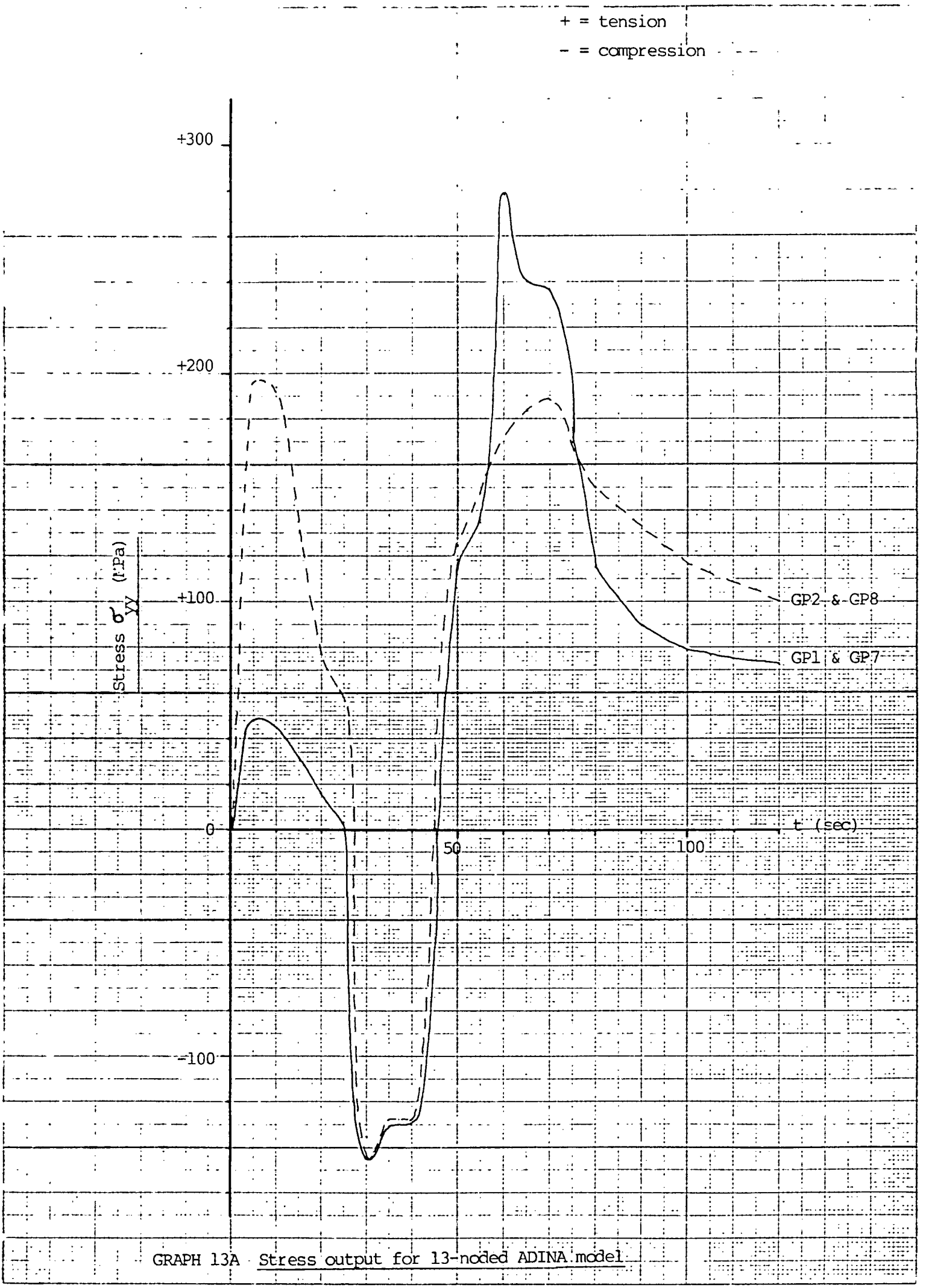

GRAPH 13A Stress output for 13-noded ADINA model

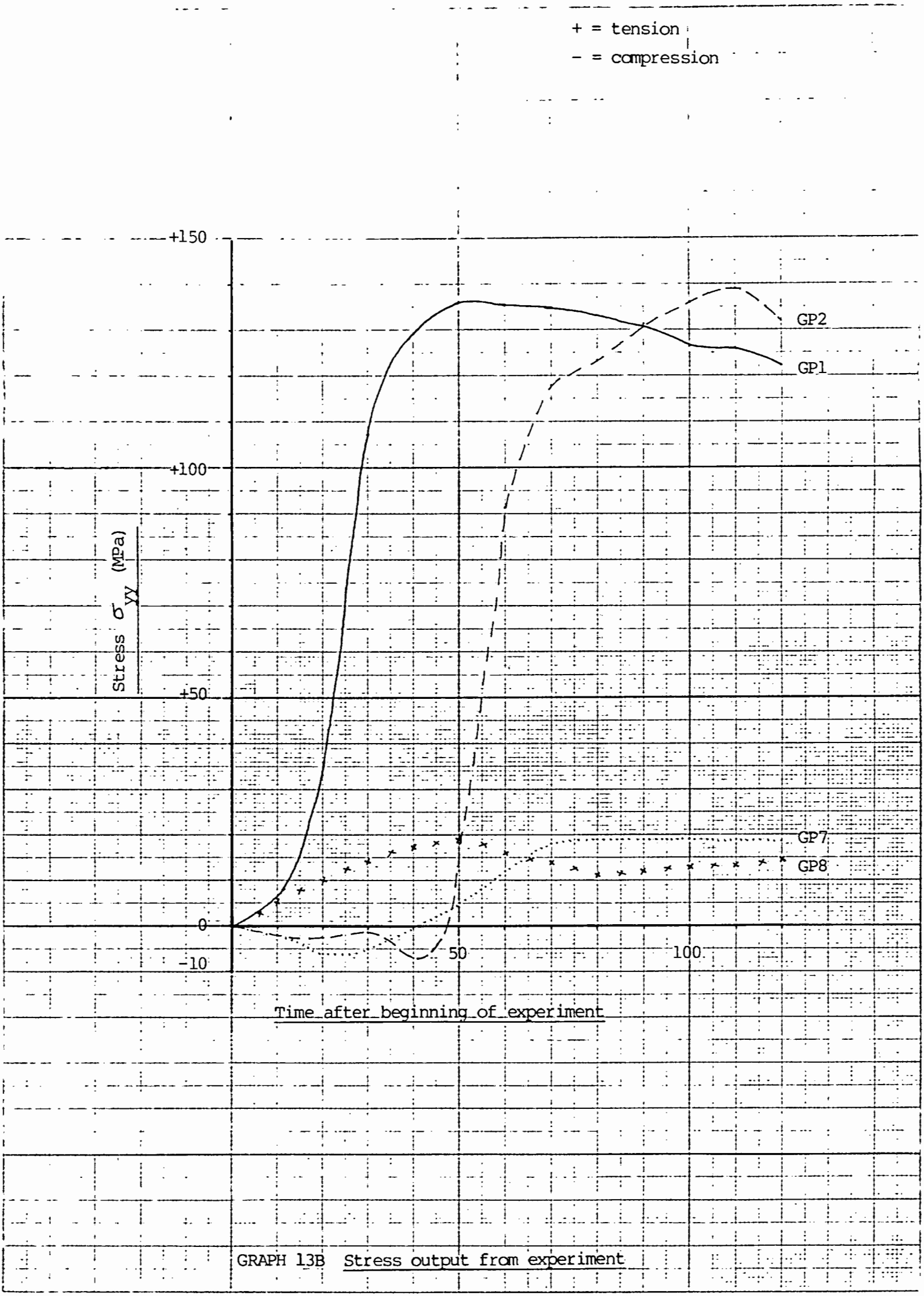

GRAPH 13B Stress output from experiment

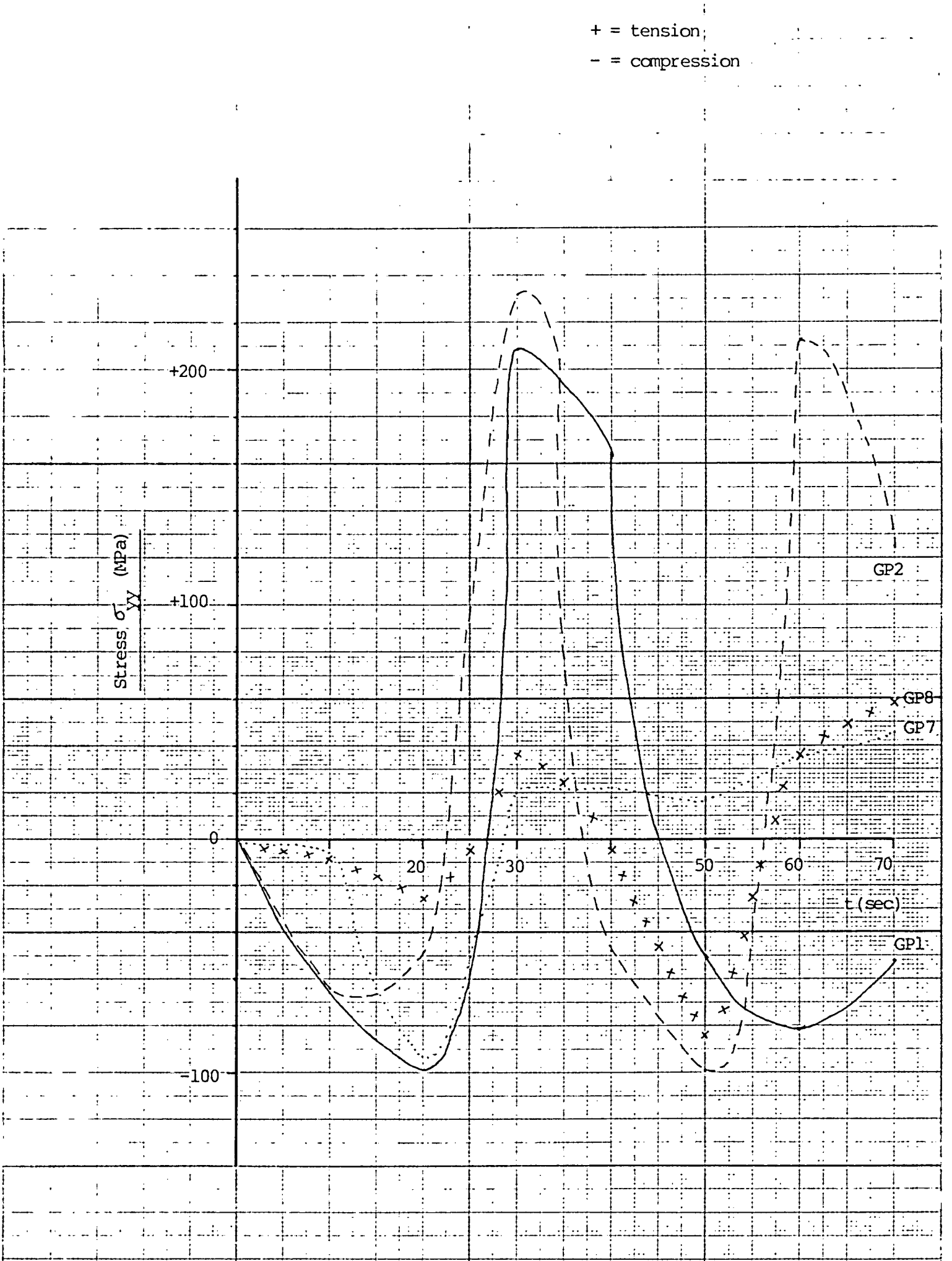

GRAPH 13C Stress output for 37-noded ADINA model

CHAPTER FOURTEEN

CONCLUSIONS AND RECOMMENDATIONS FOR FURTHER WORK IN THIS FIELD

14.1 CONCLUSIONS

According to Bathe [30], in the field of nonlinear analysis, a large number of analyses can at present only be carried out with much difficulty. For an analysis to be successful, a finite-element model must be selected that is a true representation of what we are to model. Also, this model must be able to be analyzed and yield meaningful results.

The aim of our computer analysis was to investigate the thermal and stress distributions due to welding and see if it approached reality. Obviously in work of this nature, simple modelling was essential to establish the basic nature of the welding stresses. Later in further work, these models used here could be upgraded and improved to take account of more detailed phenomena involved with welding. In this work we modelled the weld only as a high temperature being applied at a certain position for a certain time. The metallurgical phase transformations and work hardening effects were ignored.

In our thermal analysis, the finite-element temperatures agreed very well with our experimentally measured temperatures, but this was to be expected as the ADINAT program used linear heat transfer theory in a finite-element form.

In the stress analysis, however, agreement could not be reached between the experimentally measured stresses and those obtained using the finite-element model. This made one aware of the difficulties of nonlinear modelling and the fact that one cannot expect reasonable results if the finite-element model is not sophisticated enough to represent significantly the problem to be modelled. For example, to obtain more accurate results, the heat-affected-zone of our plate would have to be modelled seperately to accomodate phase transformations in the weldment. Also, the material properties of the weldment would have to be different to that of the workpiece.
Hence, we can state that if an accurate welding simulation is necessary, the finite-element model must be able to accomodate all the associated micro-processes involved with the welding process to be successful.

Finally, it is hoped that this thesis, which has covered the basic groundwork, will provide a foundation on which to base further, more sophisticated research.

14.2 RECOMMENDATIONS FOR FURTHER WORK

In this field, the scope for further work is limitless. The following recommendations can provide an incentive for further research.

1. Instead of a 2-dimensional model, a 3-dimensional model could be used which would enable the calculation of the stresses through the thickness of the workpiece.

2. A more sophisticated finite-element model could be used to model the heat-affected-zone seperately to accomodate phase transformations and other more detailed phenomena which take place in this region. Also, the material properties of the weldment would have to be different to that of the workpiece.

3. The source code of ADINA should be looked into and the relevant subroutine controlling the linking tape 56 be corrected to enable linkage between ADINAT and ADINA to take place. This would do away with the construction of multitudes of unnecessary time functions.

4. Instead of analysing the weld for only 2 minutes, this time could be extended or reduced to any length of time. The shorter time would emphasize the microactivity of the weld, whereas a long experiment time would emphasize the overall behavior of the workpiece.

5. To enable more accurate data to be collected, existing data logging programs could be rewritten to enable faster scanning times and longer experimental times to be used. These times are directly a function of the storage space availible on the recording computer.

6. More extensive experimental data could be collected by the initiation of a long term cumulative research program involving only the construction and testing of simple structures using strain gauges as before. This could provide an essential data base for the advancement of the finite-element model.

7. A detailed investigation into the ADINA thermo-elastic-plastic model ("Model 10") could be performed to investigate the occurences of negative output temperatures at the Gauss points.

8. A long-term program of material property tests could be initiated to build up a data base of the variation of material properties such as Young's modulus, thermal conductivity and yield stress with increasing temperature. In a way, the accuracy of the finite-element model used in this thesis was restricted by the lack of high temperature property data applicable to welding conditions.

REFERENCES

1. TWEEDDALE, J.G., "Welding Fabrication Volume 1", London Iliffe Books Ltd., London, 1969.

2. MILNER, D.R., APPS, R.L., "Introduction to Welding and Brazing", Pergamon Press, 1980.

3. MASUBUCHI, K., "Analysis of Welded Structures", Pergamon Press, U.K., 1980.

4. SOUTH AFRICAN INSTITUTE OF STEEL CONSTRUCTION, "Connections for Structural Steelwork Seminar", October 1982.

5. MACGINLEY, T.J., "Structural Steelwork Calculations and Detailing", Newnes-Butterworth, 1977.

6. CONSTRUCTIONAL STEEL RESEARCH AND DEVELOPMENT ORGANISATION, "Steel Designers Manual", 4th Edition Metric, Granada Publishing, 1972.

7. SCHLENKER, B.R., "Introduction to Materials Science", S.I. Edition, John Wiley and Sons, 1974.

8. KUZMANOVIĆ, B.O., WILLEMS, N., "Steel Design for Structural Engineers", Prentice-Hall, 1977.

9. KREITH, F., "Principles of Heat Transfer", 2nd Edition, International Textbook Company, 1967.

10. HOLMAN, J.P., "Heat Transfer", 4th Edition, McGraw-Hill Book Company, 1976.

11. CARLSLAW, H.S., JAEGER, J.C., "Conduction of Heat in Solids", 2nd Edition, Oxford, 1959.

12. COOK, R.D., "Concept and Applications of Finite-Element Analysis", 2nd Edition, Wiley, 1981.

13. DESAI, C.S., "Elementary Finite-Element Method", Prentice-Hall, 1979.

14. ADINA ENGINEERING, "ADINAT Users Manual", Report AE81-2, September 1981.

15. ADINA ENGINEERING, "ADINA Users Manual", Report AE81-1, September 1981.

16. TAYLOR, C., HINTON, E., OWEN, D.R.G., "Numerical Methods for Non-Linear Problems", Pineridge Press, 1980.

17. HEWLETT-PACKARD, "Practical Temperature Measurements", Application Note 290.

18. ADAMS, C.F., "Engineering Measurements and Instrumentation", English Universities Press, 1975.

19. NATIONAL BUREAU OF STANDARDS, "Circular 561 : Conversion Tables for Thermocouples", Leeds and Northrup Co., 1954.

20. MUNDAY, A.J., FARRAR, R.A., "An Engineering Data Book", MacMillan Press, 1979.

21. BATHE, K.J., "Finite-Element Methods in Engineering Analysis", Prentice-Hall, 1982.

22. INGERSOLL, L.R., ZOBEL, O.J., INGERSOLL, A.C., "Heat Conduction", Thames and Hudson, London, 1955.

23. EDE, A.J., "An Introduction to Heat Transfer Principles and Calculations", Pergamon Press, 1967.

24. INCROPERA, F.P., DE WITT, D.P., "Fundamentals of Heat Transfer", John Wiley and Sons, 1981.

25. HEWLETT-PACKARD, "Practical Strain Gauge Measurements", Application Note 290-1.

26. DALLY, J.W. and RILEY, W.F., "Experimental Stress Analysis", 2nd Edition, McGraw-Hill, 1978.

27. LLOYD, A.R., "Software for the HP3054DL Data Logger", Non-linear Structural Mechanics Research Unit Technical Report No 31, University of Cape Town, March 1983.

28. PERRY, J.H., "The Chemical Engineers Handbook", McGraw-Hill, 1941.

29. SNYDER, M.D. and BATHE, K.J., "Finite-element Analysis of Thermo-elastic Plastic and Creep Response", Report 82448-10, Massachusetts Institute of Technology, December 1980.

30. BATHE, K.J., "Applications Using ADINA - Proceedings of the ADINA Conference", Massachusetts Institute of Technology, August 1977.

APPENDICES

APPENDIX A

A.1 FINITE-ELEMENT INTEGRALS TABLE

FINITE ELEMENT MATRICES

Integral	Finite Element Evaluation
$\int_V \delta\underline{\theta}'^T \, t_{\underline{k}} \, \Delta\underline{\theta}'(i) \, dV$	$t_{\underline{K}}{}^k \, \Delta\underline{\theta}(i) = \left(\int_V \underline{S}^T \, t_{\underline{k}} \, \underline{B} \, dV \right) \Delta\underline{\theta}(i)$
$\int_{S_c} \delta\theta^S \, t_h \, \Delta\theta^S(i) \, dS$	$t_{\underline{K}}{}^c \, \Delta\underline{\theta}(i) = \left(\int_{S_c} t_h \, \underline{H}^{S\,T} \, \underline{H}^S \, dS \right) \Delta\underline{\theta}(i)$
$\int_{S_r} \delta\theta^S \, t_\kappa \, \Delta\theta^S(i) \, dS$	$t_{\underline{K}}{}^r \, \Delta\underline{\theta}(i) = \left(\int_{S_r} t_\kappa \, \underline{H}^{S\,T} \, \underline{H}^S \, dS \right) \Delta\underline{\theta}(i)$
$t+\Delta t_Q$ (in Eq.(14))	$t+\Delta t_{\underline{Q}} = \int_{S_2} \underline{H}^{S\,T} \, q^S \, dS + \int_V \underline{H}^T \, t+\Delta t_{\tilde{q}}{}^B \, dV - \left(\int_V t+\Delta t_c \, \underline{H}^T \underline{H} \, dV \right) {}^{t+\Delta t}\dot{\underline{\theta}}$
$\int_{S_c} \delta\theta^S \, {}^{t+\Delta t}h(i-1) \left({}^{t+\Delta t}\theta_e - {}^{t+\Delta t}\theta^S \right) dS$	$t+\Delta t_{\underline{Q}}{}^c(i-1) = \int_{S_c} t+\Delta t_h(i-1) \underline{H}^{S\,T} \left[\underline{H}^S \left({}^{t+\Delta t}\underline{\theta}_e - {}^{t+\Delta t}\underline{\theta}^{S(i-1)} \right) \right] dS$
$\int_{S_r} \delta\theta^S \, {}^{t+\Delta t}\kappa(i-1) \left({}^{t+\Delta t}\theta_e - {}^{t+\Delta t}\theta^S \right) dS$	$t+\Delta t_{\underline{Q}}{}^r(i-1) = \int_{S_r} t+\Delta t_\kappa(i-1) \underline{H}^{S\,T} \left[\underline{H}^S \left({}^{t+\Delta t}\underline{\theta}_e - {}^{t+\Delta t}\underline{\theta}^{S(k-1)} \right) \right] dS$

A-1

(cont'd)

Integral	Finite Element Evaluation
$\int_V \delta\underline{\theta}'^T \; {}^{t+\Delta t}\underline{k} \; {}^{t+\Delta t}\underline{\theta}'^{(i-1)} \, dV$	${}^{t+\Delta t}\underline{Q}^{k(i-1)} = \int_V \underline{B}^T \left[{}^{t+\Delta t}\underline{k}^{(i-1)} \underline{B} \; {}^{t+\Delta t}\underline{\theta}^{(i-1)} dV \right.$
$\int_S h \; \delta\theta^S \; {}^{t+\Delta t}\theta^S \, dS$	$\underline{K}^c \; {}^{t+\Delta t}\underline{\theta} = \left(\int_S h \; \underline{H}^{S\,T} \; \underline{H}^S \, dS \right) \; {}^{t+\Delta t}\underline{\theta}$
$\int_S h \; \delta\theta^S \; {}^{t+\Delta t}\theta_e \, dS$	${}^{t+\Delta t}\underline{Q}^e = \int_S h \; \underline{H}^{S\,T} \; [H^S \; {}^{t+\Delta t}\underline{\theta}_e] \, dS$

APPENDIX B

CHROMEL vs. ALUMEL THERMOCOUPLE

Degrees Centigrade — Reference Junction 0° C.

°C	0	1	2	3	4	5	6	7	8	9
					Millivolts					
0	0.00	0.04	0.08	0.12	0.16	0.20	0.24	0.28	0.32	0.36
10	0.40	0.44	0.48	0.52	0.56	0.60	0.64	0.68	0.72	0.76
20	0.80	0.84	0.88	0.92	0.96	1.00	1.04	1.08	1.12	1.16
30	1.20	1.24	1.28	1.32	1.36	1.40	1.44	1.49	1.53	1.57
40	1.61	1.65	1.69	1.73	1.77	1.81	1.85	1.90	1.94	1.98
50	2.02	2.06	2.10	2.14	2.18	2.23	2.27	2.31	2.35	2.39
60	2.43	2.47	2.51	2.56	2.60	2.64	2.68	2.72	2.76	2.80
70	2.85	2.89	2.93	2.97	3.01	3.05	3.10	3.14	3.18	3.22
80	3.26	3.30	3.35	3.39	3.43	3.47	3.51	3.56	3.60	3.64
90	3.68	3.72	3.76	3.81	3.85	3.89	3.93	3.97	4.01	4.06
100	4.10	4.14	4.18	4.22	4.26	4.31	4.35	4.39	4.43	4.47
110	4.51	4.55	4.60	4.64	4.68	4.72	4.76	4.80	4.84	4.88
120	4.92	4.96	5.01	5.05	5.09	5.13	5.17	5.21	5.25	5.29
130	5.33	5.37	5.41	5.45	5.49	5.53	5.57	5.61	5.65	5.69
140	5.73	5.77	5.81	5.85	5.89	5.93	5.97	6.01	6.05	6.09
150	6.13	6.17	6.21	6.25	6.29	6.33	6.37	6.41	6.45	6.49
160	6.53	6.57	6.61	6.65	6.69	6.73	6.77	6.81	6.85	6.89
170	6.93	6.97	7.01	7.05	7.09	7.13	7.17	7.21	7.25	7.29
180	7.33	7.37	7.41	7.45	7.49	7.53	7.57	7.61	7.65	7.69
190	7.73	7.77	7.81	7.85	7.89	7.93	7.97	8.01	8.05	8.09
200	8.13	8.17	8.21	8.25	8.29	8.33	8.37	8.41	8.46	8.50
210	8.54	8.58	8.62	8.66	8.70	8.74	8.78	8.82	8.86	8.90
220	8.94	8.98	9.02	9.06	9.10	9.14	9.18	9.22	9.26	9.30
230	9.34	9.38	9.42	9.46	9.50	9.54	9.59	9.63	9.67	9.71
240	9.75	9.79	9.83	9.87	9.91	9.95	9.99	10.03	10.07	10.11
250	10.16	10.20	10.24	10.28	10.32	10.36	10.40	10.44	10.48	10.52
260	10.57	10.61	10.65	10.69	10.73	10.77	10.81	10.85	10.89	10.93
270	10.98	11.02	11.06	11.10	11.14	11.18	11.22	11.26	11.30	11.34
280	11.39	11.43	11.47	11.51	11.55	11.59	11.63	11.67	11.72	11.76
290	11.80	11.84	11.88	11.92	11.96	12.01	12.05	12.09	12.13	12.17
300	12.21	12.25	12.29	12.34	12.38	12.42	12.46	12.50	12.54	12.58
310	12.63	12.67	12.71	12.75	12.79	12.83	12.88	12.92	12.96	13.00
320	13.04	13.08	13.12	13.17	13.21	13.25	13.29	13.33	13.37	13.42
330	13.46	13.50	13.54	13.58	13.62	13.67	13.71	13.75	13.79	13.83
340	13.88	13.92	13.96	14.00	14.04	14.09	14.13	14.17	14.21	14.25
350	14.29	14.34	14.38	14.42	14.46	14.50	14.55	14.59	14.63	14.67
360	14.71	14.76	14.80	14.84	14.88	14.92	14.97	15.01	15.05	15.09
370	15.13	15.18	15.22	15.26	15.30	15.34	15.39	15.43	15.47	15.51
380	15.55	15.60	15.64	15.68	15.72	15.76	15.81	15.85	15.89	15.93
390	15.98	16.02	16.06	16.10	16.14	16.19	16.23	16.27	16.31	16.36
400	16.40	16.44	16.48	16.52	16.57	16.61	16.65	16.69	16.74	16.78
410	16.82	16.86	16.91	16.95	16.99	17.03	17.07	17.12	17.16	17.20
420	17.24	17.29	17.33	17.37	17.41	17.46	17.50	17.54	17.58	17.62
430	17.67	17.71	17.75	17.79	17.84	17.88	17.92	17.96	18.01	18.05
440	18.09	18.13	18.17	18.22	18.26	18.30	18.34	18.39	18.43	18.47
450	18.51	18.56	18.60	18.64	18.68	18.73	18.77	18.81	18.85	18.90
460	18.94	18.98	19.02	19.07	19.11	19.15	19.19	19.24	19.28	19.32
470	19.36	19.41	19.45	19.49	19.54	19.58	19.62	19.66	19.71	19.75
480	19.79	19.84	19.88	19.92	19.96	20.01	20.05	20.09	20.13	20.18
490	20.22	20.26	20.31	20.35	20.39	20.43	20.48	20.52	20.56	20.60
500	20.65	20.69	20.73	20.77	20.82	20.86	20.90	20.94	20.99	21.03
510	21.07	21.11	21.16	21.20	21.24	21.28	21.32	21.37	21.41	21.45
520	21.50	21.54	21.58	21.63	21.67	21.71	21.75	21.80	21.84	21.88
530	21.92	21.97	22.01	22.05	22.09	22.14	22.18	22.22	22.26	22.31
540	22.35	22.39	22.43	22.48	22.52	22.56	22.61	22.65	22.69	22.73
550	22.78	22.82	22.86	22.90	22.95	22.99	23.03	23.07	23.12	23.16
560	23.20	23.25	23.29	23.33	23.38	23.42	23.46	23.50	23.54	23.59
570	23.63	23.67	23.72	23.76	23.80	23.84	23.89	23.93	23.97	24.01
580	24.06	24.10	24.14	24.18	24.23	24.27	24.31	24.36	24.40	24.44
590	24.49	24.53	24.57	24.61	24.65	24.70	24.74	24.78	24.83	24.87

CHROMEL vs. ALUMEL THERMOCOUPLE

Degrees Centigrade — Reference Junction 0° C.

°C	0	1	2	3	4	5	6	7	8	9
					Millivolts					
600	24.91	24.95	25.00	25.04	25.08	25.12	25.17	25.21	25.25	25.29
610	25.34	25.38	25.42	25.47	25.51	25.55	25.59	25.64	25.68	25.72
620	25.76	25.81	25.85	25.89	25.93	25.98	26.02	26.06	26.10	26.15
630	26.19	26.23	26.27	26.32	26.36	26.40	26.44	26.48	26.53	26.57
640	26.61	26.65	26.70	26.74	26.78	26.82	26.86	26.91	26.95	26.99
650	27.03	27.07	27.12	27.16	27.20	27.24	27.28	27.33	27.37	27.41
660	27.45	27.49	27.54	27.58	27.62	27.66	27.71	27.75	27.79	27.83
670	27.87	27.92	27.96	28.00	28.04	28.08	28.13	28.17	28.21	28.25
680	28.29	28.34	28.38	28.42	28.46	28.50	28.55	28.59	28.63	28.67
690	28.72	28.76	28.80	28.84	28.88	28.93	28.97	29.01	29.05	29.10
700	29.14	29.18	29.22	29.26	29.30	29.35	29.39	29.43	29.47	29.52
710	29.56	29.60	29.64	29.68	29.72	29.77	29.81	29.85	29.89	29.93
720	29.97	30.02	30.06	30.10	30.14	30.18	30.23	30.27	30.31	30.35
730	30.39	30.44	30.48	30.52	30.56	30.60	30.65	30.69	30.73	30.77
740	30.81	30.85	30.90	30.94	30.98	31.02	31.06	31.10	31.15	31.19
750	31.23	31.27	31.31	31.35	31.40	31.44	31.48	31.52	31.56	31.60
760	31.65	31.69	31.73	31.77	31.81	31.85	31.90	31.94	31.98	32.02
770	32.06	32.10	32.15	32.19	32.23	32.27	32.31	32.35	32.39	32.43
780	32.48	32.52	32.56	32.60	32.64	32.68	32.72	32.76	32.81	32.85
790	32.89	32.93	32.97	33.01	33.05	33.09	33.13	33.18	33.22	33.26
800	33.30	33.34	33.38	33.42	33.46	33.50	33.54	33.59	33.63	33.67
810	33.71	33.75	33.79	33.83	33.87	33.91	33.95	33.99	34.04	34.08
820	34.12	34.16	34.20	34.24	34.28	34.32	34.36	34.40	34.44	34.49
830	34.53	34.57	34.61	34.65	34.69	34.73	34.77	34.81	34.85	34.89
840	34.93	34.97	35.02	35.06	35.10	35.14	35.18	35.22	35.26	35.30
850	35.34	35.38	35.42	35.46	35.50	35.54	35.58	35.63	35.67	35.71
860	35.75	35.79	35.83	35.87	35.91	35.95	35.99	36.03	36.07	36.11
870	36.15	36.19	36.23	36.27	36.31	36.35	36.39	36.43	36.47	36.51
880	36.55	36.59	36.63	36.67	36.72	36.76	36.80	36.84	36.88	36.92
890	36.96	37.00	37.04	37.08	37.12	37.16	37.20	37.24	37.28	37.32
900	37.36	37.40	37.44	37.48	37.52	37.56	37.60	37.64	37.68	37.72
910	37.76	37.80	37.84	37.88	37.92	37.96	38.00	38.04	38.08	38.12
920	38.16	38.20	38.24	38.28	38.32	38.36	38.40	38.44	38.48	38.52
930	38.56	38.60	38.64	38.68	38.72	38.76	38.80	38.84	38.88	38.92
940	38.95	38.99	39.03	39.07	39.11	39.15	39.19	39.23	39.27	39.31
950	39.35	39.39	39.43	39.47	39.51	39.55	39.59	39.63	39.67	39.71
960	39.75	39.79	39.83	39.86	39.90	39.94	39.98	40.02	40.06	40.10
970	40.14	40.18	40.22	40.26	40.30	40.34	40.38	40.41	40.45	40.49
980	40.53	40.57	40.61	40.65	40.69	40.73	40.77	40.81	40.85	40.89
990	40.92	40.96	41.00	41.04	41.08	41.12	41.16	41.20	41.24	41.28
1000	41.31	41.35	41.39	41.43	41.47	41.51	41.55	41.59	41.63	41.67
1010	41.70	41.74	41.78	41.82	41.86	41.90	41.94	41.98	42.02	42.05
1020	42.09	42.13	42.17	42.21	42.25	42.29	42.33	42.36	42.40	42.44
1030	42.48	42.52	42.56	42.60	42.63	42.67	42.71	42.75	42.79	42.83
1040	42.87	42.90	42.94	42.98	43.02	43.06	43.10	43.14	43.17	43.21
1050	43.25	43.29	43.33	43.37	43.41	43.44	43.48	43.52	43.56	43.60
1060	43.63	43.67	43.71	43.75	43.79	43.83	43.87	43.90	43.94	43.99
1070	44.02	44.06	44.10	44.13	44.17	44.21	44.25	44.29	44.33	44.36
1080	44.40	44.44	44.48	44.52	44.55	44.59	44.63	44.67	44.71	44.74
1090	44.78	44.82	44.86	44.90	44.93	44.97	45.01	45.05	45.09	45.12
1100	45.16	45.20	45.24	45.27	45.31	45.35	45.39	45.43	45.46	45.50
1110	45.54	45.58	45.62	45.65	45.69	45.73	45.77	45.80	45.84	45.88
1120	45.92	45.96	45.99	46.03	46.07	46.11	46.14	46.18	46.22	46.26
1130	46.29	46.33	46.37	46.41	46.44	46.48	46.52	46.56	46.59	46.63
1140	46.67	46.70	46.74	46.78	46.82	46.85	46.89	46.93	46.97	47.00
1150	47.04	47.08	47.12	47.15	47.19	47.23	47.26	47.30	47.34	47.38
1160	47.41	47.45	47.49	47.52	47.56	47.60	47.63	47.67	47.71	47.75
1170	47.78	47.82	47.86	47.89	47.93	47.97	48.00	48.04	48.08	48.12
1180	48.15	48.19	48.23	48.26	48.30	48.34	48.37	48.41	48.45	48.49
1190	48.52	48.56	48.59	48.63	48.67	48.70	48.74	48.78	48.81	48.85

CHROMEL vs. ALUMEL THERMOCOUPLE

Degrees Centigrade — Reference Junction 0° C.

°C	0	1	2	3	4	5	6	7	8	9
					Millivolts					
1200	48.89	48.92	48.96	49.00	49.03	49.07	49.11	49.14	49.18	49.22
1210	49.25	49.29	49.32	49.36	49.40	49.43	49.47	49.51	49.54	49.58
1220	49.62	49.65	49.69	49.72	49.76	49.80	49.83	49.87	49.90	49.94
1230	49.93	50.01	50.05	50.08	50.12	50.16	50.19	50.23	50.26	50.30
1240	50.34	50.37	50.41	50.44	50.48	50.52	50.55	50.59	50.62	50.66
1250	50.69	50.73	50.77	50.80	50.84	50.87	50.91	50.94	50.98	51.02
1260	51.05	51.09	51.12	51:16	51.19	51.23	51.27	51.30	51.34	51.37
1270	51.41	51.44	51.48	51.51	51.55	51.58	51.62	51.66	51.69	51.73
1280	51.76	51.80	51.83	51.87	51.90	51.94	51.97	52.01	52.04	52.08
1290	52.11	52.15	52.18	52.22	52.25	52.29	52.32	52.36	52.39	52.43
1300	52.46	52.50	52.53	52.57	52.60	52.64	52.67	52.71	52.74	52.78
1310	52.81	52.85	52.88	52.92	52.95	52.99	53.02	53.06	53.09	53.13
1320	53.16	53.20	53.23	53.27	53.30	53.34	53.37	53.41	53.44	53.47
1330	53.51	53.54	53.58	53.61	53.65	53.68	53.72	53.75	53.79	53.82
1340	53.85	53.89	53.92	53.96	53.99	54.03	54.06	54.10	54.13	54.16
1350	54.20	54.23	54.27	54.30	54.34	54.37	54.40	54.44	54.47	54.51
1360	54.54	54.57	54.61	54.64	54.68	54.71	54.74	54.78	54.81	54.85
1370	54.86	54.91								

B2. THERMOCOUPLE-TO-PLATE FIXING DETAILS

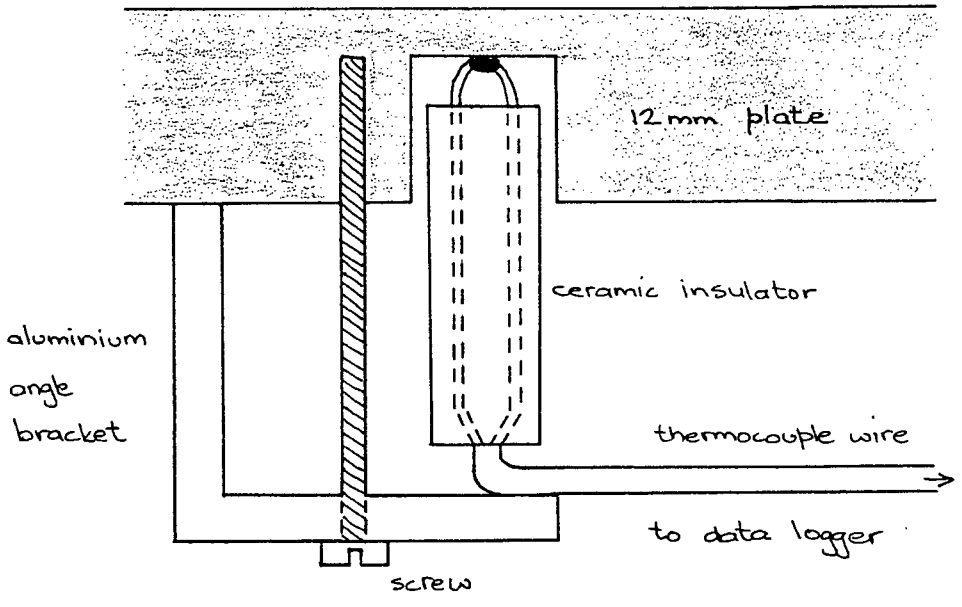

A. Complete fixing detail (not to scale)

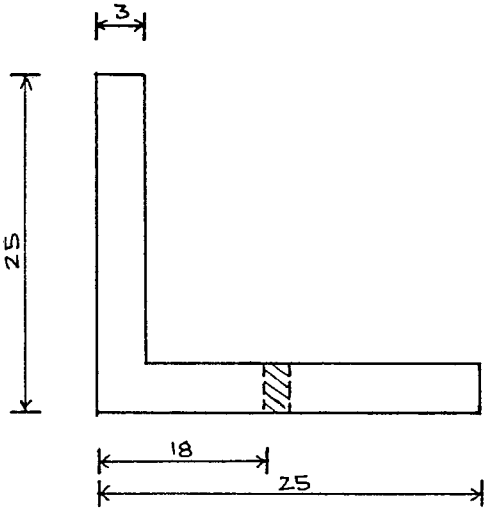

B. Angle bracket dimensions

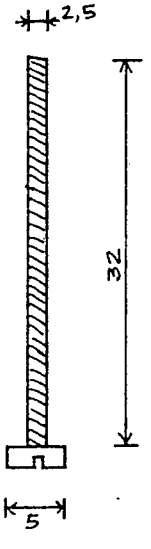

C. Screw dimensions

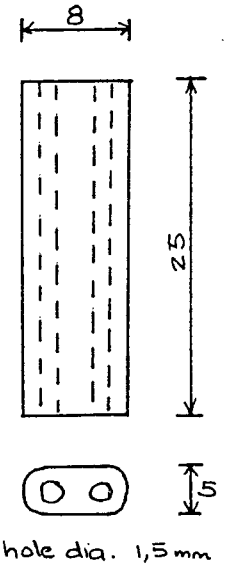

D. Ceramic Insulator dimensions

DATE/TIME: 31-8-83 (14h30) SETUP NAME: "TEST" (8mm hole) TEST AREA: Dept. Metallurgy, U.C.T.

LABEL	SLOT/CARD TYPE	CARD TERMINALS	CHANNEL	TYPE OF TRANSDUCTER	FUNCTION	VALUES MIN	VALUES TYP.	VALUES MAX	COMMENTS, LOCATION, ACTION, ETC.
Black	T. Card*	1	6	K-type thermocouple	°C	20°C		1300°C	Location: 1
Green	T. Card	2	8	K-type thermocouple	°C	20°C		1300°C	Location: 2
Double-red.	T. Card	3	9	K-type thermocouple	°C	20°C		1300°C	Location: 3
									(See sketch)

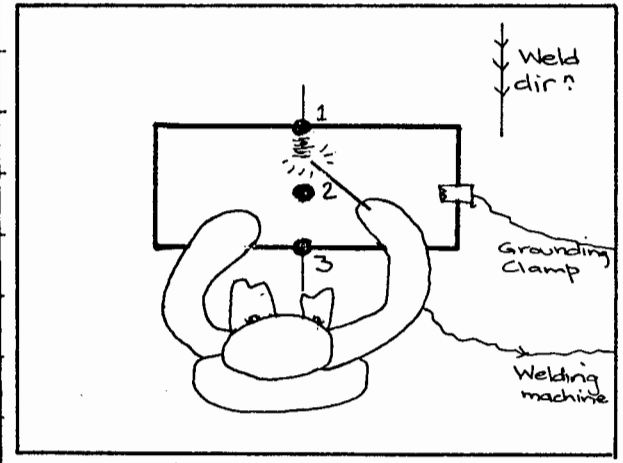

* T. Card = Thermocouple Card 44422A (Hewlett-Packard)

DATE/TIME: 14-9-83 (14h30) SETUP NAME: "RUN 1" (8mm hole) TEST AREA: Dept. Metallurgy, U.C.T.

LABEL	SLOT/CARD TYPE	CARD TERMINALS	CHANNEL	TYPE OF TRANSDUCTER	FUNCTION	VALUES			COMMENTS, LOCATION, ACTION, ETC.
						MIN	TYP.	MAX	
Black	T. Card	1	6	K-type thermocouple	°C	20°C		1300°C	Location: 1
Green	T. Card	2	8	K-type thermocouple	°C	20°C		1300°C	Location: 2
Double-red.	T. Card*	3	9	K-type thermocouple	°C	20°C		1300°C	Location: 3

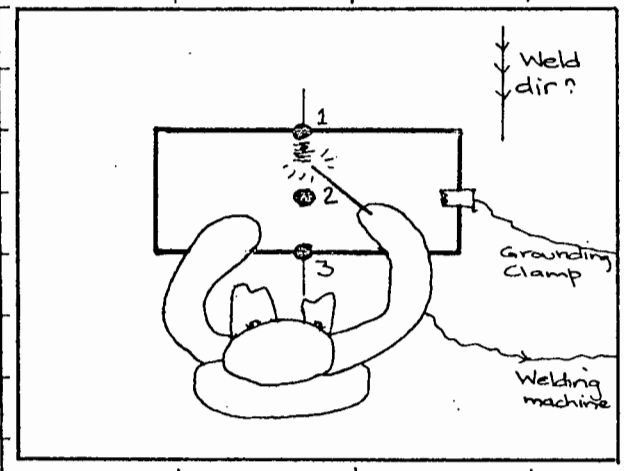

* T. Card = Thermocouple Card 44422A (Hewlett-Packard)

DATE/TIME: 14-9-83 (14h30) SETUP NAME: "RUN 2" (11,5mm hole) TEST AREA: Dept. Metallurgy, U.C.T.

LABEL	SLOT/CARD TYPE	CARD TERMINALS	CHANNEL	TYPE OF TRANSDUCTER	FUNCTION	VALUES			COMMENTS, LOCATION, ACTION, ETC.
						MIN	TYP.	MAX	
Black	T. Card	1	6	K-type thermocouple	°C	20°C		1300°C	Location: 1
Green	T. Card	2	8	K-type thermocouple	°C	20°C		1300°C	Location: 2
Double-red.	T. Card *	3	9	K-type thermocouple	°C	20°C		1300°C	Location: 3

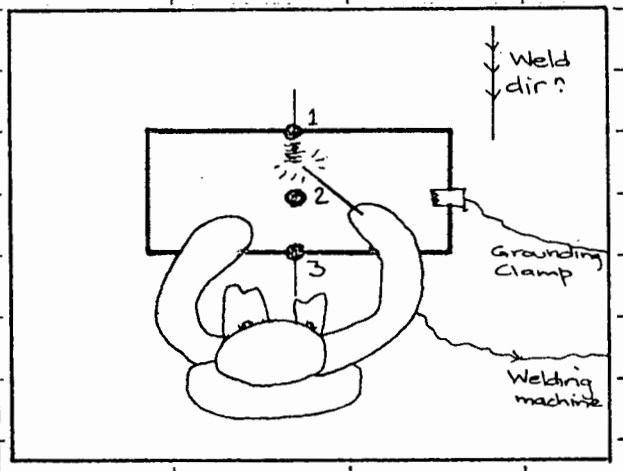

* T. Card = thermocouple card 44422A (Hewlett-Packard)

B4. OUTPUT FROM "H-P" PROGRAM (TEST)

```
H-P 01--SCAN 01---09:06:16:14:38
  06:     29.6 C    09:     30.0 C
  08:     30.0 C

H-P 01--SCAN 02---09:06:16:14:42
  06:     29.5 C    09:     30.1 C
  08:     29.9 C

H-P 01--SCAN 03---09:06:16:14:50
  06:     29.5 C    09:     29.1 C
  08      29.9 C

H-P 01--SCAN 04---09:06:16:14:59
  06:     29.5 C    09:     42.9 C
  08:     29.8 C

H-P 01--SCAN 05---09:06:16:15:07
  06:     29.6 C    09:     48.8 C
  08:     29.5 C

H-P 01--SCAN 06---09:06:16:15:15
  06:     30.3 C    09:     53.0 C
  08:     30.2 C

H-P 01--SCAN 07---09:06:16:15:23
  06:     30.6 C    09:    410.4 C
  08:     30.3 C
```

```
EXP 01--SCAN 08---09:06:16:15:31
  06:    32.0 C    09:   384.2 C
  00:    31.8 C


EXP 01--SCAN 09---09:06:16:15:39
  06:    34.1 C    09:   303.5 C
  00:   494.9 C


EXP 01--SCAN 10---09:06:16:15:47
  06:    37.5 C    09:   254.9 C
  00:   324.4 C


EXP 01--SCAN 11---09:06:16:15:55
  06:    41.5 C    09:   223.0 C
  00:   200.6 C


EXP 01--SCAN 12---09:06:16:16:03
  06:    45.5 C    09:   200.1 C
  00:   257.7 C

-----

EXP 01--SCAN 13---09:06:16:16:11
  06:    49.2 C    09:   182.8 C
  00:   237.0 C


EXP 01--SCAN 14---09:06:16:16:19
  06:    52.7 C    09:   169.0 C
  00:   219.7 C
```

```
EXP 01--SCAN 15---09:06:16:16:27
  05:     55.5 C    09:    157.8 C
  08:    204.9 C


EXP 01--SCAN 16---09:06:16:16:36
  05:     58.0 C    09:    148.4 C
  08:    192.4 C


EXP 01--SCAN 17---09:06:16:16:44
  05:     59.0 C    09:    140.4 C
  08:    181.6 C


EXP 01--SCAN 18---09:06:16:16:52
  06:     61.8 C    09:    133.5 C
  08:    172.2 C


EXP 01--SCAN 19---09:06:16:17:00
  06:     63.2 C    09:    127.6 C
  08:    164.0 C


EXP 01--SCAN 20---09:06:16:17:08
  06:     64.5 C    09:    122.5 C
  08:    156.7 C
```

B5. LISTING OF BRINKS "HOT" PROGRAM

```
10 OPTION BASE 1
20 REM BRINKS "HOT" PROGRAM
30 SHORT X(1000,4)
40 DIM A$[100]
50 A0=.226584602
60 A1=24152.106
70 A2=67233.4248
80 A3=2210340.682
90 A4=-860963914.9
100 A5=46350600000
110 A6=-1.18452E12
120 A7=1.3869E13
130 A8=-6.33708E13
140 ! X(N,1):Output volts ch 06
150 ! X(N,2):Output volts ch 08
160 ! X(N,3):Output volts ch 09
170 ! X(N,4):Output secs
180 PRINTER IS 706,80
190 I=0 @ A=.00092 @ B=1
200 ON KEY# 1,"TEST " GOTO 280
210 ON KEY# 2,"STORE" GOSUB 860
220 ON KEY# 5,"PLOT " GOSUB 660
230 ON KEY# 8,"INIT " GOSUB 1090
240 ON KEY# 3,"RECALL" GOSUB 990
250 ON KEY# 4,"PRINT " GOSUB 540
260 CLEAR @ KEY LABEL
270 GOTO 270
280 CLEAR @ DISP "ENTER EXPECTED DURATION OF TEST" @ DISP @ DISP "  (NO LO
NGER THAN 300 SECONDS )"
290 INPUT N1@ IF N1>300 THEN N1=300
300 N=IP(N1*3)
310 DISP @ DISP "ADD COMMENT" @ INPUT A$
320 REM ** DATA LOGGER COMMANDS
330 CLEAR 709
340 OUTPUT 709 ;"ARTE0VR5VT1VC1VT1TE2"
350 CLEAR @ DISP "PRESS CONT TO START TEST" @ BEEP 200,50 @ PAUSE
360 DISP "TIME IS 0  -TESTING- "
370 SETTIME 0,0
380 I=I+1
390 OUTPUT 709 ;"AC06"
400 ENTER 709 ; X(I,1)
410 OUTPUT 709 ;"AC08"
420 ENTER 709 ; X(I,2)
430 OUTPUT 709 ;"AC09"
440 ENTER 709 ; X(I,3)
450 X(I,4)=TIME
460 IF I<=N THEN GOTO 380
470 DISP
480 BEEP 200,200 @ DISP USING "21A,3D.2D,9A" ; "TEST TERMINATED AFTER " X(
N,4)," SECS"
490 DISP @ DISP USING "17A,4D,9A" ; "TEST COMPRISES 3X ",N," POINTS"
500 CLEAR @ DISP "CORRECTING FOR ROOM TEMPERATURE"
510 FOR I=1 TO N @ X(I,1)=B*(X(I,1)+A) @ X(I,2)=B*(X(I,2)+A) @ X(I,3)=B*(X
(I,3)+A) @ NEXT I
520 BEEP 100,100
530 KEY LABEL @ GOTO 270
540 ! CLEAR @ DISP "WANT TO PRINT OR DISPLAY DATA  ENTER (D/P)" @ INPUT P
$
550 ! IF P$="P" THEN PRINTER IS 706,80 ELSE PRINTER IS 1
```

```
560 PRINT A$
570 PRINT )
580 PRINT "Ch 06          Ch 08        Ch 09          Time      Index"
590 PRINT
600 FOR I=1 TO N @ PRINT USING 630 ; FNT(X(I,1)),FNT(X(I,2)),FNT(X(I,3)),X
(I,4),I
610 NEXT I
620 DISP "PRESS -CONT- TO CONTINUE" @ PAUSE
630 IMAGE 8D.2D,8D.2D,8D.2D,8D.2D,8D
640 GOTO 190
650 GOSUB 860
660 PLOTTER IS 1
670 GCLEAR
680 LOCATE 20,125,15,95
690 FRAME
700 SCALE 0,N1,0,2000
710 FXD 0,0
720 IF N1<50 THEN N2=1 ELSE N2=5
730 LAXES -10,100,0,0,N2,2
740 SETGU
750 LORG 5 @ MOVE 65,3 @ LABEL "temperature vs seconds"
760 SETUU
770 FOR I=1 TO N
780 PENUP @ PLOT X(I,4),FNT(X(I,1))
790 PENUP @ PLOT X(I,4),FNT(X(I,2))
800 PENUP @ PLOT X(I,4),FNT(X(I,3))
810 NEXT I
820 ON ERROR GOSUB 1090
830 IF X=1 THEN PCOPY 706
840 IF X=2 THEN COPY
850 GOTO 200
860 ! STORE
870 CLEAR @ CAT
880 DISP "INPUT FILE NAME" @ INPUT Z$
890 DISP "CREATE?(Y/N)"
900 INPUT X$
910 IF X$="Y" THEN CREATE Z$,3,15000
920 ASSIGN# 1 TO Z$
930 PRINT# 1 ; A$,N,N1
940 FOR I=1 TO N
950 PRINT# 1 ; X(I,1),X(I,2),X(I,3),X(I,4)
960 NEXT I
970 BEEP 100,100
980 GOTO 190
990 ! READ
1000 CLEAR @ CAT
1010 DISP "INPUT DATA FILE"
1020 INPUT Z$
1030 ASSIGN# 1 TO Z$
1040 READ# 1 ; A$,N,N1
1050 ON ERROR GOTO 1070
1060 FOR I=1 TO N @ READ# 1 ; X(I,1),X(I,2),X(I,3),X(I,4)@ NEXT I
1070 N=I-1 @ OFF ERROR
1080 GOTO 190
1090 !
1100 DISP ""
1110 DISP "    FOR  EXTERNAL PRINTER (1)"
1120 DISP "         INTERNAL PRINTER (2)"
1130 DISP "         SCREEN       (3)"
1140 DISP ""
1150 DISP "ENTER 1"
1160 DISP "      2"
```

```
1170 DISP " OR   3"
1180 INPUT X
1190 ON X GOSUB 1290,1310,1330
1200 ON ERROR GOSUB 1250
1210 LOADBIN "FCOPY"
1220 BEEP 200,200
1230 OFF ERROR
1240 RETURN
1250 CLEAR @ DISP "SYSTEM IS INITIALISED"
1260 BEEP 100,100
1270 OFF ERROR @ KEY LABEL
1280 GOTO 270
1290 PRINTER IS 706,80
1300 RETURN
1310 PRINTER IS 2
1320 RETURN
1330 PRINTER IS 1
1340 RETURN
1350 DEF FNT(V) = A0+A1*V+A2*V^2+A3*V^3+A4*V^4+A5*V^5+A6*V^6+A7*V^7+A8*V^8

1360 FOR I=1 TO N
1370 X(I,1)=FNT(X(I,1))
1380 X(I,2)=FNT(X(I,2))
1390 X(I,3)=FNT(X(I,3))
1400 NEXT I
1410 RETURN
```

B6. SAMPLE OF OUTPUT FROM BRINKS "HOT" PROGRAM (RUN 2)

RUN 2

Ch. 08	Ch. 09	Ch. 09	Time
17.05	17.12	16.95	.43
17.05	17.17	16.95	.76
17.05	17.58	17.48	1.12
17.77	17.89	17.43	1.46
21.60	17.26	16.20	1.81
28.12	17.41	16.34	2.15
44.58	16.68	17.07	2.47
519.72	16.83	17.17	2.83
1320.87	16.85	17.29	3.18
1431.80	17.17	16.17	3.52
1589.61	17.05	17.22	4.08
.16	17.38	17.19	4.54
.22	17.63	16.90	5.09
597.77	17.69	17.26	5.43
1167.39	17.12	17.09	5.78
1160.47	14.80	17.27	6.12
1228.33	16.54	16.93	6.47
1357.25	17.75	17.36	6.81
1411.65	17.26	17.29	7.16
1433.97	17.29	17.09	7.50
1516.61	17.12	16.50	7.85
1534.70	17.22	17.05	8.19
1530.06	19.40	17.09	8.54
1515.52	17.55	16.80	8.88
1498.91	17.58	16.72	9.23
1480.13	17.12	16.80	9.57
1448.35	17.77	16.85	9.92
1420.35	17.17	16.88	10.26
1385.67	17.36	17.31	10.61
1313.06	16.95	17.19	10.96
1243.72	16.58	17.31	11.30
1151.12	17.77	17.22	11.65
1109.72	17.89	17.65	11.99
1069.13	19.29	17.58	12.34
1019.46	17.32	17.02	12.68
955.70	17.61	17.24	13.03
880.12	19.51	17.38	13.37
717.92	17.89	16.85	13.72
690.61	19.72	17.36	14.06
648.17	17.37	17.75	14.41
646.64	17.71	16.70	14.75
604.27	17.80	17.04	15.10
600.07	17.73	16.51	15.44

440.77	15.40	17.51	19.41
436.87	17.93	17.42	19.83
433.17	20.72	17.33	20.17
429.65	18.27	17.28	20.32
426.31	15.39	17.24	20.71
423.15	18.31	17.20	20.91
420.16	18.31	17.17	21.07
417.34	17.76	17.14	21.21
414.68	17.43	17.12	21.34
412.17	19.13	17.10	21.47
409.80	19.31	17.08	21.58
407.56	20.39	17.07	21.68
405.44	23.44	17.06	21.77
403.43	21.93	17.05	20.47
401.53	21.70	17.75	21.41
399.73	22.46	17.51	21.84
398.03	22.38	17.24	22.01
396.42	22.31	16.66	22.35
394.77	23.02	17.07	22.70
393.71	23.06	17.53	23.04
392.05	26.17	17.61	23.37
390.5	27.41	17.85	23.73
388.82	28.60	18.04	24.08
387.49	29.87	17.36	24.42
386.07	30.43	17.09	24.77
384.23	33.05	17.65	25.11
382.71	34.49	17.54	25.46
381.58	36.27	17.67	25.80
380.20	38.22	17.87	26.15
378.91	41.51	17.46	26.47
377.67	44.66	17.65	26.84
376.37	48.49	17.67	27.15
375.16	52.85	17.63	27.53
374.00	59.17	17.05	27.87
372.73	91.64	17.14	28.22
371.32	742.45	17.82	28.56
370.50	1071.44	17.58	28.91
369.66	864	17.55	29.45
368.79	3.1	17.70	29.99
367.83	3.24	17.72	30.53
366.86	-10234.36	17.31	30.88
365.82	1694.16	17.89	31.22
363.38	1697.11	17.53	31.57
360.42	1685.58	17.43	31.91
357.49	1364.26	15.04	32.26
356.61	743.21	18.14	32.60
359.23	-779.71	17.58	32.95
352.55	-2729.24	17.26	33.29
350.76	-7701.61	17.58	33.64
347.39	-10821.06	17.68	33.99
347.23	-8517.24	16.26	34.32
344.14	-7810.33	17.92	34.65
341.32	-6471.02	17.69	35.02
341.27	-4207.48	17.53	35.37
338.73	-3124.87	17.85	35.71
337.87	-659.45	17.80	36.06
334.02	427.16	17.52	36.40
33[illegible]	1[illegible]	18.01	36.79
330.13	1477.21	17.54	37.09
328.14	1540.45	17.52	37.44
326.02	1496.79	17.78	37.79
324.20	1651.08	17.72	38.13
323.48	1648.77	17.35	38.47
321.78	1991.65	16.47	38.82

[illegible]	[illegible]	[illegible]	[illegible]
288.13	1[illegible]4.94	38.53	42.73
304.17	1[illegible]3.[illegible]	40.94	40.34
302.43	1241.08	39.43	40.64
330.54	1198.83	36.47	41.25
340.44	1157.77	34.38	39.98
307.76	1141.07	40.56	41.33
[illegible]	[illegible]	37.71	42.[illegible]
[illegible]	[illegible]	[illegible]	[illegible]
[illegible]	1033.[illegible]	40.39	42.[illegible]
[illegible]	[illegible]	41.57	[illegible]
324.58	984.[illegible]	39.01	43.[illegible]
322.64	943.03	39.43	44.20
320.60	921.26	39.25	44.04
320.36	890.76	39.30	44.45
317.65	870.02	39.33	45.03
317.34	857.43	39.91	45.38
316.61	839.11	39.30	45.72
316.53	806.50	39.76	46.07
316.80	783.57	40.00	46.41
318.26	732.31	40.30	46.76
315.62	717.62	40.00	47.10
313.85	700.23	40.21	47.47
313.71	693.52	40.93	47.79
312.38	681.48	41.78	48.14
308.70	663.90	41.95	48.48
308.97	613.63	42.21	48.83
310.04	604.70	42.16	49.17
306.77	594.96	43.14	49.52
306.69	585.79	43.89	49.86
304.78	585.34	44.06	50.21
305.24	581.73	44.54	50.55
303.76	573.23	45.71	50.90
302.02	573.81	46.34	51.24
299.40	566.76	47.05	51.59
300.15	563.51	48.17	51.93
297.41	564.98	49.89	52.28
298.65	561.96	50.55	52.62
292.94	546.96	51.52	52.97
295.98	545.48	53.05	53.31
294.88	534.89	55.22	53.66
291.09	523.14	55.34	54.00
288.08	518.76	56.97	54.35
290.90	515.00	59.78	54.69
288.10	502.66	63.48	55.04
291.97	505.66	66.83	55.38
290.29	505.73	69.95	55.73
289.37	497.46	72.69	56.07
284.77	491.32	77.26	56.42
287.32	475.59	81.42	56.77
285.21	466.59	87.87	57.11
285.42	465.33	94.22	57.46
286.40	445.26	100.51	57.80
284.11	472.21	104.48	58.15
282.58	461.31	113.09	58.47
281.79	484.44	153.60	58.84
280.87	467.41	1186.59	59.18
281.51	471.52	1294	59.59
280.79	481.63	12	60.[illegible]
279.14	444.16	96	60.60
276.68	436.26	-510.74	61.18
281.04	452.07	-101.63	61.52
276.85	443.92	-330.73	61.87
272.44	441.34	-3939.50	62.21
272.61	433.53	-3065.49	62.56

[illegible]	[illegible]	[illegible]	[illegible]
[illegible]	[illegible]	[illegible]	[illegible]
[illegible]	[illegible]	[illegible]	63.56
[illegible]	[illegible]	[illegible]	[illegible]
[illegible]	[illegible]	[illegible]	[illegible]
[illegible]	[illegible]	[illegible]	[illegible]
269.61	[illegible]	418.34	64.94
[illegible]	[illegible]	[illegible]	[illegible]
[illegible]	[illegible]	[illegible]	[illegible]
[illegible]	[illegible]	[illegible]	[illegible]
[illegible]	[illegible]	[illegible]	[illegible]
266.36	[illegible]	[illegible]	[illegible]
266.04	413.37	[illegible]	[illegible]
265.29	403.87	650.06	67.37
264.52	409.01	655.69	[illegible]
263.77	405.57	657.33	68.06
264.44	403.98	656.42	68.40
262.72	401.06	653.51	68.77
262.57	399.28	649.18	69.12
261.99	398.07	630.56	69.46
261.35	395.37	622.15	69.81
260.64	394.46	617.52	70.15
260.03	390.36	609.52	70.50
259.62	390.33	601.60	70.84
258.71	389.28	595.48	71.19
259.10	388.80	588.53	71.53
258.27	386.64	581.76	71.88
257.24	384.69	575.29	72.22
256.90	380.02	569.34	72.57
256.58	377.25	563.27	72.91
256.29	378.04	554.52	73.26
255.38	375.20	548.95	73.60
255.53	377.52	543.40	73.95
254.48	374.77	539.54	74.29
254.36	374.13	535.66	74.64
253.52	372.62	531.87	74.98
253.20	372.10	528.29	75.33
252.40	371.53	523.05	75.67
251.96	368.21	520.05	76.02
251.44	366.68	517.66	76.36
251.20	366.84	515.84	76.71
250.95	367.39	513.97	77.05
250.14	362.37	511.67	77.40
250.34	364.24	508.77	77.75
249.36	362.35	506.22	78.09
249.09	359.00	503.41	78.44
248.13	356.13	500.81	78.78
247.74	353.90	497.95	79.13
247.25	356.87	495.26	79.47
246.96	350.76	492.33	79.82
246.86	355.00	489.59	80.16
245.68	353.90	486.63	80.51
245.09	352.58	483.89	80.85
245.32	349.76	481.12	81.20
244.97	349.51	478.24	81.54
244.56	348.57	475.42	81.89
243.92	341.13	472.48	82.23
[illegible]	[illegible]	470.54	82.58
[illegible]	[illegible]	[illegible]	82.93
242.07	[illegible]	[illegible]	83.27
242.10	338.17	462.04	83.62
241.07	[illegible]	459.82	83.96
241.15	333.69	456.70	84.31
240.34	[illegible]	[illegible]	[illegible]

[illegible]	[illegible]	[illegible]	83.00
239.04	[illegible]	[illegible]	83.34
239.18	[illegible]	[illegible]	83.69
239.32	[illegible]	[illegible]	84.03
239.46	[illegible]	[illegible]	84.38
239.60	[illegible]	[illegible]	84.72
239.74	[illegible]	[illegible]	85.07
239.88	[illegible]	[illegible]	85.41
240.02	[illegible]	[illegible]	85.76
240.16	[illegible]	[illegible]	86.10
240.30	[illegible]	[illegible]	86.45
240.44	[illegible]	[illegible]	86.80
240.58	[illegible]	[illegible]	87.14
240.72	[illegible]	[illegible]	87.49
240.86	[illegible]	[illegible]	87.84
241.00	[illegible]	[illegible]	88.18
241.14	[illegible]	[illegible]	88.53
241.28	[illegible]	[illegible]	88.88
241.42	[illegible]	[illegible]	89.22
241.56	[illegible]	[illegible]	89.57
241.70	[illegible]	[illegible]	89.92
241.84	[illegible]	[illegible]	90.26
241.98	[illegible]	[illegible]	90.61
242.12	[illegible]	[illegible]	90.96
242.26	[illegible]	[illegible]	91.31
242.40	[illegible]	[illegible]	91.65
242.54	[illegible]	[illegible]	92.00
242.68	[illegible]	[illegible]	92.35
242.82	[illegible]	[illegible]	92.70
242.96	[illegible]	[illegible]	93.04
243.10	[illegible]	[illegible]	93.39
243.24	[illegible]	[illegible]	93.74
243.38	[illegible]	[illegible]	94.09
243.52	[illegible]	[illegible]	94.43
243.66	[illegible]	[illegible]	94.78
243.80	[illegible]	[illegible]	95.13
243.94	[illegible]	[illegible]	95.48
244.08	[illegible]	[illegible]	95.83
244.22	[illegible]	[illegible]	96.17
244.36	[illegible]	[illegible]	96.52
244.50	[illegible]	[illegible]	96.87
244.64	[illegible]	[illegible]	97.22

[illegible]	283.53	353.74	106.41
[illegible]	281.83	350.60	106.76
216.84	282.09	349.37	107.11
[illegible]	281.31	348.21	107.45
[illegible]	280.51	347.13	107.80
215.68	279.79	345.96	108.14
215.31	279.17	344.76	108.48
215.07	278.64	343.79	108.83
214.97	277.66	342.85	109.18
214.67	276.86	341.83	109.52
214.38	276.12	340.82	109.87
214.06	275.44	339.89	110.21
213.79	274.71	338.80	110.56
213.47	274.12	337.47	110.91
213.17	273.39	336.51	111.25
212.85	272.95	335.50	111.60
212.56	272.27	334.46	111.94
212.33	271.59	333.50	112.29
212.00	270.93	332.59	112.63
211.74	270.32	331.67	112.98
211.42	269.73	330.73	113.32
211.15	269.19	329.77	113.67
210.88	268.56	328.83	114.01
210.58	267.83	327.89	114.36
210.26	266.97	327.07	114.71
209.99	265.80	326.22	115.05
209.69	268.27	325.33	115.40
209.52	263.28	324.41	115.74
209.10	266.75	323.47	116.09
208.84	265.02	322.56	116.43
208.83	264.80	321.81	116.79
208.24	263.67	320.89	117.12
207.95	262.06	320.05	117.47
207.83	262.43	319.25	117.81
207.87	260.86	318.35	118.16
207.26	263.62	317.53	118.50
206.25	257.27	316.64	118.85
206.57	260.89	315.79	119.20
206.42	259.32	314.90	119.54
206.02	259.54	314.10	119.89
205.78	256.02	313.23	120.23
205.93	257.63	312.41	120.58
205.16	254.06	311.63	120.92
205.04	256.07	310.76	121.27
204.77	256.53	309.76	121.61
204.42	254.92	309.12	121.96
204.10	256.51	308.39	122.31
203.88	255.69	307.59	122.69
203.57	254.38	306.77	123.00
203.71	254.11	305.99	123.34
203.04	253.60	305.19	123.69
202.74	253.00	304.42	124.03
202.57	252.74	303.64	124.38
202.32	251.48	302.77	124.72
202.04	251.37	302.03	125.07
201.31	250.93	301.19	125.42
201.51	250.24	300.46	125.76

APPENDIX C

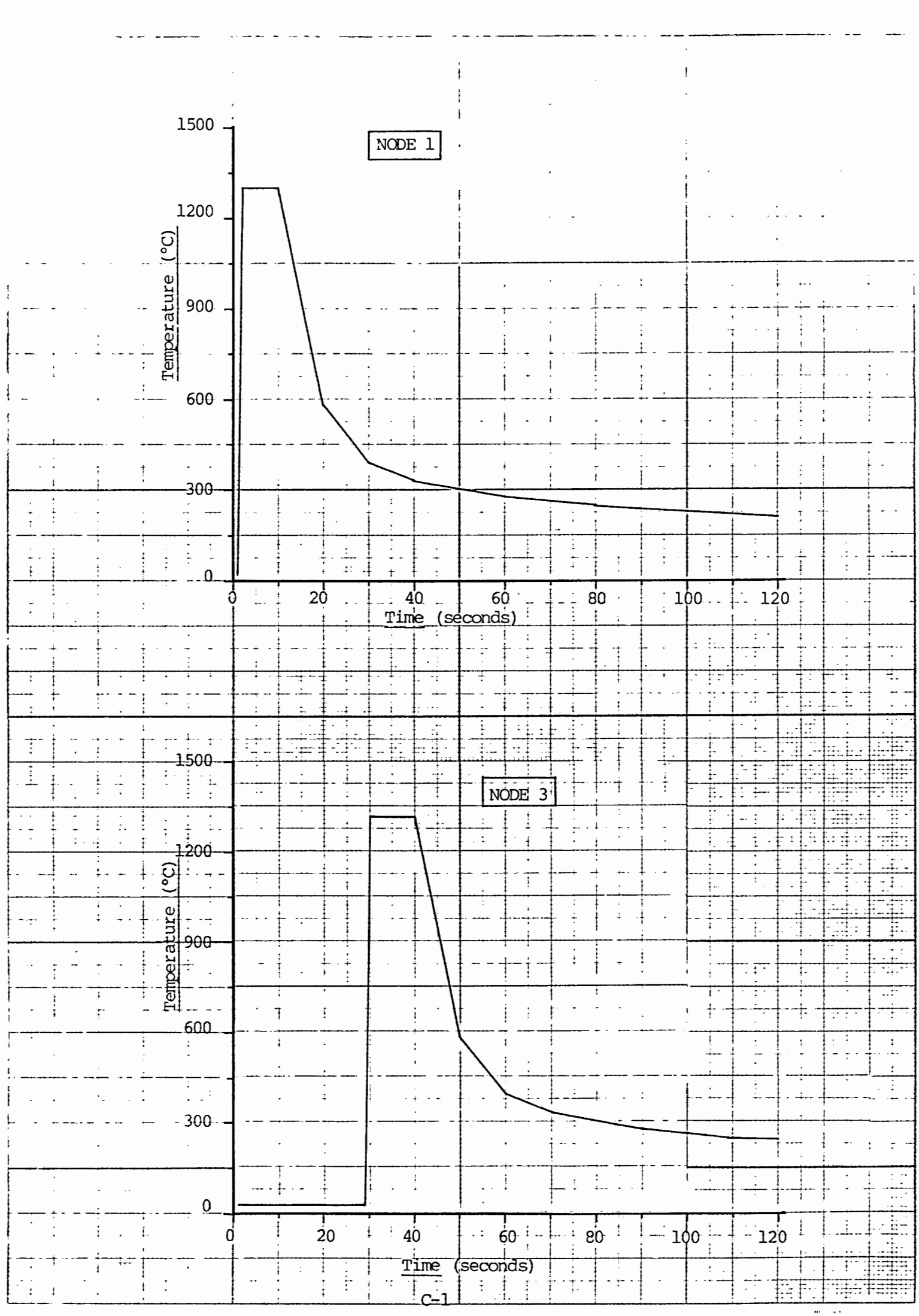
NODE 1
1500
1200
900
600
300
0
Temperature (°C)
0
20
40
60
80
100
120
Time (seconds)
NODE 3
1500
1200
900
600
300
0
Temperature (°C)
0
20
40
60
80
100
120
Time (seconds)

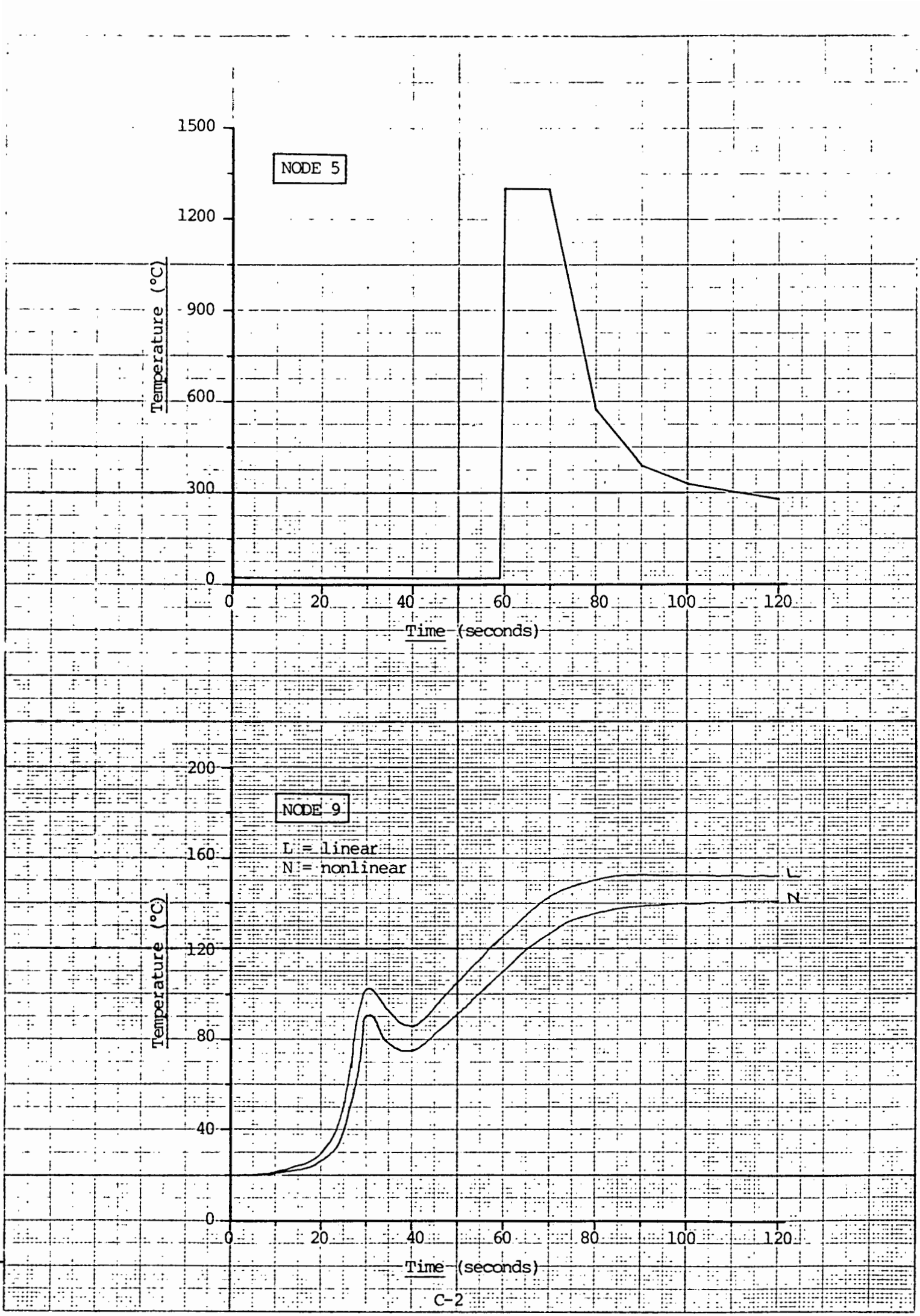
NODE 5
1500
1200
900
600
300
0
Temperature (°C)
0
20
40
60
80
100
120
Time (seconds)
NODE 9
L = linear
N = nonlinear
200
160
120
80
40
0
Temperature (°C)
L
N
0
20
40
60
80
100
120
Time (seconds)

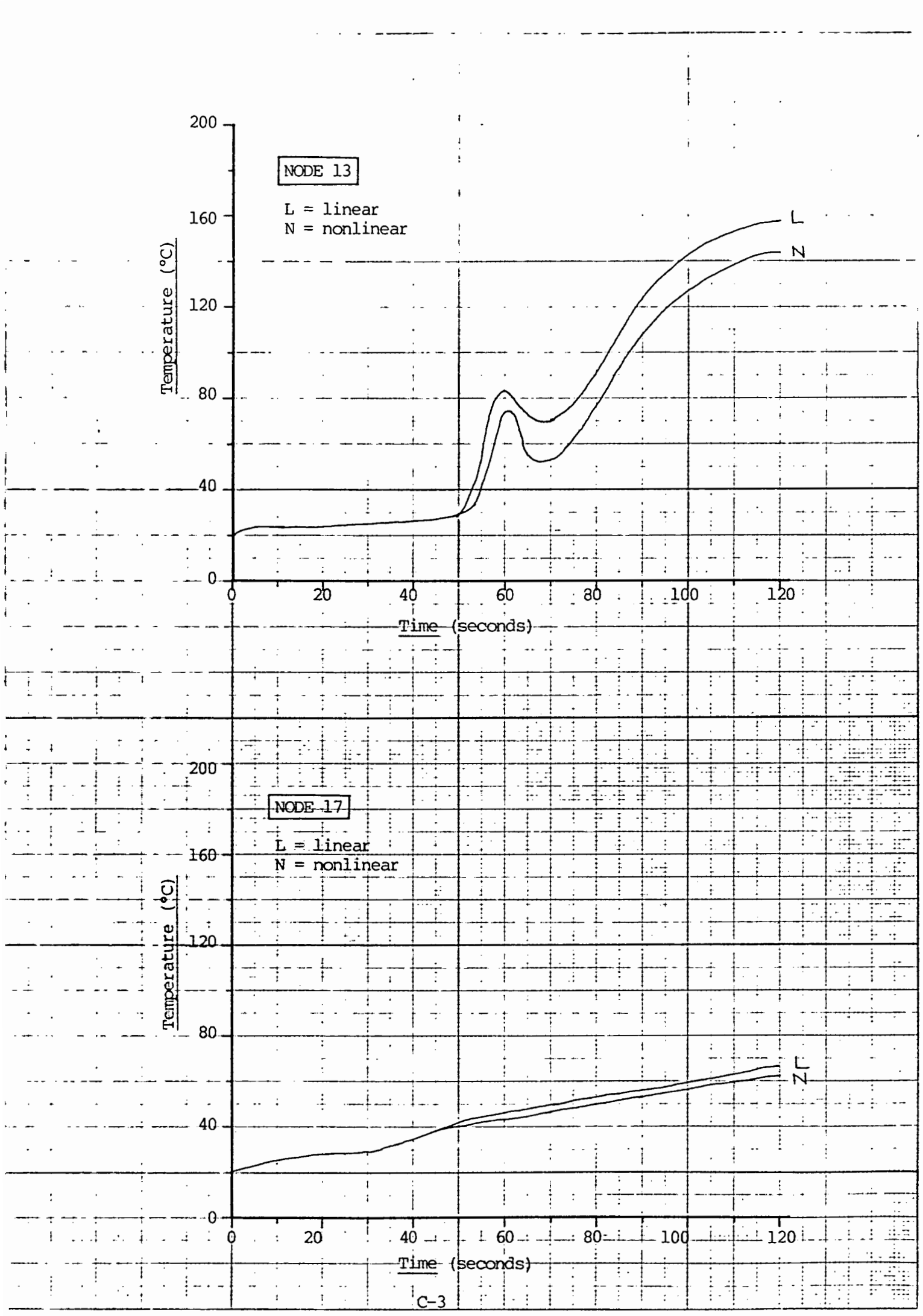
NODE 13
L = linear
N = nonlinear
Temperature (°C)
200
160
120
80
40
0
0
20
40
60
80
100
120
Time (seconds)
L
N
NODE 17
L = linear
N = nonlinear
Temperature (°C)
200
160
120
80
40
0
0
20
40
60
80
100
120
Time (seconds)
L
N

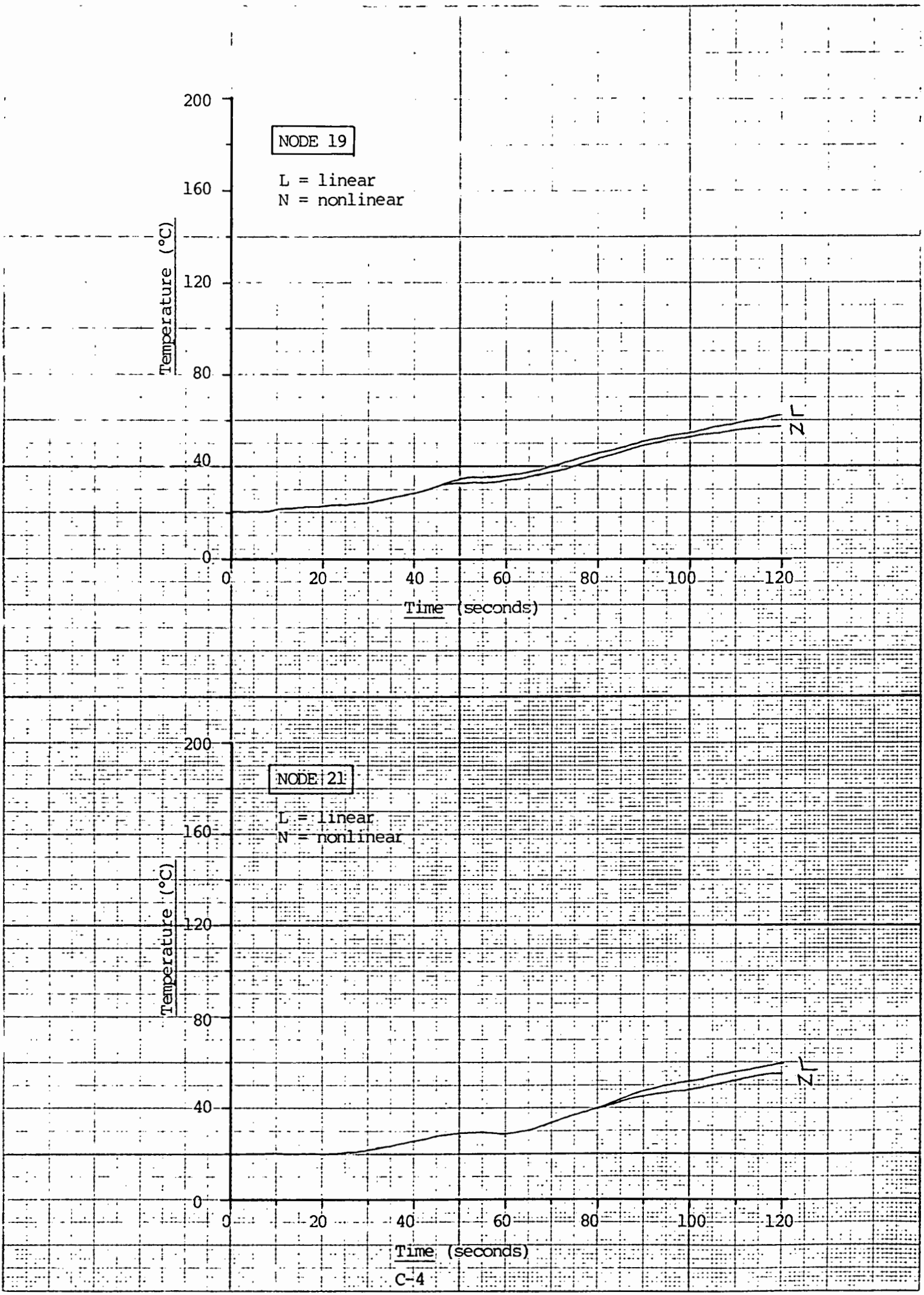
NODE 19
L = linear
N = nonlinear
Temperature (°C)
200
160
120
80
40
0
0
20
40
60
80
100
120
Time (seconds)
L
N
NODE 21
L = linear
N = nonlinear
Temperature (°C)
200
160
120
80
40
0
0
20
40
60
80
100
120
Time (seconds)
L
N

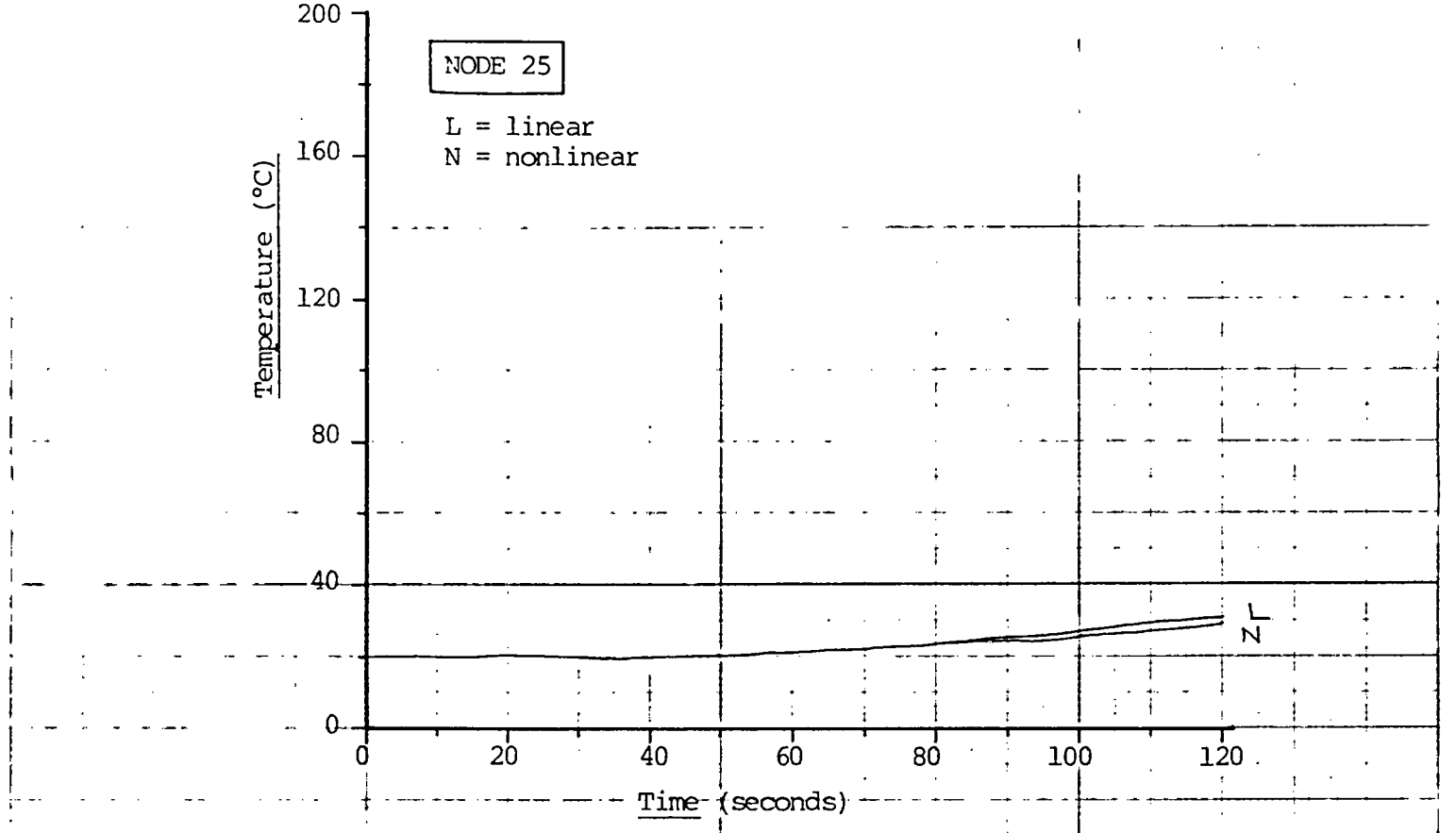
NODE 25
L = linear
N = nonlinear
Temperature (°C)
200
160
120
80
40
0
0
20
40
60
80
100
120
Time (seconds)
L
N

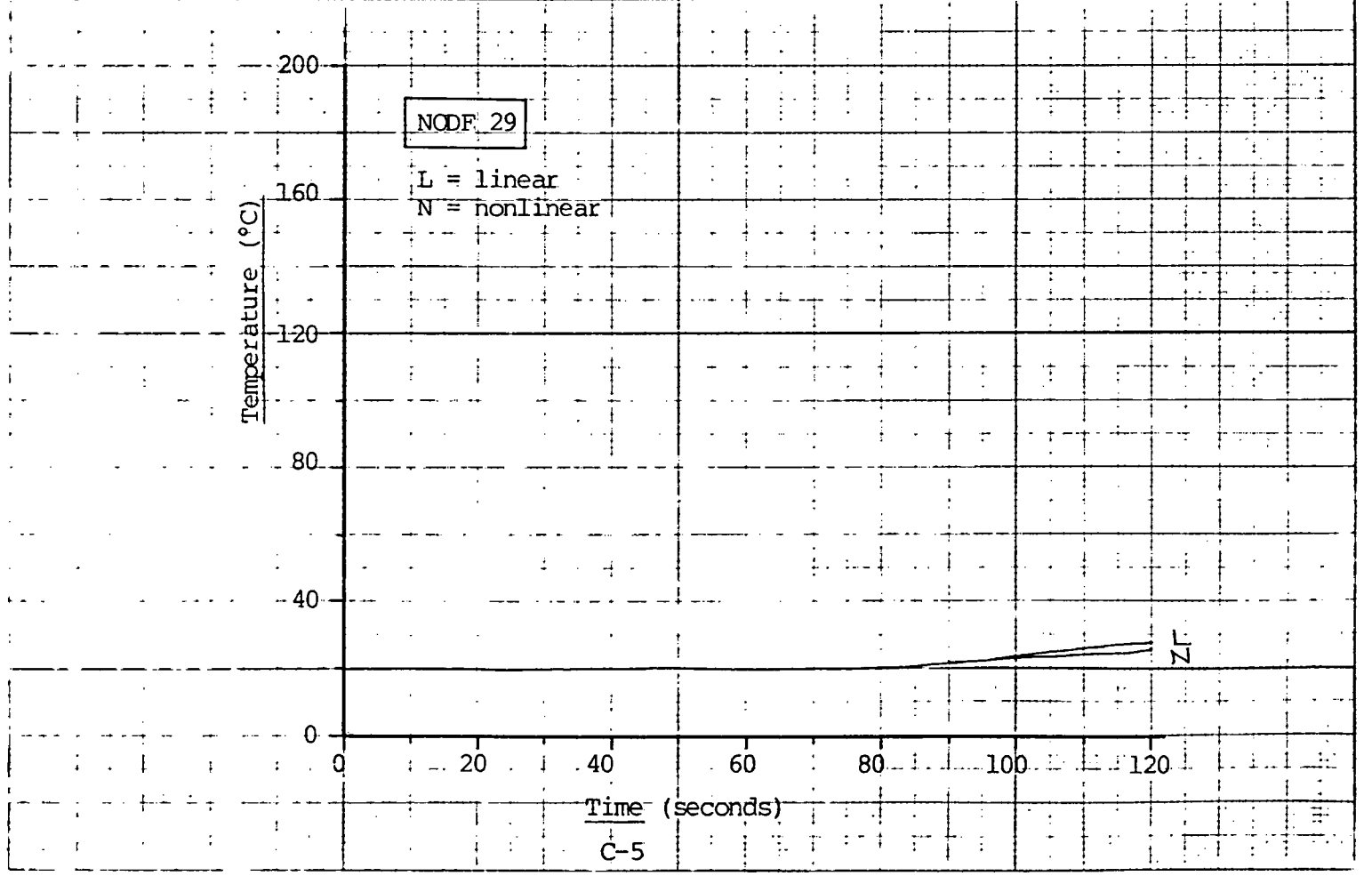
NODE 29
L = linear
N = nonlinear
Temperature (°C)
200
160
120
80
40
0
0
20
40
60
80
100
120
Time (seconds)
L
N

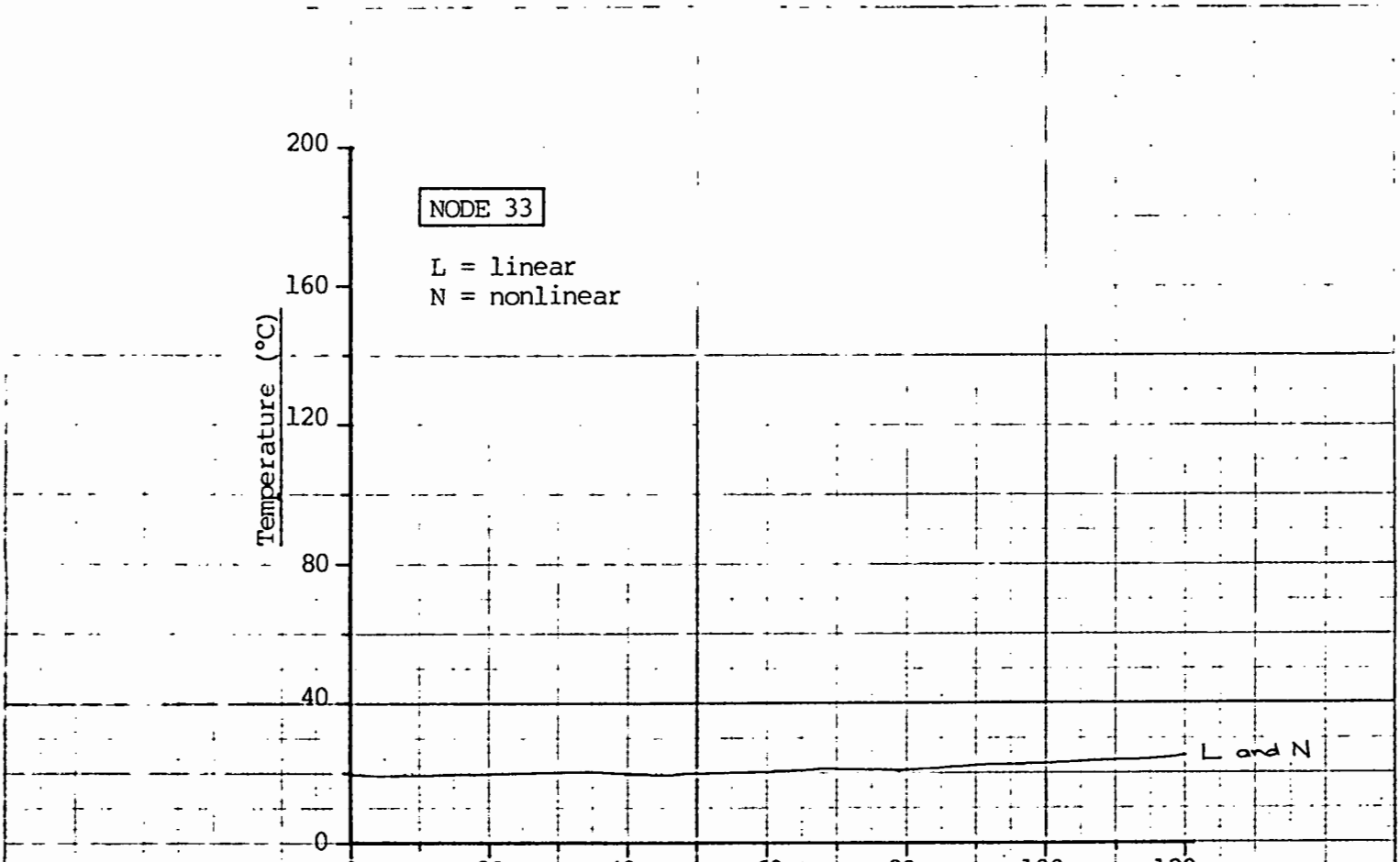
NODE 33
L = linear
N = nonlinear
Temperature (°C)
200
160
120
80
40
0
0
20
40
60
80
100
120
Time (seconds)
L and N

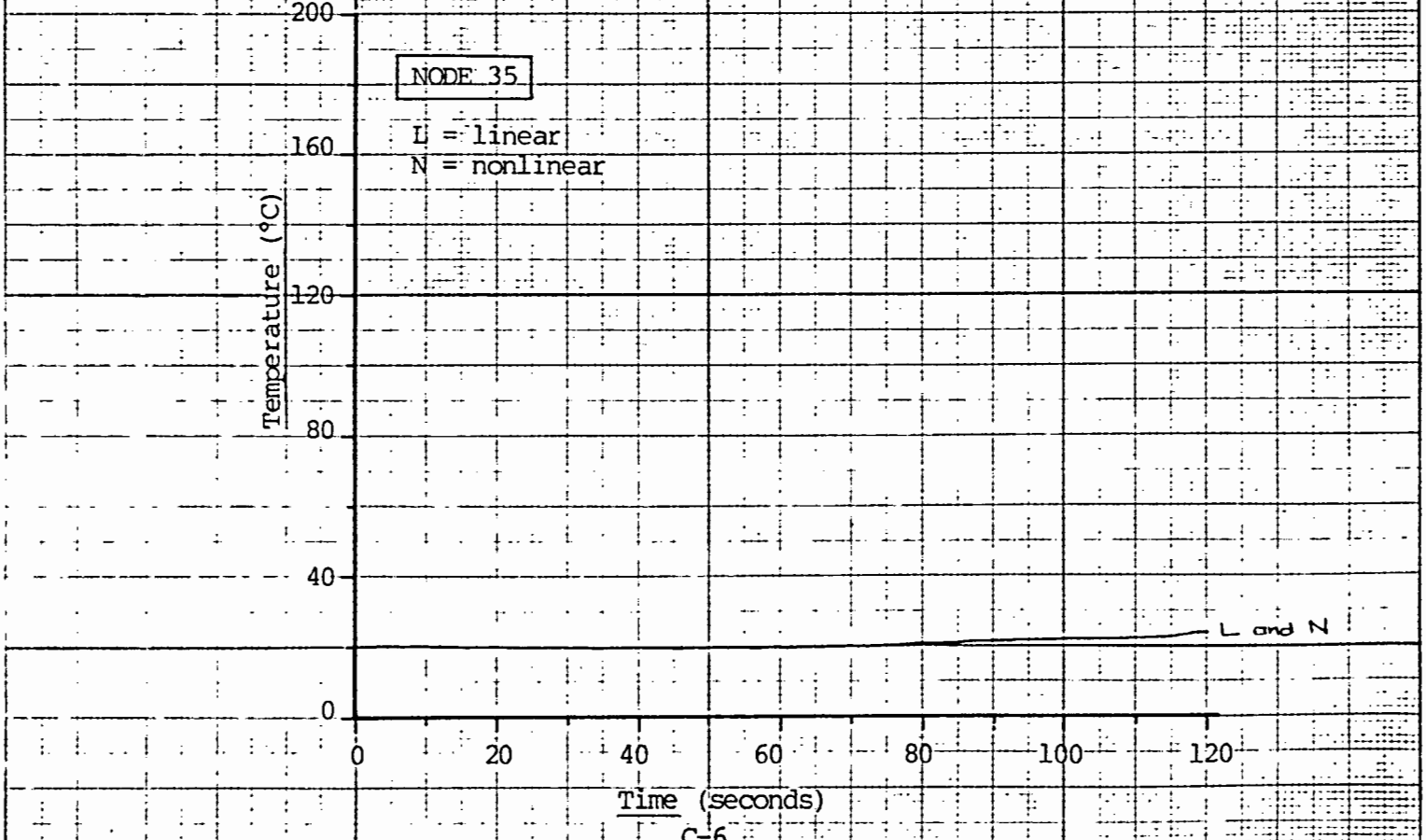
NODE 35
L = linear
N = nonlinear
Temperature (°C)
200
160
120
80
40
0
0
20
40
60
80
100
120
Time (seconds)
L and N

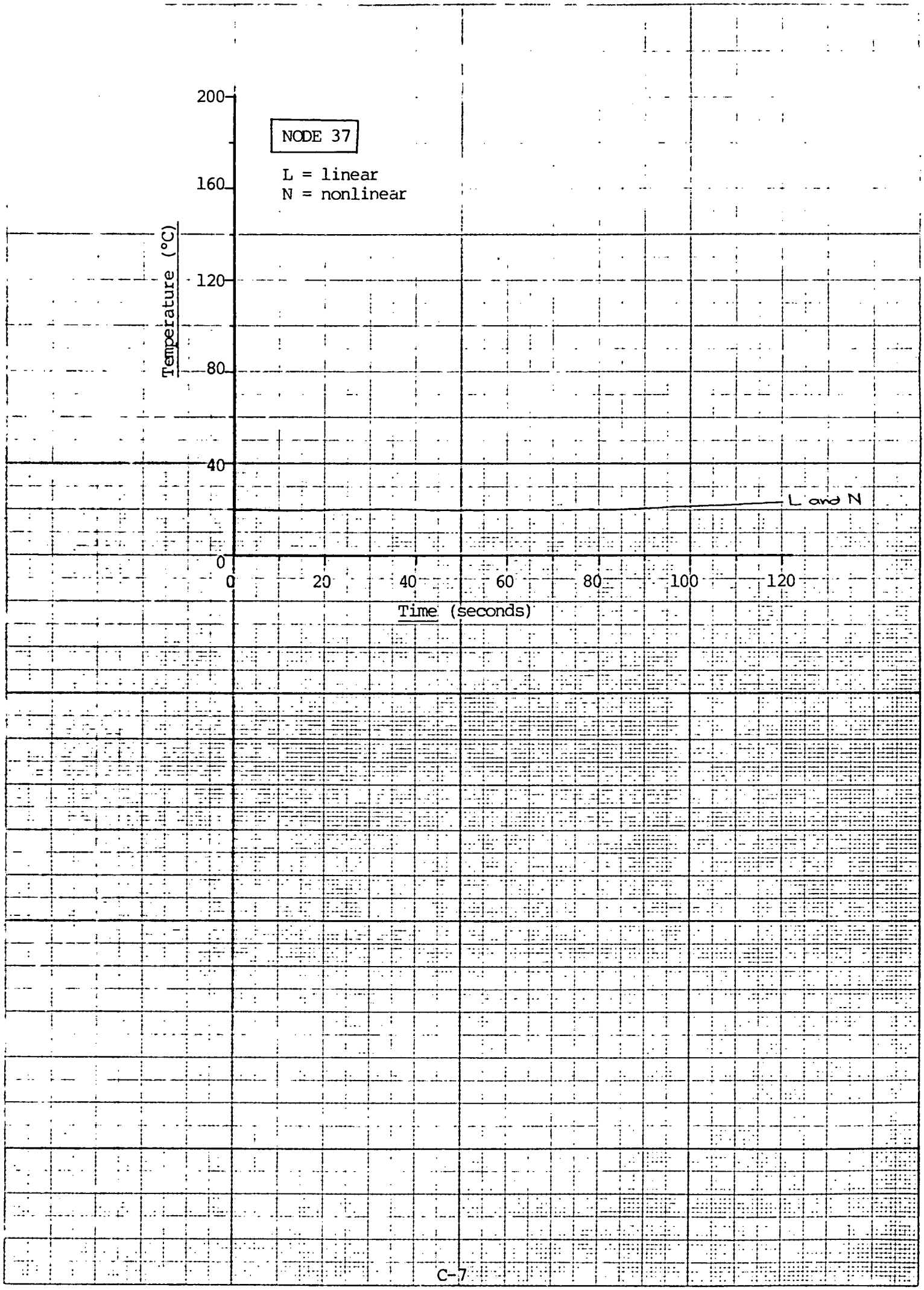
NODE 37
L = linear
N = nonlinear
Temperature (°C)
200
160
120
80
40
0
0
20
40
60
80
100
120
Time (seconds)
L and N

DATE/TIME: 13 – 10 – 1983 (11h30) SETUP NAME: "RUN 3" (11,5 mm hole) TEST AREA: Dept. Metallurgy, U.C.T.

LABEL	SLOT/CARD TYPE	CARD TERMINALS	CHANNEL	TYPE OF TRANSDUCTER	FUNCTION	VALUES			COMMENTS, LOCATION, ACTION, ETC.
						MIN	TYP.	MAX	
Black	T. Card *	1	6	K-type thermocouple	°C	20°C		1300°C	Location : 1
Green	T. Card	2	8	K-type thermocouple	°C	20°C		1300°C	Location : 2
									(See sketch)

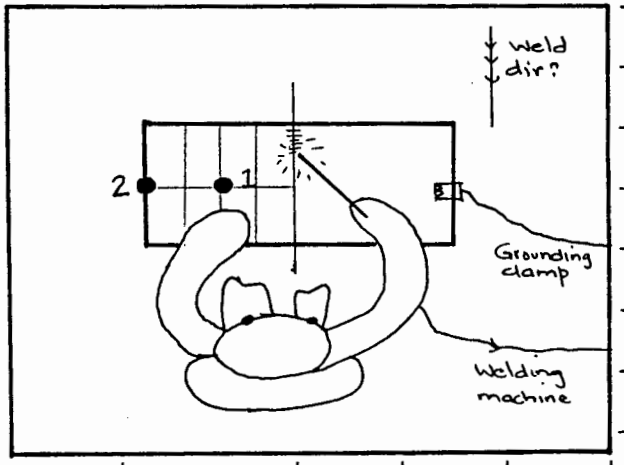

* T. Card = Thermocouple Card 44422A (Hewlett-Packard)

DATE/TIME: 13-10-83 (12h30) SETUP NAME: "RUN 4" (11,5mm hole) TEST AREA: Dept. Metallurgy, U.C.T.

LABEL	SLOT/CARD TYPE	CARD TERMINALS	CHANNEL	TYPE OF TRANSDUCTER	FUNCTION	VALUES			COMMENTS, LOCATION, ACTION, ETC.
						MIN	TYP.	MAX	
Black	T. Card *	1	6	K-type thermocouple	°C	20°C		1300°C	Location : 1
Green	T. Card	2	8	K-type thermocouple	°C	20°C		1300°C	Location : 2
									(See sketch)

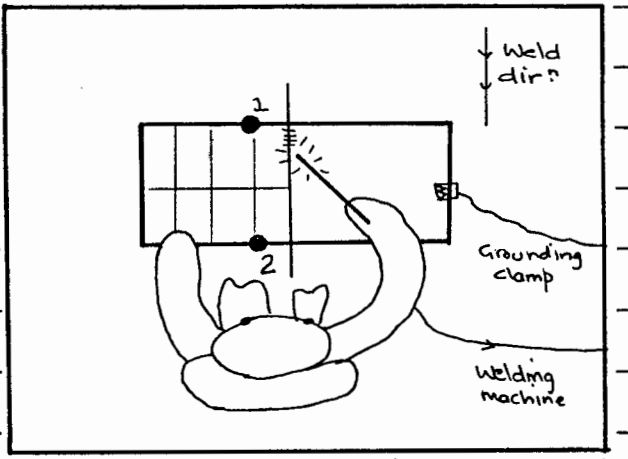

* T. Card = Thermocouple card 44422A (Hewlett-Packard)

C.3 TABULATION OF THE VALUES OF THE DISCRETIZED "STANDARD" CURVE (GRAPH 12A)

Time (sec)	Temperature (°C)	Temp/1300
0	0	0
1	20	0.015
2	1300	1.0
12	1300	1.0
20	578	0.444
30	390	0.300
40	330	0.254
60	280	0.215
80	246	0.189
120	206	0.158

APPENDIX D

D.1 TABULATION OF DISCRETIZED VALUES FROM THE CURVES SHOWN IN APPENDIX C

	Time (sec)	Temperature (°C)	Temp/1300
NODE 1	0	0	0
	1	20	0.015
	2	1300	1
	10	1300	1
	20	578	0.444
	30	390	0.3
	40	330	0.254
	60	280	0.215
	80	246	0.189
	120	206	0.158
NODE 2	0	0	0
	1	20	0.015
	29	20	0.015
	30	1300	1
	40	1300	1
	50	578	0.444
	60	390	0.3
	70	330	0.254
	90	280	0.215
	110	246	0.189
	120	231	0.178
NODE 3	0	0	0
	1	20	0.015
	59	20	0.015
	60	1300	1
	70	1300	1

	Time(sec)	Temperature (°C)	Temp/1300
	80	578	0.444
	90	390	0.3
	100	330	0.254
	120	280	0.215
NODE 4	0	0	0
	1	20	0.015
	10	24	0.018
	20	24	0.018
	60	112	0.086
	80	138	0.106
	120	144	0.111
NODE 5	0	0	0
	1	24	0.018
	50	24	0.038
	70	52	0.040
	100	128	0.098
	120	144	0.111
NODE 6	0	0	0
	1	20	0.015
	120	62	0.048
NODE 7	0	0	0
	1	20	0.015
	50	32	0.024
	120	58	0.045

	Time (sec)	Temperature (°C)	Temp/1300
NODE 8	0	0	0
	1	20	0.015
	30	20	0.015
	120	54	0.042
NODE 9	0	0	0
	1	20	0.015
	120	29	0.022
NODE 10	0	0	0
	1	20	0.015
	80	20	0.015
	120	25	0.019
NODE 11	0	0	0
	1	20	0.015
	80	20	0.015
	120	25	0.019
NODE 12	0	0	0
	1	20	0.015
	80	20	0.015
	120	24	0.018
NODE 13	0	0	0
	1	20	0.015
	90	20	0.015
	120	23	0.017

D2. TABULATION OF THE OUTPUT OF THE STRESS FROM ADINA FOR THE 13 NODED MODEL

	σ_{yy} (MPa)			
t(sec)	GP1	GP2	GP7	GP8
10	45.4	194	45.5	194
20	15.9	76.8	15.3	76.8
30	-145	-143	-283	-280
40	-130.8	-128.3	-141.9	-136.6
50	118	124.8	102.2	113.0
60	279.4	115.3	285.2	217.6
70	237.9	187.2	237.7	186.2
80	115.3	150.8	117.0	148.3
90	88.9	132.3	89.3	131.7
100	78.4	116.2	78.4	116.1
110	75.9	109.4	75.8	109.2
120	72.3	100.8	72.2	100.7

D3. SKETCHES OF EXPERIMENTAL FRAME

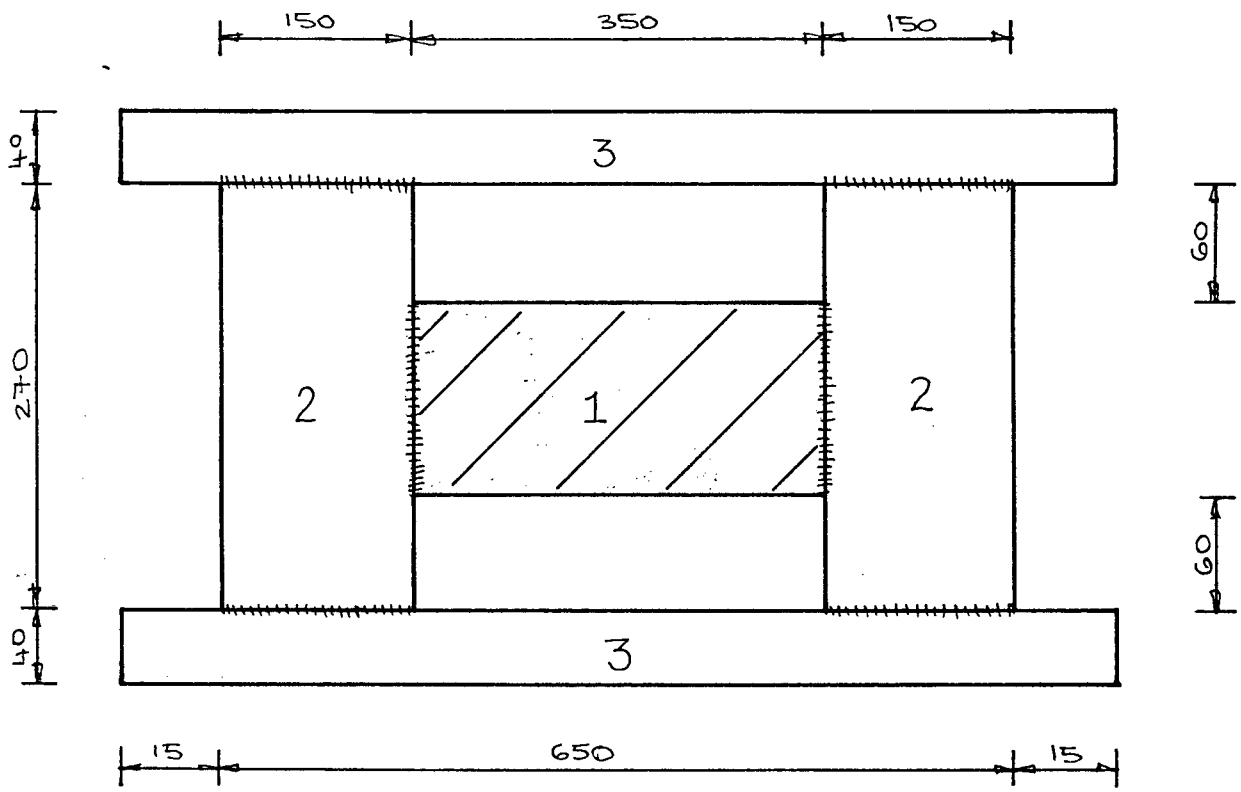

PLAN

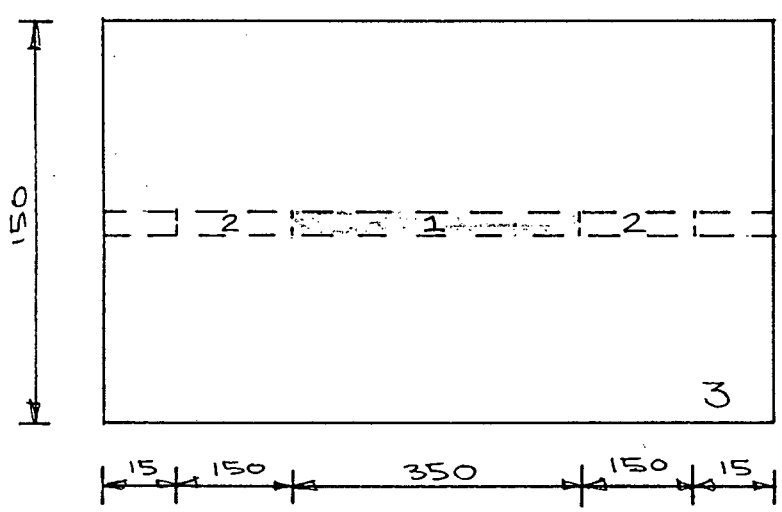

SIDE VIEW

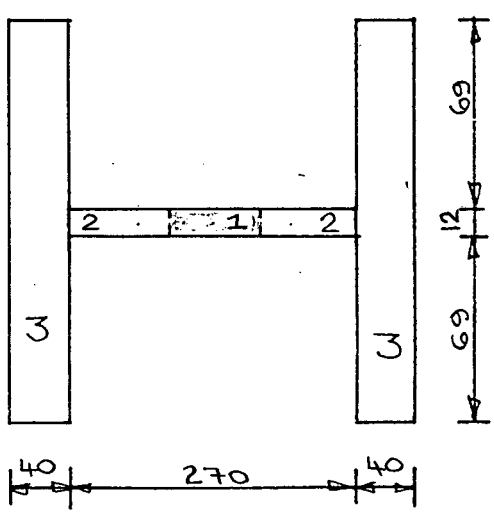

EDGE VIEW

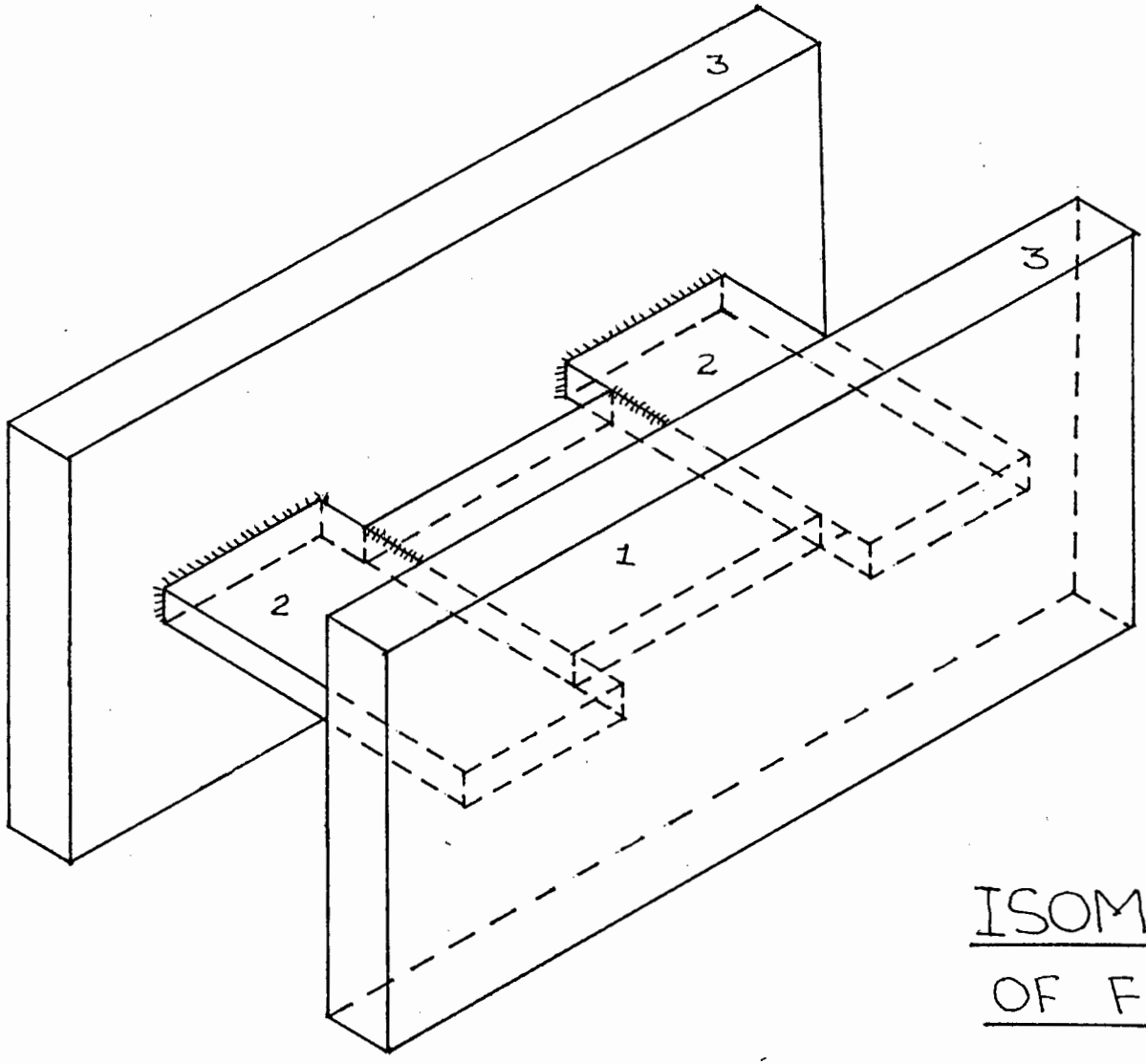

ISOMETRIC VIEW OF FRAME

D4. TABULATION OF THE STRESS OUTPUT AS MEASURED BY THE HP DATA LOGGER

	σ_{yy} (MPa)			
t(sec)	GP1	GP2	GP7	GP8
10	5.67	-1.47	-5.25	5.25
20	33.18	-2.31	-6.72	10.08
30	107.94	-1.89	-5.04	14.07
40	129.15	-7.14	-1.05	17.01
50	137.55	15.12	5.04	19.32
60	137.76	91.98	11.97	16.17
70	135.87	118.65	18.06	14.28
80	133.98	123.06	18.27	11.76
90	131.88	131.88	18.48	12.18
100	126.84	136.92	18.27	12.81
110	126.00	139.44	18.27	13.44
120	122.01	132.72	18.27	14.28
Steady state	42	52	32	36

D5. TABULATION OF THE OUTPUT STRESS FROM ADINA FOR THE 37-NODED MODEL

	σ_{yy} (MPa)			
t(sec)	GP1	GP2	GP7	GP8
10	-66.8	-64.5	-6.1	-8.3
20	-99.7	-49.7	-93	-25.26
30	208.1	232.0	20.0	36.33
40	164.09	-47.6	21.2	-1.70
50	-50.7	-99.8	17.27	-84.2
60	-82.1	212.1	35.2	35.6
70	-53.1	125.8	43.2	58.3

D6. EXAMPLE OF DATA LOGGER OUTPUT

```
-----------------------------------------------
SCAN NUMBER  6

TIME ELAPSED      46 SECONDS
Channel 20    615 Microstrain
Channel 21   -34 Microstrain
Channel 22   -5 Microstrain
Channel 23    81 Microstrain
-----------------------------------------------
SCAN NUMBER  7

TIME ELAPSED      55 SECONDS
Channel 20    655 Microstrain
Channel 21    72 Microstrain
Channel 22    24 Microstrain
Channel 23    92 Microstrain
-----------------------------------------------
SCAN NUMBER  8

TIME ELAPSED      64 SECONDS
Channel 20    656 Microstrain
Channel 21    438 Microstrain
Channel 22    57 Microstrain
Channel 23    77 Microstrain
-----------------------------------------------
SCAN NUMBER  9

TIME ELAPSED      74 SECONDS
Channel 20    647 Microstrain
Channel 21    565 Microstrain
Channel 22    86 Microstrain
Channel 23    68 Microstrain
-----------------------------------------------
SCAN NUMBER  10

TIME ELAPSED      83 SECONDS
Channel 20    638 Microstrain
Channel 21    586 Microstrain
Channel 22    87 Microstrain
Channel 23    56 Microstrain
-----------------------------------------------
SCAN NUMBER  11

TIME ELAPSED      92 SECONDS
Channel 20    628 Microstrain
Channel 21    628 Microstrain
Channel 22    88 Microstrain
Channel 23    58 Microstrain
-----------------------------------------------
SCAN NUMBER  12

TIME ELAPSED     101 SECONDS
Channel 20    604 Microstrain
Channel 21    652 Microstrain
Channel 22    87 Microstrain
Channel 23    61 Microstrain
-----------------------------------------------
```

COURSES COMPLETED IN PARTIAL FULFILLMENT OF THE M.SC. (ENG) DEGREE AT THE UNIVERSITY OF CAPE TOWN

COURSES		DATE CREDITED	CREDITS
CE 524	Structural Dynamics	1982	3
CE 533	Bridge Engineering	1982	4
CE 551(a)	Frame Analysis	1982	2
CE 551(b)	Introduction to the Theory of Elasticity	1982	2
CE 551(c)	Plates and Shells	1982	2
CE 552(a)	Introduction to Finite Element Analysis	1982	2
CE 552(b)	Finite Element Analysis	1982	3
CE 554	Computer Aided Design	1982	3
		TOTAL	21

COURSE CREDITS : 21
THESIS CREDITS : 20
TOTAL : 41

TOTAL CREDIT REQUIREMENTS FOR THE M.SC. (ENG) DEGREE : 40

UNIVERSITY OF CAPE TOWN

DEPARTMENT OF CIVIL ENGINEERING

CE 524 - STRUCTURAL DYNAMICS

FINAL EXAMINATION 1982

This is a take-home examination. The paper will be handed out at 5.30 p.m. on Wednesday, November 3rd, and the completed project must be submitted to Mrs. V. Atkinson, Room 2, Department of Civil Engineering, Snape Building, before 4.30 p.m. on Wednesday, November 10th.

Candidates must include a declaration with their submission to the effect that the work is entirely their own, and that they have not consulted others in the process of preparing their answers.

Grades of 1st, 2nd and 3rd will not be given : the examination result will be either PASS or FAIL.

Attached to this paper is a schematic diagram of a frame of a five-storey building which is to be constructed in Cape Town. All the data is given in the diagram and a computer printout is attached which gives the frequencies and mode shapes for a number of lower modes.

Adopting a maximum ground acceleration of 0,18 g, and using Newmark's recommendations, construct a design spectrum which could be used as a basis for seismic design with 5% damping. Also, adopting a ductility factor of 2,5 , prepare an inelastic spectrum based on Newmark's recommendation.

Using this inelastic spectrum, find the maximum displacements and accelerations of the lowest *FOUR* modes of the structure. Hence estimate the maximum displacement at roof level and the maximum base shear.

Without carrying out any detailed calculations, describe fully how you would go about calculating the maximum bending moment in the ground floor column.

PROBLEM DATA

Mass: There is a lumped mass of 20 000 kg at each node together with a rotary-inertia of 12 000 kg m^2.

Beams:

$E = 250 \times 10^9$ N/m^2

$\nu = 0.25$

$\rho = 0.$

$I = 4.167 \times 10^{-3}$ m^4

$A = 0.2$ m^2.

$A_s = 0.167$ m^2

Shear Walls:

E, ν, ρ as for beams

thickness = 0.35 m

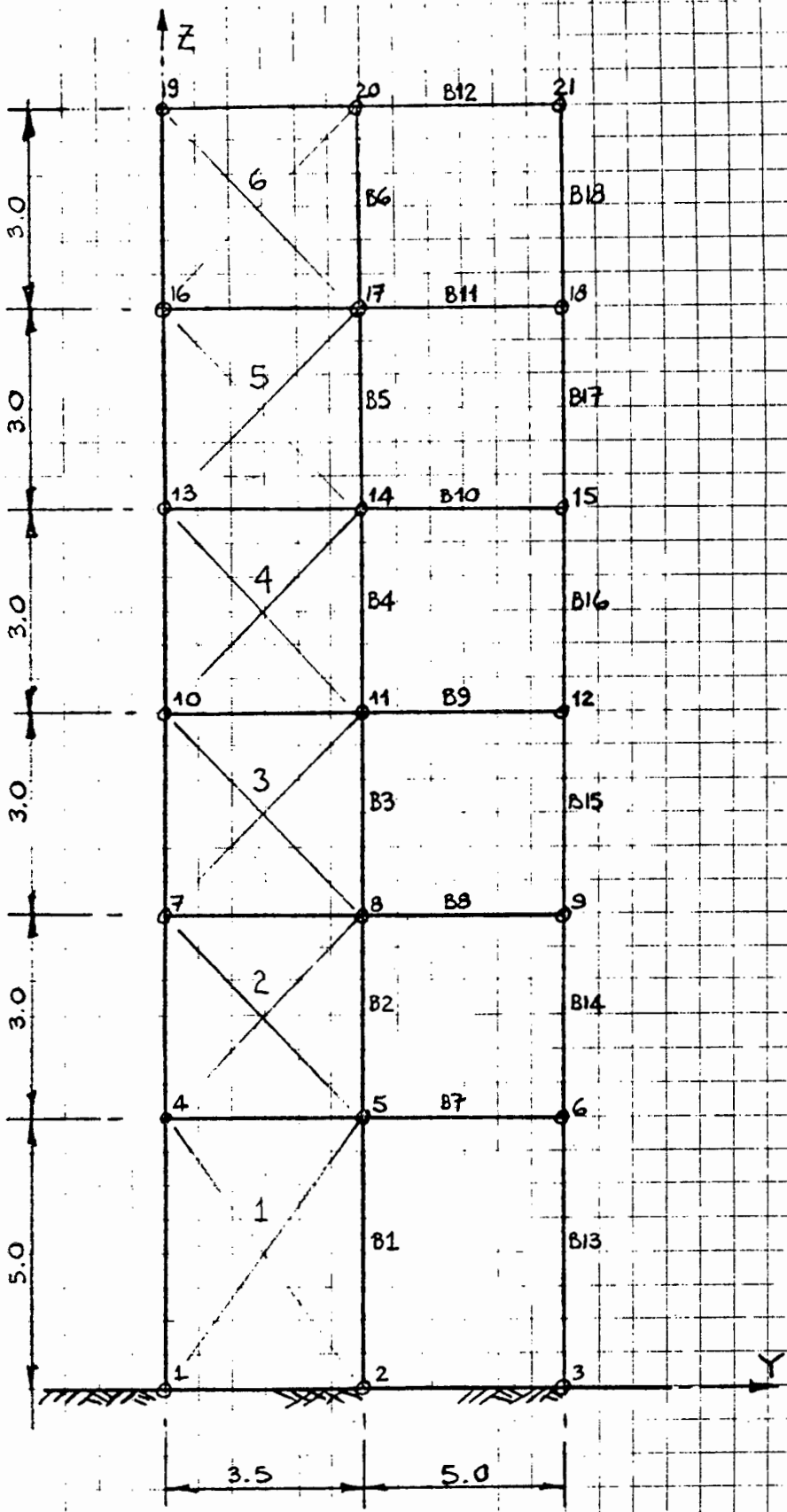

Plane Shear Wall Elements

B8 Beam/Column Elements

UNIVERSITY OF CAPE TOWN

DEPARTMENT OF CIVIL ENGINEERING

EXAMINATION, JUNE 1982

CE 533 - BRIDGE ENGINEERING

Time allowed: FOUR hours Examination Date: 26 June

OPEN BOOK

1. Write brief notes, of about one page, on each of the following topics:

   (a) categories of structural action and bridge types;

   (b) future of composite steel-concrete bridges in South Africa;

   (c) arch and suspension road bridges;

   (d) total cost of a major bridge;

   (e) continuity of bridge decks;

   (f) grillage analysis of bridge superstructures;

   (g) desirable features of expansion joints on bridge decks;

   (h) use of Corten steel for bridges;

   (i) the nature of railway traffic loading;

   (j) concept of loaded length of road bridges;

   (k) environmental aspects of bridges.

[6 marks each]

2. For each of the three bridge sites on the attached sheets, select the most suitable type of bridge structure and construction.

   (i) Draw adequate sketches of the superstructure, substructure and foundations directly on these sheets and hand them in.

   (ii) Describe the method of construction and write down any necessary further explanations in the examination book.

[12 marks each]

2. (a)/.....

2. (a) A straight and level two-lane road bridge, 12 m wide is required across a 2 km wide river basin. The river is to be dammed at a later stage to form a lake for water sport, which requires 10 m freeboard. Provision must be made for future widening of 4 m on each side. The site is 10 km from the south coast of Natal.

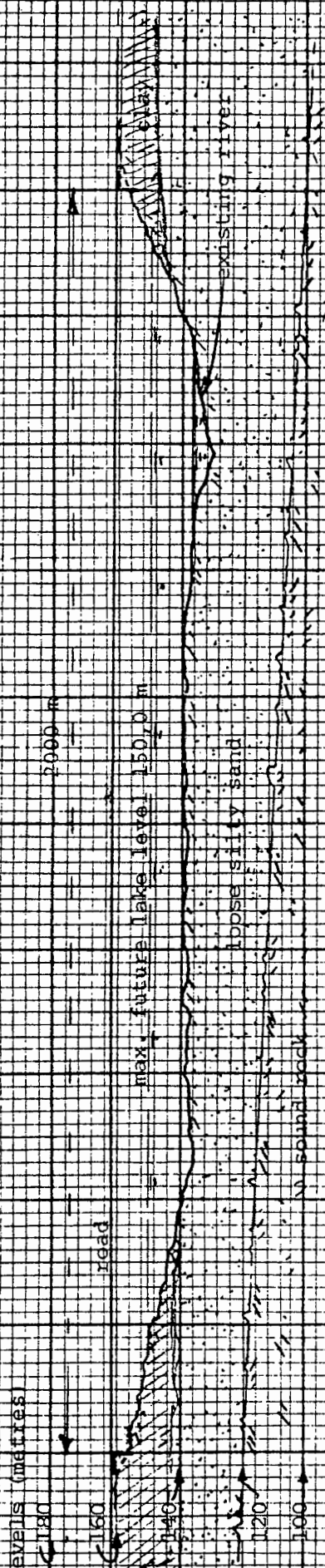

2. (b) A double track railway bridge is required at 30° skew across an existing marshalling yard in the Karroo. Disruption of one day per week on only one pair of adjacent tracks at a time is permitted. The site is flat and level, and the aim is for minimum difference in track levels. A 5,0 m vertical clearance is required and must also be maintained during construction.

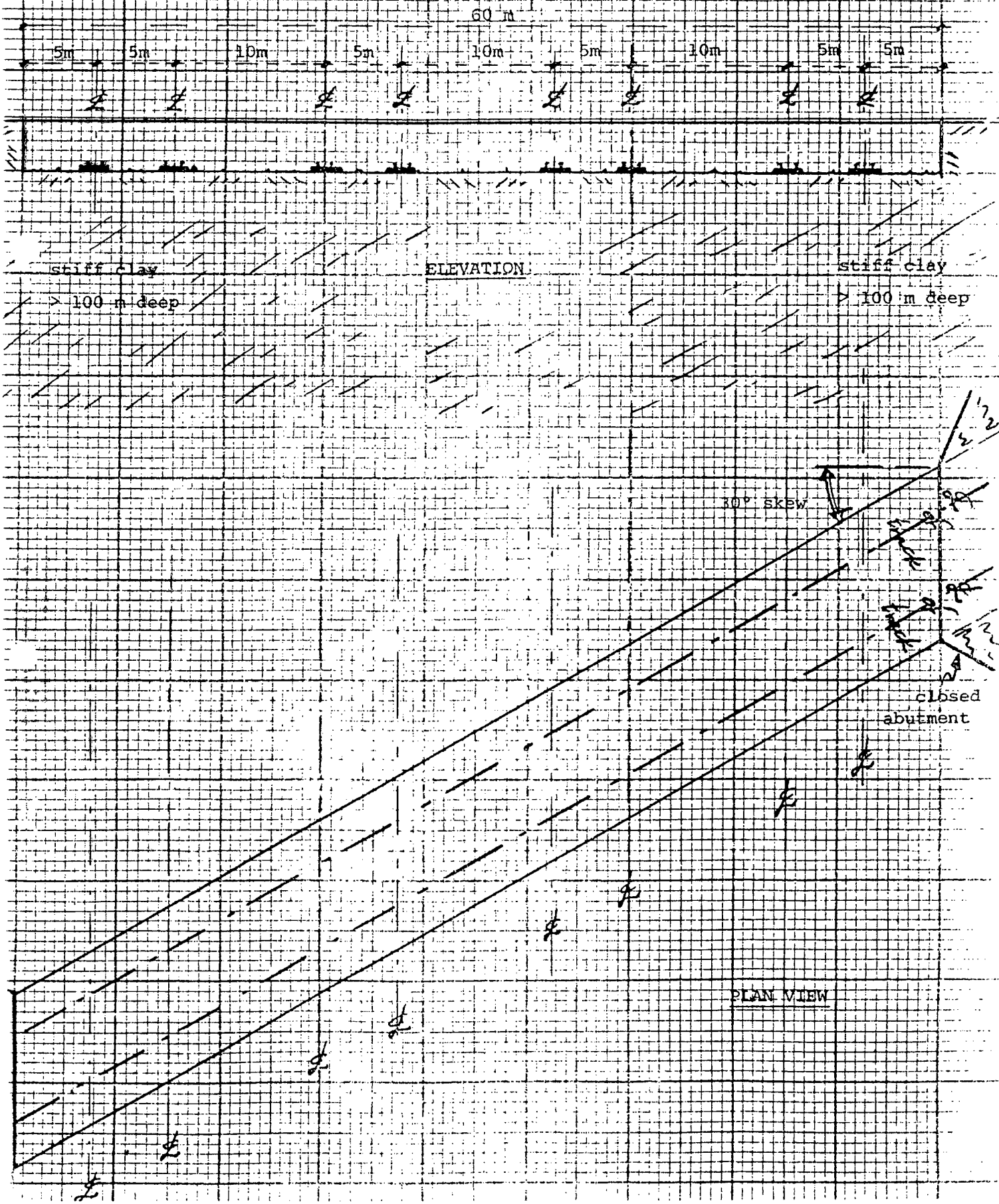

2. (c) A straight sloping conveyor belt bridge is required from a factory to a silo square across an existing six-lane dual carriageway freeway near Cape Town. The 2 m wide conveyor must be fully enclosed against the weather. Provision must be made for the possibility of dismantling and relocation of the bridge, including its supports.

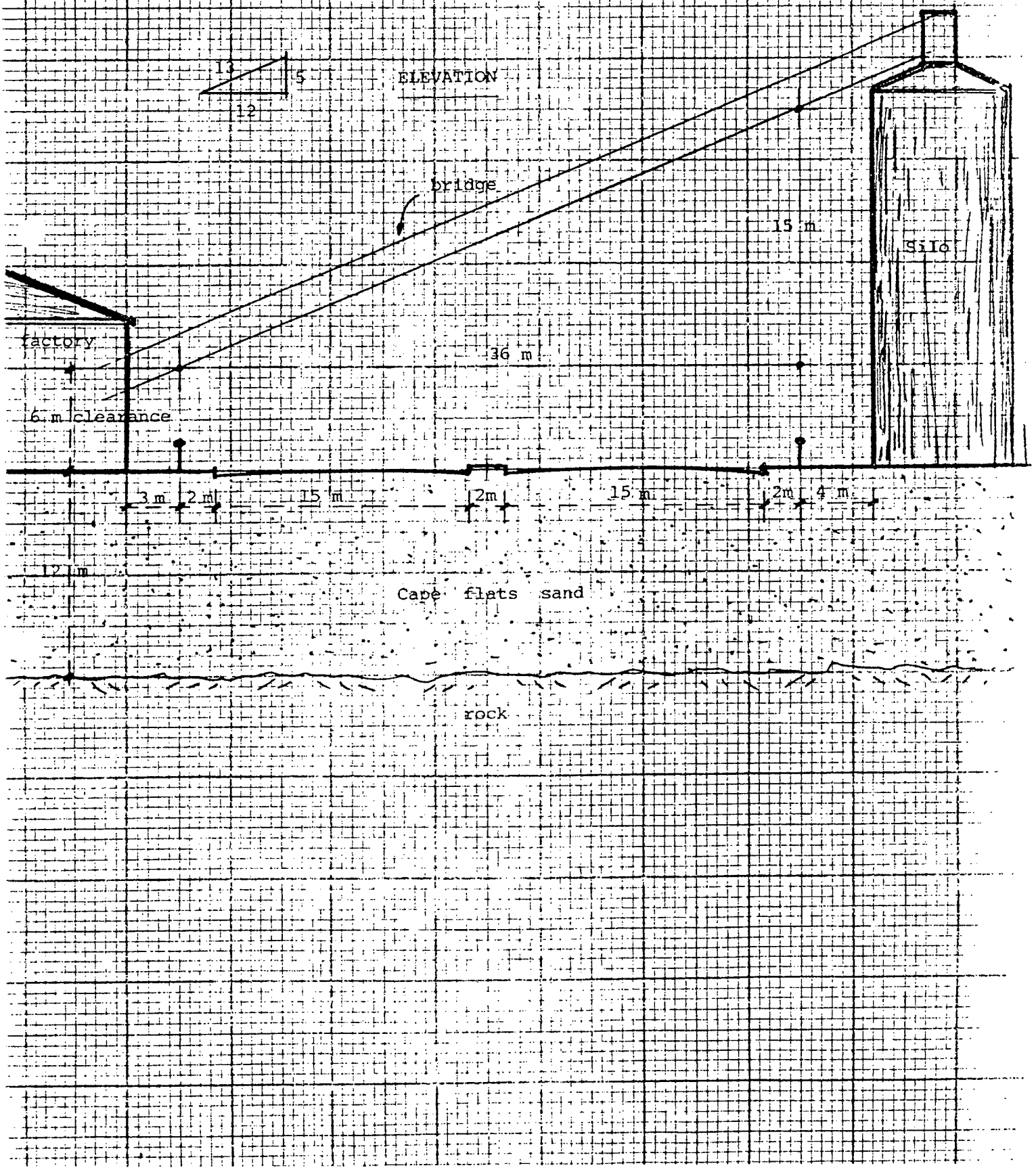

UNIVERSITY OF CAPE TOWN

DEPARTMENT OF CIVIL ENGINEERING

UNIVERSITY EXAMINATION : JUNE 1982

CE 551(a) : FRAME ANALYSIS

Time Allowed: 3 Hours

Answer all three questions. All questions carry the same mark. Lecture notes and Assignment solutions may be consulted.

1. The horizontal cantilever of uniform cross-section shown in Figure 1 is made up of a straight bar AB, of length R, and a quarter-circular arc BC, of radius R and length $\frac{1}{2}\pi R$, connected rigidly and tangentially to it. A vertical load W is applied at C.

   Determine the vertical deflection, slope and twisting-rotation at C. Ignore axial and shear strains. Express your answer in terms of W, R, EI and GJ.

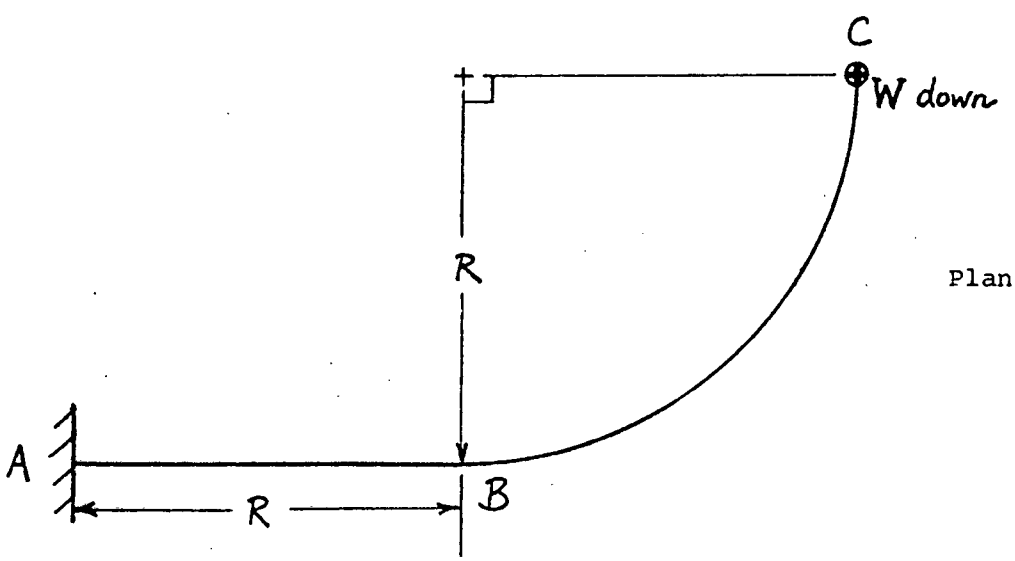

Plan View

Figure 1

2. The parabolic arch shown in Figure 2 has span L and height h. It is pin-jointed to rigid abutments on the same horizontal level at A and D. The flexural rigidity of the arch varies over the span and is proportional to the secant of the angle of slope α, with a minimum value EI_o at the mid-span apex C. The axial stiffness also varies but is proportional to the cosine of the angle of slope α with a maximum value EA_o at the apex C.

Determine the reactions at A and D when a vertical load W is applied at the quarter point B, $\frac{1}{4}$L horizontally from A. Include both bending and axial strains but ignore strains due to shear.

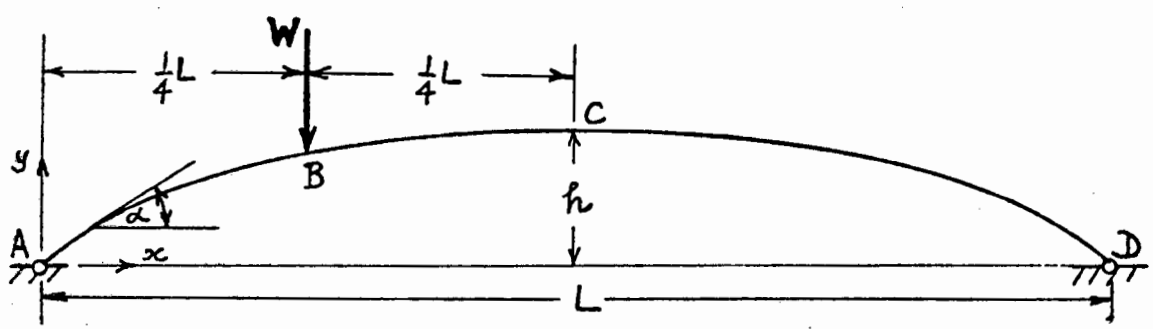

Figure 2

3. The mechanical stability model shown in Figure 3 consists of a rigid bent bar ACD, with AC at right angles to CD. The length L of AC is much greater than the length e of CD.

The bar is pinned at its lower end A to a rigid support and AC is initially vertical. Rotation about A is resisted by a linear spring of stiffness k. One end of the spring is attached to AC at B, distance a from A, while the other end E is attached to a trolley, which is free to move vertically, so that BE always remains horizontal. When AC is vertical the spring is unstretched.

A vertical load P is applied at D. For $e = 0$, determine the bifurcation point by small displacement analysis.

For $e > 0$, use large displacement analysis to derive a general expression for P in terms of k, a, L, e and trigonometrical functions of θ. Hence determine the maximum value of P and the angle θ at which it occurs for a given $\frac{e}{L}$. Plot a graph of P against θ for $\frac{e}{L} = 0{,}1$.

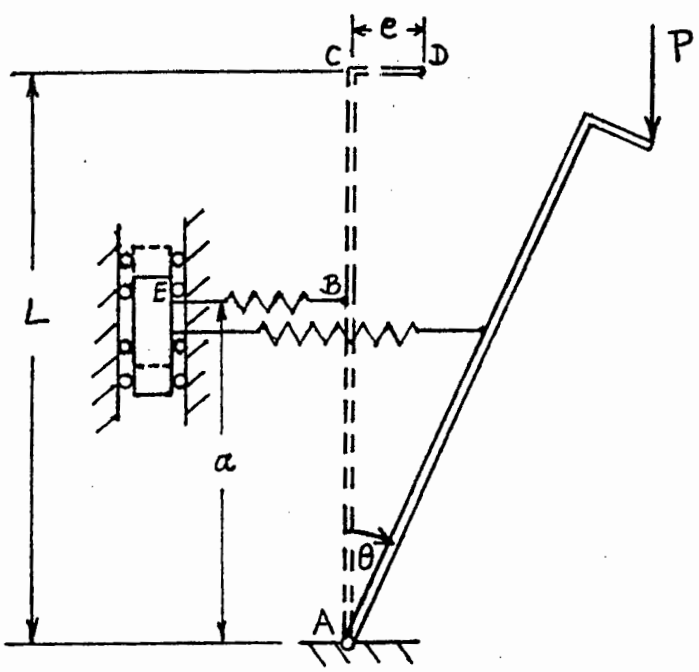

Figure 3

UNIVERSITY OF CAPE TOWN

DEPARTMENT OF CIVIL ENGINEERING

UNIVERSITY EXAMINATION : JUNE 1982

CE 551(b) : INTRODUCTION TO THE THEORY OF ELASTICITY

TIME ALLOWED: 2 hours Full Marks 100

1. Find the reactions at the ends of the beam subjected to a uniformly distributed load as shown in the diagram below. Use the stress function provided and check your answer using statics. Sketch the stress profile in the x direction at the end of the cantilever.

$$\phi(x,y) = x^2(Ay^2+By^3) + Cy^2 - \frac{2w}{5d}y^3 + Dy^4 - \frac{w}{5d^3}y^5$$

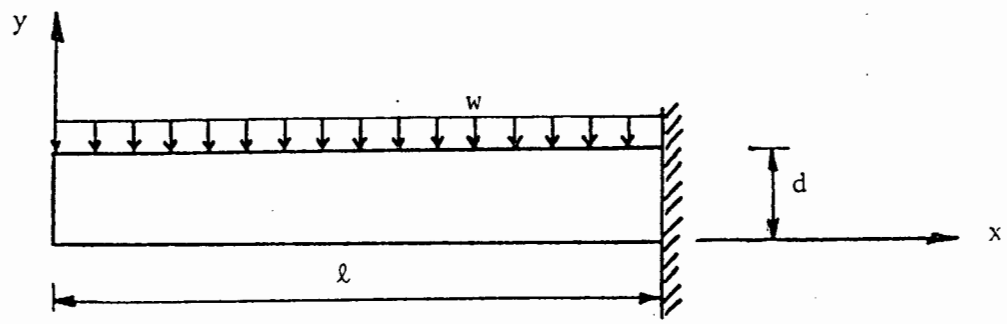

[40]

2. (a) Find the radial stress distribution in terms of r and θ for the semi-infinite body subject to a concentrated load as shown in the diagram below. Find the resultants of this stress distribution at some radius r.

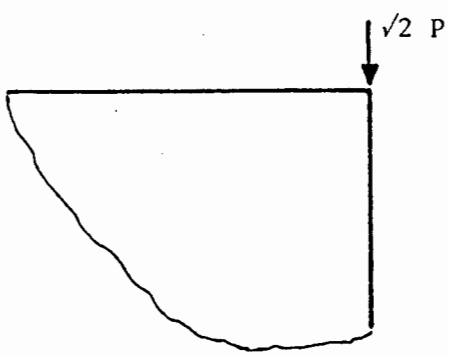

[10]

2 (b) For a concentrated force acting at an angle ψ on a semi-infinite plane the simple radial solution for the stresses can be used if θ is measured from the line of action of the force. Rewrite the radial stress in terms of θ and ψ for the co-ordinate system as shown below. Use the result from (a) to verify this answer.

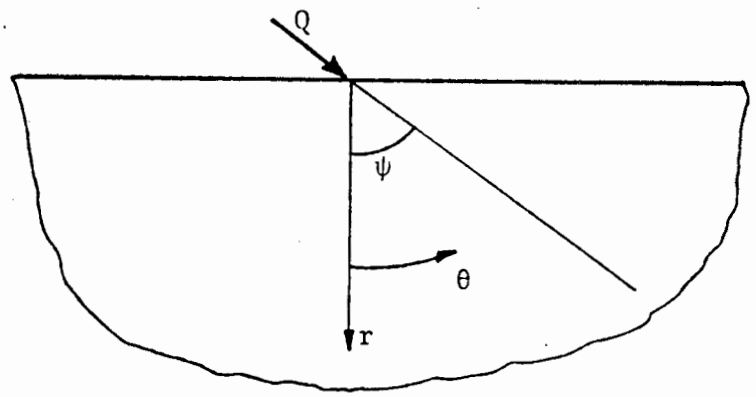

[10]

3. The beam shown in the diagram below is the same as that in Question 1, but with a different co-ordinate system. Determine the reactions at the ends of the beam and also find an expression for the stress in the x direction. Use the principle of virtual work and the assumed displacement function provided. Sketch the stress profile in the x direction at the end of the cantilever. Compare this with your answer to Question 1 and comment.

$$v(x) = \frac{w}{336\ EI}\ x^4 + Ax^3 + Bx^2 + Cx + D$$

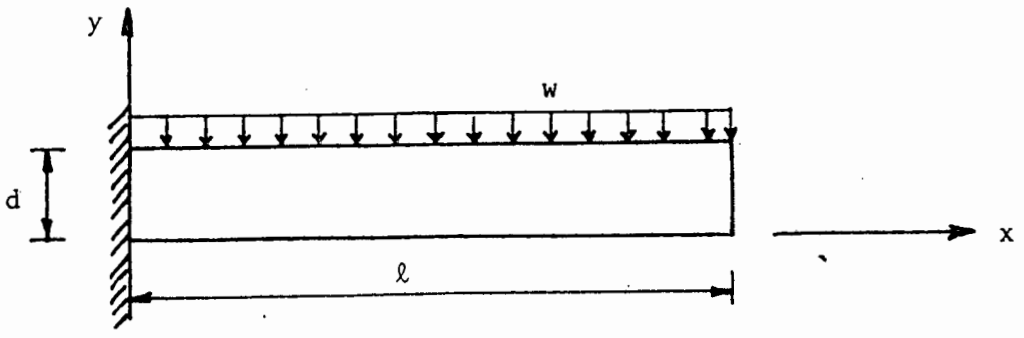

[40]

Formulae which may be useful:

$$\int \cos^2 ax\,dx = \frac{x}{2} + \frac{\sin 2ax}{4a}$$

$$\int \sin^2 ax\,dx = \frac{x}{2} - \frac{\sin 2ax}{4a}$$

$$\int \cos ax \sin ax\,dx = \frac{\sin^2 ax}{2a}$$

$$\cos(x \pm y) = \cos x \cos y \mp \sin x \sin y$$

$$\sin(x \pm y) = \sin x \cos y \pm \cos x \sin y$$

UNIVERSITY OF CAPE TOWN

DEPARTMENT OF CIVIL ENGINEERING

UNIVERSITY EXAMINATION - OCTOBER 1982

CE 551(c) PLATES AND SHELLS

Time Allowed: 3 hours Examination Date: 29 October 1982

ANSWER ALL THREE QUESTIONS

1. A simply supported thin circular plate is loaded by a rotationally symmetric load as shown, with a maximum edge value of p_o per unit area.

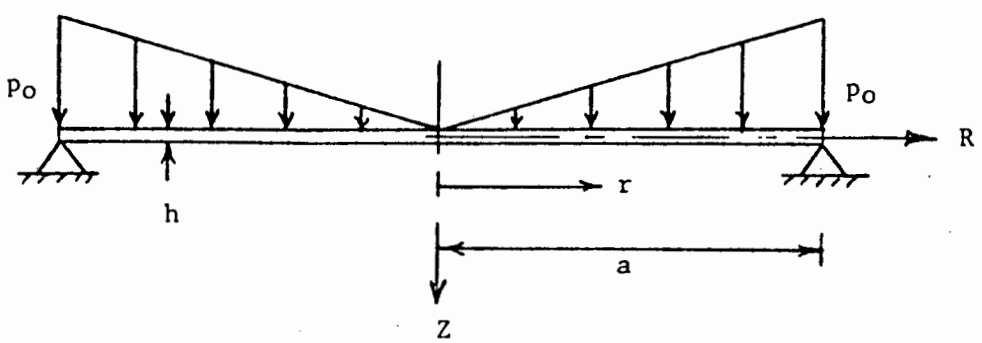

Find the deflection and the bending moment at the centre of the plate if:

$E = 30.0\ GN/m^2$ $\nu = 0.2$

$p_o = 10.0\ kN/m^2$ $h = 0.3\ m$

$a = 10.0\ m$

[45 marks]

2. A thin elliptic plate with fully clamped edges is subjected to a uniform transverse load q_o per unit area, as shown.

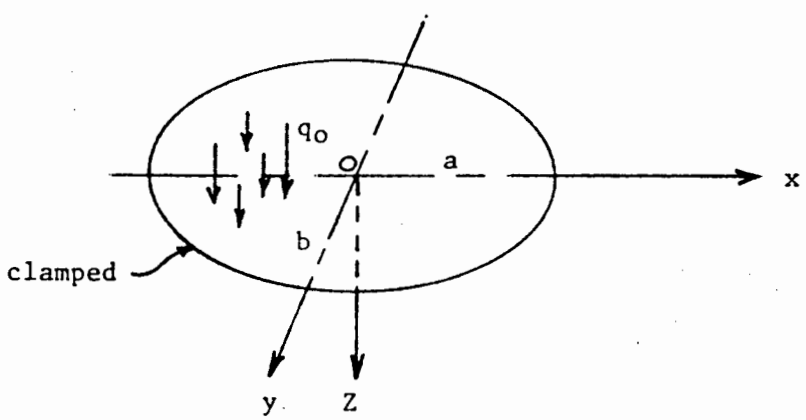

The equation/...

2. (continued)

The equation of the plate boundary is given by

$$\frac{x^2}{a^2} + \frac{y^2}{b^2} = 1$$

The assumed transverse deflection w can be given by

$$w = A\left(\frac{x^2}{a^2} + \frac{y^2}{b^2} - 1\right)^2$$

where A is a constant, and the assumed deflection satisfied the Lagrange equation.

(a) Show that the assumed transverse deflection w satisfies the boundary conditions of a clamped plate.

(b) Determine expressions for the deflection w and the bending moments M_x and M_y.

(c) Hence find the midspan deflection and bending moments if:

E	= 30.0 GN/m^2	ν	= 0.2	h	= 0.3 m
a	= 5.0 m	b	= 3.0 m	q_o	= 10.0 kN/m^2

[36 marks]

3.

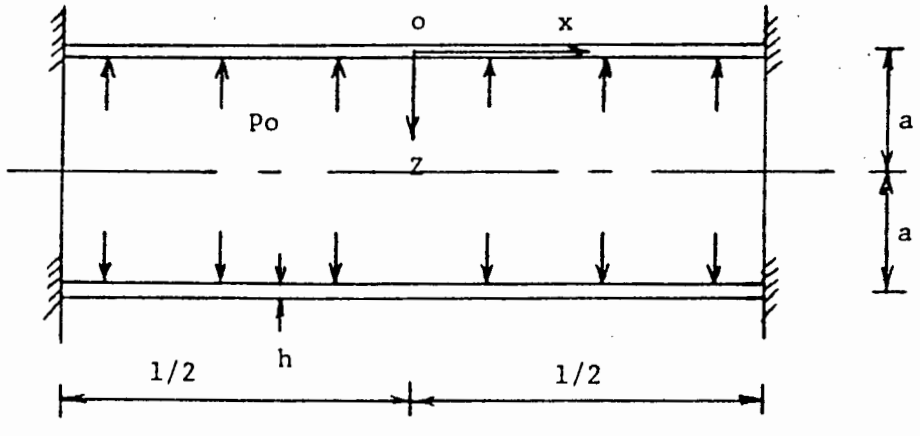

A cylindrical pressure vessel of length l and radius a is subjected to an internal pressure p_o. If the ends of the cylinder are rigidly clamped, and assuming that the length is not large in comparison with the radius, i.e. using bending theory, the general form of the transverse deflection can be given by

w = /.....

3. (continued)

$$w = A_1 \sin \beta x \sinh \beta x + A_2 \sin \beta x \cosh \beta x + A_3 \cos \beta x \sinh \beta x + A_4 \cos \beta x \cosh \beta x + w_p$$

where $w_p = \frac{Z}{4\beta^4 D}$ is a particular solution of the compatibility equation

$$\frac{d^4 w}{dx^4} + 4\beta^4 w = \frac{Z}{D}$$

and $\beta^4 = \frac{Eh}{4a^2 D}$.

Determine expressions for the constants A_i in the general equation for the deflection w satisfying clamped boundary conditions.

Note: $\frac{d}{d\theta}(\cosh \theta) = \sinh\theta$

$\frac{d}{d\theta}(\sinh \theta) = \cosh\theta$

$\cosh^2\theta - \sinh^2\theta = 1$

$\sinh\theta \cosh\theta = \frac{1}{2} \sinh 2\theta$

[19 marks]

- - - - -

UNIVERSITY OF CAPE TOWN

DEPARTMENT OF CIVIL ENGINEERING

UNIVERSITY EXAMINATION : JUNE 1982

CE 552(a) : INTRODUCTION TO FINITE ELEMENT METHOD

TIME ALLOWED: 2 hours TOTAL MARKS: 100

ANSWER ALL QUESTIONS

OPEN BOOK

1. Illustrate the direct (virtual work) and minimization of total potential energy finite element formulations by deriving the stiffness matrix for the linear truss element.

[15 marks]

2. (a) From energy principles, one can argue summability of stiffnesses, i.e. stiffness matrices can be calculated element by element and then summed according to element connectivity. What does this imply in terms of the nature of approximation functions in finite element analysis ?

(b) What are the properties of Lagrange and Hermite approximation polynomials ?

(c) In potential energy formulations, how does one decide on the suitable type of approximation to use ? Give reasons.

(d) Approximation functions have to satisfy certain criteria to ensure convergence of the finite element solution. What are these criteria ?

[20 marks]

3. Consider the three-node quadratic isoparametric truss element in Fig.(a). Show that if node 2 is specified to be at the quarter point, Fig.(b), the stress has a singularity of $1/\sqrt{x}$ at node 1.

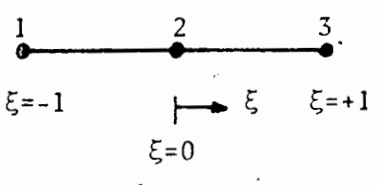

(a) Parent element

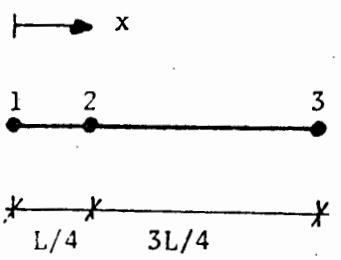

(b) Mapped $\frac{1}{4}$ point element

(Hint: stress is given by $\sigma=DBu$).

[20 marks]

.... page 2.

4. The stiffness matrix for the assemblage of axially loaded bars shown in the diagram below can be expressed as

$$K_{ij} = \begin{bmatrix} 1 & 0 & -1 & 0 & 0 \\ 0 & 2 & -2 & 0 & 0 \\ -1 & -2 & 6 & -3 & 0 \\ 0 & 0 & -3 & 7 & -4 \\ 0 & 0 & 0 & -4 & 4 \end{bmatrix}$$

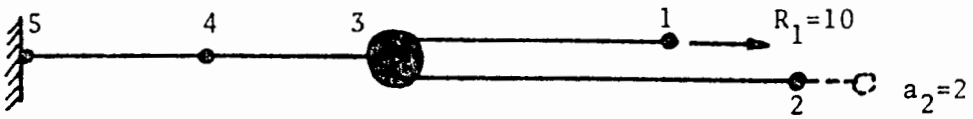

For a load R_1=10 applied at node 1 and a displacement a_2=2 prescribed at node 2, solve the equilibrium equations

$$K_{ij}\, a_j = R_i$$

where a_j and R_i are the displacement and load vectors defined as

$$a_j = \begin{bmatrix} a_1 \\ a_2 \\ a_3 \\ a_4 \\ a_5 \end{bmatrix}, \quad R_i = \begin{bmatrix} R_1 \\ R_2 \\ R_3 \\ R_4 \\ R_5 \end{bmatrix}$$

[15 marks]

5. Consider the tie supported cantilever shown below.

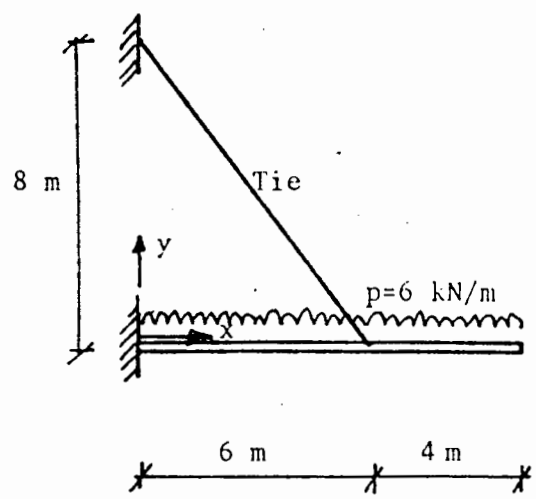

Tie: EA = 400 MN

Beam: EI = 20 MNm^2

EA = 800 MN

(neglect shear strains)

5(cont).. page 3.

Question 5 (continued)

Carry out the finite element calculations up to the equation solving stage. Then assuming some displacements, show how the stress resultants can be obtained.

Use linear isoparametric truss elements and conventional cubic beam elements.

Clearly show each of the main steps in the finite element calculation.

[30 marks]

TOTAL : [100 marks]

UNIVERSITY OF CAPE TOWN

DEPARTMENT OF CIVIL ENGINEERING

UNIVERSITY EXAMINATION - NOVEMBER 1982

CE 552(b) - FINITE ELEMENT ANALYSIS

This examination will extend until
12.00 noon on 16th November 1982

A bicycle manufacturer has an idea for a new wheel which he wishes to analyse numerically (see attached diagram).

He is uncertain as to whether there are sufficient spokes and what their diameter should be in order to prevent collapse of the wheel.

You are required to present a brief written report with adequate numerical analysis indicating your views on the suitability of the number of spokes and what diameter they should be so that the yield stress is not exceeded in any spoke, assuming linear elastic behaviour. Your report should make clear to the client the reasons for all decisions which you make regarding the analysis.

The report should answer the following:

(i) the recommended spoke diameter
(ii) what the deflection at A is
(iii) which is the highest stressed spoke and what the stress in this spoke is
(iv) the highest stress in the rim.

Problem Data.

Rubber Tyre: (Treat as linear elastic material)

$E = 1.61 \times 10^6$ N/m^2

$\nu = 0,45$

$\rho = 913$ kg/m^3

Aluminium:

$E = 70 \times 10^9$ N/m^2

$\nu = 0.3$

$\sigma_y = 50 \times 10^6$ N/m^2 (yield stress)

$\rho = 2720$ kg/m^3

2/....

Loading: Horizontal force at A = 0.75 kN

Vertical force at A = 0.50 kN

Boundary Conditions:

The wheel is assumed to be 'locked', i.e. fixed to the ground at its point of contact.

Notes:

1. The spokes are assumed to be pinned at both ends.

2. Do not alter the number of spokes.

3. It is suggested that you do not use more than one element per spoke for each component.

4. To maintain stability fix the two nodes on either side of the tyre/ground contact point.

- - - - - -

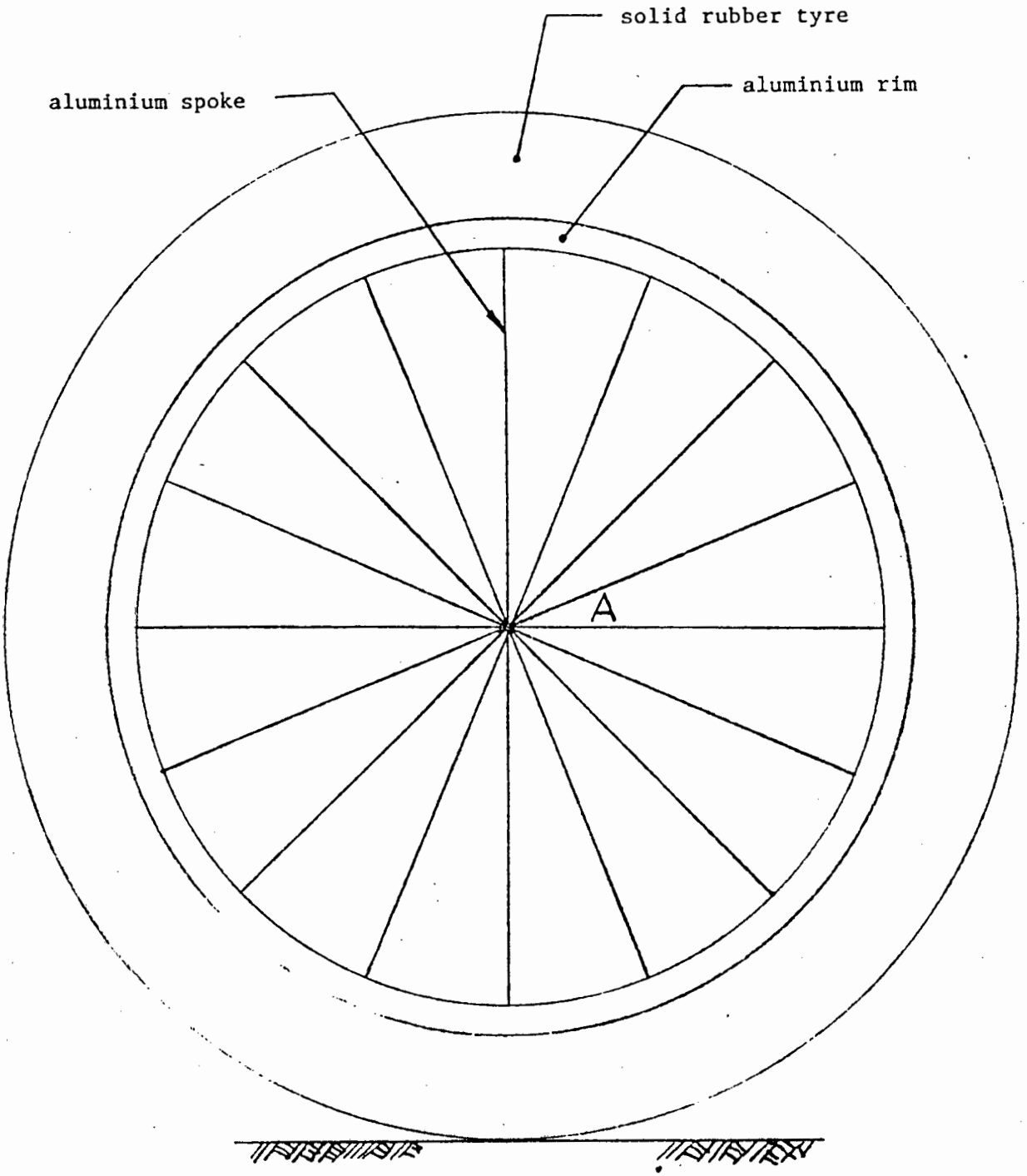

Wheel outer diameter = 1 m

Tyre thickness = 100 mm

Rim thickness = 30 mm

BICYCLE WHEEL

UNIVERSITY OF CAPE TOWN

DEPARTMENT OF CIVIL ENGINEERING

UNIVERSITY EXAMINATION - NOVEMBER 1982

CE 554 - COMPUTER-AIDED DESIGN

Time Allowed : 3 hours

Examination Date: 6 November 1982

ANSWER BOTH QUESTIONS

Question 1.

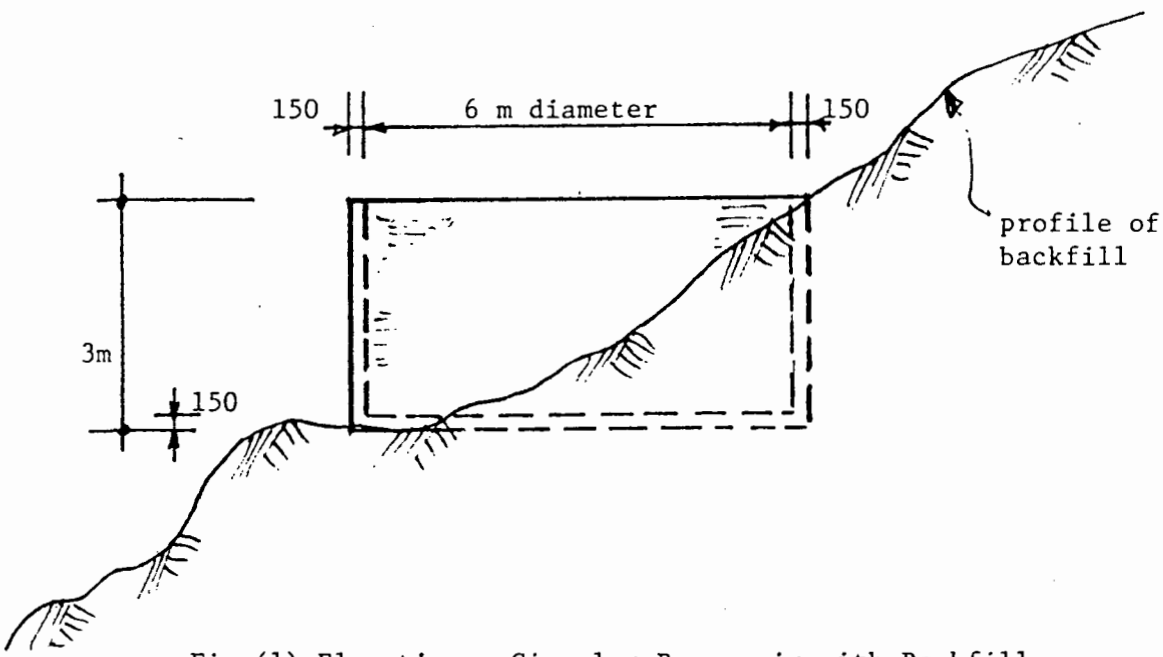

Fig.(1) Elevation - Circular Reservoir with Backfill

(i) Describe the type of finite elements which would be suitable for the analysis and design of the reinforced concrete reservoir shown in Fig. (1). Provide as much information about these elements as you can without going into the theoretical details which would be necessary for the formulation of the finite element method of analysis.

[20]

(ii) Indicate the element subdivision which you would consider to be suitable for this analysis.

[10]

(iii) What alternative methods of finite element analysis can be used in this type of structure. Show a proposed subdivision of the elements for each method together with a description of each type of element.

[15]

(iv) What information do you expect to get from each type of finite element analysis described above.

[5]

50

Question 2/....

Question 2.

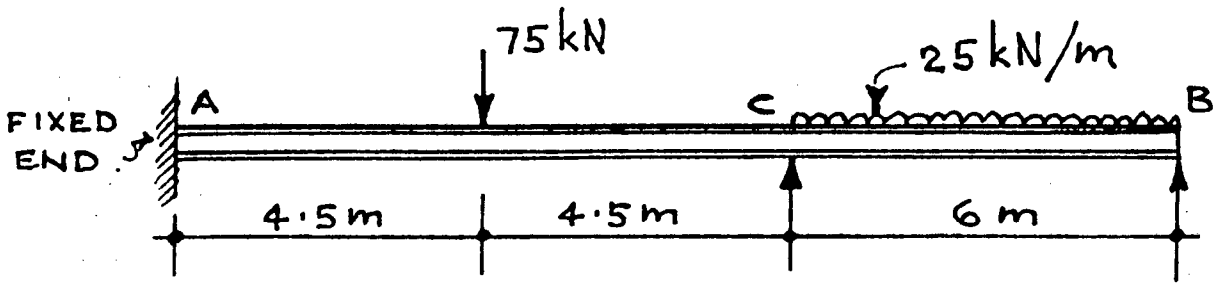

Fig.(2) - 2-Span Beam

(i) Use the dynamic programming method together with the elastic-plastic analysis technique to determine the optimum structural cost for the 2-span beam shown in Fig.(2). Each span can have different cross sectional properties. Assume that the relative cost of each section can be calculated from the mass times the span.

A table of available sections is as follows:

Section	1	2	3	4
Mass kg/m	25	31	41	45
M_p	77	92	144	178

[40]

(ii) What are the disadvantages of this approach.

[10]

50

- - - - - - -